



Diese Dissertation haben begutachtet:  
Prof. Dr. Ulrich SCHUBERT

Prof. Dr. Nicola HÜSING

## DISSERTATION

# **Synthesis of CeO<sub>2</sub>-Based Materials by Combination of Sol- Gel and Solvothermal Processing and their Application for Catalytic CO Oxidation**

ausgeführt zum Zwecke der Erlangung des akademischen Grades eines Doktors  
der Naturwissenschaften

unter der Leitung von  
O. Univ.Prof. Dr. Ulrich SCHUBERT

Institut für Materialchemie (E165)

Eingereicht an der Technischen Universität Wien

Fakultät für Technische Chemie

Von

Dipl.-Ing. Dr. Jingxia YANG

Mat.Nr. 1228620

Portnergasse 15/27, 1220 Wien

Wien, am 31.07.2014

*Few things are impossible in themselves;  
and it is often for want of will,  
rather than of means, that man fails to succeed.*

*--La Rocheforcauld, French writer*

## Acknowledgements

This work has been finished under lots of selfless helps; here I would like to express my thanks to the following nice and kind people:

Thanks to Prof. Schubert for giving me the chance to work in his group and all his in time supporting. He is always wise to point out the direction for my research, tolerant with my bad English and encourages me for each presentation. The knowledge I gained from him is not only limited to the scientific work, but also in the personal development.

Thanks to Prof. Nicola Hüsing for willing to be the second reviewer for my dissertation, and willing to travel to Vienna for my oral defense in this hot summer time.

Thanks to Liliana for bringing me into the world of CO oxidation, explaining and answering my stupid questions about the catalytic characterization and the proof for the dissertation. Thanks to Hao for the XPS measurements and the numerous help during our shifting to the new apartment. Thanks to Dr. Karin Föttinger for kindly allowing me to use the kinetic setup for CO oxidation. Thanks to Prof. Günther Rupprechter for his novel insight and nice correction during the manuscript writing.

Thanks to Dr. Johannes Akbarzadeh and Prof. Herwig Peterlik for their fast SAXS measurement and the nice fitting and explanation of the results. Thanks to Elisabeth Eitenberger for the nice SEM measurement. Thanks to Dr. Stefan Löffler and Dr. Michael Stöger-Pallach of USTEM center for the kind help and patient sample searching about the (HR)TEM and EDX measurement. Thanks to Dr. Johannes Ofner for the measurement of almost one hundred Raman spectra and the extremely time-consuming Raman mapping. All of them have made my thesis more colorful!

Thanks to my *former* and present colleagues, who form a nice working atmosphere: Andre (for the nice organization of Solids4fun doctoral school), Anita (for the sweet smile), *Aparna* (for sharing me lots of funny story and broadening my eyes to India), Catarina (for the last several powder XRD measurement, and also the nice suggestion during my Portugal travelling), *Christian* (for leading me into the ligand synthesis), Christine (for the nice single crystal and part of powder XRD measurements), Elisabeth (for being the nice hood neighbor), Felix, Harald (for

each problem I met with TU cards and the computer and network problem), *Hongzhi* (for reminding me the operation of the equipment), *Jacob, Jasmin, Johannes* (a nice companion in Solids4fun program), *Maia* (for the discussion about future), *Matthias* (for showing me the process of Ph.D defense application), *Marco, Marina* (for showing me the first eyes about my aboard life and the sol-gel world), *Martin* (for helping me to recognize the hand-writing of Prof. Schubert), *Melitta* (for lots of document preparations), *Michael* (for showing me the NMR measurement and analysis), *Miriam, Partrik, Rupali, Rupert* (for the pump repairing), *Sarah* (for nicely taking care TGA and IR equipment), *Stefan B.* (for leading my first step into the precursor synthesis), *Stephan R.* (for bringing me numerous chemical and experimental stuff ), *Sven* (for the nice help about FESEM and EDX measurement), *Van An, Valeria* (for being my nice and funny office mate) and *Wenjing* (for telling me lots of tips during my pregnancy).

Thanks to FWF and Solids4fun doctoral school, who provided the funding and nice study program during this Ph.D study! And also thanks to the professors and students in this school, who widened my knowledge in physics, theoretical calculation and photonic science.

Thanks to all my friends out of University in Vienna, who spend lot of time with me for travelling, shopping, dining and playing cards, making my life plenitude. And also thanks to all my friends in China, who convey many funny stories and help me with every demand I asked, letting me feel that I am not always in abroad.

Thanks to my parents, parents in-law and my brother, for encouraging and supporting me for this study pursing. Thanks to my husband *Renzhe*, for every cooking and accompanying, and for the abstract translation. The appreciation to him can be written with more than thousand words. And also thanks to my unborn girl *Duoduo*, for giving me new kinds of life feeling and not bringing me too much un-wellness (though I had to cut down part of my experimental plan). All of them are my strong back-supporting and motivation for going forward.



## Zusammenfassung

Wegen der guten Sauerstoff-Speicherung-Freisetzung-Kapazität von  $\text{CeO}_2$ , wird es häufig als Katalysator oder Katalysatorträger für CO-Oxidation eingesetzt. Dafür sind die hohe Oberfläche sowie die rasche Bildung der dissoziierten Sauerstoffatome zwei wichtige Eigenschaften. In dieser Arbeit wurde  $\text{CeO}_2$  durch den Sol-Gel-Prozess synthetisiert, wobei Cer-tetrabutoxid als Ausgangsmaterial verwendet wurde. Das erhaltene Gel wurde unter diversen Bedingungen behandelt, um ein Material mit den oben genannten Eigenschaften zu erhalten. Nachdem die optimalen Syntheseparameter für  $\text{CeO}_2$  herausgefunden wurden, wurde  $\text{CeO}_2$  durch  $\text{Co}_3\text{O}_4$  oder Graphen modifiziert, um die katalytische Kapazität des Materials weiter zu erhöhen.

$\text{CeO}_2$  wurde zuerst aus einem Gel, welches aus Acetaldoximat-modifiziertem Cer(IV)-t-butoxid (CeB) in Gegenwart des nichtionischen Tensids Pluronic F127 erhalten wurde, durch die Kombination von Sol-Gel und Solvothermal-Prozess synthetisiert. Cer(IV)-t-butoxid wurde statt dem oft eingesetzten Ammoniumcernitrat verwendet, um das Material zuverlässiger und regulierbarer zu machen. Die postsynthetische Behandlung des Gels und die Zusammensetzung des Gemischs der Ausgangsmaterialien erwiesen sich als äußerst wichtig für die hohe Oberfläche des Cerdioxids und einen höheren  $\text{Ce}^{3+}$ -Anteil. Die Calcinierung in Luft oder unter Stickstoff wurde verglichen mit der solvothermalen Behandlung in Ethanol oder Wasser und der Kombination dieser zwei Methoden. Das erhaltene Material bestand aus 3,5–5,5 nm Cerdioxid-Nanopartikeln. Die höchste spezifische Oberfläche ( $277 \text{ m}^2/\text{g}$ ) wurde nach der solvothermalen Behandlung erhalten; sie reduzierte sich auf  $180 \text{ m}^2/\text{g}$ , wenn anschließend Calcinierung an Luft durchgeführt wurde, um die verbleibenden organischen funktionellen Gruppen zu beseitigen. Der höchste  $\text{Ce}^{3+}$ -Anteil war 18% nach der Solvothermal-Behandlung in Ethanol und zusätzlicher Calcinierung an Luft. CO-Oxidation in Gegenwart von ausgewählten Proben deutete an, dass die katalytische Aktivität zur Oberfläche des Katalysators proportional ist. Der höchste Wert wurde erhalten, wenn die Probe in Ethanol solvothermal behandelt wurde. Die Reaktionsgeschwindigkeit der besten Probe war ungefähr 75 mal höher als mit kommerziellem Cerdioxid.

Da die Kombination vom Sol-Gel und Solvothermal-Prozess (in Ethanol) zu  $\text{CeO}_2$  mit hoher Oberfläche und hohem  $\text{Ce}^{3+}$ -Anteil führte, wurde diese Methode auch eingesetzt, um  $\text{Co}_3\text{O}_4$ -modifiziertes  $\text{CeO}_2$  ( $\text{Co} : \text{Ce} = 1:4$ ), welches eine niedrigere light-on-Temperatur ( $T_{10\%}$ ) als  $\text{CeO}_2$

besitzt, zu synthetisieren. Die Verteilung des Cobalts wurde durch die unterschiedliche Zugabe der  $\text{Co}^{2+}$  Ionen zu den Gelen kontrolliert. Im Syntheseweg 1 (gekennzeichnet als **1**) wurde ein Cerdioxid Gel zuerst synthetisiert, gefolgt von der  $\text{Co}(\text{OAc})_2$  Zugabe zum Gel während der Solvothermal-Behandlung. Im Syntheseweg 2 (gekennzeichnet als **2**) wurde eine Mischung aus CeB und  $\text{Co}(\text{OAc})_2$  verwendet um ein Gel für die Solvothermal-Behandlung zu produzieren. Im Syntheseweg 3 (gekennzeichnet als **3**) wurden CeB und  $\text{Co}^{2+}$  Ionen durch *p*-Carboxylbenzaldehydoxim (POBC-H) vernetzt um einen Single-Source Precursor (SSP) herzustellen, welcher zu einem Gel für die Solvothermal-Behandlung umgewandelt wurde. Drei verschiedene Strukturen wurden damit erhalten:  $\text{Co}_3\text{O}_4$  Nanopartikel an der Oberfläche der  $\text{CeO}_2$  Partikel (**1**), koexistierende  $\text{Co}_3\text{O}_4$  und  $\text{CeO}_2$  Nanopartikel (**2**) oder Cobaltoxid Strukturen homogen verteilt in  $\text{CeO}_2$  (**3**). Die Beziehung zwischen den verschiedenen Strukturen und Eigenschaften von  $\text{Co}_3\text{O}_4$ - $\text{CeO}_2$  wurde hinsichtlich der Kristallitphase, Partikelgröße, Oberfläche und katalytischer Aktivität für CO Oxidation erforscht. Material **1**, in welchem  $\text{Co}_3\text{O}_4$  Nanopartikel an der Oberfläche der  $\text{CeO}_2$  Partikel feinverteilt sind, hat die höchste katalytische Aktivität. Variation des Anteils an Co (10%-80%) bei Syntheseweg 1 belegte die Bedeutung der Feinverteilung der  $\text{Co}_3\text{O}_4$  Phase.

Graphen (rGO) wurde danach in  $\text{CeO}_2$  Materialien eingesetzt, und Graphen-ähnliche organische Rückstände wurden während der Solvothermal-Behandlung beobachtet. Der Einsatz des Graphens war günstig für die CO Oxidation. rGO wurde aus chemisch reduziertem Graphenoxid (GO) synthetisiert, welches durch Hummers Methode hergestellt wurde. Sowohl Ethanol als auch *L*-Ascorbinsäure wurden als Reduktionsmittel für rGO verwendet. Letzteres konnte zwar die Qualität des rGOs (d. h. mit weniger Fehlstellen) erhöhen, produzierte aber organische Rückstände auf den Partikeln und inhibierte damit deren Wachsen. rGO konnte die katalytische Aktivität von  $\text{CeO}_2$ , aber nicht von  $\text{Co}_3\text{O}_4$ - $\text{CeO}_2$  erhöhen.

## Abstract

Due to the good oxygen storage-release capacity of  $\text{CeO}_2$ , it is widely used for CO oxidation as catalyst or catalyst support. To this aim, high surface area and fast formation of dissociated oxygen atoms are two important properties. In this research,  $\text{CeO}_2$  was synthesized by the sol-gel method using cerium tetra-butoxide as precursor, and the obtained gels were treated under different conditions in order to get materials with these properties. After optimizing the synthesis parameters for  $\text{CeO}_2$ ,  $\text{Co}_3\text{O}_4$  and graphene were used to modify  $\text{CeO}_2$  to get composite materials with high catalytic activity.

First,  $\text{CeO}_2$  was synthesized by combined sol-gel and solvothermal processing of gels obtained from acetaldoximate-modified cerium(IV) *t*-butoxide (CeB) in the presence of the non-ionic surfactant Pluronic F127. The use of CeB as precursor contrasts very favorably with the often used ceric ammonium nitrate and results in more reliable and tailorable properties of the final materials. The kind of post-synthesis treatment of the gels and the composition of the precursor mixture proved to be crucial for obtaining high surface area ceria with a high  $\text{Ce}^{3+}$  proportion. Calcination in air or under nitrogen was compared with solvothermal treatment in ethanol or water and a combination of solvothermal treatment and calcination. The obtained materials were composed of 3.5–5.5 nm ceria nanoparticles. The highest specific surface area of 277  $\text{m}^2/\text{g}$  was obtained after solvothermal treatment, and 180  $\text{m}^2/\text{g}$  when solvothermal treatment was followed by calcination in air to remove residual organic groups. The highest  $\text{Ce}^{3+}$  proportion was 18% after solvothermal treatment in ethanol and additional calcination in air. CO oxidation on selected samples indicated that the catalytic activity scaled with the surface area and thus was largest for samples solvothermally treated in ethanol. The reaction rate of the best sample was about 75-times larger than that of commercial ceria.

As the combination of sol-gel and solvothermal (in ethanol) processing can yield  $\text{CeO}_2$  with high surface area and  $\text{Ce}^{3+}$  proportion, it was adopted to synthesize  $\text{Co}_3\text{O}_4$ -modified  $\text{CeO}_2$  (Co : Ce = 1:4) in order to lower the ignition temperature of  $\text{CeO}_2$  for CO oxidation. The distribution of Co was controlled by variations of introducing  $\text{Co}^{2+}$  ions into the gels. In route 1 (labeled as **1**), a ceria gel was synthesized first, followed by  $\text{Co}(\text{OAc})_2$  addition to the gel during solvothermal treatment. In route 2 (labelled as **2**), a mixture of CeB and  $\text{Co}(\text{OAc})_2$  was subjected to get the gel for solvothermal treatment. In route 3 (labelled as **3**), CeB and  $\text{Co}^{2+}$  ions were interlinked by

means of *p*-carboxybenzaldehyde oxime (POBC-H) to form a single-source precursor (SSP), which was transformed to a gel for solvothermal treatment. Three different morphologies were obtained, that is Co<sub>3</sub>O<sub>4</sub> nanoparticles located on the surface of CeO<sub>2</sub> particles (**1**), coexisting Co<sub>3</sub>O<sub>4</sub> and CeO<sub>2</sub> nanoparticles (**2**) or Co oxide structures homogeneously distributed within CeO<sub>2</sub> (**3**). The effect of the different morphologies on the properties of Co<sub>3</sub>O<sub>4</sub>-CeO<sub>2</sub> was investigated with regard to the crystallite phase(s), particle size, surface area and catalytic activity for CO oxidation. Material **1** with Co<sub>3</sub>O<sub>4</sub> nanoparticles finely dispersed on the surface of CeO<sub>2</sub> particles had the highest catalytic activity. Change of the Co proportion (10%-80%) of samples prepared by route 1 proved the importance of a finely dispersed Co<sub>3</sub>O<sub>4</sub> phase.

Finally, graphene (rGO) was introduced into the CeO<sub>2</sub>-based materials as graphene-like organic residues were found during solvothermal treatment. This was beneficial for CO oxidation. rGO was synthesized by chemical reduction of graphene oxide (GO), which was prepared according to Hummer's method. Both ethanol and *L*-ascorbic acid were used as reductive agents for rGO. The latter improved the quality of rGO (less defects), but resulted in more organic residues on the particles which inhibited the particle growth. The rGO composite improved the catalytic activity of CeO<sub>2</sub>, but not that of Co<sub>3</sub>O<sub>4</sub>-CeO<sub>2</sub> prepared by route 1.

## **Parts of this work have been published**

“High Surface Area Ceria for CO Oxidation Prepared from Cerium t-Butoxide by Combined Sol-Gel and Solvothermal Processing”, Yang, J.; Lukashuk, L.; Li, H.; Foettinger, K.; Rupprechter, G.; Schubert, U., *Catal. Lett.*, 2014, **144**, 403-412.

## **Parts of this work have been submitted for publication**

“Different synthesis protocols for  $\text{Co}_3\text{O}_4$ - $\text{CeO}_2$  catalysts. Part 1: Influence on the morphology on the nanoscale”, Yang, J.; Lukashuk, L.; Akbarzadeh, J.; Stöger-Pollach, M.; Peterlik, H.; Foettinger, K.; Rupprechter, G.; Schubert, U., *Chem. Eur. J.*, 2014, submitted

## Abbreviations

°	Degree
a.u.	Arbitrary units
AC	Calcination in air
AO	Acetaldoxime
ATR	Attenuated total reflection
BE	Binding energy
BET	Brunauer, Emmett and Teller
BJH	Barrett, Joyner and Halenda
CAN	Ceric ammonium nitrate, $(\text{NH}_4)_2\text{Ce}(\text{NO}_3)_6$
CeB	Cerium <i>tert</i> -butoxide
$\text{Co}(\text{OAc})_2$	Cobalt acetate tetrahydrate dried under vacuum for more than 5h
$\text{Co}(\text{OAc})_2 \cdot 4\text{H}_2\text{O}$	Cobalt acetate tetrahydrate
CO-TPR	CO temperature programmed reaction
D of GO	Diamond band of GO in Raman
$D_{\text{BJH}}$	BJH desorption pore diameter $\text{N}_2$ sorption
DME	1,2-dimethoxyethane.
DMSO	Dimethylsulfoxide
$D_{\text{XRD}}$	Crystallite size calculated from XRD pattern
$E_a$	Apparent activation energy
EDX	Energy-dispersive X-ray spectroscopy
EtOH	Ethanol
F127	Triblock copolymer Pluronic F127, molecular weight ~12600, $\text{H}(\text{OCH}_2\text{CH}_2)_x(\text{OCH}_2\text{CHCH}_3)_y(\text{OCH}_2\text{CH}_2)_z\text{OH}$

$F_{2g}$ of $CeO_2$	Ce-O-Ce symmetric vibration in $F_{2g}$ mode
G of GO	Graphite band of GO in Raman
GO	Graphene oxide
Gp	Graphene
$H_2$ -TPR	$H_2$ temperature programmed reduction
I(D)/I(G)	Intensity ratio of diamond band to graphite band
IR	Infrared
NAC	First calcination in $N_2$ atmosphere, and then further calcination in air
NMR	Nuclear magnetic resonance
$p/p^0$	Relative pressure
POBC-H	<i>p</i> -carboxybenzaldehyde oxime
$q$	Scattering vector
$R_{Coxxx^\circ C}$	Reaction rates on the basis of the unit amount of Co at $xxx^\circ C$
rGO	Reduced graphene oxide
$R_{xxx^\circ C}$	Normalized specific reaction rates of CO oxidation on a unit surface area at $xxx^\circ C$
$r_{xxx^\circ C}$	Reaction rate of CO oxidation at $xxx^\circ C$ per gram
SAXS	Small angle X-ray scattering
$S_{BET}$	Surface area from $N_2$ sorption
SEM	Scanning electron microscopy
Sol/gel-ST	Combination of sol-gel and solvothermal method
Sol-ST	Sols were solvothermally processed without gelation
SSP	Single-source precursor
ST	Solvothermal treatment
STE	Solvothermal treatment in ethanol

STE-AC	Further calcined in air after solvothermal treatment in ethanol
STH	Solvothermal treatment in H <sub>2</sub> O
STH-AC	Further calcined in air after solvothermal treatment in H <sub>2</sub> O
t	Time
T	Temperature
T <sub>10%</sub>	Reaction temperature for 10% CO conversion
T <sub>90%</sub>	Reaction temperature for 90% CO conversion
TEM	Transmission electron microscopy
TGA	Thermogravimetric analysis
Uv-Vis	Ultraviolet-visible
Vc	Vitamin C, <i>L</i> -ascorbic acid
wt%	Weight percent
XPS	X-ray photoelectron spectroscopy
XRD	X-ray diffraction

## NMR Abbreviations

δ	Chemical shift
s	Singlet
d	Doublet
br	Broad peak



## Table of Contents

1. Introduction .....	1
1.1 Sol-gel processing .....	1
1.1.1 Sol-gel chemistry .....	2
1.1.2 Heat-treatment .....	6
1.2 CeO <sub>2</sub> materials and CO oxidation .....	9
1.2.1 CeO <sub>2</sub> materials .....	9
1.2.2 CO oxidation with CeO <sub>2</sub> .....	10
1.3 Research goals .....	12
2. Pure CeO <sub>2</sub> .....	14
2.1 Introduction .....	14
2.2. Advantage of solvothermal treatment in sol-gel process .....	15
2.2.1 Gel preparation .....	15
2.2.2 Influence of different post-synthesis treatments .....	18
2.3 Influence of solvothermal treatment .....	20
2.3.1 Influence of the sol composition .....	20
2.3.2 Calcination after solvothermal treatment .....	23
2.3.3 Catalytic properties .....	27
2.4 Influences of solvothermal temperature (T) and time (t) .....	33
2.4.1 Influence of solvothermal temperature (T) .....	34
2.4.2 Influence of different solvothermal reaction time (t) .....	37
2.5 Role of gel processing for CeO <sub>2</sub> samples .....	42
2.6 Summary .....	46
3. Co <sub>3</sub> O <sub>4</sub> modified CeO <sub>2</sub> .....	48
3.1 Introduction .....	48

3.2 Influence of Co precursor adding sequence .....	49
3.2.1 Synthesis of Ce-L-B-L'-Co single source precursor .....	50
3.2.2 Materials characterization.....	51
3.2.3 Structure model.....	58
3.2.4 Structural evidence from CO-TPR (temperature-programmed reactions) .....	61
3.2.5 Catalytic properties .....	65
3.3 Influence of the Co oxide proportion .....	69
3.3.1 Basic material properties .....	69
3.3.2 Influence of the Co proportion on the catalytic properties .....	72
3.4 Summary.....	74
4. Graphene-CeO <sub>2</sub> and graphene-Co <sub>3</sub> O <sub>4</sub> -CeO <sub>2</sub> composites .....	75
4.1 Introduction .....	75
4.2 Synthesis of rGO-CeO <sub>2</sub> composites .....	77
4.2.1 Influence of the rGO amount.....	77
4.2.2 Influence of <i>L</i> -Ascorbic acid (Vc).....	85
4.3 Synthesis of rGO-Co <sub>3</sub> O <sub>4</sub> -CeO <sub>2</sub> composites.....	92
4.4 Summary.....	99
5. Summary .....	101
6. Experimental section.....	105
6.1 Characterization.....	105
6.1.1 Materials structure characterization.....	105
6.1.2 Catalytic properties test .....	106
6.2 Synthesis of pure CeO <sub>2</sub> samples.....	107
6.2.1 Synthesis of cerium <i>tert</i> -butoxide.....	107
6.2.2 CeO <sub>2</sub> synthesized with different post-synthesis treatment .....	108

6.2.3 CeO <sub>2</sub> synthesized with different sol composition.....	110
6.2.4 CeO <sub>2</sub> synthesized under different solvothermal conditions.....	112
6.3 Synthesis of Co <sub>3</sub> O <sub>4</sub> modified CeO <sub>2</sub> samples .....	114
6.3.1 Synthesis of the Ce-L-B-L'-Co single source precursor .....	114
6.3.2 Synthesis of Co <sub>3</sub> O <sub>4</sub> modified CeO <sub>2</sub> by different routes.....	114
6.3.3 Synthesis of CeO <sub>2</sub> modified by different proportion of Co <sub>3</sub> O <sub>4</sub> via 'route 1'.....	116
6.4 Synthesis of graphene-CeO <sub>2</sub> and graphene-Co <sub>3</sub> O <sub>4</sub> -CeO <sub>2</sub> composites.....	117
6.4.1 Synthesis of graphite oxide.....	117
6.4.2 Synthesis of rGO-CeO <sub>2</sub> composites.....	118
6.4.3 Synthesis of rGO-Co <sub>3</sub> O <sub>4</sub> -CeO <sub>2</sub> composites .....	119
7. References .....	121
8. Curriculum vitae.....	128

## 1. Introduction

### 1.1 Sol-gel processing

Sol-gel processing is a very efficient way to prepare materials in different forms and different compositions. The form variation can be achieved by modifying the preparation process like dip-coating or gel-casting, and then thin films or monoliths would be obtained. The composition adjusting is much more interesting, because for multi-components materials, the sol-gel method has much more advantages than other methods. Sol-gel processing and its application in materials synthesis are summarized in Figure 1.1.

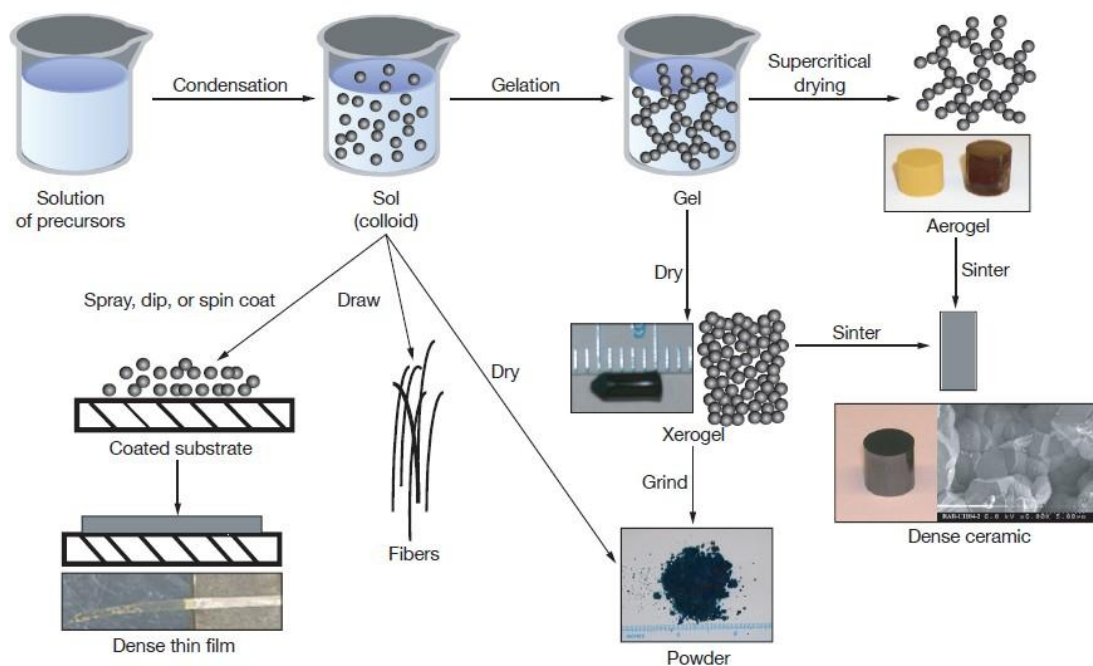


**Figure 1.1** Sol-gel processing and application in materials synthesis, taken from ref [1]

Sol-gel processing can be divided into two main parts: sol-gel chemistry and post-synthesis treatment. The sol-gel chemistry normally decides the composition of the final product while the post-treatment modifies the morphology of material. Post-treatment often includes the calcination process, which removes the organic residues and forms crystalline phases.

Sometimes, the post-synthesis treatment can also change the composition of the final product, such as some modification of functional groups. In the following part, only the sol-gel chemistry and the heat treatment are introduced, which have close relationship with this dissertation.

### 1.1.1 Sol-gel chemistry

Sol-gel chemistry is based on two important processes: hydrolysis and condensation. As silica sol-gel is the best and most investigated material in sol-gel chemistry, it is used here to illustrate the hydrolysis and condensation processes, as shown in the following equations. The silicon alkoxide could be exchanged by any other kind of metal alkoxides  $M(OR)_n$ , and the hydrolysis as well as condensation of them would be similar as those of silicon alkoxides.

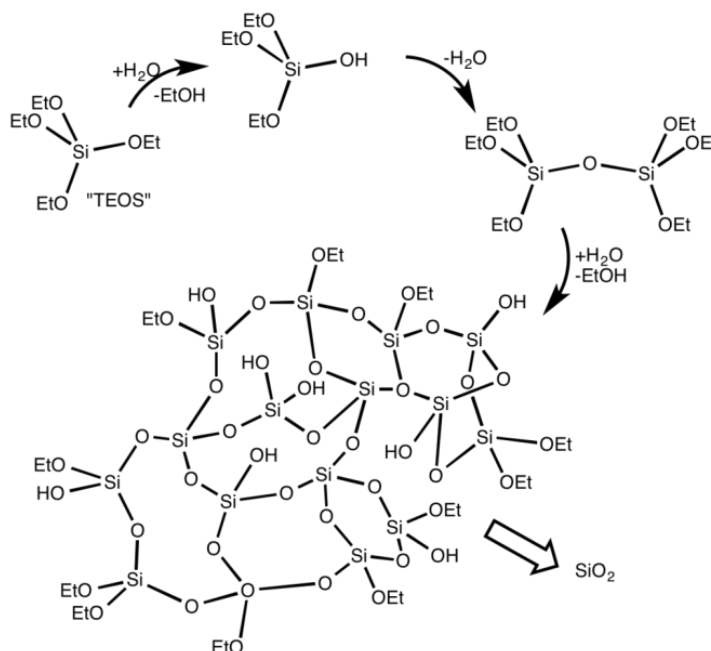
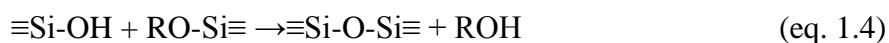
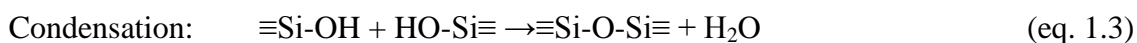
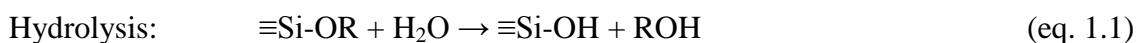


**Figure 1.2** Simplified representation of the condensation of tetraethyl orthosilicate (TEOS) in sol-gel processes, taken from ref [2]

The materials structure can be modified easily during sol-gel processing. After the hydrolysis and condensation steps, an M-O-M metal oxo network is formed, as shown in Figure 1.2. For some  $M(OR)_n$ , the hydrolysis and condensation rates are too fast to handle. For example, titanium alkoxides  $Ti(OR)_4$  are normally used as precursors to prepare  $TiO_2$ . But because the hydrolysis and condensation of  $Ti(OR)_4$  are too fast, cracks are easily formed during the preparation. Therefore ligands are normally used to slow down the hydrolysis and condensation rate. The material's structure can also be modified by the ligands with more than one functional group [3-5] to form pre-organized metal-ligand networks, as shown in Figure 1.3. The pre-organized metal-ligand network could change the materials structure depending on the type of the ligand, like the chain length [6, 7], or the functional group of the ligand [8].

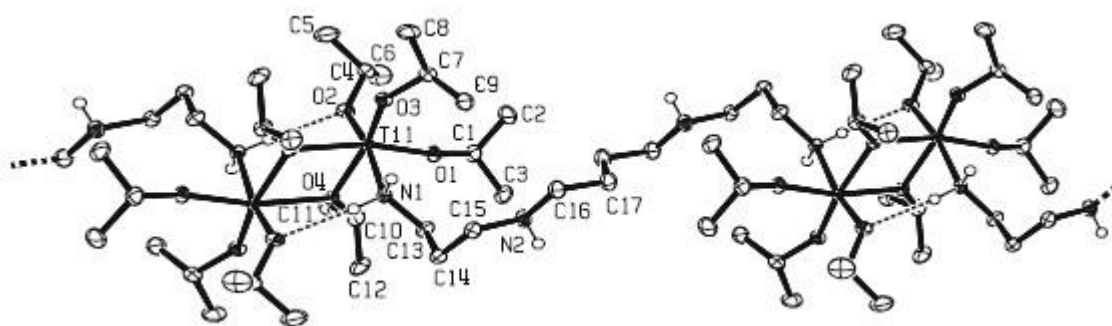


**Figure 1.3** Molecular structure of  $[Ti_2(OiPr)_8(C_{10}H_{26}N_4)_\infty]$ , the dotted lines represent NH--O hydrogen bonds. Taken from ref [4]

Surfactants are also often used as additives in sol-gel chemistry, which serve as templates to create special structures in the metal-ligand/oxo network. In the following heat-treatment process, the surfactant would be removed, leaving the metal oxide with special pore structures [9], as shown in Figure 1.4. Inorganic-surfactant composites are formed by the co-assembly of surfactants with soluble inorganic precursors. Ordered nanoporous inorganic materials are produced by selectively removing of the organic template from the composite. The example shows the formation of a hexagonal honeycomb-type structure, but a wide range of ordered structures can be produced in a similar manner. Surfactants can be classified as soft templates. There are also hard templates, like polystyrene sphere [10, 11] etc., which have almost the same role as surfactants.

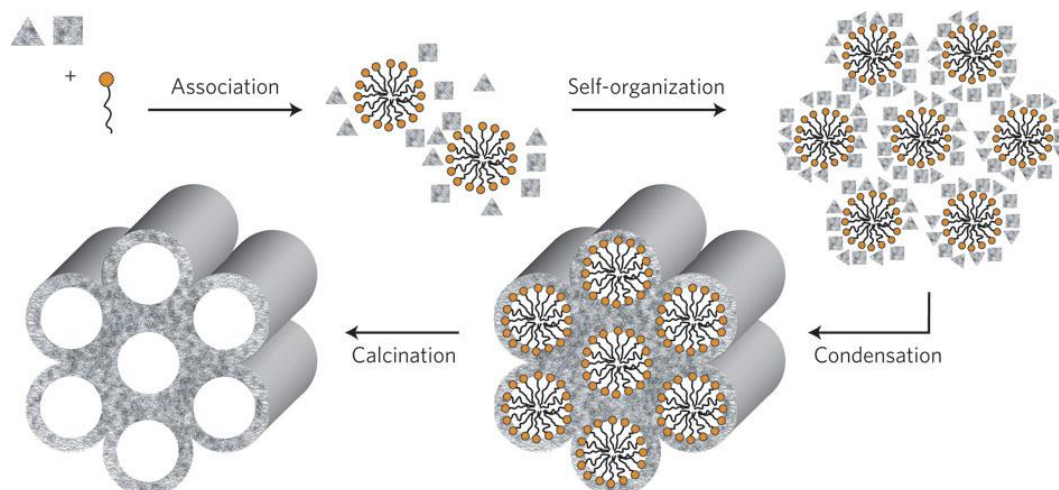


**Figure 1.4** Formation mechanism of templated nanoporous silicas. Taken from ref [9]

As sol-gel processing is a solution method based on the metal alkoxide hydrolysis and condensation, the material composition can also be adjusted besides the material structure. Here only binary compounds are chosen as an example, and this could be expanded to multi-component materials. Normally there are three ways to get materials with more than one component, as listed below.

(1) Adding the A and B precursor at different times.

Normally this method is used to prepare materials with core-shell or layer-by-layer structure. First  $A(OR)_n$  is used to prepare an A sol, and the A sol is processed to get small gel spheres or thin films. Sometimes the A spheres or thin films would be further calcined to form  $AO_x$  structures. Then the A sphere or thin film is dipped into the B gel obtained from the  $B(OR)_m$  precursor, and the A-B core-shell structure or layer-by-layer structure would form. One example is shown in Figure 1.5, where Rhodamine B (RB) dye-doped  $TiO_2$ - $SiO_2$  core-shell composite microspheres were synthesized.

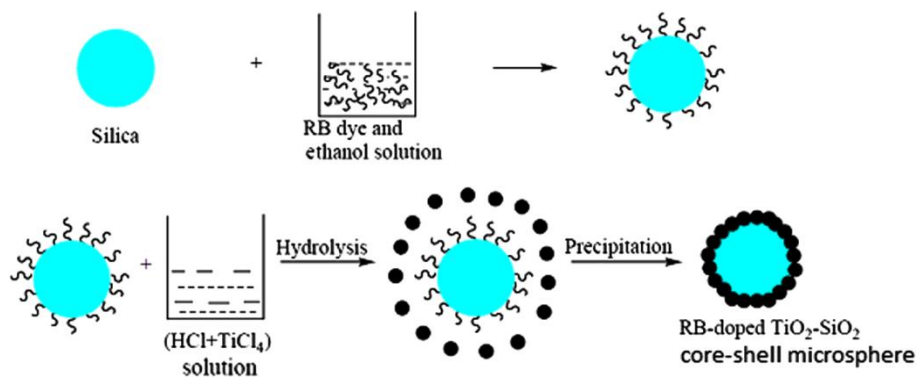


**Figure 1.5** Synthesis of Rhodamine B (RB) dye-doped  $\text{TiO}_2\text{-SiO}_2$  core-shell composite microspheres by the sol-gel method. Taken from ref [12]

(2) Adding A and B precursor at the same time.

This procedure can be divided into two variations: (a) the A and B precursors are not connected with each other; (b) A and B are connected by some ligand or they are part of one molecule.

In most research, method (a) is used, because the separate precursors are easy to get and the processing is much easier compared to the other method. But the disadvantages are also clear, especially when the A and B precursors have different hydrolysis and condensation rates, then phase separation can happen. Thus, method (b) has attracted more and more attention. Method (b) uses the concept of single source precursors, to connect A and B. Typical single-source precursors for sol-gel processing are bimetallic alkoxides where the two metals are bridged by alkoxo groups which, however, are lost upon hydrolysis and condensation. An alternative approach is to link the individual metal components through organic groups. To this end, precursors of the type  $(\text{RO})_n\text{M-X-Y-X}'\text{-M}'$  are required, where  $\text{M}(\text{OR})_n$  is a metal alkoxide moiety,  $\text{M}'$  is the second metal (metal ion or another metal alkoxide moiety), X and X' are the coordinating groups, and Y is a chemically inert spacer. Possible synthesis routes of such precursors are shown in Figure 1.6. Phase separation can thus be avoided. There are several examples from previous research in our group [13-15].



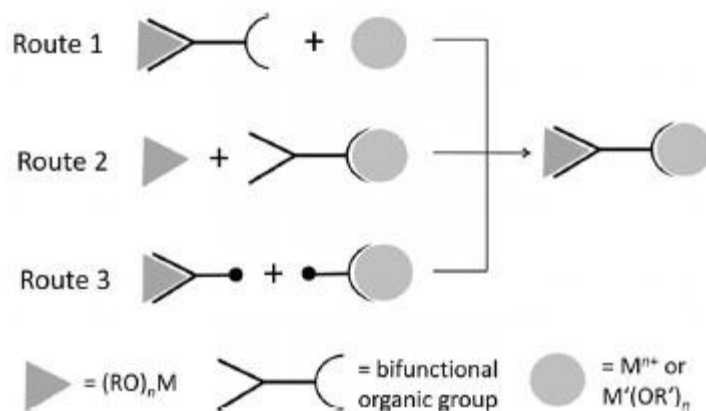


**Figure 1.6** Synthesis routes for bimetallic precursors with organic linkers. Taken from ref [16]

### 1.1.2 Heat-treatment

Sol-gel chemistry of organically modified precursors results in hybrid materials, which still contain organic residues like the ligands and surfactants. For some applications like catalytic and photovoltaic applications, the organic residues need to be removed to get crystalline phases, which are necessary for electron excitation and transfer. Thus, heat treatment is also one of the important stages for sol-gel processing of purely inorganic materials. Heat treatment could improve the material properties in the following ways:

- Remove impurities and additives, like ligands, surfactants and residual solvents;
- Improve crystallinity or change the crystalline phase. Sometimes a specific crystalline phase results in better properties. For example, anatase  $TiO_2$  exhibits better photocatalytic performance than rutile;
- Reduce the defects of grain boundary. This is very important for semiconductors. Normally the defects exist on grain boundaries, which can cause electron-hole combination and block the electron transfer;
- Enhance mechanical strength. Calcination at high temperature will result in ceramics with high density and less pores, being beneficial for the mechanical strength;
- Improve material properties, like applications as catalysts, solar cells or fuel cells.

Heat treatment can be carried out in different ways, depending on the anticipated material properties. Normally the calcinations are done in air in a Muffle furnace (Figure 1.7). But

sometime the calcinations need special conditions, such as a reductive atmosphere or under high pressure, thus special calcination devices are needed. Depending on different calcination conditions, the heat treatments are divided as follows:

- (1) Calcination in air. The temperature can be up to 1500 °C, depending on the design and the used material. It is easy to handle, and there are no shape limitation for the sample. Normally it is used to remove organic residues and prepare metallic oxide with crystalline phases. The materials can be in different forms, like powder, bulk, thin films etc.



**Figure 1.7** Muffle furnace



**Figure 1.8** Tube furnace

- (2) Calcination in a specific atmosphere, like  $H_2$ ,  $N_2$ ,  $NH_3$ , etc. This needs quartz tube furnaces (Figure 1.8) which allow the gas flow go through. The temperature can be up to 1200 °C. Operation is not so easy because the tube should be well closed, avoiding contact of the sample with air. Due to the tube shape of the oven the forms of the sample are also limited. This could be used to prepare non-oxide materials (nitride, sulphide, etc.) and to adjust the composition of the material (under reductive atmosphere  $H_2$ ).
- (3) Microwave calcination. As the samples are heated by microwave, the temperature can only reach 200 °C. Sometimes this temperature is not high enough, thus further calcination or extraction are needed. But this process is environmentally friendly and requires less energy than convention calcination. Normally it is used to prepare materials with homogeneous structure. As the grain growth is suppressed by microwave, this treatment could be used to prepare materials with small particle size and high surface area.

(4) Calcination under pressure. This can also be sub-divided depending on the origin of the pressure. (i) If the pressure comes from outside, then a special pressure furnace will be used, as shown in Figure 1.9. The two arms of the oven press the sample and at the same time vacuum is also produced. Very dense ceramic bulk materials or pellets will be produced. In this case, the temperature can be up to 2200 °C and the pressure up to 30 Mpa (decrease along with the increase of temperature). (ii) The pressure comes from inside in a sealed container (normally an autoclave, Figure 1.10) with solvent. The pressure has a close relationship with the solvent volume and the temperature. It increases along with the raise of solvent volume and the temperature. Depending on the design and the material of the autoclave, the temperature can be up to 300 °C and the pressure can be 20 Mpa. This process can be used to prepare crystalline materials with quite small particle size and extremely high surface area.



**Figure 1.9** Pressure furnace



**Figure 1.10** Autoclave without stirring (left) and with stirring (right)

Every calcination process has its own advantages and disadvantages, thus it can be chosen according to different purposes. For example, when non-oxide materials are prepared, the calcination in specific atmosphere is the best choice. When small particle size and high surface area are needed, the calcination under microwave radiation or in autoclave is much better.

## 1.2 CeO<sub>2</sub> materials and CO oxidation

### 1.2.1 CeO<sub>2</sub> materials

Cerium (IV) oxide (CeO<sub>2</sub>, ceria) has a fluorite structure, belonging to space group  $Fm\bar{3}m$ . The catalytic properties of ceria have attracted worldwide interest, especially as automotive catalytic converters, because of its high oxygen storage-release capacity [17]. The release and storage of oxygen is mediated by creation and annihilation of oxygen vacancies in ceria and a continuous change of the ceria stoichiometry between two limiting cases, CeO<sub>2</sub> and Ce<sub>2</sub>O<sub>3</sub> [18]. Since ceria can become non-stoichiometric in oxygen content (i.e. it can release oxygen without decomposing) depending on the partial pressure of oxygen, it can release or take in oxygen in the exhaust stream of a combustion engine. For example, the bulk-truncated CeO<sub>2</sub> (111) facet (Figure 1.11 a) readily loses some oxygen atoms to give the cubic Ce<sub>2</sub>O<sub>3</sub> (111) facet (Figure 1.11 b) when the partial pressure of oxygen is low. And when the partial pressure of oxygen is high, Ce<sup>3+</sup> can be converted to Ce<sup>4+</sup> (e.g., Ce<sub>2</sub>O<sub>3</sub> + 1/2 O<sub>2</sub> → 2CeO<sub>2</sub>) with extra O atoms, which is beneficial for the catalytic oxidation reaction. Thus, ceria can buffer the exhaust composition through its oxygen storage capacity (OSC).

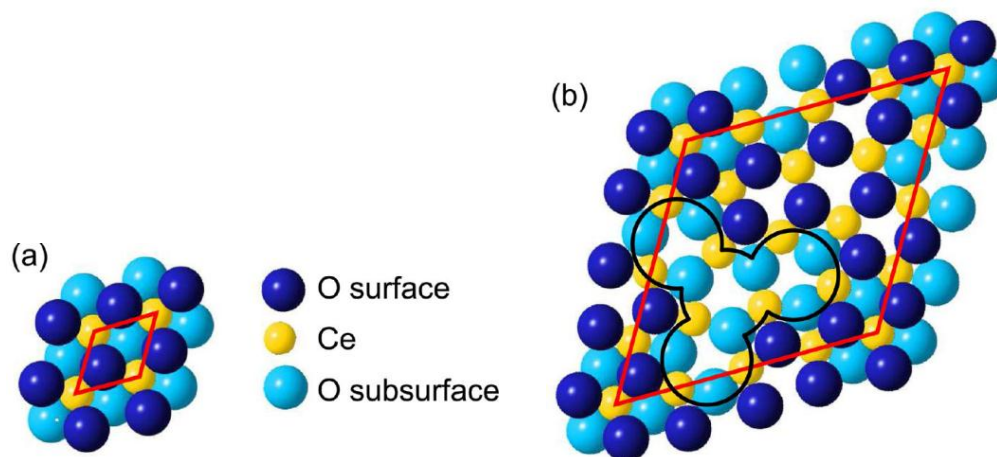


**Figure 1.11** Schematic top view of a bulk-truncated CeO<sub>2</sub> (111) (a) and cubic Ce<sub>2</sub>O<sub>3</sub> (111) (b). Surface unit cells are marked red in both (a) and (b). In (b), the structural motif of surface oxygen vacancies is outlined in black. Taken from ref [18]

### 1.2.2 CO oxidation with $\text{CeO}_2$

Carbon monoxide (CO) is a toxic and harmful air pollutant. It not only affects human beings but also vegetation and indirectly increases global warming. An estimate has shown that vehicular exhaust contributes about 64% of the CO pollution in developed countries [19]. Besides the vehicular pollution, CO is also a by-product of the  $\text{H}_2$  production from methanol or ethanol reforming, in which preferential CO oxidation is necessary [20]. Due to the high energy barrier from CO to  $\text{CO}_2$ , catalysts are normally used to accelerate the CO conversion. Figure 1.12 shows the sketch of a CO oxidation kinetic test. A mixture of CO and  $\text{O}_2$ , balanced by He, is normally used as the test gas.

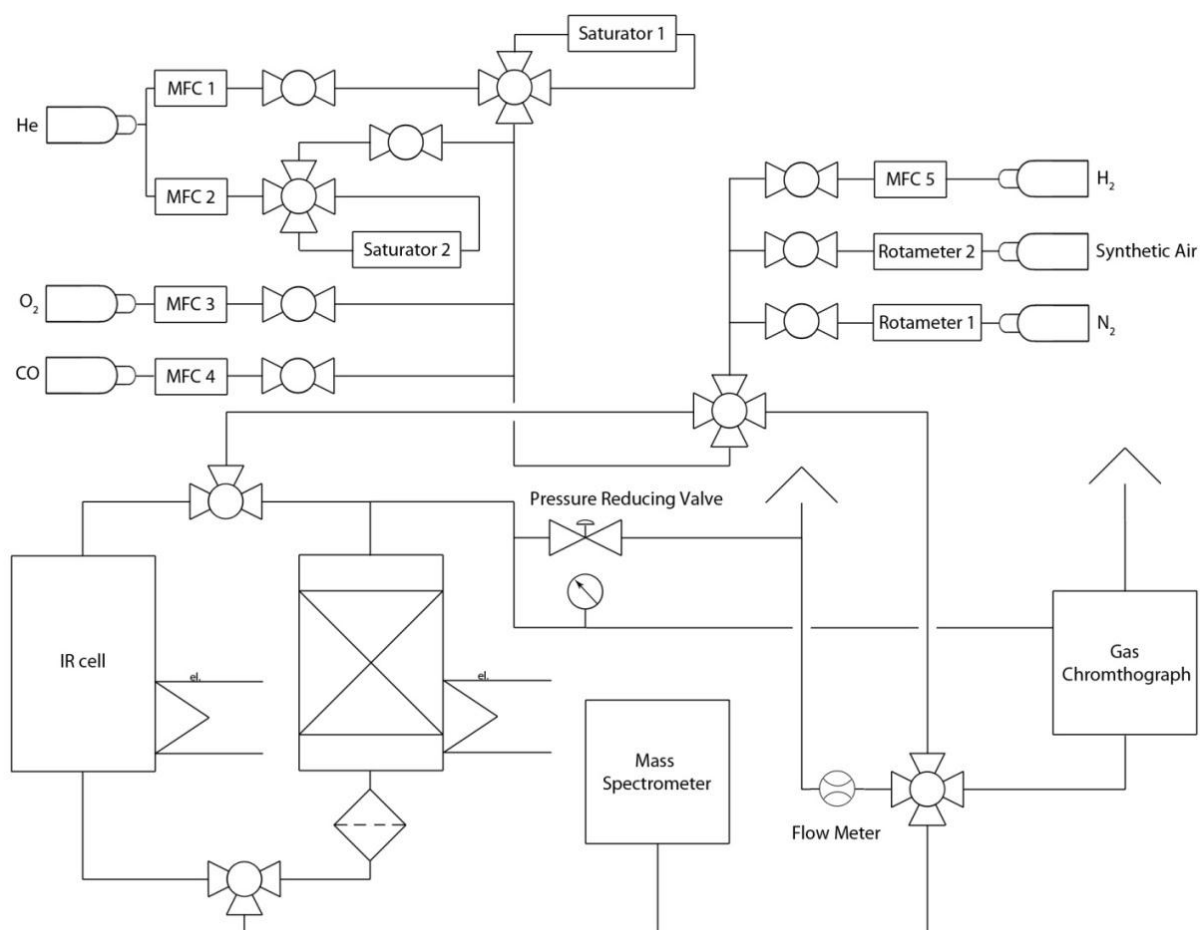


**Figure 1.12** Sketch of CO oxidation kinetic test, taken from ref [21]

When CO converts to CO<sub>2</sub> over a catalyst, the following steps are normally occurring, as shown in the following equations [22, 23], where  $\nu$  represents an empty site on the catalyst:



The activation energy for eq. 1.6 is nearly 0, this mechanism therefore predicts that the overall reaction should be first order in O<sub>2</sub> and inverse-first-order in CO, with an activation energy equal to the heat of adsorption of CO [24]. With ceria supported metals, there is an additional pathway for forming O<sub>ad</sub> by transfer of oxygen from ceria to the metal, shown in eq. 1.9. Although the activation energy of eq. 1.9 is not known, it should be different from the heat of adsorption [22].



Although CeO<sub>2</sub> has excellent oxygen storage capacity, it was rarely used alone for CO oxidation because of the high ignition temperature. It is one of the crucial components of three-way catalysts and serves mainly as a support for the dispersion of noble metals (e.g. Pd, Pt and Rh), preventing their sintering at high temperatures. Additionally it stabilizes the oxygen concentration in the exhausts due to the storage/release capacity associated with the fast Ce<sup>4+</sup>/Ce<sup>3+</sup> redox cycle. Furthermore, noble metals supported on ceria have demonstrated a potential in important industrial catalytic processes such as preferential CO oxidation and water gas shift reaction [25-28]. CeO<sub>2</sub> as a support was reported to increase the catalytic activity of these reactions remarkably. The enhancement in the catalytic activity was assigned to the metal-support interactions between noble metal and ceria [28, 29] and CeO<sub>2</sub> recently has been named as an “active support”. However, the limited availability and high cost of noble metals requires the rational design and development of new efficient low-cost catalysts. From this aspect, Co<sub>3</sub>O<sub>4</sub> has attracted a great attention in the past decade as an alternative to noble metals. In particular, Co<sub>3</sub>O<sub>4</sub>-CeO<sub>2</sub> catalysts were found to be active for CO oxidation, preferential CO oxidation,

hydrocarbon and diesel soot oxidation [30-33]. Thus, two aspects are very important for the CeO<sub>2</sub> materials: (1) Ce<sup>3+</sup> percentage or oxygen vacancies [18], because it was suggested that nano-scaled ceria with abundant oxygen vacancies would enhance the catalytic activity [34, 35]; (2) surface area, because it can provide more sites for gas molecule adsorption and reaction.

### 1.3 Research goals

CeO<sub>2</sub> materials are normally prepared from solution using an inorganic precursor, like precipitation [36, 37], sol-gel [38, 39] and solvothermal [40, 41]/hydrothermal [42-45] methods. The sol-gel method has many advantages for materials synthesis and design, because the materials composition and structure can be influenced by the proper choice of precursors and processing conditions, as described in section 1.1.

Inorganic cerium salts, such as Ce(NO<sub>3</sub>)<sub>3</sub>·6H<sub>2</sub>O [46-50], CeCl<sub>3</sub>·7H<sub>2</sub>O [51] and ceric ammonium nitrate((NH<sub>4</sub>)<sub>2</sub>Ce(NO<sub>3</sub>)<sub>6</sub>, CAN) [52], were mainly used as precursors for sol-gel processing of ceria (including the citrate-gel route) because they are commercially available. Qi et.al. found that the choice of the precursor [Ce(NO<sub>3</sub>)<sub>3</sub> and (NH<sub>4</sub>)<sub>2</sub>Ce(NO<sub>3</sub>)<sub>6</sub>] influenced the structure, surface state, reducibility and CO oxidation activity of Cu doped CeO<sub>2</sub> materials [53]. Thus, new ceria precursors, like cerium tetra-butoxide, might provide new structural features and properties for the prepared CeO<sub>2</sub> materials. One of the main issues for this research is how cerium tetra-butoxide as precursor influences the materials compared with inorganic cerium precursors in sol-gel processing.

As the prepared CeO<sub>2</sub> is used for CO oxidation, the Ce<sup>3+</sup> percentage and surface area are two important factors. Both have close relationship with the crystallite size. The smaller the crystallite size of the CeO<sub>2</sub> particle is, the higher are the Ce<sup>3+</sup> percentage and the surface area. Because the materials structure is much influenced by the post-synthesis treatment, it is very important to find a suitable treatment, which could give CeO<sub>2</sub> with high Ce<sup>3+</sup> percentage and large surface area.

Because of the high ignition temperature of CeO<sub>2</sub>, Co<sub>3</sub>O<sub>4</sub>-CeO<sub>2</sub> is used here for CO oxidation. The superior activity of Co<sub>3</sub>O<sub>4</sub>-CeO<sub>2</sub> catalysts is attributed to the synergetic interactions between cobalt and ceria that enhances textural and structural properties by modifying Ce<sup>3+</sup>/Ce<sup>4+</sup> and Co<sup>2+</sup>/Co<sup>3+</sup> redox properties. As a result, the oxygen mobility is boosted, which makes more

oxygen available for the oxidation processes and improves the activity of catalysts [54-56]. These interactions are mainly determined by the component distribution, i.e. high dispersion of active phase on the surface or small crystallite size [57]. Thus, another important aspect of this research was how to prepare  $\text{Co}_3\text{O}_4\text{-CeO}_2$  with different  $\text{Co}_3\text{O}_4$  distribution, and how the distribution influences the CO oxidation activity.

During the research, organic residues with graphene-like structure were found after the  $\text{CeO}_2$  or  $\text{Co}_3\text{O}_4\text{-CeO}_2$  samples were solvothermally treated in ethanol. Much published work has proven that graphene/semiconductor composite could improve the materials properties, like graphene/ $\text{TiO}_2$  in photocatalytic applications [58], graphene/ $\text{ZnO}$  for capacitors [59, 60], graphene/ $\text{CeO}_2$  for catalysts [61] or fuel cells [62] and so on. The outstanding electron transfer property of graphene could benefit for the semiconductor application, in which electron separation and transfer are needed. But for CO oxidation, it is still unknown whether adding of graphene to  $\text{CeO}_2$  could improve the catalytic ability, and how the added amount influences the CO oxidation activity.

All in all, this research was focused on the synthesis of  $\text{CeO}_2$ -based materials by the sol-gel method using cerium tetra-butoxide as precursor. The influence of post-synthesis treatment was investigated to get  $\text{CeO}_2$  with small particle size and high surface area. After the synthesis parameters for  $\text{CeO}_2$  were optimized,  $\text{Co}_3\text{O}_4$  was added to improve the CO oxidation activity. The distribution of  $\text{Co}_3\text{O}_4$  in  $\text{CeO}_2$  phase was changed by different adding sequences of the Co precursor during sol-gel processing, and the influence of the different  $\text{Co}_3\text{O}_4$  distribution on CO oxidation was investigated. As graphene-like organic residues were found in the above research, graphene was added to study its effects on the material structure and CO oxidation.



## 2. Pure CeO<sub>2</sub>

### 2.1 Introduction

Cerium alkoxides are less often employed as precursors to prepare CeO<sub>2</sub> because they are not easily available commercially and more reactive to humidity. Nevertheless, metal alkoxides have often advantages and result in different materials textures and properties. Cerium alkoxides were used, for example, to prepare ceria thin films [63, 64] or bimetallic oxides [65-67].

Apart from the precursor, the post-synthesis treatment of the gels is also an important parameter influencing the materials properties. The gels obtained by sol-gel processing are often heat-treated in air, sometimes also in N<sub>2</sub> or a combination of both, to remove residual organic groups. Recently, a combined sol-gel and solvothermal process was applied for the preparation of titania, and the prepared TiO<sub>2</sub> possessed a special microstructure with high surface area [68, 69]. In previous work on titania, our group had shown that modification of the metal alkoxide with acetaldoxime (**AO**) resulted in materials with superior properties, especially when combined with the non-ionic surfactant Pluronic F127 as a pore-forming agent [70]. AO and F127 were therefore also used in this work. Although the oximate-modified cerium alkoxide precursor was not characterized there is good reason to assume that the structure of the precursors is the same as that of oximate-substituted zirconium alkoxides (eq. 2.1), given the general similarity of Zr and Ce alkoxides [71]. Substitution of metal alkoxides by bidentate ligands (such as oximate) not only moderates the reaction rates of metal alkoxides, but also results in additional porosity/surface area upon heat-treatment of the gels [6, 70, 72].



Here, the influence of different precursors (ammonia cerium nitrate (**CAN**) and cerium *tert*-butoxide (**CeB**)) on the morphology and microstructure of ceria was investigated in addition to different post-synthesis treatment of the obtained gels. Furthermore, the catalytic activity of CeO<sub>2</sub> samples for CO oxidation was tested, where the surface area ( $S_{\text{BET}}$ ) is a very important parameter. Besides, the influences of the solvothermal solvents, temperature, and reaction time were also investigated.

## 2.2. Advantage of solvothermal treatment in sol-gel process

Originally only different cerium precursors were compared (cerium alkoxide vs. cerium inorganic salts) by using the same synthesis process, to explore the advantage of cerium alkoxides. But during the research, it is found that the post-treatment has a big influence on the material properties besides the cerium precursor. Different post-synthesis treatments were tried after sol-gel processing in order to get CeO<sub>2</sub> with high surface area, including the traditional calcination in the air, first in the N<sub>2</sub> and then in the air, and solvothermal treatment.

### 2.2.1 Gel preparation

Sols were prepared from CeB (or CAN), acetaldoxime (AO), F127 and 1,2-dimethoxyethane (DME) in a 1:2:0.005:40 ratio. In some reactions no F127 was added to check the influence of the surfactant. Gelation was induced by exposure to ambient humidity at room temperature. The obtained gel solids were then treated by different methods:

- Calcination at 500 °C in air for 2h in an Al<sub>2</sub>O<sub>3</sub> crucible; heating rate 2 °C/min (AC);
- Calcination at 500 °C in N<sub>2</sub> for 3h in an Al<sub>2</sub>O<sub>3</sub> crucible, followed by calcination in air for 2h; heating rate 2 °C/min (NAC).
- Solvothermal treatment at 200 °C for 6h (ST) in a 60 mL autoclave with 30 mL solvent (gel prepared from 5 mmol of CeB). Two different solvents were used, *viz.* EtOH (STE) and H<sub>2</sub>O (STH).
- Solvothermal treatment, followed by calcination as described for AC (ST-AC). (Figure 2.1)

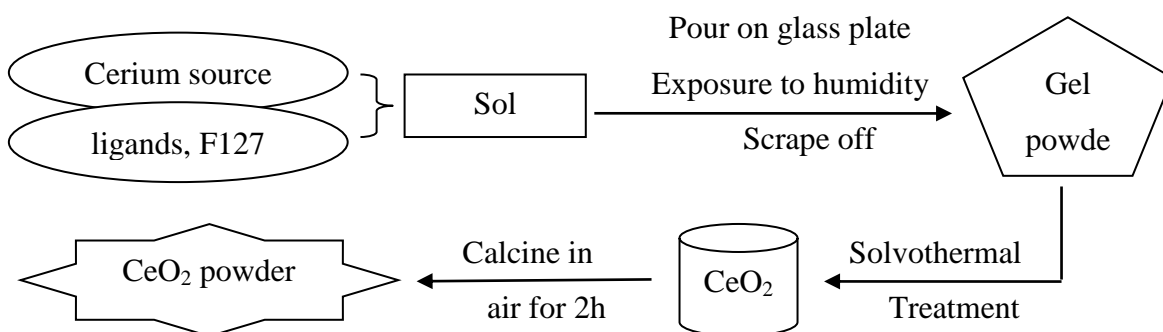


**Figure 2.1** Schematic synthesis protocol for CeO<sub>2</sub> by a combination of sol-gel and solvothermal processing

The labeling of the samples is as follows: (i) precursors A/B/C, (ii) post synthesis treatment. For example, CeB/AO/F127-AC is a sample prepared from CeB, AO and F127, followed by calcination in air (AC).

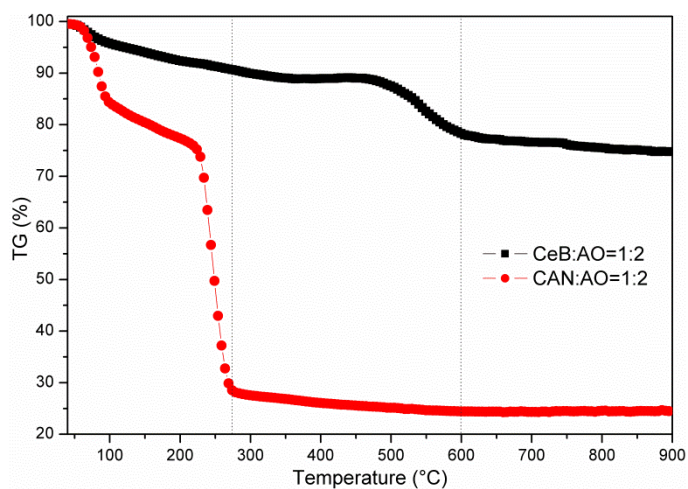


**Figure 2.2** TGA of gel powder made from different cerium precursors.

Materials obtained from either CeB or CAN were first compared by TGA (Figure 2.2) and SEM measurements (Figure 2.3). When CeB was used, the onset temperature in TGA was about 495 °C, and decomposition was complete at about 600 °C, with 22% weight loss. In contrast, when CAN was used, the onset temperature was about 230 °C and the gel decomposed completely below 300 °C, with a weight loss of about 72%. This indicates that part of the material was lost during the TGA measurements due to deflagration. It should be pointed out that samples obtained from CAN sometimes exploded upon AC or NAC calcination. The solid obtained from CAN after sol-gel processing was water-soluble; thus no network had been formed with ambient moisture.

Scanning electron micrographs of CeB/AO/F127-NAC showed small and homogeneously dispersed particles (Figure 2.3a), while CAN/AO/F127-NAC (Figure 2.3b) had a sponge-like appearance. The latter is due to the exothermic decomposition during which large gas volumes are produced.

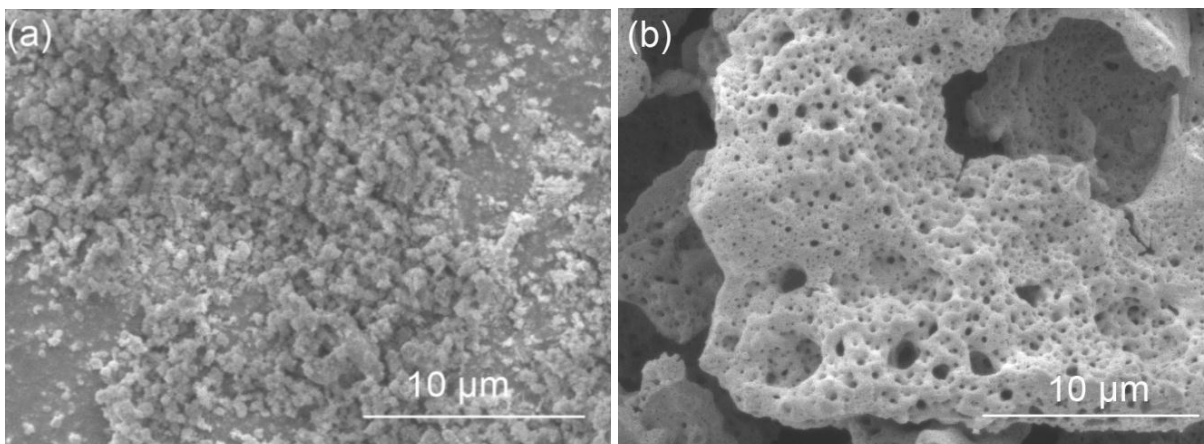


**Figure 2.3** SEM of (a) CeB/AO/F127-NAC and (b) CAN/AO/F127-NAC

The XRD of the samples after AC or NAC calcination are shown in Figure 2.4. All samples were pure ceria (PDF-No. 34-0394), but the particle sizes of the samples obtained from CeB were smaller. Comparison of CeB/AO/F127-AC (average particle size 9.2 nm) and CeB/AO/F127-NAC (8.6 nm) showed that the different calcination methods did not significantly influence the crystal phase or the particle size.

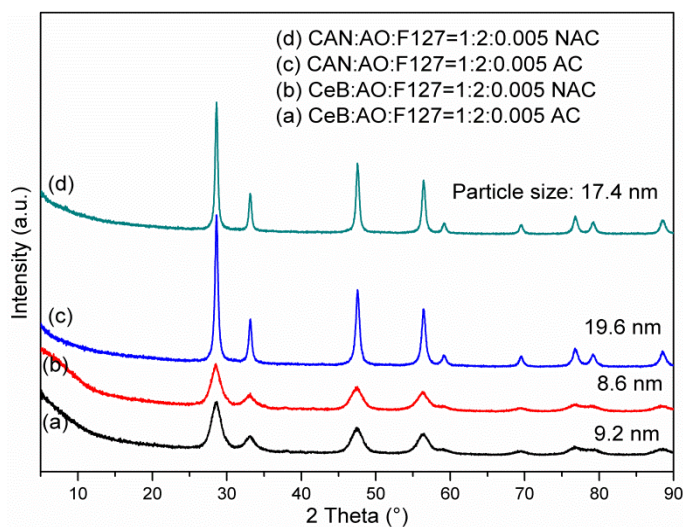


**Figure 2.4** XRD patterns of samples calcined by AC or NAC. The particle sizes were calculated by the Scherrer equation based on the strongest reflection at 28.6°.

The exothermic decomposition of CAN and the solubility of the obtained gel render CAN unappealing as precursor. For this reason CAN-derived samples will no longer be considered in the following.

### 2.2.2 Influence of different post-synthesis treatments

The results of BET measurements of the gels obtained from CeB and treated differently after gelation are summarized in Table 2.1. All AC and NAC samples had similar N<sub>2</sub> sorption isotherms, therefore only that of CeB/AO/F127-NAC is shown in Figure 2.5. The isotherm is a mixture of type IV and III according to the IUPAC definition [73], corresponding to meso-/macro-porous materials. Table 2.1 shows that for AC calcination, the surface area ( $S_{\text{BET}}$ ) was only 8.6 m<sup>2</sup>/g without F127 and 12.8 m<sup>2</sup>/g with F127, *i.e.* the surface area was not too much changed by the presence of F127 in this system. Although the surface area of CeB/AO/F127-NAC (20.1 m<sup>2</sup>/g) was almost twice the value of CeB/AO/F127-AC, it is still too small to be interesting for catalytic applications.

**Table 2.1** BET results for CeB:AO = 1:2 samples with different post-synthesis treatment.

F127	Calcination	$S_{\text{BET}}$ (m <sup>2</sup> /g) <sup>a</sup>	$D_{\text{BJH}}$ (nm) <sup>b</sup>
-	AC	8.6	7.0
+	AC	12.8	12.1
+	NAC	20.1	11.1
+	STE	277.0	3.4
+	STH	133.6	5.5

<sup>a</sup>  $S_{\text{BET}}$ : BET surface area, error  $\pm 5\%$  (from repeated experiments)

<sup>b</sup>  $D_{\text{BJH}}$ : BJH desorption pore diameter,  $\pm 0.5$  nm (from repeated experiments)

Because standard calcination methods did not provide samples with high surface areas, solvothermal treatment (ST) was tested, and both EtOH and H<sub>2</sub>O were used as ST solvent (samples labeled STE and STH, respectively). The N<sub>2</sub> sorption isotherms and pore size distribution of CeB/AO/F127-ST are shown in Figure 2.6 and the derived parameters are summarized in Table 2.1. The shape of the isotherms shows that CeB/AO/F127-STH is mesoporous, while CeB/AO/F127-STE is microporous with relatively small external surface. The latter material had a very high surface area of 277.0 m<sup>2</sup>/g, while the value for CeB/AO/F127-STH was 133.6 m<sup>2</sup>/g. The surface area of the materials can thus be strongly

improved by ST treatment, and the used solvent also had a significant influence on the surface area and especially the pore size distribution (Figure 2.6 right).

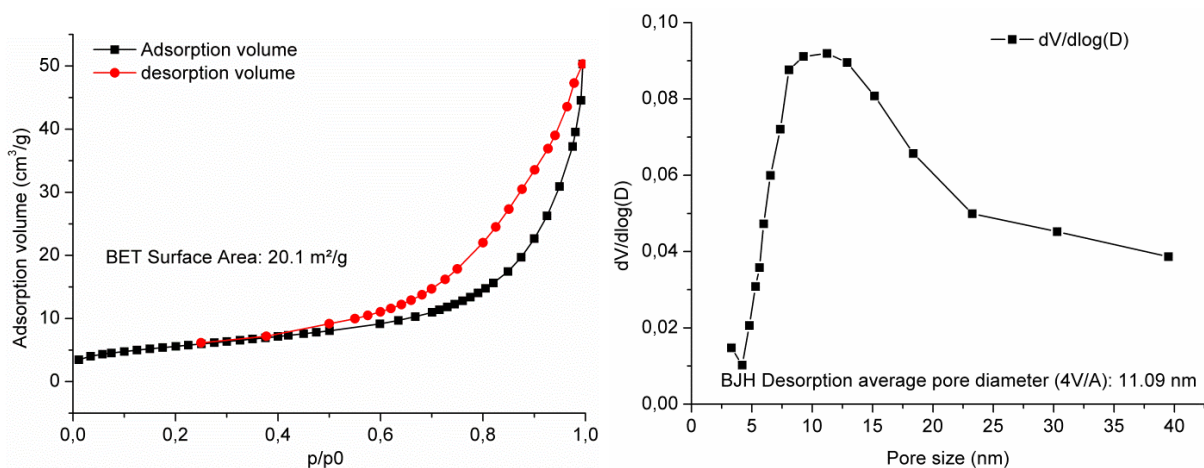


**Figure 2.5** N<sub>2</sub> adsorption-desorption isotherm (left) and pore size distribution (right) for CeB/AO/F127 calcined at 500 °C for 3h in N<sub>2</sub> and then 2h in air (NAC).

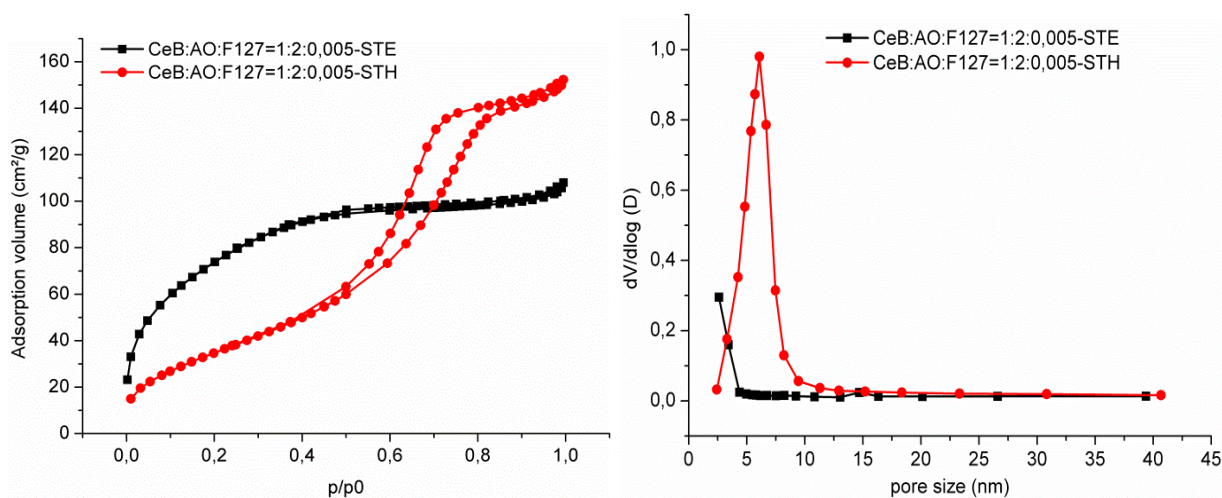


**Figure 2.6** N<sub>2</sub> adsorption-desorption isotherms (left) and pore size distribution (right) for samples after solvothermal treatment in ethanol (STE) or H<sub>2</sub>O (STH).



## 2.3 Influence of solvothermal treatment

### 2.3.1 Influence of the sol composition

After evaluation of the best post-synthesis treatment, the influence of the sol composition on the materials properties was investigated in more detail. To this end, the following experiments were performed:

- CeB: only CeB in DME in the ratio CeB:DME = 1:40.
- CeB/AO: CeB and AO in DME in the ratio of CeB:AO:DME = 1:2:40.
- CeB/F127: CeB and F127 in DME in the ratio CeB:F127:DME = 1:0.005:40.
- CeB/AO/F127: CeB, AO and F127 in DME in the ratio CeB:AO:F127:DME = 1:2:0.005:40.

The samples were solvothermally treated (STE or STH), with all other preparation parameters being the same.

TGA measurements (Figure 2.7) indicated that all samples still contained organic groups after solvothermal treatment, as expected. The weight loss of the samples treated in EtOH was almost the same ( $11.5 \pm 1.0\%$ , Figure 2.7 left). When the solvent was changed to H<sub>2</sub>O, however, the weight loss was much lower ( $4.0 \pm 0.2\%$ , Figure 2.7 right). It can be concluded that during *hydrothermal* treatment, the organic constituents attached on the gel particles are already cleaved to a much larger extent than in the case of solvothermal treatment in ethanol.

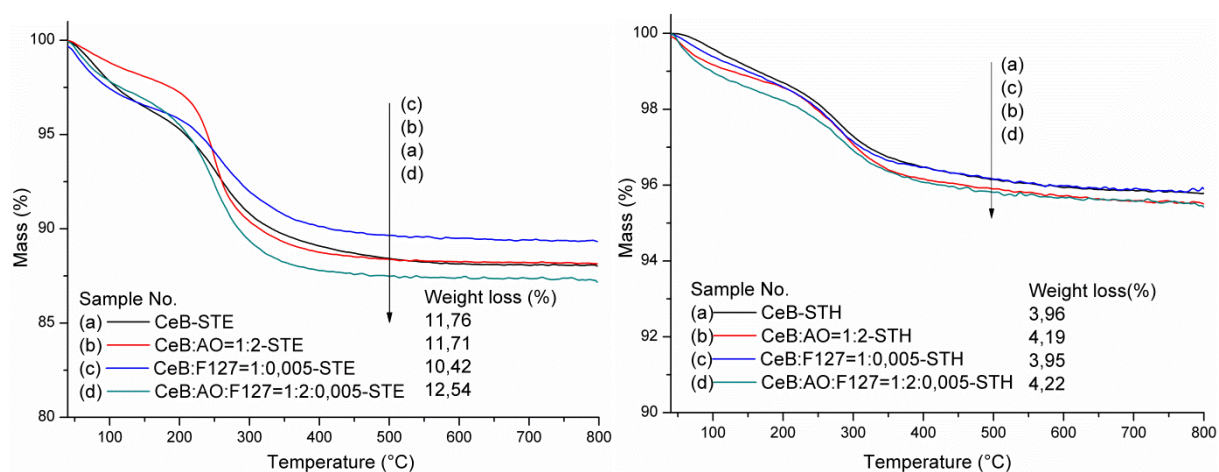


**Figure 2.7** TGA curves for different CeB samples treated by STE (left) or STH (right)

This conclusion was confirmed by IR measurements. When EtOH was used as a solvent (Figure 2.8 left), all spectra showed strong bands at about 1300~1650 cm<sup>-1</sup> (C-O, C=O, COO) and 800~1000 cm<sup>-1</sup> (Ce-O-Ce), and weak bands at 2954 cm<sup>-1</sup> (CH<sub>3</sub>) and 2845 cm<sup>-1</sup> (CH<sub>2</sub>). The strong bands at 1635, 1541 and 1258 cm<sup>-1</sup> indicated the presence of larger proportions of carboxylate groups. The appearance of such groups on the surface of ceria nanoparticles after solvothermal treatment in alcohols was reported by Slostowski et al [74]. When H<sub>2</sub>O was used as solvent (Figure 2.8 right), only strong bands at about 1000 cm<sup>-1</sup> were observed. Generally, the fundamental stretching bands (Ce-O) for CeO<sub>2</sub> materials are in the range 400-500 cm<sup>-1</sup> [75]. Thus, the observed bands at 800~1000 cm<sup>-1</sup> can be attributed to the overtones. They may slightly shift depending on the surface groups. The weak bands at 1564 and 1264 cm<sup>-1</sup> indicated that there was only a small carboxylate proportion.

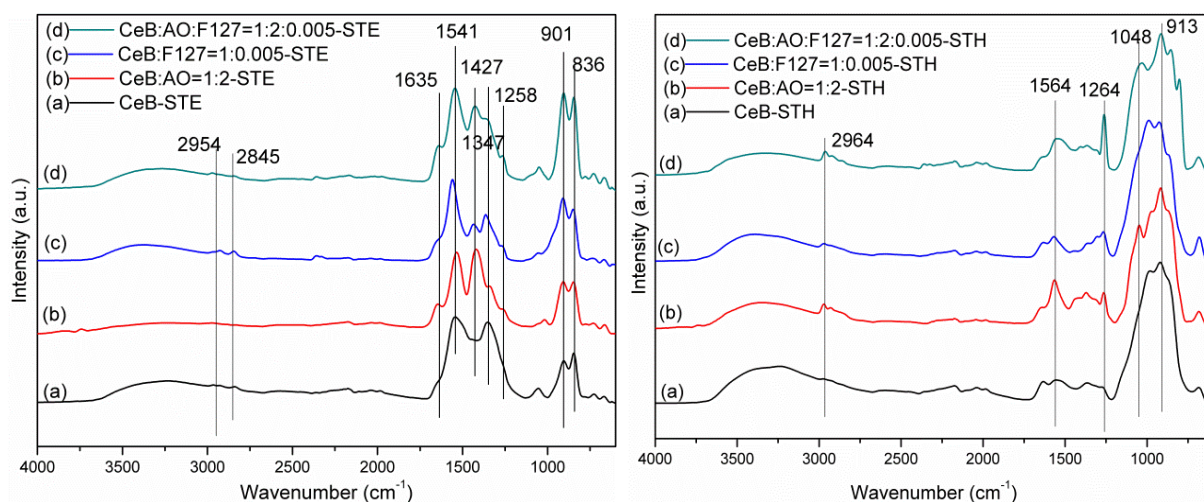


**Figure 2.8** IR spectra of CeB samples treated by STE (left) or STH (right).

The results of N<sub>2</sub> sorption measurements are given in Table 2.2. For the STE samples the surface areas were in the following order: CeB/AO/F127-STE (277 m<sup>2</sup>/g) > CeB/F127-STE (247 m<sup>2</sup>/g) > CeB/AO-STE (210 m<sup>2</sup>/g) > CeB-STE (193 m<sup>2</sup>/g). When H<sub>2</sub>O was used as solvent, however, the surface area was CeB/F127-STH (181 m<sup>2</sup>/g) > CeB/AO-STH (167 m<sup>2</sup>/g) > CeB-STH (146 m<sup>2</sup>/g) > CeB/AO/F127-STE (133 m<sup>2</sup>/g). Except CeB/AO/F127-ST, the sequence was similar for both series. The surface areas for the STE samples were about 50 m<sup>2</sup>/g higher than that of STH samples, which may be due to the residual organic groups during solvothermal processing with EtOH, as reported earlier for ceria [74] and also indicated by the IR spectra



(Figure 2.8 left). The organic groups therefore appear to stabilize smaller particles and a higher porosity, and thus result in higher surface areas.

**Table 2.2** BET results summary of samples prepared by ST and ST-AC treatment

ST solvent	Sol composition	ST series		ST-AC500 °C series	
		S <sub>BET</sub> (m <sup>2</sup> /g) <sup>a</sup>	D <sub>BJH</sub> (nm) <sup>b</sup>	S <sub>BET</sub> (m <sup>2</sup> /g) <sup>a</sup>	D <sub>BJH</sub> (nm) <sup>b</sup>
EtOH	CeB	193.3	4.5	22.4	5.0
	*CeB/AO	210.5	3.2	92.4	3.1
	CeB/F127	246.9	6.2	153.3	5.3
	*CeB/AO/F127	277.0	3.4	88.9	3.9
H <sub>2</sub> O	CeB	146.6	3.8	143.3	3.7
	CeB/AO	167.1	5.7	165.8	5.6
	CeB/F127	181.3	4.6	178.5	4.7
	*CeB/AO/F127	133.6	5.5	132.4	5.4

<sup>a</sup> BET surface area; error  $\pm$  5%

<sup>b</sup> BJH desorption pore diameter;  $\pm$  0.5 nm for STE series,  $\pm$  0.1 nm for STH series

\* Samples were synthesized at least 2 times, and the average values are given here.

When EtOH was used, only CeB/F127 had a very narrow pore size distribution in the mesoporous range (Figure 2.9). When H<sub>2</sub>O was used, all samples except CeB-STH had almost the same pore size distribution, with the narrowest for CeB/AO/F127. The use of acetaldoxime for modification of the starting cerium alkoxide had different influence on the pore size when different ST solvents were used. With EtOH the pore size was narrow when AO was added, while the pore size widened when H<sub>2</sub>O was used.

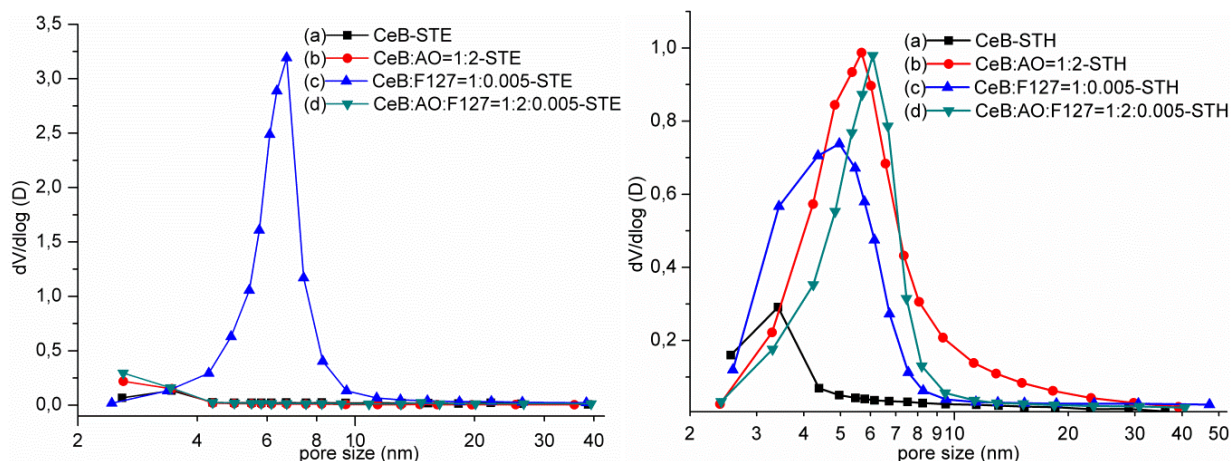


**Figure 2.9** Pore size distribution for different samples after STE (left) and STH (right) treatment

### 2.3.2 Calcination after solvothermal treatment

The previous experiments had shown that residual organic groups were present after solvothermal treatment, especially in ethanol. To check how removal of the residual organic groups would influence the properties of the materials, selected samples were calcined in air after solvothermal treatment. The IR spectra of CeB/AO/F127-STE after calcination at different temperatures are shown in Figure 2.10 left. The carboxylate groups were almost completely decomposed after heat treatment at 300 °C, as already indicated by the TGA measurements (Figure 2.7), and only small residues remained after temperature treatment above 500 °C. The Ce-O-Ce region had a new band at 986 cm<sup>-1</sup> after calcination at 300 °C. This band became stronger with increasing temperature, while the original bands at 924 and 852 cm<sup>-1</sup> were only slightly reduced.

The changes of CeB/AO/F127-STH were similar to that of the STE samples (Figure 2.10, right). Significant differences between the STE-AC and the STH-AC samples were, however, that the new band at 990 cm<sup>-1</sup> of the STH-AC sample became much stronger during calcination than that of the STE-AC sample, while the original bands at 924 and 852 cm<sup>-1</sup> and other small bands became weaker.

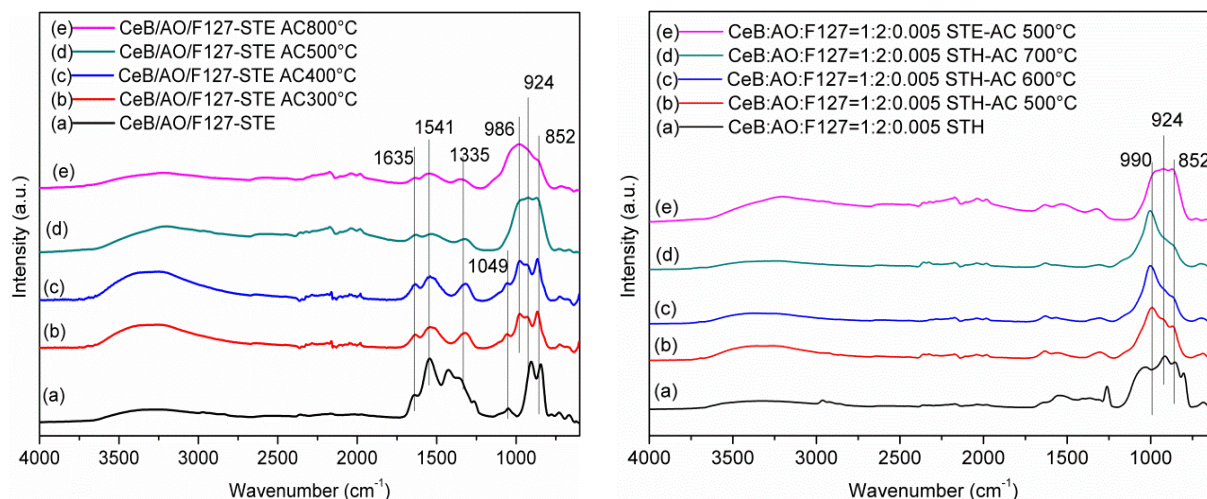


**Figure 2.10** IR spectra of CeB/AO/F127-STE (left) and CeB/AO/F127-STH (right) calcined in air at different temperatures.

The experiment indicated that calcination in air at 500 °C removes most of the residual organic groups without causing excessive sintering of the materials. For the following experiments, the samples were therefore treated at 500 °C.

BET measurements after calcination (Table 2.2) showed that the surface area and average pore size of the STH samples were not significantly changed. In contrast, the surface area of the STE-AC samples was significantly reduced compared with the corresponding STE samples while the average pore sizes only changed slightly. For example, CeB/AO/F127-STE had a surface area of 277 m<sup>2</sup>/g and an average pore size of 3.4 nm, but the corresponding values of CeB/AO/F127-STE-AC changed to 88.9 m<sup>2</sup>/g and 3.9 nm, respectively. The change of the surface area of the STE samples can possibly be attributed to the higher proportion of organic constituents present after solvothermal treatment and their removal upon AC. The surface area of the STE samples after calcination is in each case significantly lower than that of the STH samples, while the average pore diameters are in the same range.

The XRD pattern after calcination (Figure 2.11) showed that all samples were nanocrystalline CeO<sub>2</sub> with similar particle sizes in the range 3.5–5.5 nm (calculated by the Scherrer equation based on the strongest peak at 28.6°). Interestingly, this was only half the size than that of the particles obtained by AC or NAC calcination (Figure 2.4), i.e. without solvothermal treatment.

For comparison, the particle sizes of two samples after solvothermal treatment prior to calcination were also analyzed. The average particle size of CeB/AO/F127-STE was < 3 nm (4.0 nm after calcination) and that of CeB/AO/F127-STH was 5.1 nm (5.3 nm after calcination). The crystallite size of the final material is thus determined by the solvothermal treatment and is not significantly changed when the residual surface groups are removed upon subsequent calcination.

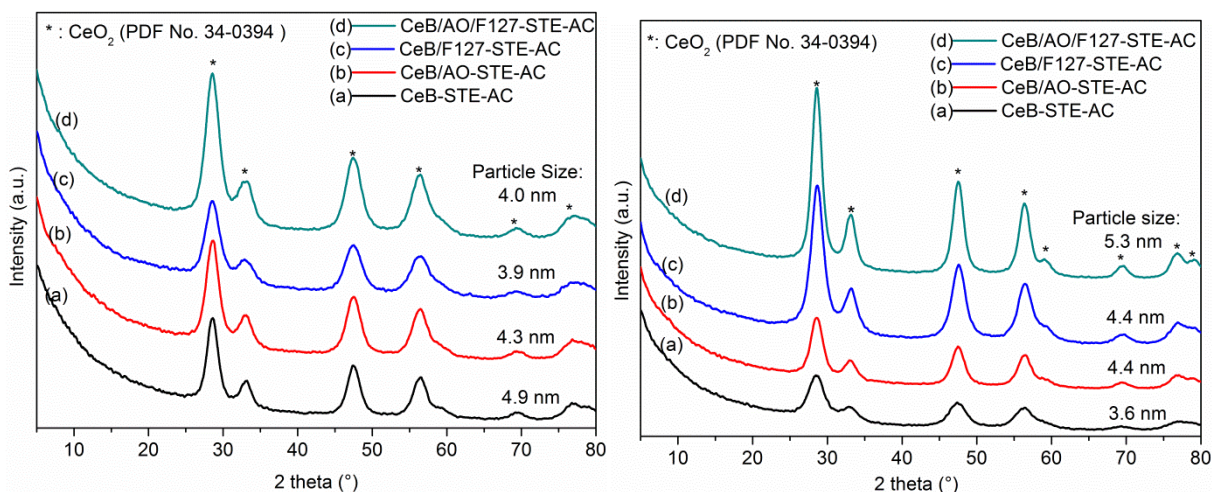


**Figure 2.11** XRD patterns for samples after STE-AC (left) and STH-AC (right) calcination

A possible explanation for the different particle sizes (and surface areas) between the AC and STE-AC or STH-AC series is that dissolution-deposition equilibria under solvothermal conditions determine the particle size (Figure 2.12). Similar results were found for ceria solvothermally treated in different alcohols [74]. The obtained particles are capped by residual (organic) groups which are then removed upon calcination. Only crystallite sizes can be determined by XRD, but no information is obtained about agglomeration/aggregation of the crystallites. The lower BET surface area in the STE series (see Table 2.2) may thus be due to a more pronounced agglomeration/aggregation of the nanocrystals. In contrast, when the initially obtained gels were calcined without prior ST, removal of the organic groups and mass transport coincide and the formation of larger particles is thus favored.



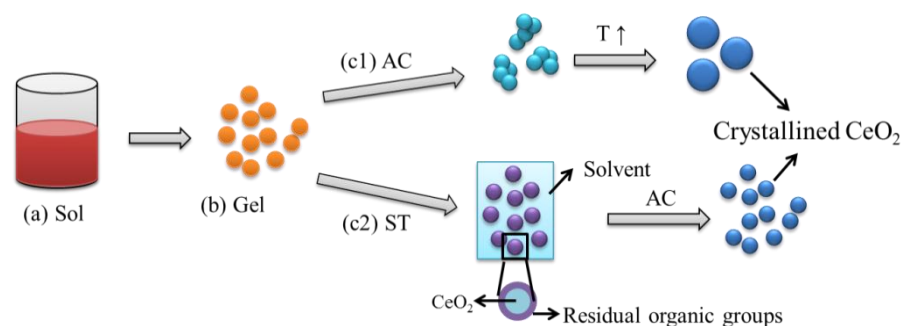


**Figure 2.12** Growth sketch of CeO<sub>2</sub> by different post-synthesis treatments

In order to get more information on the influence of calcination, CeB/AO/F127-STE, CeB/AO/F127-STE-AC and CeB/AO/F127-STH-AC were characterized by HRTEM (Figure 2.13). Only (111) lattice fringes with a distance of 0.31 nm were observed for the STE and STH-AC samples, while the (200) lattice fringes, with 0.27 nm distance, were also observed for STE-AC.

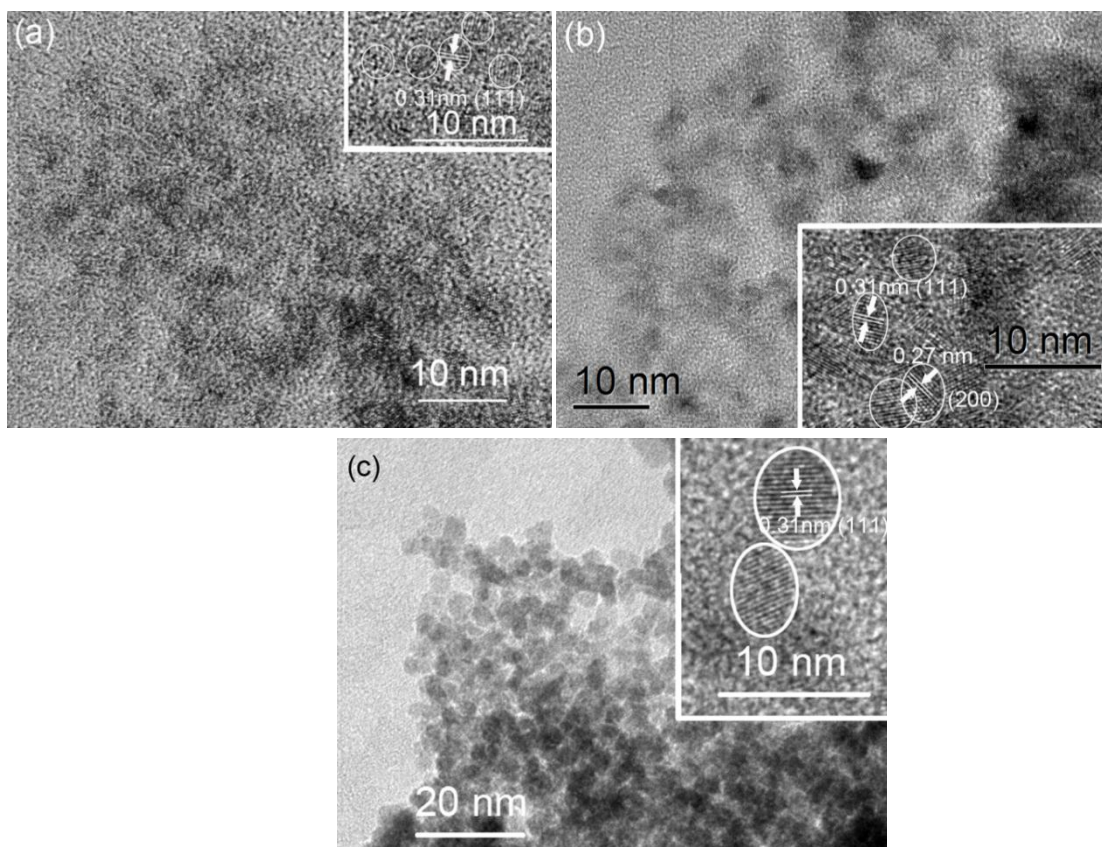


**Figure 2.13** HRTEM images of sample (a) CeB/AO/F127-STE, (b) CeB/AO/F127-STE-AC and (c) CeB/AO/F127-STH-AC. The inserts are higher magnifications of the same image

### 2.3.3 Catalytic properties

The catalytic activity for CO oxidation was tested for three samples, i.e. CeB/AO/F127-STE, CeB/AO/F127-STE-AC and CeB/AO/F127-STH-AC (Figure 2.14), with commercial CeO<sub>2</sub> serving for comparison. The ignition temperature ( $T_{10\%}$ , the reaction temperature required for 10% CO conversion) of commercial CeO<sub>2</sub> is 528 °C and the light-off temperature  $T_{90\%}$  (the temperature at which 90% conversion of CO is achieved) is  $\gg 650$  °C at the conditions specified in the Experimental Section. Both  $T_{10\%}$  and  $T_{90\%}$  are much lower for the three samples prepared in our work (Table 2.3); the order is CeB/AO/F127-STE < CeB/AO/F127-STE-AC < CeB/AO/F127-STH-AC.

For a better comparison of the catalytic activity of the different samples, the normalized reaction rates at 250°C per gram ( $r_{250^\circ\text{C}}$ ) and per unit surface area ( $R_{250^\circ\text{C}}$ ) are also shown in Table 2.3. It must be pointed out that commercial CeO<sub>2</sub> is a macroporous material. Since the BET method takes into account only pores smaller than 50 nm, the total surface area (including the macropores) is underestimated and thus the calculated value  $R_{250^\circ\text{C}}$  of commercial CeO<sub>2</sub> overestimated. The sequence of  $r_{250^\circ\text{C}}$  is CeB/AO/F127-STE > CeB/AO/F127-STE-AC > CeB/AO/F127-STH-AC > commercial CeO<sub>2</sub>. The reaction rate at 250°C ( $r_{250^\circ\text{C}}$ ) of the best sample CeB/AO/F127-STE is about 75-times larger than that of commercial CeO<sub>2</sub>, that at 300°C about 125-times larger.

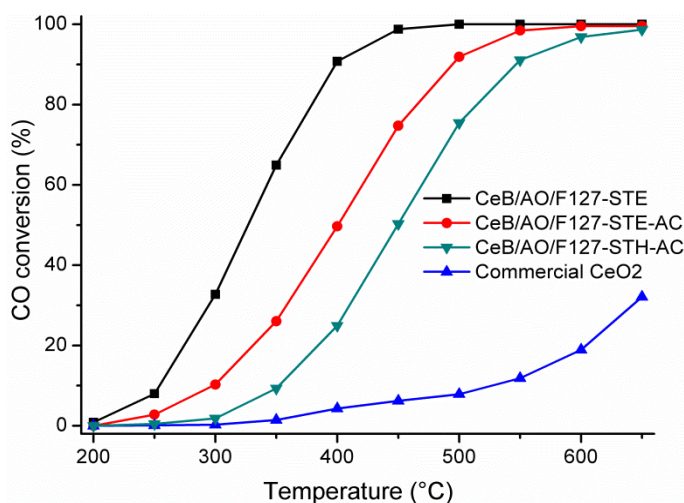


**Figure 2.14** CO oxidation at different temperatures for CeO<sub>2</sub> samples (20 mg), compared with commercial CeO<sub>2</sub>.

The CO oxidation activity of the STE and STE-AC catalysts correlates with the specific surface area (Table 2.3). An about three times higher surface area of STE produces about three times higher rates. This can be seen from comparing the reaction rate per surface area, i.e. the amount of CO converted on a unit surface area of the catalyst at 250°C ( $R_{250^\circ\text{C}}$ ), which are basically identical. Accordingly, when the specific activities of the two catalysts CeB/AO/F127-STE and CeB/AO/F127-STE-AC are compared based on weight, the rates  $r_{250^\circ\text{C}}$  (reaction rate of CO oxidation at 250°C per gram) show an about threefold difference. Commercial ceria roughly fits into this sequence; the specific surface area is about 180-times smaller than that of CeB/AO/F127-STE (with the above reservations about the value of  $S_{\text{BET}}$ ), which reduces  $r_{250^\circ\text{C}}$  by a factor of 75.

**Table 2.3** Properties of different ceria samples (20 mg) for CO oxidation

Sample	$P_{\text{XRD}}^{\text{a}}$ (nm)	$S_{\text{BET}}^{\text{b}}$ (m <sup>2</sup> /g)	$D_{\text{BJH}}^{\text{c}}$ (nm)	$\text{Ce}^{3+\text{d}}$ (%)	$T_{10\%}^{\text{e}}$ (°C)	$T_{90\%}^{\text{f}}$ (°C)	$R_{250^\circ\text{C}}^{\text{g}}$ (mol/s·m <sup>2</sup> )	$r_{250^\circ\text{C}}^{\text{h}}$ (mol/s·g)
CeB/AO/F127- STE	<3	277.0	3.4	12	253	398	$2.32 \times 10^{-8}$	$6.42 \times 10^{-6}$
CeB/AO/F127- STE-AC	4.0	88.9	3.9	18	298	494	$2.52 \times 10^{-8}$	$2.24 \times 10^{-6}$
CeB/AO/F127- STH-AC	5.3	132.4	5.4	12	353	546	$2.75 \times 10^{-9}$	$3.64 \times 10^{-7}$
Commercial CeO <sub>2</sub>	57	1.5	16.8	8*	528	>>650	$5.76 \times 10^{-8}$	$8.63 \times 10^{-8}$

<sup>a</sup> Crystallite size calculated by Scherrer equation from XRD

<sup>b</sup> BET surface area; error  $\pm 5\%$

<sup>c</sup> BJH desorption pore diameter;  $\pm 0.5$  nm for STE series,  $\pm 0.1$  nm for STH series

<sup>d</sup>  $\text{Ce}^{3+}$  ratio from XPS, error  $\pm 2$

<sup>e</sup> Reaction temperature for 10% CO conversion

<sup>f</sup> Reaction temperature for 90% CO conversion

<sup>g</sup> Normalized specific reaction rates of CO oxidation on a unit surface area at 250 °C

<sup>h</sup> Reaction rate of CO oxidation at 250 °C per gram

\* Value taken from Ref. [17]

The third sample CeB/AO/F127-STH-AC exhibits a specific surface area somewhat larger than CeB/AO/F127-STE-AC but shows lower rates (both  $R_{250^\circ\text{C}}$  and  $r_{250^\circ\text{C}}$ ) by a factor of ten. This must be due to other parameters besides the surface area. Different effects have been made responsible for activity differences of ceria in the literature. For example, the crystallite size of CeO<sub>2</sub> is known to be a crucial factor for CO oxidation because size may affect the abundance of oxygen vacancies and thus of associated Ce<sup>3+</sup> ions. Smaller crystallite sizes induce a higher fraction of oxygen vacancies due to lower barrier of vacancy formation [76, 77]. One of the proposed mechanisms for CO oxidation on CeO<sub>2</sub> is oxidation by lattice oxygen of CeO<sub>2</sub> with subsequent creation of oxygen vacancies (and Ce<sup>3+</sup>) which in turn induces formation of active oxygen species [78, 79].

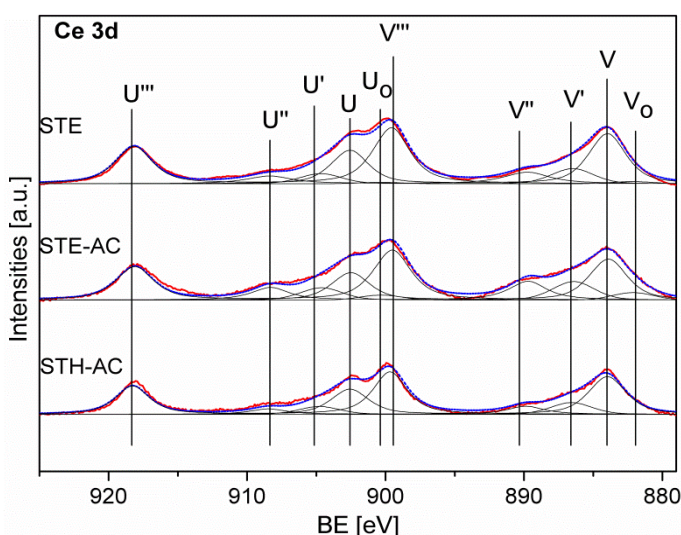


**Figure 2.15** XPS spectra of the Ce 3d region for CeB/AO/F127-STE, CeB/AO/F127-STE-AC and CeB/AO/F127-STH-AC (red: raw spectrum; blue: peak sum after fitting; black: fitted peaks)

In order to evaluate the Ce<sup>3+</sup> proportion, XPS spectra were recorded to characterize the three samples (see Figure 2.15 and Table 2.3). The Ce 3d region is composed of several doublets ( $v$  denotes Ce 3d<sub>5/2</sub>,  $u$  denotes Ce 3d<sub>3/2</sub>). Specifically,  $v_0$ ,  $v'$ ,  $u_0$ ,  $u'$  belong to Ce<sup>3+</sup> species, whereas  $v$ ,  $v''$ ,  $v'''$ ,  $u$ ,  $u''$  and  $u'''$  belong to Ce<sup>4+</sup> species [80]. In order to estimate the Ce<sup>3+</sup> / (Ce<sup>3+</sup>+Ce<sup>4+</sup>) ratio, the relative peak area of the  $u_0$  ( $v_0$ ) and  $u'$  ( $v'$ ) with respect to the area of the entire Ce 3d region was determined [53]. The results (Table 2.3) indicate that the Ce<sup>3+</sup> proportion



can be influenced by the synthesis parameters to some extent. When CeB/AO/F127-STE-AC and CeB/AO/F127-STH-AC are compared, the EtOH solvent used in solvothermal process appears to result in a higher Ce<sup>3+</sup> proportion. This may be due to the fact that EtOH is reductive and can be oxidized to acetaldehyde or carboxylate [74]. Besides the solvent, the post-synthesis treatment can also influence the Ce<sup>3+</sup> proportion. While CeB/AO/F127-STE had only 12% Ce<sup>3+</sup>, the Ce<sup>3+</sup> proportion of CeB/AO/F127-STE-AC increased to 18% when calcined in air. One possible explanation is that decomposition of the carboxylate group might require some oxygen from the ceria, causing oxygen deficiency.

Furthermore, the Ce<sup>3+</sup> proportion is also related to the CeO<sub>2</sub> band gap, and a smaller band gap corresponds to higher amount of Ce<sup>3+</sup> [81, 82]. The reflectance UV-Vis spectra were recorded for CeB/AO/F127-STE-AC and CeB/AO/F127-STH-AC, and the band gaps were calculated using the Kubelka-Munk function and Tauc plot [83], as shown in Figure 2.16. The CeO<sub>2</sub> materials were treated as direct allowed transition as the calculated band gap is closer to the theoretical value 3.2 eV, as reported before [84]. The direct band gap for commercial CeO<sub>2</sub> is also given for reference, but it is not comparable to the synthesized samples because of the big crystal size. For the synthesized samples, the band gaps are in the following sequence: CeB/AO/F127-STE-AC (2.78 eV) < CeB/AO/F127-STH-AC (3.09 eV) < commercial CeO<sub>2</sub> (3.24 eV). CeB/AO/F127-STE-AC should therefore have a higher proportion of Ce<sup>3+</sup> than CeB/AO/F127-STH-AC. The band gaps calculated from UV-Vis reflectance correspond with the XPS results.

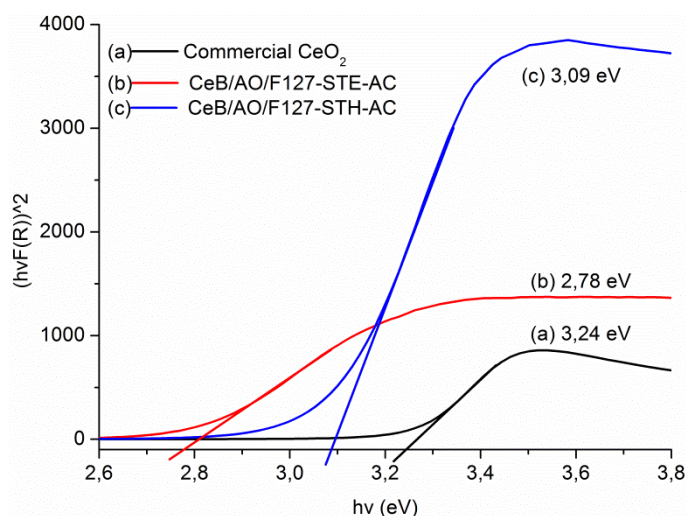


**Figure 2.16** Plots of  $(hvF(R))^2$  vs. photon energy for CeO<sub>2</sub> samples

Nevertheless, a correlation between the Ce<sup>3+</sup> proportion and the specific catalytic activity was not observed. The Ce<sup>3+</sup> proportion may explain the difference between the specific catalytic activity of the STH-AC and STE-AC samples, the latter has a higher Ce<sup>3+</sup> proportion, resulting in higher CO oxidation activity. On the other hand, however, STE and STH-AC have a comparable Ce<sup>3+</sup> proportion but STE has one magnitude higher catalytic activity.

In CO temperature programmed reaction (CO-TPR) experiments, CO<sub>2</sub> and H<sub>2</sub> evolutions were observed when the samples were exposed to CO and heated to 900 °C (Figure 2.17). The CO<sub>2</sub> evolution showed three peaks for all samples, i.e. <400 °C, 450–600 °C, and >650 °C. In the literature, these features were attributed to the removal of surface lattice oxygen, water gas shift between CO and surface OH groups (CO + OH → 1/2 H<sub>2</sub> + CO<sub>2</sub>), and extraction of bulk oxygen, respectively [85]. Interestingly, the low temperature CO<sub>2</sub> peak of STE is shifted by around 50 °C to low temperature relative to the STE-AC and STH-AC samples. In addition, STE also exhibits, besides the main H<sub>2</sub> peak at 500~570 °C (which is due to the water gas shift reaction), an additional feature at around 320 °C, which was not observed for the other samples. The H<sub>2</sub> evolution at low temperature for STE could be attributed to reactions involving the residual organic group after the synthesis. This would also explain the shift of CO<sub>2</sub> evolution to lower temperature for STE.

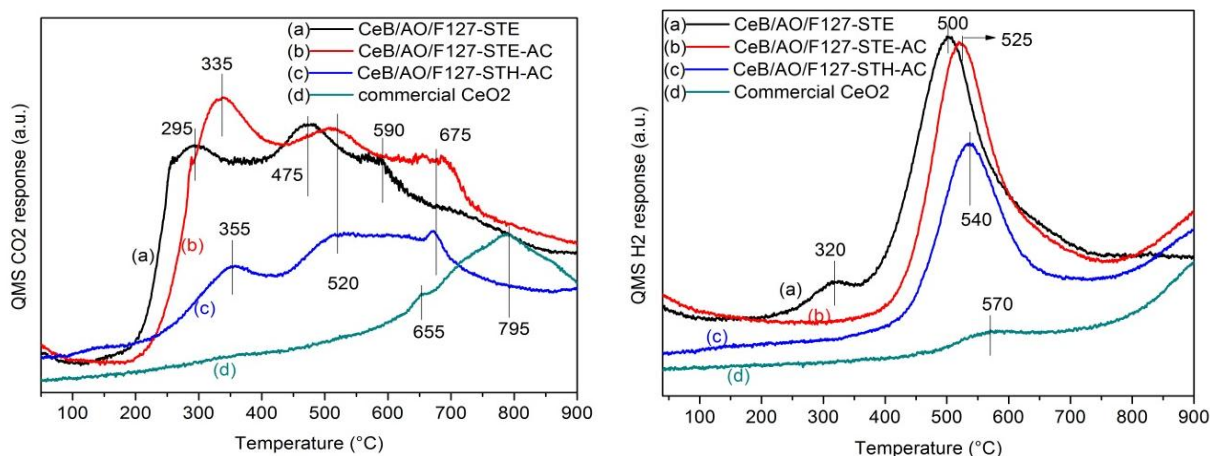


**Figure 2.17** CO<sub>2</sub> (left) and H<sub>2</sub> (right) evolution during CO-TPR over different CeO<sub>2</sub> samples (20 mg)

The Raman spectra also gave evidence for the advantage of using EtOH for solvothermal treatment, and explained why the STE sample has a better catalytic activity than others, as shown in Figure 2.18. The sample prepared from EtOH showed two bands at 1388 and 1577 cm<sup>-1</sup>,

which are characteristic for graphene (Gp). The graphene-like layers were also observed in SEM images in the following section (eg. Figure 2.23 and Figure 2.28). The two graphene bands were not visible in the STH and STE-AC samples, indicating the graphene-like layer did not exist there. It is well known that graphene can transfer electrons very fast, which could promote CO oxidation in the STE sample.

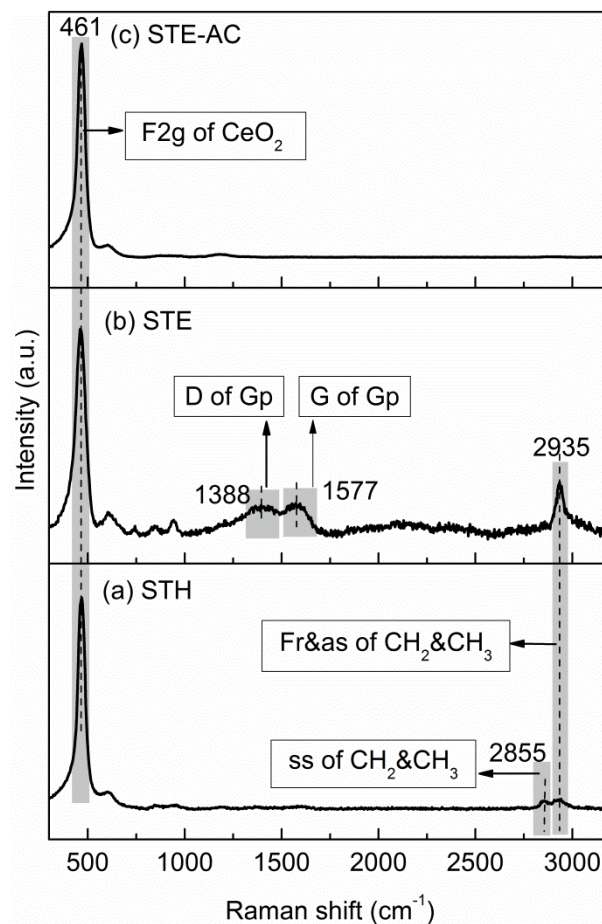


**Figure 2.18** Raman spectra of CeB/AO/F127-STH, CeB/AO/F127-STE and CeB/AO/F127-STE-AC

The formation of carbon residues is a normal phenomenon for solvothermal treatment. For example, the TiO<sub>2</sub>/C composite, which was obtained in solution with a glycerol/ethanol ratio of 5/75, contained 1.2 mass% carbon and exhibited both superior adsorption capability and visible-light photocatalytic activity [86]. The author believed that glycerol served as the carbon source, which was thermally decomposed to amorphous carbon during solvothermal processing. Similarly Nd and C co-doped TiO<sub>2</sub> (Nd-C-TiO<sub>2</sub>) samples were successfully prepared by a facile

calcination-assisted solvothermal reaction without addition of any other C precursors except the Ti source and ethanol, and carbonate species and C-doped TiO<sub>2</sub> were formed [87]. Although the literature did not report Raman investigations to detect the structure of carbon residues, all of them showed a performance improvement of the synthesized materials because of the carbon residues. In the research reported in this thesis on the synthesis of CeO<sub>2</sub>, the organic residues with graphene-like structure are closely related to the use of the ethanol solvent, as there are no D and G bands in the sample synthesized by H<sub>2</sub>O as solvent. Thus, the organic residues possibly form from ethanol by thermal decomposition during the solvothermal treatment. This can be also proven by the weight loss in Figure 2.7, which only changes along with the solvothermal solvent, rather than the gel components.

As discussed above, the oxidation of CO by ceria depends on the surface area and the oxygen vacancies (Ce<sup>3+</sup>), but the surface OH groups and the graphene-like residues can also contribute to the reaction. The same catalytic activity of STE and STE-AC may be due to the compensation of the Ce<sup>3+</sup> proportion (which is lower for STE) and the influence of highly reactive OH groups and graphene-like layers resulting from the residual organic species in the STE sample. STE-AC and STH-AC do not contain such OH groups and graphene-like layers, as the organic species were largely removed during the calcination. Therefore, despite the missing OH groups and graphene-like residues, the specific activity exhibited by STE-AC is the result of a high Ce<sup>3+</sup> content. A possible explanation for the different specific catalytic activity may thus be the different CeO<sub>2</sub> surface states formed by the different post-synthesis treatment. The reductive ability of EtOH might be a key factor.

#### **2.4 Influences of solvothermal temperature (T) and time (t)**

As already described in section 2.3, the solvent of solvothermal treatment is an important factor for the CeO<sub>2</sub> properties. When compared with H<sub>2</sub>O as solvent, ethanol results in CeO<sub>2</sub> with higher surface area and larger amount of Ce<sup>3+</sup>. In this part, the solvent was fixed to ethanol and the gel composition was also kept constant: CeB:AO:F127= 1:2:0.005. The influences of the solvothermal temperature (T) and the solvothermal reaction time (t) were investigated.

### 2.4.1 Influence of solvothermal temperature (T)

The solvothermal solvent was fixed to ethanol and the reaction time to 6 h, only the solvothermal temperature was changed from 140 °C to 200 °C. The synthesized samples were characterized by TGA and IR to detect the organic residues after the solvothermal treatment.

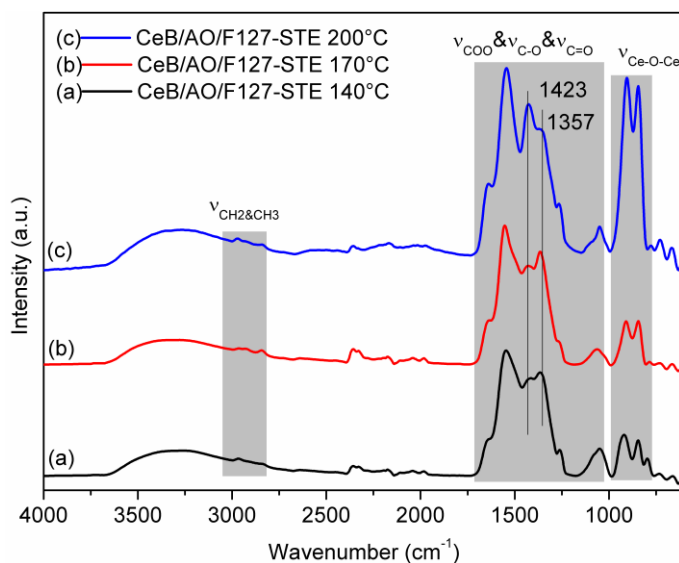


**Figure 2.19** IR curves of CeO<sub>2</sub> samples synthesized at different ST temperatures

Figure 2.19 shows the IR spectra of samples synthesized at different solvothermal temperatures. The bands in the range of 800-1000 cm<sup>-1</sup> correspond to Ce-O-Ce, and the intensities of the peaks increase with increasing of solvothermal temperature. The bands in the range of 1050-1650 cm<sup>-1</sup> belong to carboxylate groups, which may have different coordination form, like non-coordinated, bridging or chelating coordination [88]. The intensity changes of the bands at 1423 cm<sup>-1</sup> and 1357 cm<sup>-1</sup> may be caused by the change of the carboxylate coordination. Besides, there are still a few CH<sub>2</sub> & CH<sub>3</sub> groups in all samples.

TGA curves of the three samples are given in Figure 2.20. The decomposition trend and the weight loss are similar for all three samples. All decompositions are finished at about 300 °C with a weight loss of ca. 12%.

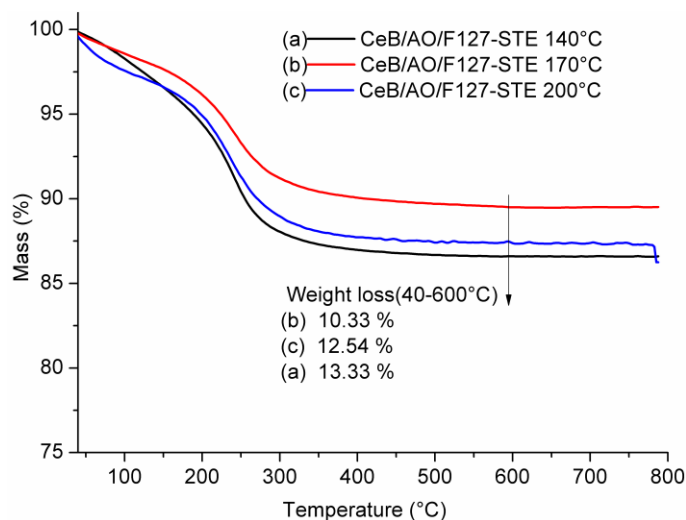


**Figure 2.20** TGA curves of CeO<sub>2</sub> samples synthesized at different ST temperatures

Figure 2.21 shows the XRD patterns of CeO<sub>2</sub> samples synthesized at different temperatures. All the three samples are similar, but the crystallite size increased slightly with increasing the solvothermal temperature. The crystallite size is 1.89 nm for the sample solvothermally treated at 140 °C for 6 h. When the temperature increased to 170 °C, the size increased to 2.07 nm. Further increasing the temperature to 200 °C resulted in an increased crystallite size of 2.12 nm.

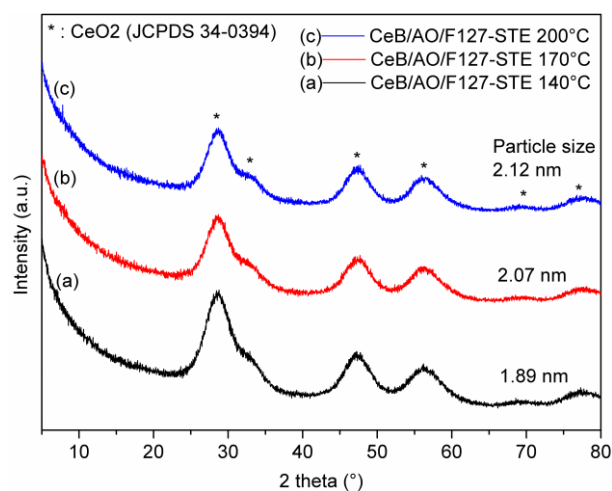


**Figure 2.21** XRD patterns of CeO<sub>2</sub> samples synthesized at different ST temperatures

CeO<sub>2</sub> samples, synthesized at different temperatures, were characterized by N<sub>2</sub> sorption, and the isotherms and pore size distributions are given in Figure 2.22. The isotherms are type I according to IUPAC classification [73], which corresponds to microporous solids having

relatively small external surfaces. Generally, the BET surface areas increased along with the increase of solvothermal temperature, while the pore sizes changed in the opposite direction. For example, when the sample CeB/AO/F127-STE treated at 140 °C, the surface area is 195.9 m<sup>2</sup>/g while the pore size is 3.65 nm. When the temperature increased to 200 °C, the surface area increased to 277.0 m<sup>2</sup>/g while the pore size decreased to 3.43 nm.

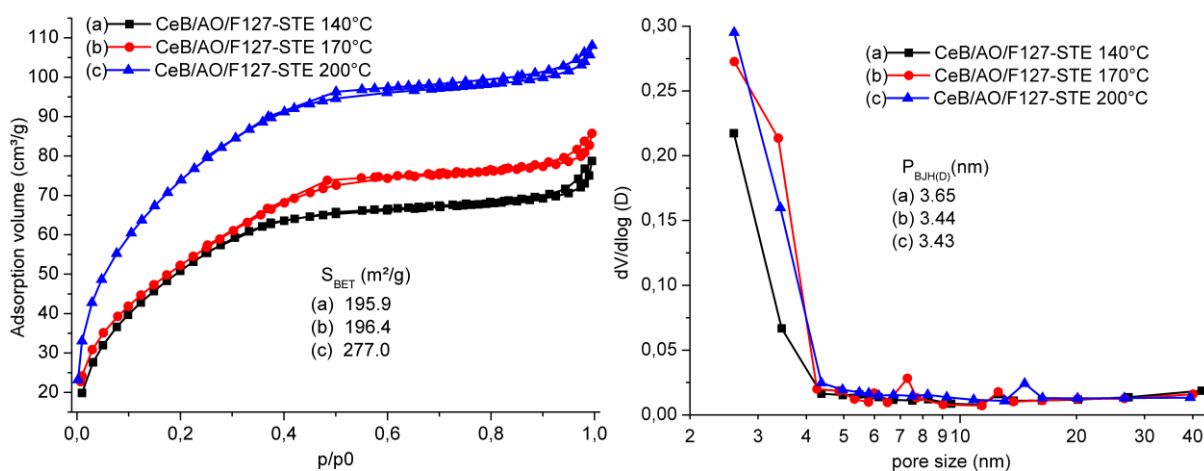


**Figure 2.22** N<sub>2</sub> adsorption-desorption isotherms (left) and pore size distributions (right) for CeO<sub>2</sub> samples synthesized at different ST temperatures

Figure 2.23 shows the SEM images of samples treated at 140 °C and 200 °C for 6 h, respectively. The sizes are larger than that detected by XRD, indicating agglomeration/aggregation between the tiny crystallite particles. The ST temperature has almost no influence on the size of the agglomerated/ aggregated particles, but there are more organic-like films in the sample prepared at 140 °C. There may be two reasons: (1) the organic residues are not totally removed during the washing process; (2) the organic residues have stronger connection with the CeO<sub>2</sub> particles when the ST temperature is relatively lower, and the temperature is not high enough to cleave the organic residues with graphene-like structures.



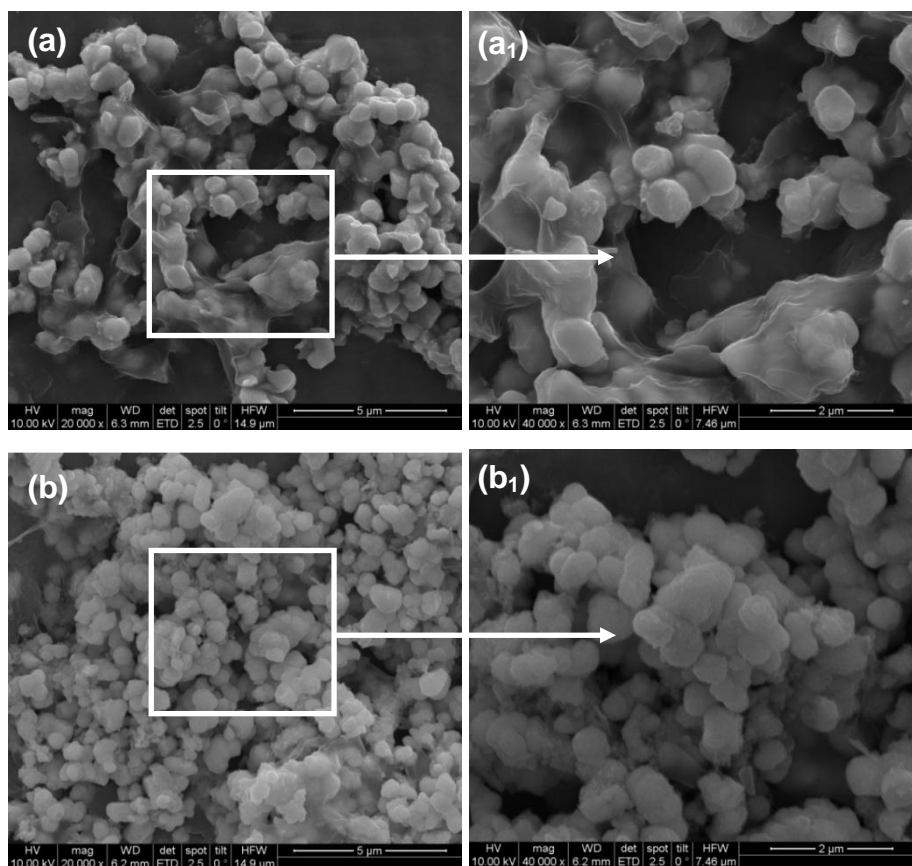


**Figure 2.23** SEM images of samples treated at 140 °C (a, a<sub>1</sub>) and sample treated at 200 °C (b, b<sub>1</sub>) for 6 h respectively

The changes of solvothermal temperature have almost no effect on the crystallite phase and the weight loss of the system. Although the total weight of the organic residues (like the carboxylate groups) were almost the same for all samples, the change of the solvothermal temperature could alter the interaction between the organic groups (like the carbonate groups) and CeO<sub>2</sub>, which would further change the surface area. The higher the solvothermal temperature is, the larger the surface area becomes. But due to the limitation of the used equipment, the highest possible temperature was 200 °C.

#### 2.4.2 Influence of different solvothermal reaction time (t)

The influence of the solvothermal reaction times on the structure of the synthesized CeO<sub>2</sub> was investigated while other parameters were fixed (In this case, the solvothermal temperature was fixed to 200 °C, the solvent was fixed to ethanol and the gel content also kept constant:



CeB:AO:F127= 1:2:0.005). The ST reaction times were changed from 3 h to 24 h to check the effect on the material properties.

IR was used to characterize the samples, as shown in Figure 2.24. The peaks can also be divided into two regions: 800-1000 cm<sup>-1</sup> (Ce-O-Ce) and 1050-1650 cm<sup>-1</sup> (COO, C-O, C=O). For the carboxylate region (1050-1650 cm<sup>-1</sup>), the band positions and relative intensities slightly changed when the reaction time was varied from 3 h to 24 h. For the Ce-O-Ce region, the situation is a little complicate. When the reaction time was less than 12 h, the Ce-O-Ce region had two bands at both 908 cm<sup>-1</sup> and 846 cm<sup>-1</sup>. When the reaction time was prolonged over 18 h, there was only one band at 846 cm<sup>-1</sup>.

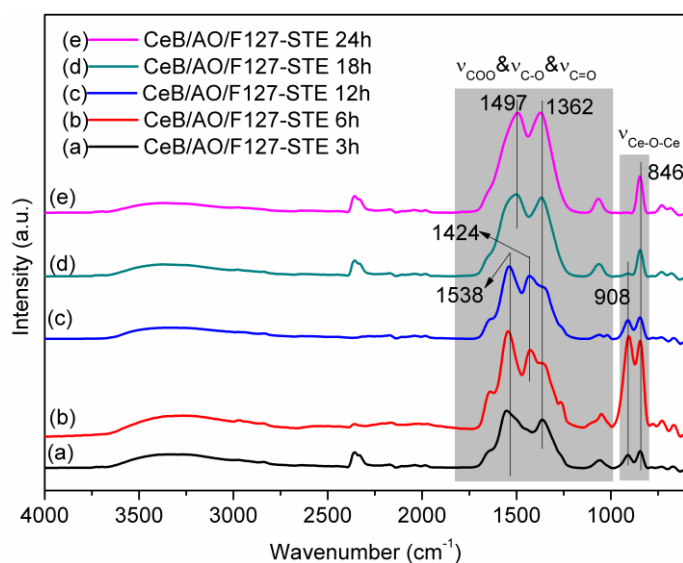


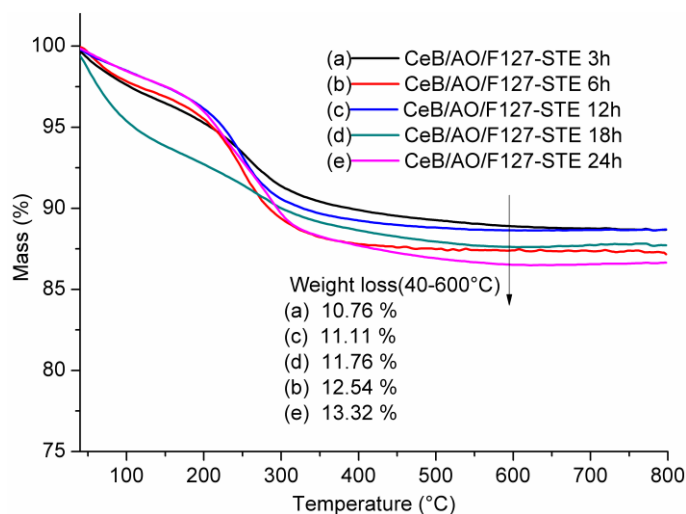
**Figure 2.24** IR curves of CeO<sub>2</sub> samples synthesized with different ST reaction times

The combination bands, overtones and Fermi resonances are normally used to explain and assign peaks in vibrational spectra with un-known fundamental vibrations. Combination bands and overtones generally have lower intensities than the fundamentals, and Fermi resonance causes a split and shift in intensity of bands with similar energies and identical symmetries. As the XRD showed no phase transformation of CeO<sub>2</sub>, the change of the Ce-O-Ce region may be influenced by the way how the carboxylate groups are coordinated to CeO<sub>2</sub> and how the defects change for the ST CeO<sub>2</sub> nanoparticles. This resulted in the alternation of combination bands, overtones and Fermi resonances of the ST CeO<sub>2</sub> materials.

As reported before, the fundamental vibrational bands of CeO<sub>2</sub> appeared at 400-500 cm<sup>-1</sup> [89], and the bands observed in the 850-950 cm<sup>-1</sup> range belong to the first overtone. As far as the carboxylate groups are concerned, the band of 1538 cm<sup>-1</sup> shifted to 1497 cm<sup>-1</sup>, which might indicate that the coordination mode of COO<sup>-</sup> changed [88]. Thus the vibration of the surface Ce-O changed, and the band at 908 cm<sup>-1</sup> might be caused by bridging of COO.

The intensity change of the bands may be caused by the Fermi resonances on the overtone [90]. A Fermi resonance is the shifting of the energies and intensities of absorption bands in an infrared or Raman spectrum. It is a consequence of quantum mechanical mixing [91]. Fermi resonance most often occurs between normal and overtone modes, if they are nearly coincident in energy. It does not really lead to additional bands in the spectrum, but will let the weaker mode gain intensity (becomes more allowed), and the more intense band decreases in intensity. Two conditions must be satisfied for the occurrence of Fermi resonance: (1) the two vibrations must have the same symmetries; (2) the transitions (accidentally) have almost the same energy.

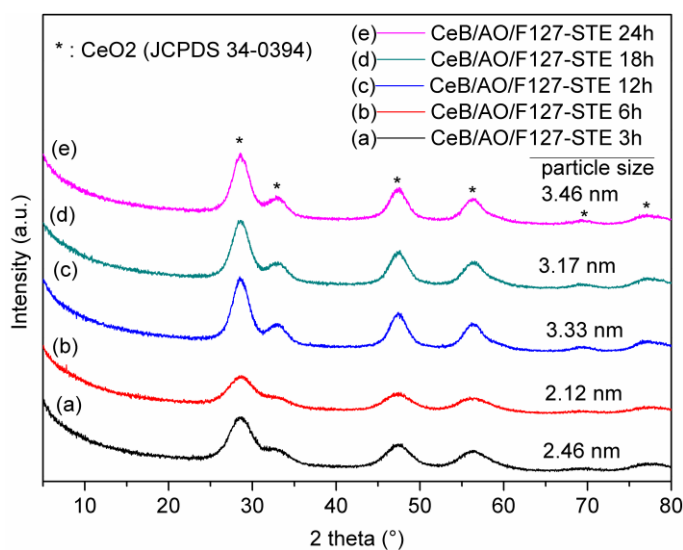
Thus, the relatively high intensity of sample treated after 6 h maybe have nearly coinciding in energies for both fundamental and first overtone bands, which is a special stage formed during the dissolution-deposition equilibriums under solvothermal treatment. And a relatively strong Fermi resonance occurred in this case, resulting in strong first overtone bands.



**Figure 2.25** TGA curves of CeO<sub>2</sub> samples synthesized with different ST reaction times

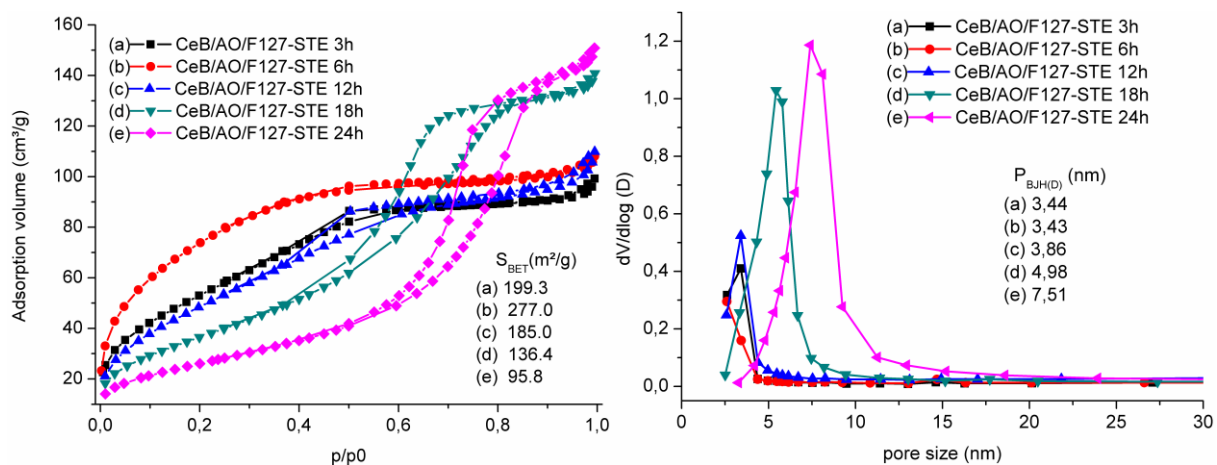
The TGA curves (Figure 2.25) for all samples are not special. The decompositions for all samples were finished at about 300 °C with a weight loss of ca. 12%.

The XRD patterns of samples prepared with different ST reaction times are shown in Figure 2.26. The changes of crystallite size follow no trend, but are all in the 2.1~3.5 nm range. It needs to be pointed out that the ST sample treated for 6 h has the smallest crystallite size, which might be evidence that the sample is a special stage formed during the dissolution-deposition equilibriums under solvothermal conditions, as discussed in the above IR explanation.

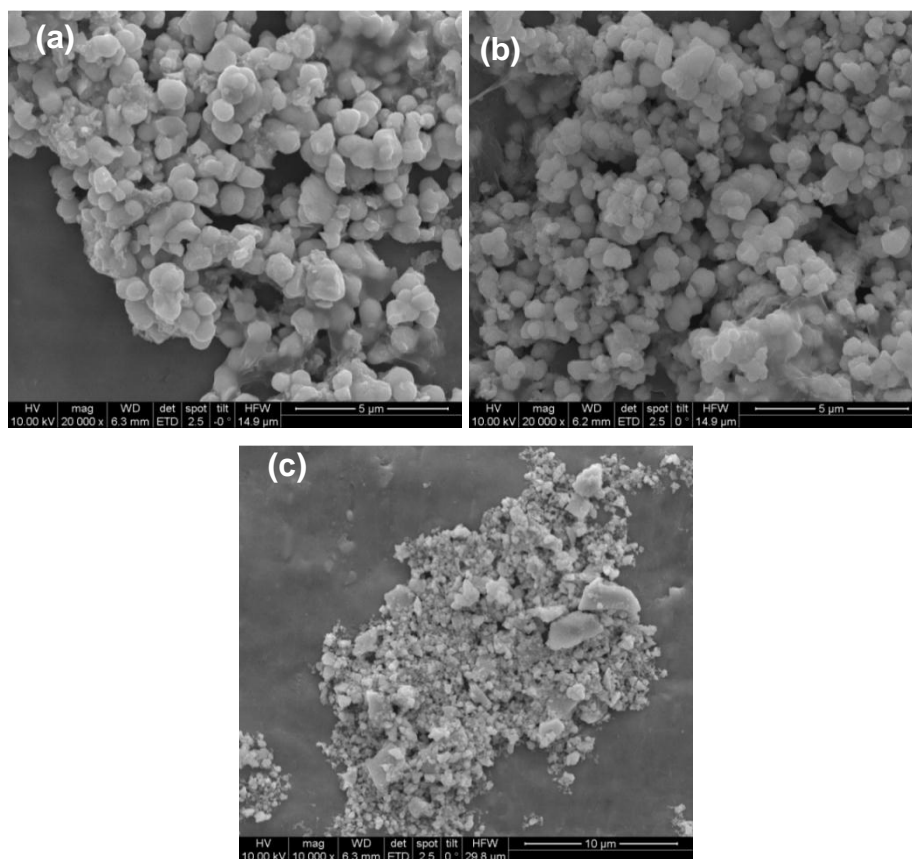


**Figure 2.26** XRD patterns of CeO<sub>2</sub> samples synthesized with different ST reaction times

The samples synthesized with different ST reaction times were characterized by N<sub>2</sub> sorption, and the isotherms and pore size distributions are given in Figure 2.27. The isotherms for samples reacted less than 12 h are type I according to IUPAC classification [73], which corresponds to microporous solids having relatively small external surfaces. But when the reaction time was longer than 18 h, the isotherms changed to type IV, indicating that the materials are mesoporous. The specific surface area, except the one of the sample reacted for 3h, decreased along with the extension of the reaction time, from 277.0 m<sup>2</sup>/g for 6 h to 95.8 m<sup>2</sup>/g for 24 h. The pore sizes increased with prolonging of reaction time, and the maximum dV/dlog(D) value also increased, indicating that the pore size distribution are narrowed along with the reaction time.



**Figure 2.27** N<sub>2</sub> adsorption-desorption isotherms (left) and pore size distributions (right) for CeO<sub>2</sub> samples synthesized with different ST reaction times



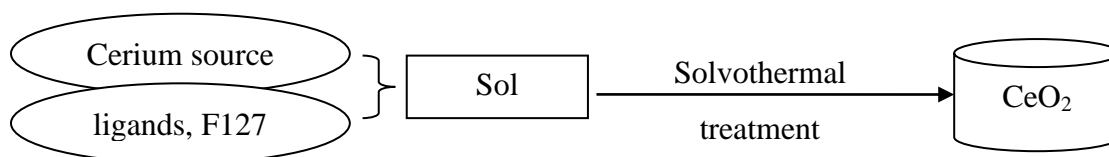
**Figure 2.28** SEM of CeO<sub>2</sub> samples ST treated at 200°C for 3 h (a), 6 h (b), and 24 h (c)

Figure 2.28 displays the SEM images of samples prepared at 200 °C for different times. Generally the size of the agglomerated/aggregated particles became smaller along with prolonged of the reaction time. But huge agglomerations/aggregations were observed for samples prepared for 24 h.

The reaction time of the solvothermal treatment also has almost no effect on the crystallite phase and the weight loss of the system. It mainly influenced the IR spectra, surface area, pore size distribution and the agglomerations/aggregations of crystalline particles. Longer reaction times resulted in lower surface area and larger pore size.

### 2.5 Role of gel processing for CeO<sub>2</sub> samples

During normal solvothermal processing the solution (sol) is directly transferred into the autoclave, and then it is sealed for reaction at high temperature for a certain time. In our research, solid gel powders were put into the autoclave for the following heat-treatment. Thus the following experiment was designed: the prepared sol was directly transferred into the autoclave for solvothermal reaction, as shown in Figure 2.29. This process was named sol-ST, in order to distinguish from the previous one (Figure 2.1, sol/gel-ST). The sol content and all the other synthesis parameters were kept the same (solvent EtOH, 200 °C, 6 h or 18 h).



**Figure 2.29** Schematic synthesis protocol of CeO<sub>2</sub> by traditional solvothermal (sol-ST) processing

The IR curves of CeO<sub>2</sub> prepared by sol-ST and sol/gel-ST were compared in Figure 2.30. The extension of the reaction time had almost no influence on the IR curves of the CeO<sub>2</sub> sample prepared by sol-ST method. Different to sol/gel-ST samples, the vibration bands for sol-ST sample are only obvious in the 1050-1650 cm<sup>-1</sup> (COO, C-O, C=O) region, and there were almost no bands in the 800-1000 cm<sup>-1</sup> (Ce-O-Ce) region, even when the reaction time increased from 6 h to 18 h. The key reason might be that there is no pre-formed oxo network, and only tiny

colloids/particles formed by ligand-modified CeB precursors exist in the sol. The tiny colloid particles could re-construct easily under the solvothermal conditions.

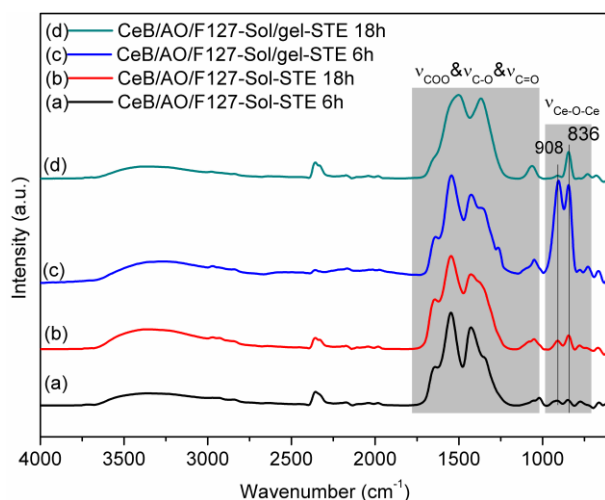


**Figure 2.30** IR curves of CeO<sub>2</sub> prepared from sol-ST (a, b) and sol/gel-ST (c, d) method for different reaction times

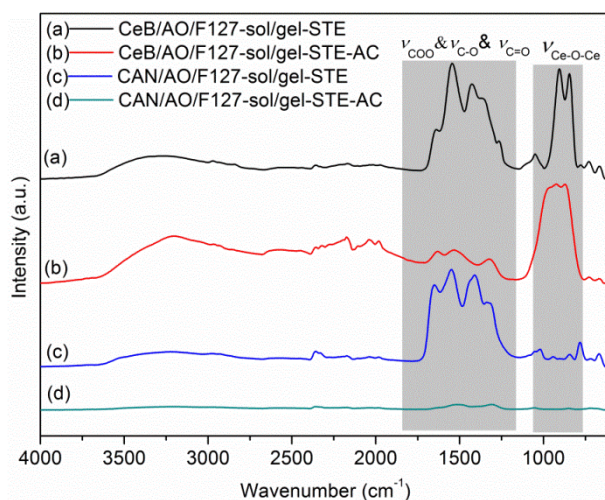


**Figure 2.31** IR curves of CeO<sub>2</sub> prepared from sol/gel-ST with different precursors (a) & (b) using CeB as precursor, (c) & (d) using CAN as precursor

The special Ce-O-Ce bond of CeB after sol-gel processing can also be proven by Figure 2.31. When CAN was used instead of CeB as precursor and other parameters were kept the same (Figure 2.31 (c) & (d)), the prepared sample showed no Ce-O-Ce overtone in the range of 800-1000 cm<sup>-1</sup>. This may be because CAN cannot form a Ce-O-Ce oxo network during the ‘gel’ (exposed to the air) processing either. Thus both CeB and gel processing are necessary for the formation of Ce-O-Ce first overtone.

The TGA curves (Figure 2.32) of all samples are not special. Decomposition of all samples was finished at about 300 °C. The samples prepared from sol-ST have about 2% weight loss more than those prepared by the sol/gel-ST method.

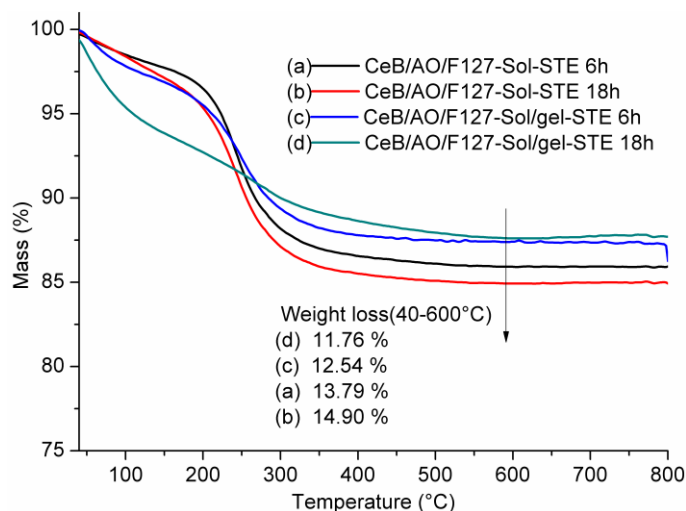


**Figure 2.32** TGA curves of CeO<sub>2</sub> prepared from sol-ST (a, b) and sol/gel-ST (c, d) method for different reaction times

Figure 2.33 shows the XRD patterns of CeO<sub>2</sub> prepared by sol-ST and sol/gel-ST for different times. Compared with the samples prepared by sol/gel-ST method, the samples of sol-ST showed almost no change along with the prolonging of the reaction time. Both sol-ST samples prepared for 6 h and 18 h have almost the same particle size of 2.1-2.2 nm.

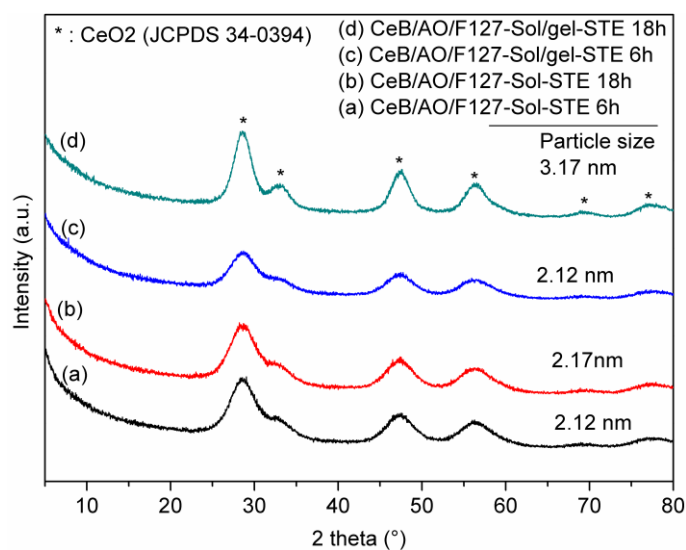


**Figure 2.33** XRD patterns of CeO<sub>2</sub> prepared from sol-ST (a, b) and sol/gel-ST (c, d) method for different reaction times



N<sub>2</sub> sorption was also used to characterize the samples synthesized by the sol-STE method, and the isotherms and pore size distributions are displayed in Figure 2.34. The isotherms (Figure 2.34 left (a) & (b)) for samples prepared by sol-STE are a little complicated, more like a mixture of type I and type II in IUPAC classification, which indicated that the materials were composed of both micropores and macropores. This can also be proven by the pore size distribution in the right of Figure 2.34. When compared to the materials synthesized by the sol/gel-STE method, besides the maximum at about 5 nm, the  $dV/d\log(D)$  value of sol-STE samples increased along with the enlargement of the pore size, which indicated that the proportion of pores with larger size increased. Unlike the sol/gel-STE samples, the surface area for sol-STE samples did not change too much when the reaction time was changed from 6 h to 18 h, and both are around 250 m<sup>2</sup>/g. The pore size distribution became narrower when the reaction time was longer for both sol-STE and sol/gel-STE samples. The pore size of the sol-STE sample was a little larger than that of the sol/gel-STE sample when the reaction time was the same. For example, it was 3.43 nm of the sol/gel-STE sample for 6 h while the size increased to 4.75 nm of the sol-STE sample for 6 h.

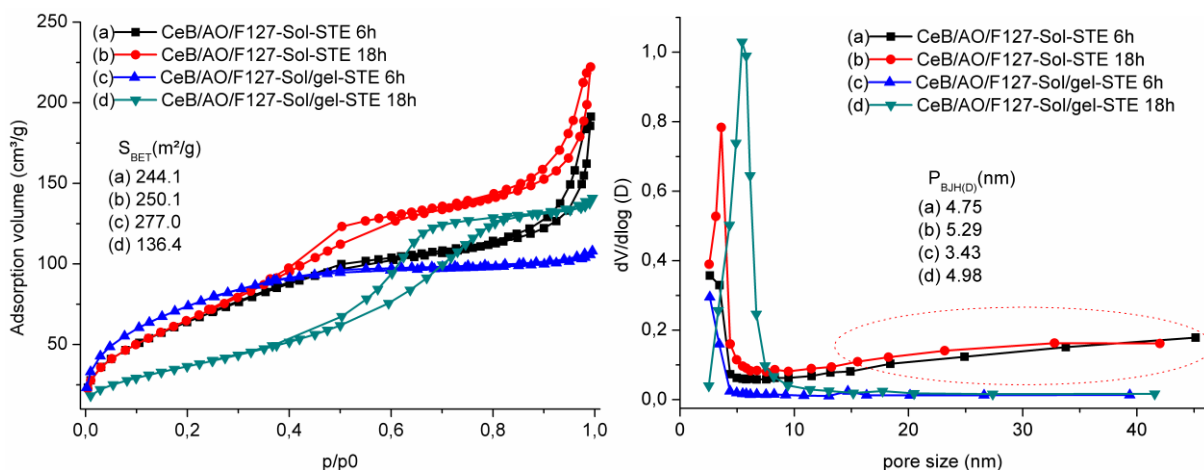


**Figure 2.34** N<sub>2</sub> adsorption-desorption isotherms (left) and pore size distributions (right) for CeO<sub>2</sub> prepared from sol-ST (a, b) and sol/gel-ST (c, d) method at different reaction time

SEM images of samples prepared by different methods at 200 °C for 6 h are shown in Figure 2.35. The morphologies for both samples are totally different. Although the crystallite sizes are similar (Figure 2.33), the agglomerations/aggregations for sol-ST sample are obviously smaller than that of sol/gel-ST. The diameter of agglomerations / aggregations for sol-ST sample is about 100-200 nm, while the diameter of agglomerations / aggregations for sol/gel-ST sample is about



~500 nm. This may also relate to the weaker Ce-O-Ce network formed by sol-ST method, thus smaller agglomerations / aggregations particles were preferred.

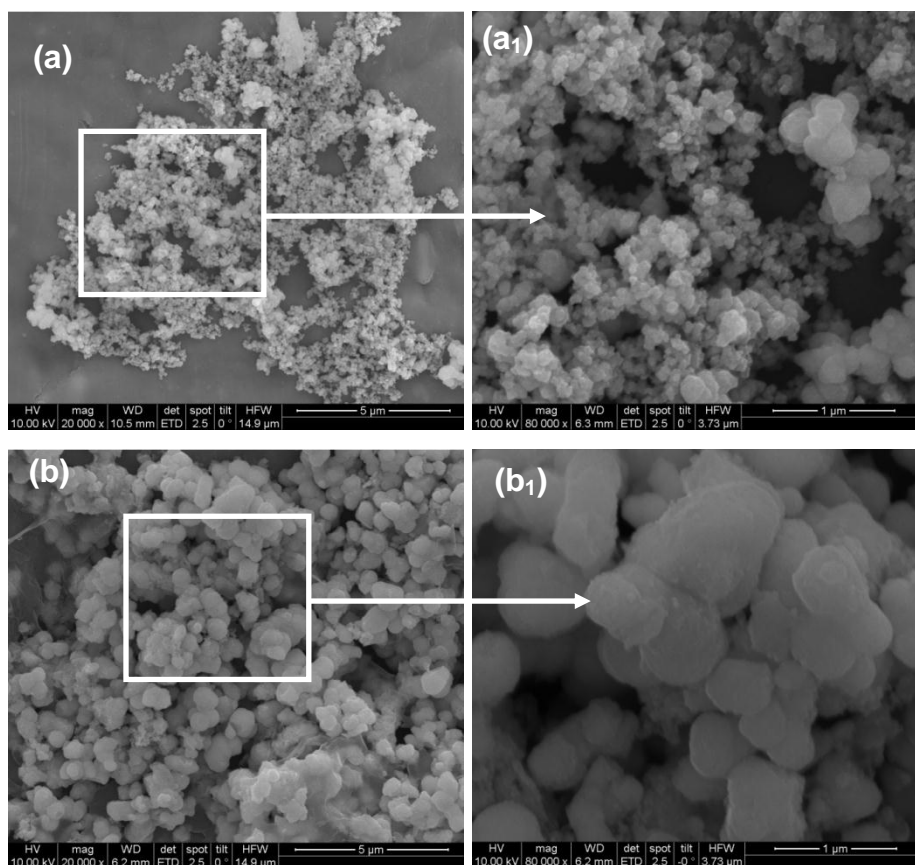


**Figure 2.35** SEM images of samples treated by sol-ST method (a, a<sub>1</sub>) and sol/gel method (b, b<sub>1</sub>) at 200 °C for 6 h

The samples prepared from the sol-ST method are a little different, as reflected by IR, TGA, XRD, BET and SEM. Sol-ST samples are stable with change of the reaction time, while the structure of sol/gel-ST samples changed along with the reaction time. The sol-ST samples have smaller agglomerations/aggregations compared with sol/gel-ST samples, and have no obvious first Ce-O-Ce overtone in the range of 800~1000 cm<sup>-1</sup>.

## 2.6 Conclusion

In this work, high surface area CeO<sub>2</sub> was prepared from cerium *t*-butoxide by the combination of sol-gel processing and solvothermal treatment. Different parameters were investigated and the effects of them on the material structures and properties can be summarized as follows:

- (1) **Precursor:** the use of cerium alkoxides as sol-gel precursor for ceria has clear advantages compared with (NH<sub>4</sub>)<sub>2</sub>[Ce(NO<sub>3</sub>)<sub>6</sub>], for high product yield and high surface area;
- (2) **Post-synthesis treatment:** Solvothermal treatment in either ethanol or water resulted in materials with distinctly higher specific surface areas and smaller crystallite sizes than by calcination alone (either in the air or N<sub>2</sub>+air). Specific surface areas of up to 277 m<sup>2</sup>/g were obtained which is unprecedented for ceria (commercial ceria ranges around 2 m<sup>2</sup>/g);
- (3) **Gel composition for solvothermal treatment:** gels were typically made from acetaldoximate-substituted cerium *t*-butoxide in the presence of the surfactant F127. The absence of acetaldoximate or/and F127 can influence the surface area of the product, and the highest surface area was obtained for the material prepared in the presence of all the three components followed by solvothermal treatment in EtOH;
- (4) **Solvent of solvothermal treatment:** both H<sub>2</sub>O and EtOH were used as solvent. The solvent can influence the organic residues after solvothermal treatment and the material's surface area. When EtOH was used as solvent, there were more organic residues on the ceria surface, which have a graphene-like structure. Furthermore, the Ce<sup>3+</sup> proportion is also higher for samples prepared from EtOH (the highest value reached 18%), which contributed to higher catalytic activity of the material;
- (5) **Temperature of solvothermal treatment:** Changes of solvothermal temperature have almost no effect on the crystallite phase and the weight loss, but can influence the surface area of the material. The higher the solvothermal temperature is, the larger the surface area becomes.
- (6) **Reaction time of solvothermal treatment:** The reaction time mainly influenced the IR spectra, surface area, pore size distribution and the agglomerations/aggregations of crystallite particles. A longer reaction time resulted in lower surface area and larger pore size.
- (7) **Role of gel processing:** The gel processing can form strong Ce-O-Ce bonds and a pre-organization of the oxo network, which resulted in a narrow pore size distribution.

### 3. Co<sub>3</sub>O<sub>4</sub> modified CeO<sub>2</sub>

#### 3.1 Introduction

Co<sub>3</sub>O<sub>4</sub>-CeO<sub>2</sub> catalyst is a better substitution for noble metal-CeO<sub>2</sub> system, because of the nice activity for CO oxidation, preferential CO oxidation, hydrocarbon and diesel soot oxidation [30-33]. In catalysis it is generally known, that a high specific surface area (SSA) is one of the main conditions to assure a high dispersion of the second phase and, in consequence, a high amount of available active sites. Meeting this requirement strongly depends on the choice of the particular preparation method. Comparing preparation methods, impregnation (IMP), precipitation-oxidation (PO), co-precipitation (CP) and hydrothermal (HT) methods, Tang and coworkers have found out that Co<sub>3</sub>O<sub>4</sub>-CeO<sub>2</sub> (20% CeO<sub>2</sub>) catalysts prepared by means of IMP and PO are the most active for CO oxidation, because IMP yields well-dispersed ceria that strongly interacts with the cobalt oxide and the PO method yields the highest surface area [30]. However, the conventional and most frequently used preparation methods for the synthesis of Co<sub>3</sub>O<sub>4</sub>-CeO<sub>2</sub> catalysts such as impregnation and co-precipitation have disadvantages: relatively small SSA and a large crystallite size that leads to a poor dispersion of these two phases. An attempt to increase a SSA for Co<sub>3</sub>O<sub>4</sub>-CeO<sub>2</sub> using a surfactant as template appeared to be not successful, because as prepared materials require further calcination at high temperatures in order to remove the organic residues. That automatically causes a drop in SSA and an increase of the crystallite size [31, 46]. Preparation of Co<sub>3</sub>O<sub>4</sub>-CeO<sub>2</sub> with high SSA and well dispersed phases still remains a great challenge.

In the previous chapter of this thesis on the preparation of CeO<sub>2</sub>, a high SSA and small ceria particles (3.5–5.5 nm) of CeO<sub>2</sub> were obtained from acetaldoximate-modified cerium *tert*-butoxide (CeB) by combination of sol-gel processing and solvothermal treatment [72]. It was also shown that the sol composition was a very important parameter apart from the processing parameters. Modification of CeB with acetaldoxime (AO) resulted in materials with superior properties, especially when combined with the nonionic surfactant Pluronic F127 as a pore-forming agent [70, 72].

We therefore employed acetaldoximate-modified CeB and the surfactant F127, as well as the optimized reaction and processing conditions also to the synthesis of high surface-area Co<sub>3</sub>O<sub>4</sub>-CeO<sub>2</sub> (solvothermal treatment in ethanol (STE) followed, optionally, by calcination in air (AC) for removal of organic groups). The Co precursor (cobalt acetate, Co(OAc)<sub>2</sub>) was added by three different routes to modify the materials structure and Co distribution, and thus to find out which route results in the most active material for CO oxidation. After figuring out the best method for adding the Co precursor, the influence of the Ce:Co ratio were also investigated.

### 3.2 Influence of Co precursor adding sequence

Taking into account that the dispersion of the oxides is an important factor that determines the catalytic activity, we extended our studies to the question how Co is introduced into/onto CeO<sub>2</sub> during preparation. To this end, three methods were compared with a fixed Ce: Co ratio of 4:1:

*Route 1:* A ceria gel was synthesized by sol-gel processing of CeB. Cobalt acetate was then added to the gel, and the mixture was put into an autoclave for solvothermal processing in ethanol.

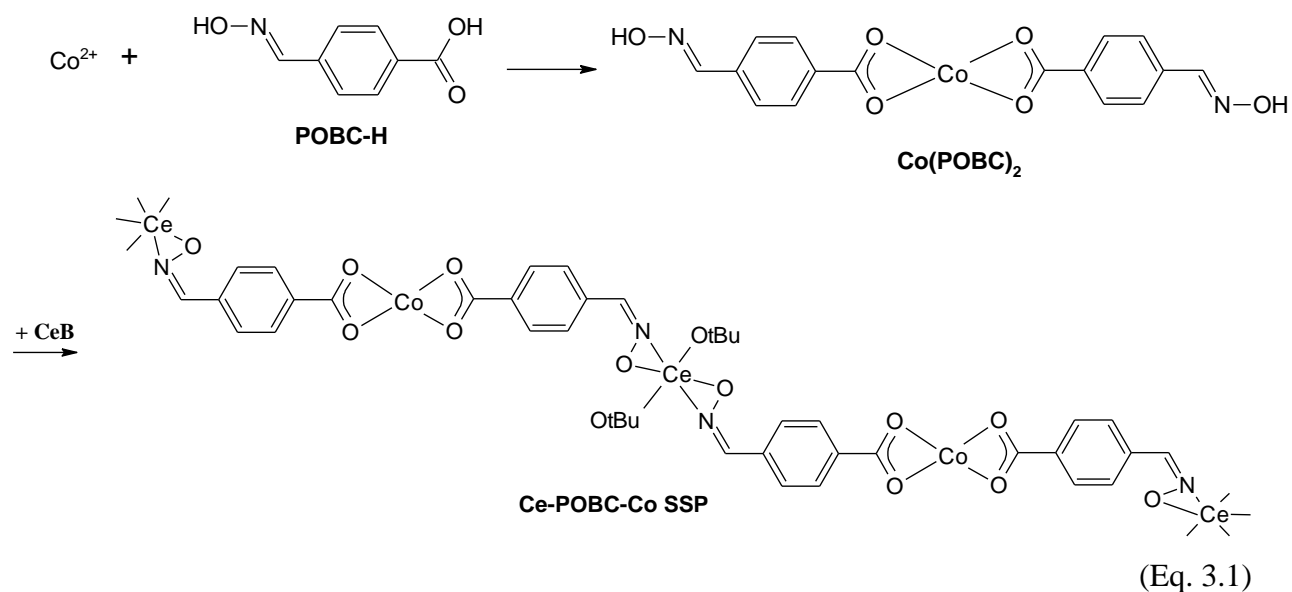
*Route 2:* CeB and cobalt acetate were mixed together during sol-gel processing and then treated solvothermally. It is known that co-processing of metal alkoxides and the acetate of a second metal results in mixed-oxide structures [92].

*Route 3:* CeB and cobalt acetate were first connected by a bifunctional ligand to form a single-source precursor (SSP), which was then subjected to sol-gel processing followed by solvothermal treatment. Previous work had shown that tethering both metal moieties during sol-gel processing by means of a bifunctional organic group L-B-L', where L and L' coordinate to different metals, avoids macroscopic phase separation and results in a more homogeneous distribution of both metals through all stages of the synthesis [15].

The samples are labeled as follows: the gels obtained after sol-gel processing are labelled "1", "2" or "3", according to the preparation method. "STE" refers to solvothermal treatment in ethanol and the samples are labeled 'x-STE'. To investigate the influence of the organic groups, part of the samples (1-3) was heat-treated in air at 500 °C after solvothermal treatment. These samples are labeled 'x-STE-AC'. For example, "3-STE-AC" is a sample prepared by route 3 with solvothermal post-synthesis treatment followed by calcination.

### 3.2.1 Synthesis of Ce-L-B-L'-Co single source precursor

*Route 3* uses the concept of single source precursor, thus evidence of the synthesis of a Ce-L-B-L'-Co single source precursor is described first. Formation of the single source precursor according to Eq. 3.1 cannot be verified by means of NMR because of the paramagnetic properties of Co, and therefore only FTIR was used to monitor the reaction (Figure 3.1).



In the spectrum of POBC-H (Figure 3.1a), the bands at 1687, 1610, 1290, and 999  $\text{cm}^{-1}$  correspond to  $\nu_{\text{C=O}}$ ,  $\nu_{\text{C=N}}$ ,  $\nu_{\text{C-O}}$ , and  $\nu_{\text{N-O}}$ , respectively. After reaction of POBC-H with two molar equivalents of  $\text{Co}(\text{OAc})_2$ , the  $\nu_{\text{C=O}}$  band was shifted from 1687 to 1536  $\text{cm}^{-1}$  and that of  $\nu_{\text{C-O}}$  from 1290 to 1377  $\text{cm}^{-1}$  (Figure 3.1e). In contrast, the bands of  $\nu_{\text{C=N}}$  and  $\nu_{\text{N-O}}$  shifted only slightly, from 1610 to 1609  $\text{cm}^{-1}$  for  $\nu_{\text{C=N}}$  and from 999 to 974  $\text{cm}^{-1}$  for  $\nu_{\text{N-O}}$ . These changes in the IR spectra indicate that  $\text{Co}^{2+}$  was coordinated to the COO groups, while the NOH groups did not react at this stage (step 1 in Eq. 3.1). After addition of CeB to Co-POBC (Figure 3.1f), the intensities of  $\nu_{\text{C=N}}$  and  $\nu_{\text{N-O}}$  bands decreased, suggesting reaction of the NOH groups with CeB and formation of the Ce-POBC-Co single source precursor (step 2 in Eq. 3.1). Whether one or two OR groups of CeB were substituted by oximate groups cannot be determined by IR spectroscopy. Based on previous investigations of oximate-substituted zirconium alkoxides,

Zr(OR)<sub>4-x</sub>(O-N=CRR')<sub>x</sub> [71], and given the general similarity of Zr and Ce alkoxides, di-substitution as shown in Eq. 3.1 is more likely. The degree of substitution, however, would hardly influence the outcome of sol-gel reactions.

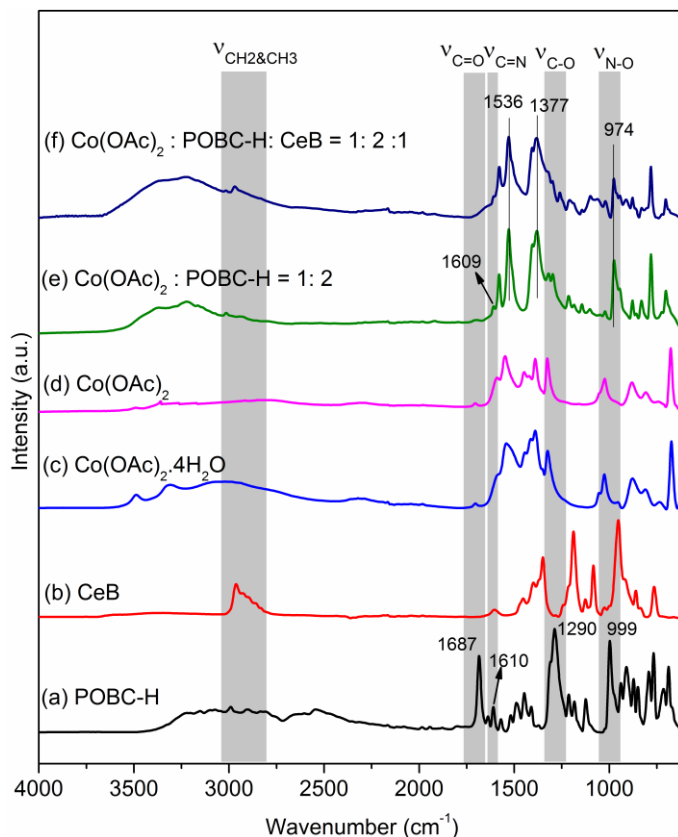


**Figure 3.1** IR spectra of samples related to Ce-POBC-Co single source precursor

### 3.2.2 Materials characterization

The IR spectra of **1-STE** and **2-STE** samples after solvothermal treatment were almost the same (Figure 3.2 left), except the Co-O vibration at 661 cm<sup>-1</sup> in sample **1-STE**, indicating that Co oxide species were only formed for sample **1-STE** in this stage. The IR spectrum of sample **3-STE** is quite different, and the peak intensity of organic groups in the range of 1250~1750 cm<sup>-1</sup> (COO 1535, 1402 cm<sup>-1</sup>; N-O 1015 cm<sup>-1</sup>) suggests that more organic groups were retained during solvothermal treatment.

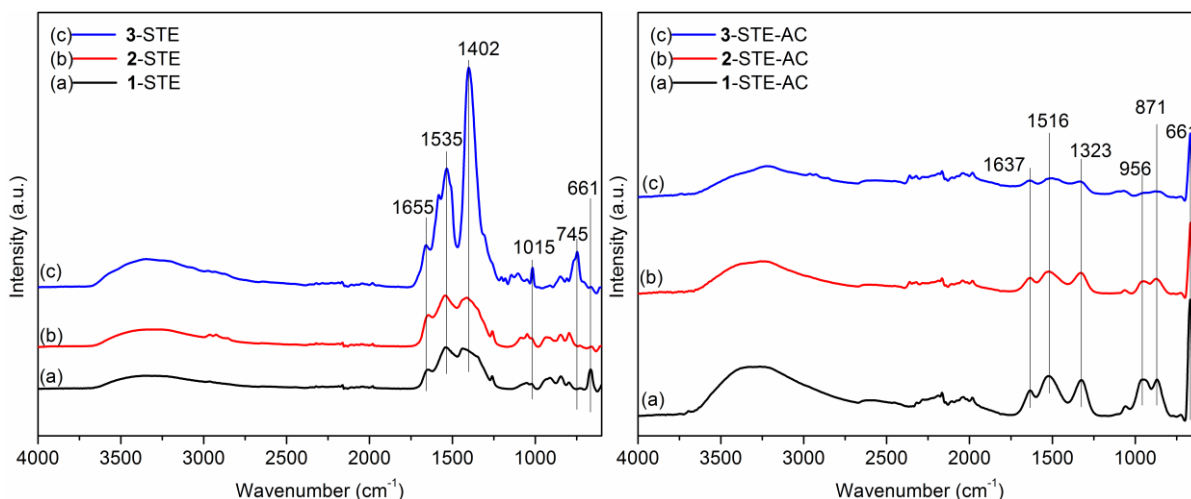


**Figure 3.2** IR spectra of Co oxide-modified CeO<sub>2</sub> samples, after STE treatment (left) and after STE-AC treatment (right)

This was also observed by TGA (Figure 3.3), where the weight loss of sample **3-STE** is 26.7% due to the POBC ligand. In each case, most of the organic components were removed below 350 °C, but there was still a small weight loss till 450 °C.

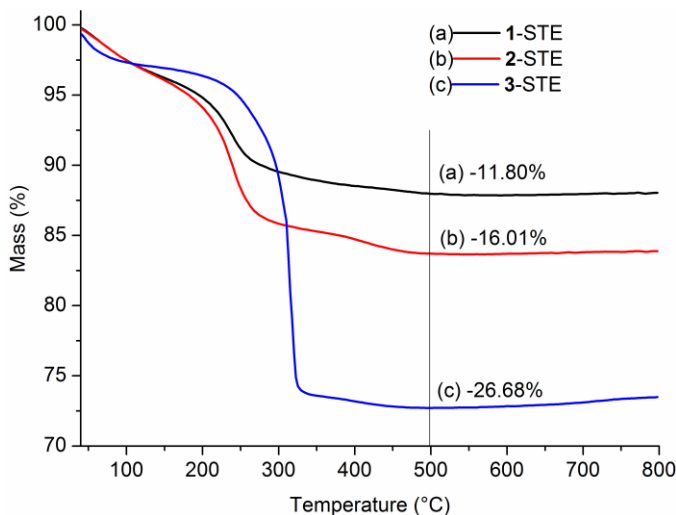


**Figure 3.3** TGA curves of Co<sub>3</sub>O<sub>4</sub> modified CeO<sub>2</sub> STE

The solvothermally treated samples were therefore calcined at 500 °C for 2 h (*STE-AC*) to remove the organic constituents. The IR spectra of the calcined samples are given in Figure 3.2 right. All samples have Co-O vibrations at 661 cm<sup>-1</sup> with the peak intensity of sample **1-STE-AC**

being the strongest, indicating the formation of cobalt oxide species. Furthermore, the first overtones of Ce-O vibration ( $956\text{ cm}^{-1}$  and  $871\text{ cm}^{-1}$ ) can also be observed for sample **1-STE-AC** and **2-STE-AC**, but not for sample **3-STE-AC**. Thus the peak intensity change of the first Ce-O overtone might suggest the different dispersion of Co in sample **3**. The more homogeneous Co is dispersed, the lower intensity of the first overtone is.

XRD of the Co oxide-modified CeO<sub>2</sub> samples after STE (Figure 3.4 left) showed weak reflexions of Co<sub>3</sub>O<sub>4</sub> only for **1-STE**, while the other two STE samples had only CeO<sub>2</sub> reflexions. This is in line with the IR spectra where only for **1-STE** the characteristic Co-O band was observed (Figure 3.2 left). The size of the ceria crystallites, as calculated by Scherrer's equation, was in the range 2.5–3.5 nm (see insert in Figure 3.4 left). When the STE samples were further treated in air at 500 °C for 2 h, the crystallite size increased to 5.5–7.5 nm (see Figure 3.4 right). The smallest increase in size was for **1-STE**. After calcination, all the samples showed weak Co<sub>3</sub>O<sub>4</sub> reflexions at about  $37.5^\circ$  in line with the IR spectra (Figure 3.2, right). Due to the low peak intensity, it was not possible to calculate the Co<sub>3</sub>O<sub>4</sub> crystallite size.

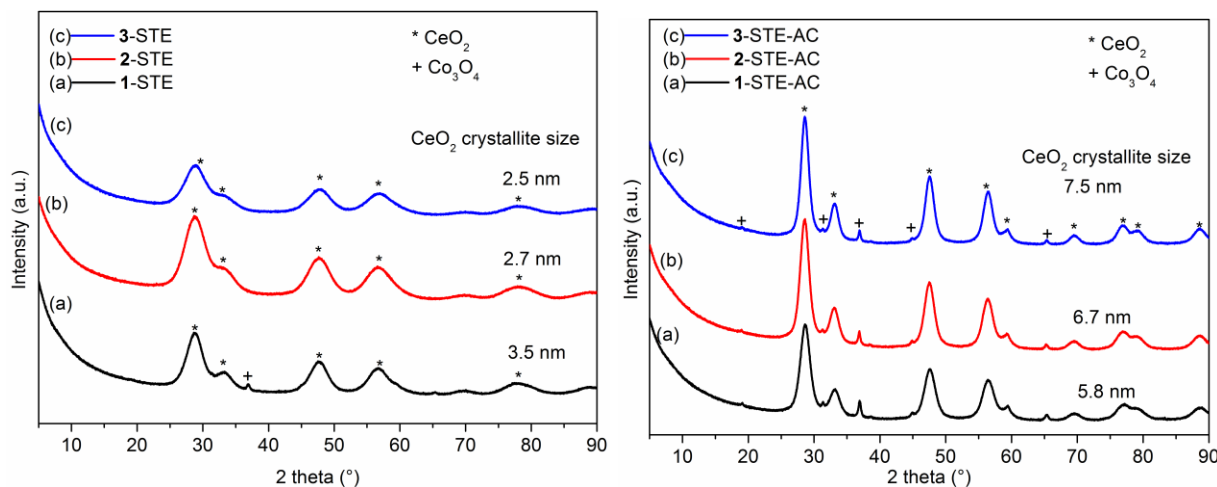


**Figure 3.4** XRD patterns of Co<sub>3</sub>O<sub>4</sub> modified CeO<sub>2</sub> samples, after STE treatment (left) and after STE-AC treatment (right)

According to N<sub>2</sub> adsorption experiments (Figure 3.5), sample **1-STE** is mesoporous with an essentially monomodal pore size distribution in the lower mesoporous range. In contrast, **2-STE** and **3-STE** have a bimodal pore size distribution with pore sizes both in the lower and upper



mesoporous range. All three STE samples have high surface areas in the range 215–270  $\text{m}^2/\text{g}$  (see insert in Figure 3.5).

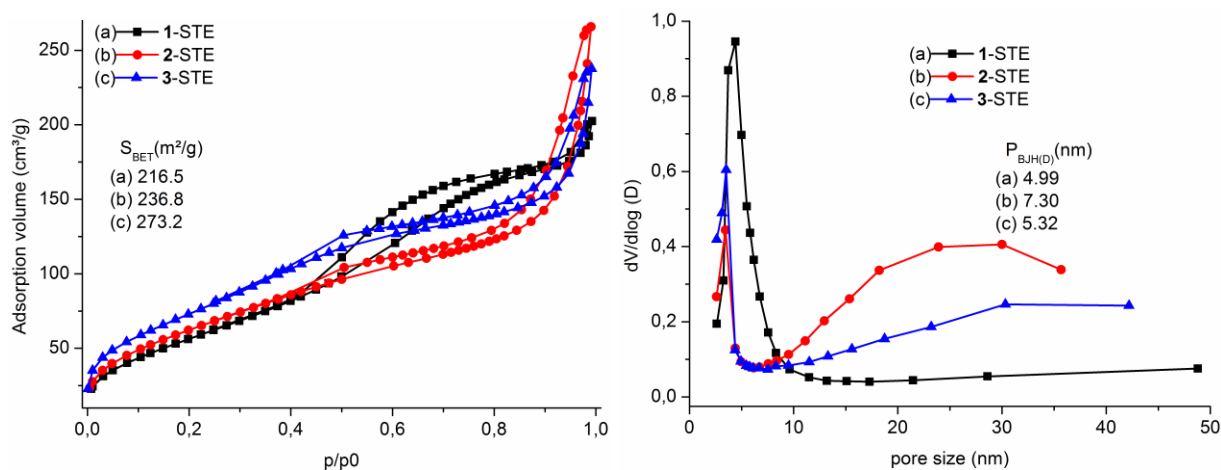


**Figure 3.5**  $\text{N}_2$  adsorption-desorption isotherms (left) and pore size distributions (right) after STE treatment

After calcination at 500  $^\circ\text{C}$  for 2 h (Figure 3.6), the pore size distribution of sample 1-STE-AC was essentially the same. In the samples 2-STE-AC and 3-STE-AC, however, the smaller pores had largely disappeared due to the calcination process. In all samples the surface area decreased drastically to 25–96  $\text{m}^2/\text{g}$ .

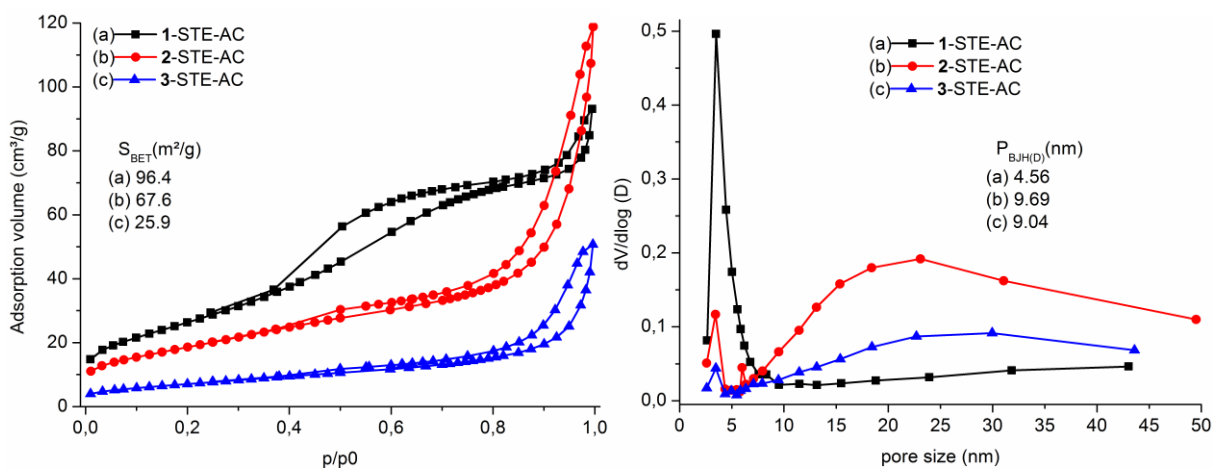


**Figure 3.6**  $\text{N}_2$  adsorption-desorption isotherms (left) and pore size distributions (right) for the STE-AC samples

SEM was also used to characterize the  $\text{Co}_3\text{O}_4$  modified  $\text{CeO}_2$  samples after STE and STE-AC treatment, as shown in Figure 3.7. The left row is the morphologies of STE samples, while the right row is that of the corresponding STE-AC samples.

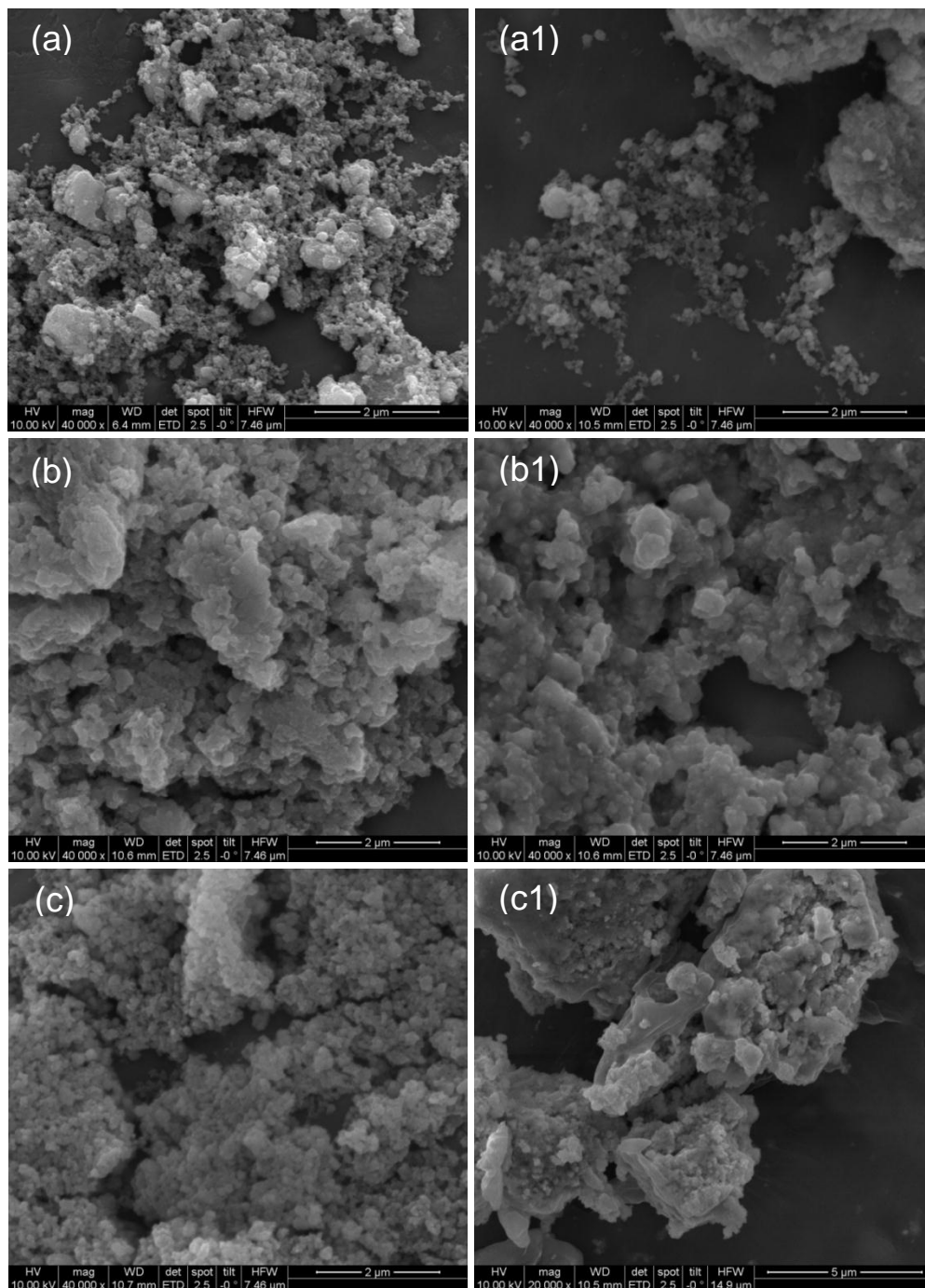


**Figure 3.7** SEM of for  $\text{Co}_3\text{O}_4$  modified  $\text{CeO}_2$  STE and STE-AC (marked by 1) samples. (a) Route 1, (b) Route 2, (c) Route 3

All the STE samples are composed of small particles, and some are agglomerated / aggregated. Agglomeration / aggregation is more serious for **1-STE** and **2-STE** (Figure 3.7 (a) and (b)), while the **3-STE** have much better dispersion (Figure 3.7 (c)). This may be because **1-STE** and **2-STE** had less organic residues on the surface than **3-STE**. In order to lower the surface energy, the small particles agglomerate / aggregate. Sample **3-STE** may still contain the bifunctional ligand, which stabilized the small particles.

When all three STE samples were further calcined at 500 °C for 2 h in the air, the single particles became larger. Besides the particle size, the agglomeration / aggregation situation also changed significantly. After calcination, **1-STE-AC** has the best dispersion and **3-STE-AC** the worst. The serious agglomeration / aggregation of sample **3-STE-AC** may be attributed to the removal of the bifunctional ligand during the calcination process, which increased the surface energy of the particles.

EDX for the three STE samples were also checked (Figure 3.8). All the samples have a Ce:Co ratio about 4:1, but sample **1-STE** contains slightly less Co than **2-STE** and **3-STE**. This may be because the Ce and Co precursor interacted weakly due to the separate formation of the ceria gel, and a small amount of Co was still dissolved in the solvothermal solvent as Co<sup>2+</sup> ions.

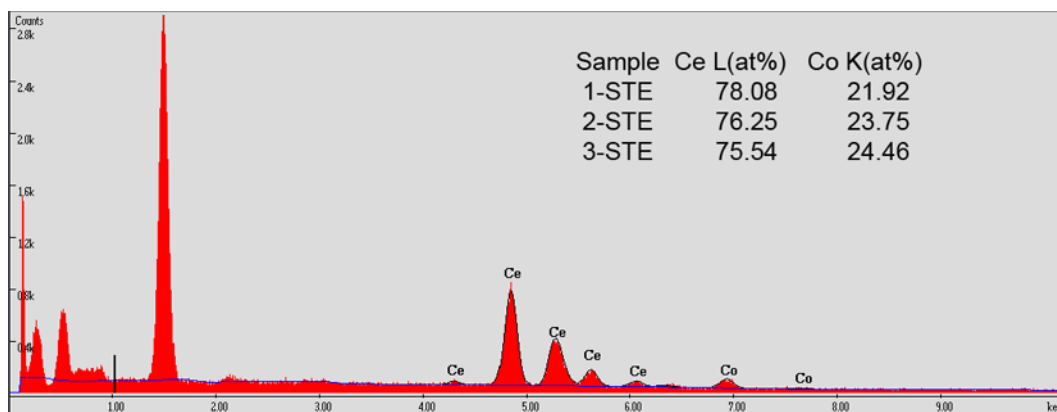


**Figure 3.8** EDX results of STE treated samples. The given spectrum is that of **1-STE**, and the spectra for other two samples are similar. Thus only the numerical results are given here.

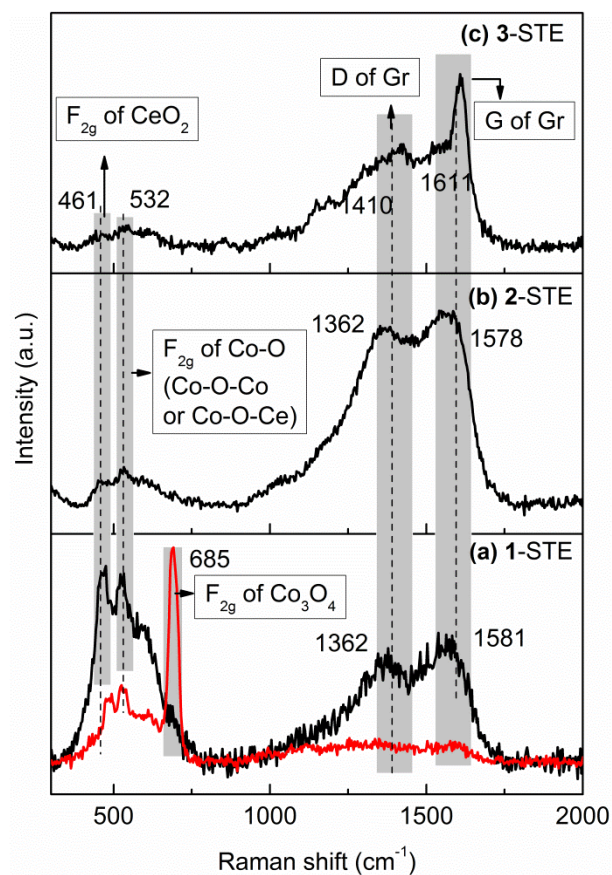


**Figure 3.9** Raman spectra of different  $\text{Co}_3\text{O}_4$  modified  $\text{CeO}_2$  samples after STE treatment

Different  $\text{Co}_3\text{O}_4$  modified  $\text{CeO}_2$  samples after STE treatment were characterized by Raman spectra, as shown in Figure 3.9. Because the high laser intensity will burn the organic residues, and only 1% intensity of the laser was used, the penetration depth was not very large, resulting in a lower intensity of the  $\text{CeO}_2$  phase. Spectra were taken from at least three points of the same sample. While 1-STE showed two different types of spectra at different detecting points, samples 2-STE and 3-STE showed almost the same spectra. For sample 1-STE, two parts were observed:  $\text{CeO}_2$ -graphene &  $\text{Co}_3\text{O}_4$ - $\text{CeO}_2$ -graphene. The graphene D-band and G-band indicated that the organic residues after STE treatment had a graphene-like structure, which is similar to  $\text{CeO}_2$  STE sample with graphene-like residues in section 2.2.3. The band intensity of graphene showed that it prefers to stay on the surface of the  $\text{CeO}_2$  phase, rather than the  $\text{Co}_3\text{O}_4$  phase, because there were almost no graphene bands on points consisting mainly of  $\text{Co}_3\text{O}_4$  (red line in Figure 3.9 (a)). The other two samples also showed graphene-like bands, but the band intensity ratio of 3-STE was quite different to the other two samples. As the D-band is related to a breathing mode of  $\kappa$ -

point photons of A<sub>1g</sub> symmetry, and the G-band can be attributed to the splitting of the E<sub>2g</sub> stretching mode of graphite which reflects the proportion of the sp<sup>2</sup> C atoms [93-95]. The I(D)/I(G) ratio is a measure of disordered carbon, as expressed by the sp<sup>3</sup>/sp<sup>2</sup> carbon ratio, and an increase of I(D)/I(G) reflects the degradation of crystallinity of graphitic materials [96]. Thus the relatively strong intensity of the G band of **3**-STE indicated a decrease of I(D)/I(G) ratio, with a higher crystallinity of graphitic materials compared to the other two samples. Besides the graphene bands, all the three samples showed CeO<sub>2</sub> (461 cm<sup>-1</sup>) and Co-O (532 cm<sup>-1</sup>) bands, but only **1**-STE showed a Co<sub>3</sub>O<sub>4</sub> band. This corresponds to XRD and IR results.

### 3.2.3 Structure model

Since XRD did not give information on the Co-containing structures in the materials after solvothermal processing, SAXS measurements were carried (Figure 3.10). An obvious difference between the three samples is that **3**-STE has a more pronounced shoulder, which indicates homogeneous particles with a diameter of about 2.2 nm. Additionally, there is possibly some weak (electrostatic) interaction, which was taken into consideration by using an additional structure factor from a hard sphere model. This agrees with the literature, where materials prepared from single source precursors were reported to be more homogeneous. [15, 97]

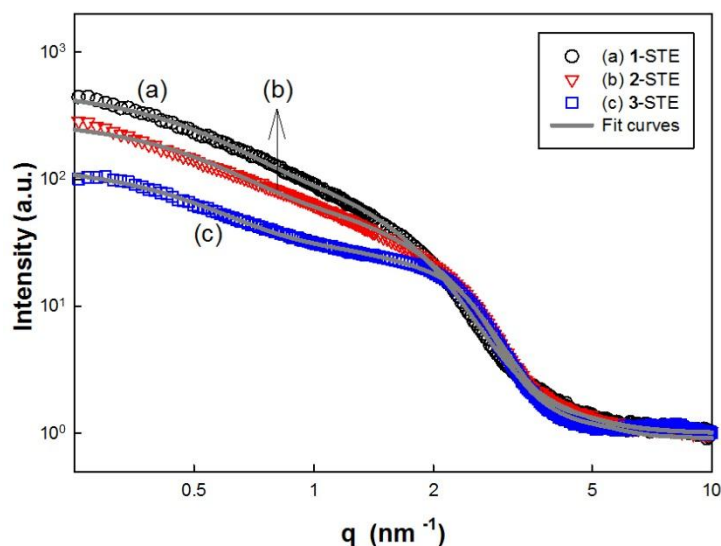


**Figure 3.10** SAXS curves of Co<sub>3</sub>O<sub>4</sub> modified CeO<sub>2</sub> samples after STE treatment

The intensity distribution for **1**-STE and **2**-STE is broader and has a considerable higher value towards low  $q$ -values, which indicates a bimodal size distribution with a much higher amount of additional large particles. The SAXS results support that the nanoparticles are homogenous in the case of **3**-STE with a negligible amount of large particles, whereas probably pure CeO<sub>2</sub> and CeO<sub>2</sub> with CoO<sub>x</sub> nanoparticles coexist for **1**-STE and **2**-STE. This leads to a broad additional distribution of nanoparticles with a larger size, the mean value being approximately twice the size of the pure CeO<sub>2</sub> nanoparticles.

For the characterization of the samples after calcination, TEM and HRTEM were used. Because all the STE samples can only gave information on CeO<sub>2</sub> and no Co oxide structures were detected; only the images of **1**-STE are given here (Figure 3.11) while the images of all STE-AC samples are given (Figure 3.12).

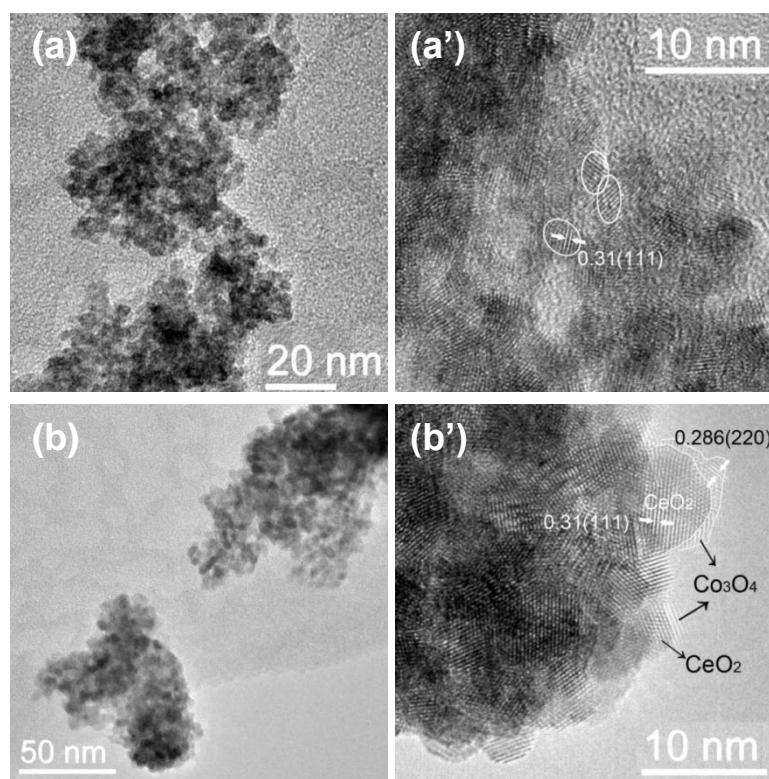


**Figure 3.11** TEM and HRTEM images of sample **1** treated by STE (a, a') and STE-AC (b, b')

From the TEM images of **1**-STE and **1**-STE-AC (Figure 3.11a and Figure 3.11b), it can be concluded that the aggregates before and after AC treatment are similar. The particles in **1**-STE are about 3~4 nm with (111) lattice fringes (0.31 nm), corresponding to CeO<sub>2</sub>. No Co<sub>3</sub>O<sub>4</sub>

crystallite phase was observed maybe due to the very small amount. The CeO<sub>2</sub> particle size of sample 1-STE-AC is about 7~10 nm. When the edges of the particles are focused, two different lattice fringes can be found. One lattice fringe with little contrast has a distance of 0.31 nm, which corresponds to the (111) facet of CeO<sub>2</sub>. The other lattice fringe with slightly brighter contrast has a distance of 0.286 nm, belonging to the (220) facet of Co<sub>3</sub>O<sub>4</sub> [98]. From Figure 3.11b' it can be seen that Co<sub>3</sub>O<sub>4</sub> stayed on the surface of CeO<sub>2</sub> aggregates, forming partly core-shell structure.

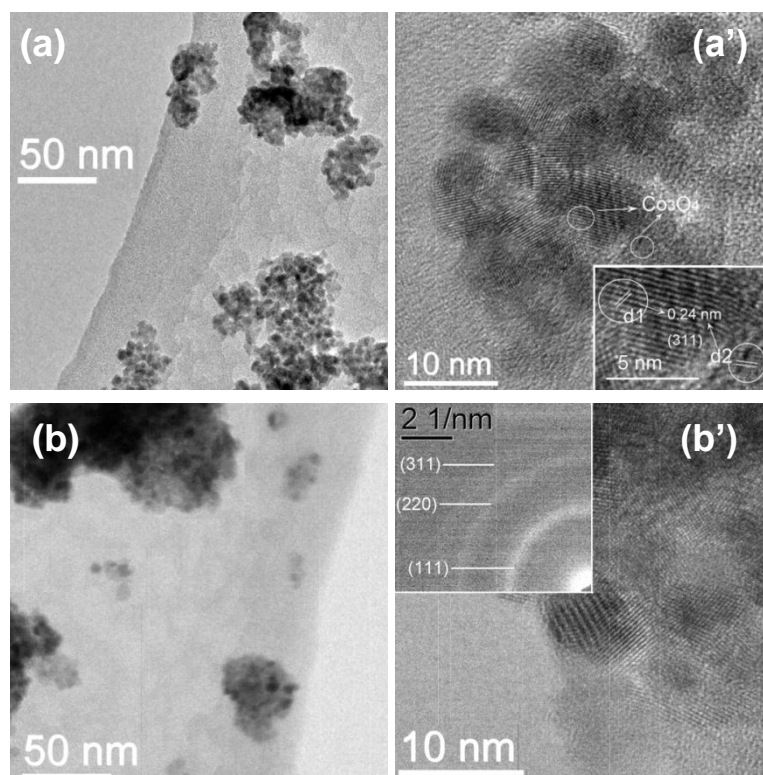


**Figure 3.12** TEM and HRTEM images of sample **2** (a, a') and **3** (b, b') treated by STE-AC. The insert in (b') is the SAED pattern.

The dispersion situation of sample 2-STE-AC is almost the same as that of sample 1-STE-AC, but sample 3-STE-AC is strongly aggregated (Figure 3.12). HRTEM showed that sample 2-STE-AC (Figure 3.12a') contains tiny Co<sub>3</sub>O<sub>4</sub> particles (1~2 nm) besides CeO<sub>2</sub> particles. Contrary to 1-STE-AC, the Co<sub>3</sub>O<sub>4</sub> particles are located in between the CeO<sub>2</sub> particles. In contrast, no indications for crystalline Co<sub>3</sub>O<sub>4</sub> (nano-) particles were found for 3-STE-AC (Figure 3.12b'), despite the very weak reflections of crystalline Co<sub>3</sub>O<sub>4</sub> in powder XRD and the fact that the proportion of Co was the same as in the other two samples. Thus, because of the single source



precursor, the Co oxide particles are either amorphous or very small, and well dispersed between the CeO<sub>2</sub> grains.

The HRTEM images clearly show that the CoO<sub>x</sub> distribution in/on ceria strongly depends on the preparation method. Co<sub>3</sub>O<sub>4</sub> crystallites were formed both in **1-STE-AC** and **2-STE-AC**, but their distribution is different. In **1-STE-AC**, small Co<sub>3</sub>O<sub>4</sub> crystallites were already present after STE treatment according to XRD (Figure 3.4). The HRTEM images indicate that the Co<sub>3</sub>O<sub>4</sub> crystallites are preferentially located at the surface of the CeO<sub>2</sub> particle aggregates, which apparently were already formed during sol-gel processing. For route 2, both Ce and Co precursors were present during formation of the sol, and CoO<sub>x</sub> structures could easier be formed in between the aggregated CeO<sub>2</sub> grains. Moreover, up to 5% Co can be incorporated into the CeO<sub>2</sub> lattice [46]. Both HRTEM and SAXS investigations show that the Co distribution in **3-STE-AC** is more homogeneous from the very beginning through all steps of the preparation process, as expected. The morphologies of Co<sub>3</sub>O<sub>4</sub>/CeO<sub>2</sub> materials prepared by the three different methods are schematically shown in Figure 3.13. Sample **1** may have a core-shell like structure, with Co<sub>3</sub>O<sub>4</sub> particles discontinuously coating on CeO<sub>2</sub> particles/ aggregates. Sample **2** might be a structure with tiny Co<sub>3</sub>O<sub>4</sub> particles mixed with CeO<sub>2</sub>. And the structure of sample **3** has the most homogeneous Co distribution.

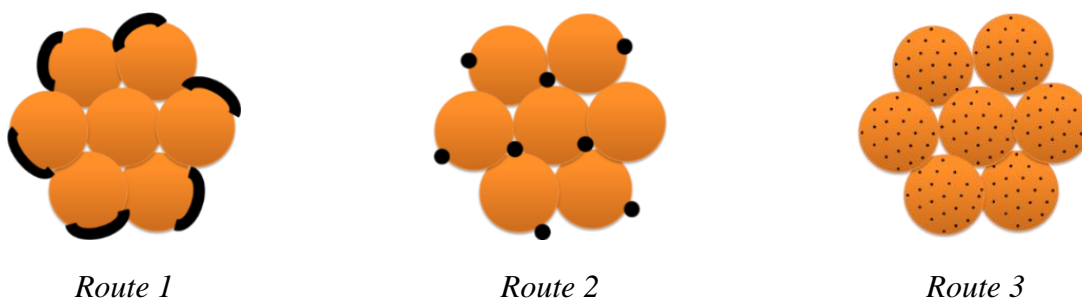


**Figure 3.13** Suggested structure of Co<sub>3</sub>O<sub>4</sub> modified CeO<sub>2</sub> samples (yellow: CeO<sub>2</sub>, black: Co<sub>3</sub>O<sub>4</sub>)

#### 3.2.4 Structural evidence from CO-TPR (temperature-programmed reactions)

Many reports [55, 99-101] showed that the reduction of Co<sub>3</sub>O<sub>4</sub> is a two-step process: Co<sup>3+</sup> → Co<sup>2+</sup> → Co<sup>0</sup>. The CO-TPR over commercial Co<sub>3</sub>O<sub>4</sub> showed the same trend, as shown in Figure 3.14. The CO<sub>2</sub> evolution of commercial Co<sub>3</sub>O<sub>4</sub> can be divided into two stages: (I) <270 °C,



removal of surface lattice oxygen (O<sub>SL</sub>),  $\text{Co}^{3+}_{\text{SL}} \rightarrow \text{Co}^{2+}_{\text{SL}}$ ; (II)  $>275$  °C, removal of bulk lattice oxygen (O<sub>BL</sub>),  $\text{Co}^{3+}_{\text{BL}} \rightarrow \text{Co}^{2+}_{\text{BL}}$ , and further reduction of  $\text{Co}^{2+} \rightarrow \text{Co}^0$ .

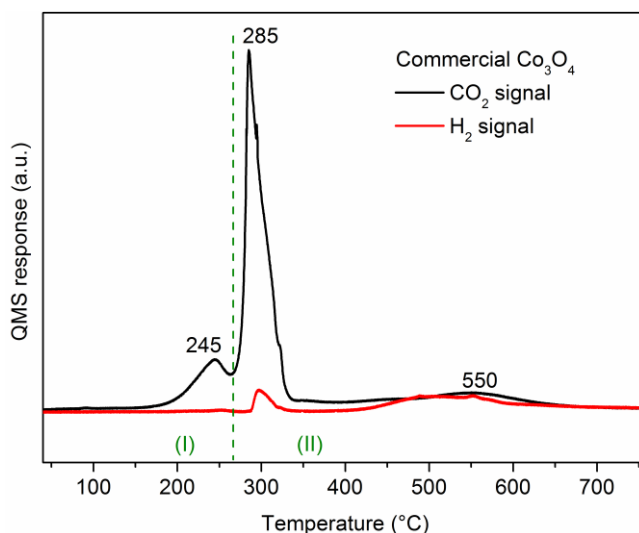


**Figure 3.14** CO<sub>2</sub> and H<sub>2</sub> evolution during CO-TPR over commercial Co<sub>3</sub>O<sub>4</sub>

When CeO<sub>2</sub> and Co<sub>3</sub>O<sub>4</sub> were mixed together, all peaks of CO<sub>2</sub> and H<sub>2</sub> evolution characteristic for CeO<sub>2</sub> were overlapping or weakened because Co<sub>3</sub>O<sub>4</sub> exhibits a much higher reducibility [102, 103]. The peak positions characteristic of Co<sub>3</sub>O<sub>4</sub> may slightly shift because of the different distribution and a synergistic effect with CeO<sub>2</sub>. This is also true for the H<sub>2</sub>-TPR results [46, 55, 102, 104].

CO-TPR was performed for all six samples (three STE samples and the corresponding STE-AC samples), as shown in Figure 3.15 and Figure 3.16. The results clearly show that the CO<sub>2</sub> evolution behavior of Co<sub>3</sub>O<sub>4</sub> strongly depends on the preparation route, which is related to the type of Co introduction and subsequent heat-treatment. Based on CO-TPR [102, 103] and H<sub>2</sub>-TPR [46, 100, 102] of Co<sub>3</sub>O<sub>4</sub>-CeO<sub>2</sub> reported before, the peaks for all synthesized samples, except 3-STE, were assigned to four regions:

#### **Region I (<270 °C):**

Reaction of O<sub>SL</sub> (lattice oxygen on the surface) of Co<sub>3</sub>O<sub>4</sub> due to reduction of  $\text{Co}^{3+} \rightarrow \text{Co}^{2+}$  at the interface between Co<sub>3</sub>O<sub>4</sub> and CeO<sub>2</sub>:  $\text{CO} + \text{O}_{\text{SLCo}_3\text{O}_4} \rightarrow \text{CO}_2$ ;

**Region II (270 °C-350 °C):**

Reaction of O<sub>BL</sub> (lattice oxygen in the bulk) of “independent” (i.e. not contacting ceria) Co<sub>3</sub>O<sub>4</sub> (Co<sup>3+</sup> → Co<sup>2+</sup>) that weakly interacts with CeO<sub>2</sub>:  $\text{CO} + \text{O}_{\text{BLCo}_3\text{O}_4} \rightarrow \text{CO}_2$ .

Water gas shift reaction from OH groups on Co<sub>3</sub>O<sub>4</sub>, including both the independent surface of Co<sub>3</sub>O<sub>4</sub> (at slightly lower temperature) and the interface of CeO<sub>2</sub> and Co<sub>3</sub>O<sub>4</sub> (at slightly higher temperature):  $\text{OH}_{\text{Co}_3\text{O}_4} + \text{CO} \rightarrow \frac{1}{2} \text{H}_2 + \text{CO}_2$ ;

**Region III (350 °C-500 °C):**

Reaction of O<sub>BL</sub> on CoO, which interacts with CeO<sub>2</sub> to Co<sup>0</sup>:  $\text{CO} + \text{O}_{\text{BLCoO}} \rightarrow \text{CO}_2$ .

Water gas shift reaction from OH groups of CeO<sub>2</sub>:  $\text{OH}_{\text{CeO}_2} + \text{CO} \rightarrow \frac{1}{2} \text{H}_2 + \text{CO}_2$ ;

**Region IV (>500 °C):**

Reaction of O<sub>BL</sub> on CeO<sub>2</sub>:  $\text{CO} + \text{O}_{\text{BLCeO}_2} \rightarrow \text{CO}_2$ .

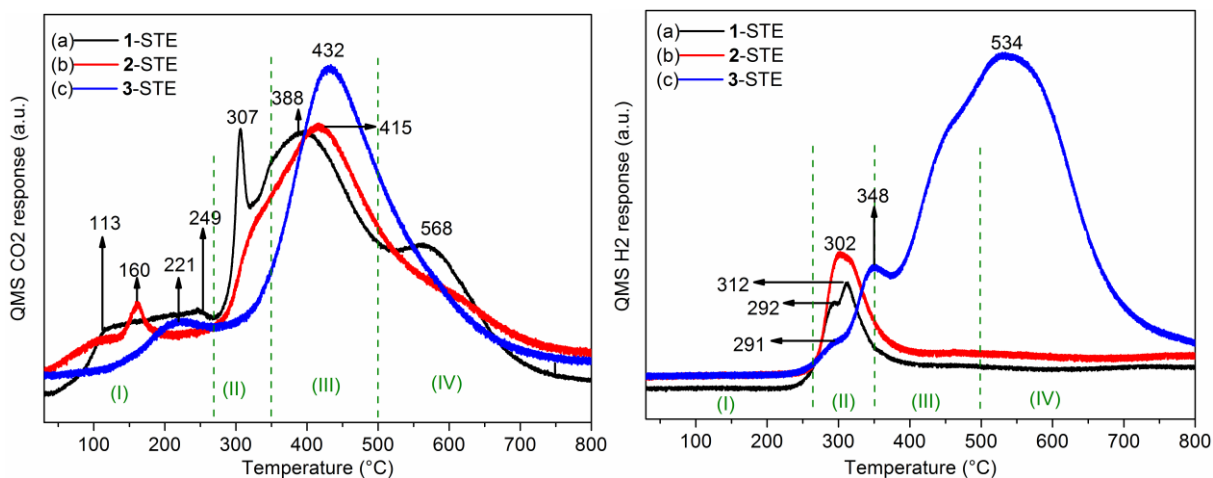


**Figure 3.15** CO<sub>2</sub> (left) and H<sub>2</sub> (right) evolution during CO-TPR over Co<sub>3</sub>O<sub>4</sub> modified CeO<sub>2</sub> STE samples (20 mg)

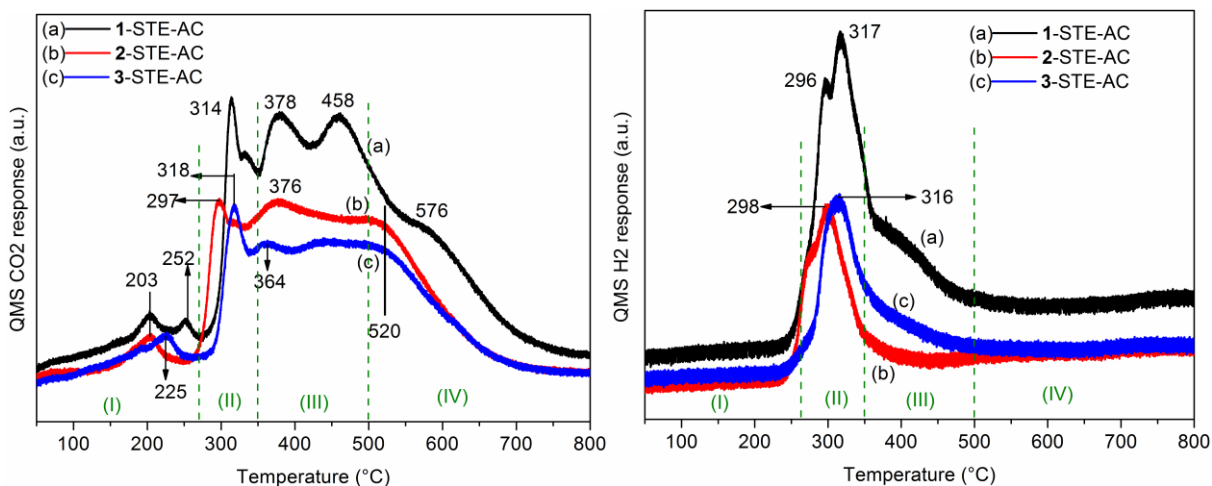


**Figure 3.16**  $\text{CO}_2$  (left) and  $\text{H}_2$  (right) evolution during CO-TPR over  $\text{Co}_3\text{O}_4$  modified  $\text{CeO}_2$  STE-AC samples (20 mg)

The large peaks in  $\text{CO}_2$  (300-600 °C) and  $\text{H}_2$  evolution (400-700 °C) for sample **3-STE** are caused by the POBC ligand, which is still present after the solvothermal treatment. Since the peaks in region II are related to independent or bulk-like  $\text{Co}_3\text{O}_4$  phase, it is possible to deduce the dispersion state of the  $\text{Co}_3\text{O}_4$  phase from the intensity of this peak. For STE samples, only sample **1-STE** has a sharp peak in this region, while sample **2-STE** has a weak shoulder and sample **3-STE** has no peak at all, indicating that the amount of the available  $\text{Co}_3\text{O}_4$  (on the surface or near the surface) for CO oxidation is **1-STE** > **2-STE** >> **3-STE**. From this it could be deduced that the dispersion of  $\text{Co}_3\text{O}_4$  in the different catalysts is **1-STE** < **2-STE** << **3-STE**.

After calcination, all STE-AC samples showed sharp peaks in region II, only the intensities were different, indicating that part of the Co in **2-STE-AC** and **3-STE-AC** had fused. The intensity change of the peaks in region II indicated the amount of Co that can be used for CO oxidation. For **2-STE-AC** and **3-STE-AC**, although some of Co was fused, there may still be some Co in the body of  $\text{CeO}_2$ , which cannot participate in CO oxidation. The  $\text{H}_2$  evolution of STE-AC samples in region II showed a similar trend. Sample **1-STE-AC** produced the most  $\text{H}_2$ , but **2-STE-AC** and **3-STE-AC** produced only half the amount of  $\text{H}_2$ . Thus it can be deduced that **1-STE-AC** exhibited most  $\text{Co}_3\text{O}_4$  on the surface of  $\text{CeO}_2$ , while the other two samples had only about half the amount of  $\text{CoO}_x$  on the  $\text{CeO}_2$  surface. This is consistent with the HR-TEM results in the section 3.2.3.

### 3.2.5 Catalytic properties

The catalytic activity for STE samples prepared by three different routes was evaluated in the CO oxidation reaction (5% CO, 12.5% O<sub>2</sub>, He balanced) as a function of reaction temperature (Figure 3.18). The temperature of 10% CO conversion/ignition temperature ( $T_{10\%}$ ), the temperature of 90% CO conversion  $T_{(90\%)}$ , reaction rate at 130 °C ( $r_{130^{\circ}\text{C}}$ ), specific reaction rates ( $R_{130^{\circ}\text{C}}$ ) and the reaction rates on the basis of the unit amount of Co ( $R_{\text{Co}130^{\circ}\text{C}}$ ) are summarized in Table 3.1 (CO conversion at 130 °C was below 20% for all samples). In order to examine the stability of STE samples during catalytic reaction, the CO conversion were recorded not only upon heating, but also upon subsequent cooling (<2% conversion) and re-heating (Figure 3.17).

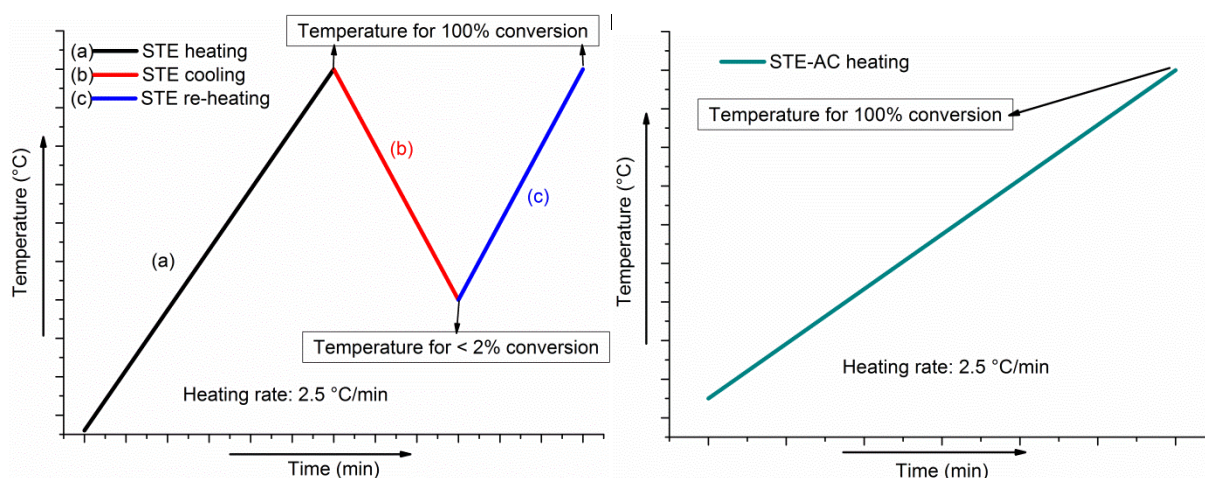


**Figure 3.17** Heating program of catalytic test for STE samples (left) and STE-AC samples (right)

The  $T_{10\%}$  for STE samples are: 117 °C (**1-STE**) < 140 °C (**2-STE**) < 194 °C (**3-STE**) which is in a good agreement with CO-TPR data (section 3.2.4). In the same order are  $T_{90\%}$  values for STE samples: 155 °C (**1-STE**) < 184 °C (**2-STE**) < 244 °C (**3-STE**). Thus, the catalyst **1-STE** prepared by introduction of Co after formation of amorphous CeO<sub>2</sub> is the most active and needs lower temperature to oxidize CO completely than catalysts **2-STE** and **3-STE**, where Ce and Co were introduced simultaneously into the sol. This is also valid for  $r_{130^{\circ}\text{C}}$ ,  $R_{130^{\circ}\text{C}}$  and  $R_{\text{Co}130^{\circ}\text{C}}$  (Table 3.1).  $R_{\text{Co}130^{\circ}\text{C}}$  was 68.7 mmol CO/mmol Co·h for **1-STE**, while for the 20% Co<sub>3</sub>O<sub>4</sub>-CeO<sub>2</sub> prepared by conventional co-precipitation method the  $R_{\text{Co}130^{\circ}\text{C}}$  is only around 1.2 mmol CO/mmolCo·h [105].

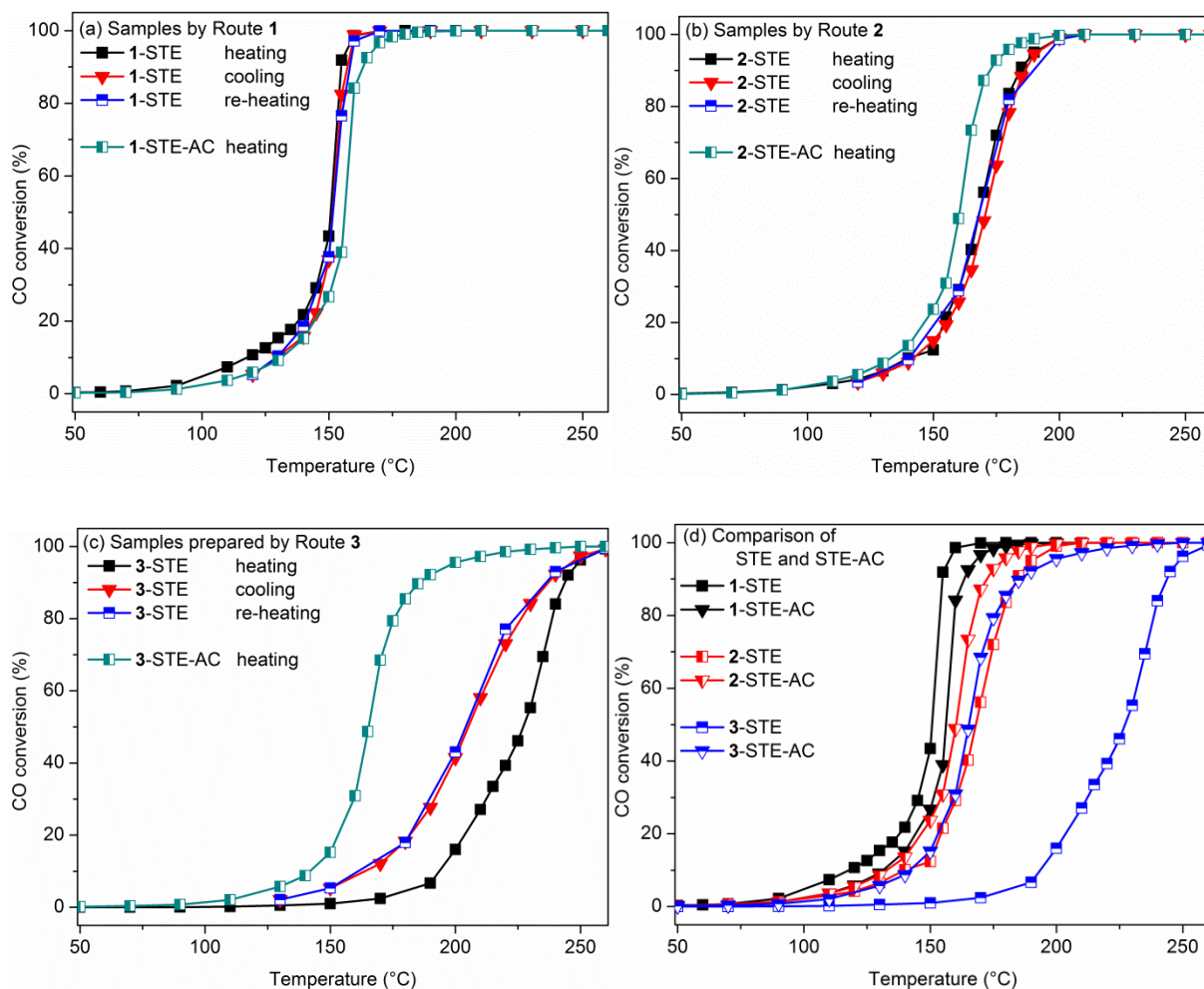


**Figure 3.18** CO oxidation over  $\text{Co}_3\text{O}_4$  modified  $\text{CeO}_2$  samples

The apparent activation energy ( $E_a$ ) for all the STE and STE-AC samples was calculated from Arrhenius-type plots using the conversion data below 30%, as shown in Figure 3.19. The sample **1-STE** has the lowest  $E_a$  47.4 kJ/mol, while the **3-STE** shows the highest  $E_a$  77.5 kJ/mol. The  $E_a$  of **1-STE** is similar to that of ceria supported noble metal catalyst, like Pd/ $\text{CeO}_2$  (48-52 kJ/mol for 0.5 wt% Pd loaded  $\text{CeO}_2$  [29], 40 kJ/mol for 1 wt% Pd loaded  $\text{CeO}_2$  [106]), Pt/ $\text{CeO}_2$  (42-63 kJ/mol for 0.5 wt% Pt loaded  $\text{CeO}_2$  [29], 44 kJ/mol for 1 wt% Pt loaded  $\text{CeO}_2$  [107]) and Au/ $\text{CeO}_2$  (46-56 kJ/mol [108]). Thus, the combination of sol-gel and solvothermal processing allows obtaining very active cobalt-modified ceria catalysts, which could be used as a substitution of noble metal loaded  $\text{CeO}_2$ , and route **1** yielded the sample with highest catalytic activity, by adding the Co precursor after Ce-gel formation.



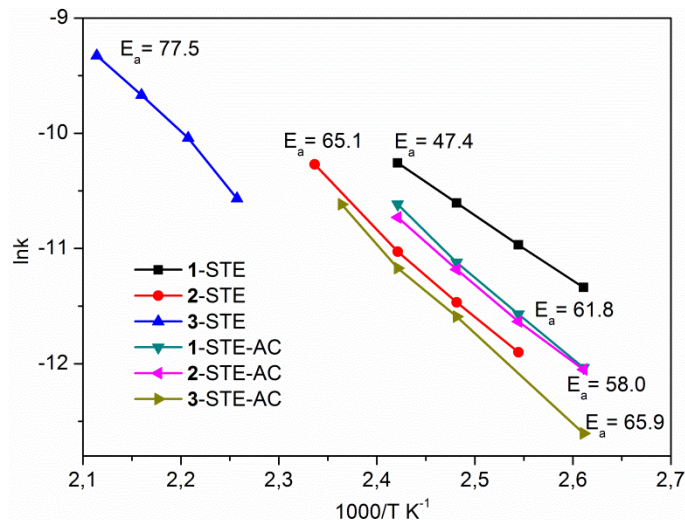


**Figure 3.19** Arrhenius-type plots for CO oxidation over STE and STE-AC samples

Comparing the activity of STE samples and the sequence of Co introduction it can be noted that **3-STE** sample, in which the single source precursor was used, is less active than the other two STE samples prepared from two individual precursors. This can be attributed to the proportion of organic residues, which were left after solvothermal treatment. In order to check this, the CO conversion was recorded along with heating and as well as during subsequent cooling and re-heating. It is noted that sample **1-STE** (Figure 3.18 (a)) and **2-STE** (Figure 3.18 (b)) did not show a loss of activity during several test cycles (heating, subsequent cooling and re-heating). In contrast, the CO conversion curves during heating and subsequent cooling do not coincide for sample **3-STE** (Figure 3.18 (c)). Interestingly, the CO conversion increased during the cooling stage and remained the same during re-heating. The shift of CO oxidation to lower temperature range for the **3-STE** might be due to the partial organic compound decomposition (e.g. of the POBC organic ligand) when the temperature was raised to 260 °C. Based on these data we can conclude that the highest activity of the catalyst prepared by route **1** is due to the cleaner surface (TGA) and more  $\text{Co}_3\text{O}_4$  on the  $\text{CeO}_2$  surface (supported oxide structure), which was also revealed by HRTEM, and CO-TPR (section 3.2.3 and section 3.2.4).

In order to figure out the influence of the post-synthesis calcination, the samples calcined at 500 °C for 2 h (STE-AC) were also tested in CO oxidation reaction. When comparing the STE samples with the corresponding STE-AC samples (Figure 3.18 (d)), sample **2-STE-AC** and especially **3-STE-AC** had a higher CO conversion than the related STE samples. In contrast, **1-**

STE-AC exhibited lower CO conversion than that of its STE sample. Therefore, the high proportion of organic residues which were left after solvothermal treatment could block the reaction sites, resulting in lower activity of **2-STE** and **3-STE** compared to the calcined samples **2-STE-AC** and **3-STE-AC**. The high temperature treatments for **2-STE** and **3-STE-AC** are required to remove organic residues and increase their catalytic activity. However, the high temperature calcination also causes partial structure collapse and a decrease of surface area. For the **1-STE** sample, with the smallest amount of organic residues, this thus results in lowering the catalytic activity of **1-STE-AC**. Therefore, for **1-STE** the post calcination is not necessary.

**Table 3.1** Summary of CO conversion for Co<sub>3</sub>O<sub>4</sub>-modified CeO<sub>2</sub>

<b>Sample</b>	<sup>a</sup> <b>T</b> <sub>10%</sub> (°C)	<sup>b</sup> <b>T</b> <sub>90%</sub> (°C)	<sup>c</sup> <b>r</b> <sub>130°C</sub> (mol/s·g)	<sup>d</sup> <b>R</b> <sub>130°C</sub> (mol/s·m <sup>2</sup> )	<sup>e</sup> <b>R</b> <sub>Co130°C</sub> (mmol CO/ mmol Co·h)	<sup>f</sup> <b>E</b> <sub>a</sub> (kJ/mol)
<b>1-STE</b>	117	155	2.48×10 <sup>-5</sup>	1.14×10 <sup>-7</sup>	68.7	47.4±0.3
<b>2-STE</b>	140	184	1.05×10 <sup>-5</sup>	4.42×10 <sup>-8</sup>	29.1	65.1±3.1
<b>3-STE</b>	194	244	8.37×10 <sup>-7</sup>	3.06×10 <sup>-9</sup>	2.3	77.5 ±4.3
<b>1-STE-AC</b>	131	163	1.48×10 <sup>-5</sup>	1.53×10 <sup>-7</sup>	41.0	61.8±1.8
<b>2-STE-AC</b>	133	173	1.39×10 <sup>-5</sup>	2.06×10 <sup>-7</sup>	38.5	58.0±1.7
<b>3-STE-AC</b>	142	186	9.25×10 <sup>-6</sup>	3.57×10 <sup>-7</sup>	25.6	65.9±2.3

a Reaction temperature for 10% CO conversion

b Reaction temperature for 90% CO conversion

c Reaction rate of CO oxidation at 130 °C per gram

d Normalized specific reaction rates of CO oxidation on a unit surface area at 130 °C

e Reaction rates on the basis of the unit amount of Co at 130 °C

f Apparent activation energy

Interestingly, the differences in the catalytic activity between the STE-AC samples, prepared by different routes of Co introduction, are not as obvious as for the STE samples. For example, the ignition temperature  $T_{10\%}$  of sample **1**-STE-AC and **2**-STE-AC, at 131 °C and 133 °C respectively, are nearly the same, while it is 142 °C for sample **3**-STE-AC. The same is valid for  $r_{130^\circ\text{C}}$ ,  $R_{130^\circ\text{C}}$ , and  $R_{\text{Co}130^\circ\text{C}}$  (Table 3.1). Independent of the sequence of Co introduction, all STE-AC samples exhibit similar catalytic activity. This might be due to two reasons related to the Co<sub>3</sub>O<sub>4</sub> phase, which is a dominant player in CO oxidation (see section 3.2.4): (1) for sample **1**, the partial collapse of the structure during calcination had buried part of Co in the body; (2) for sample **2** and **3**, the migration of Co<sub>3</sub>O<sub>4</sub> from the bulk and accumulation of Co<sub>3</sub>O<sub>4</sub> phase on the surface during the calcination may benefit the CO oxidation. Thus, cleaner surface, higher SSA and more Co<sub>3</sub>O<sub>4</sub> on the surface are main factors for the Co<sub>3</sub>O<sub>4</sub> modified CeO<sub>2</sub> catalyst, resulting in the best catalytic activity of sample **1** for both STE and STE-AC treatment.

### 3.3 Influence of the Co oxide proportion

#### 3.3.1 Basic material properties

From section 3.2 it can be seen that the route by which the Co precursor is added can influence the materials properties of Co<sub>3</sub>O<sub>4</sub> modified CeO<sub>2</sub>. Adding the cobalt precursor after the formation of the ceria gel, followed by solvothermal processing in ethanol give materials with the best CO oxidation activity. In the following, this synthesis method was used, and only the added amount of cobalt acetate was changed. The molar percentage of Co(OAc)<sub>2</sub>/(CeB+Co(OAc)<sub>2</sub>) (Co% as short) was changed from 10% to 80%, and the influence of this change on the materials properties was monitored.

The ratio of crystalline phases and the surface area are two important parameters to influence the materials' catalytic properties. Figure 3.20 shows the XRD patterns of CeO<sub>2</sub> samples modified by different amounts of Co<sub>3</sub>O<sub>4</sub> and treated by STE and STE-AC. The sample prepared with 10% Co and treated by STE showed CeO<sub>2</sub> diffraction peaks, and all the other samples showed also diffraction of Co<sub>3</sub>O<sub>4</sub> besides CeO<sub>2</sub>. The intensity of the Co<sub>3</sub>O<sub>4</sub> diffraction peaks increases along with the increasing Co precursor amount, and the STE-AC samples have larger particle sizes than the corresponding STE samples. The crystallite sizes of STE samples are summarized in Table 3.2. When the sample with 10% Co was treated only by STE processing,



Co may be incorporated in the lattice of  $\text{CeO}_2$ , as reported before [46]. The  $\text{CeO}_2$  crystallite sizes for all samples are in the range of 2.5-3.5 nm, and the crystallite sizes for  $\text{Co}_3\text{O}_4$  are about 25 nm.

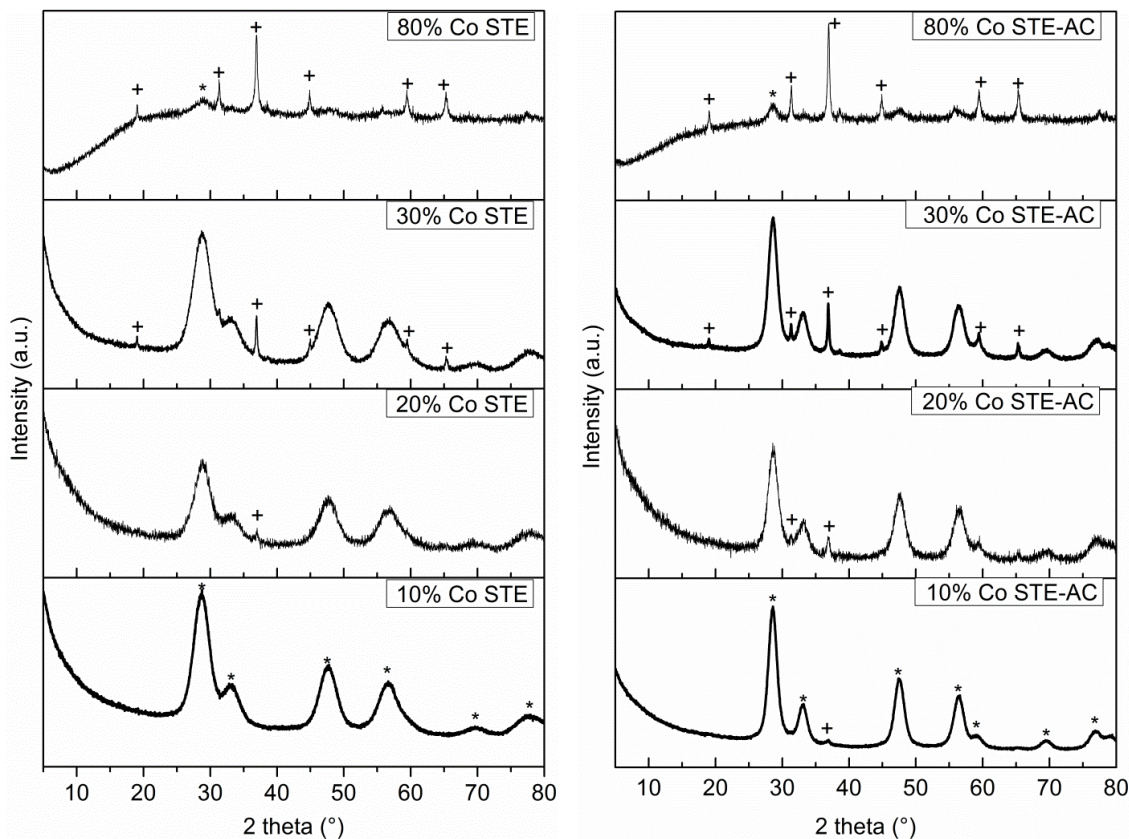


**Figure 3.20** XRD patterns of  $\text{CeO}_2$  samples modified by different proportions of  $\text{Co}_3\text{O}_4$  and treated by STE (left) and STE-AC (right). \* indicates  $\text{CeO}_2$ , + indicates  $\text{Co}_3\text{O}_4$

The surface areas were characterized by  $\text{N}_2$  sorption, and the  $\text{N}_2$  adsorption-desorption isotherms and pore size distributions for all STE (Figure 3.21) and STE-AC (Figure 3.22) samples were plotted. Except samples with 80% Co, all other isotherms belong to materials with mainly mesopores and a small proportion of macropores, and the pore size distributions are narrow. The samples with 80% Co (both STE and STE-AC) are inverse, with mainly macropores and small amount of mesopores. The changes of the pore type along with the increase of Co ratio are the same as reported before [109, 110].

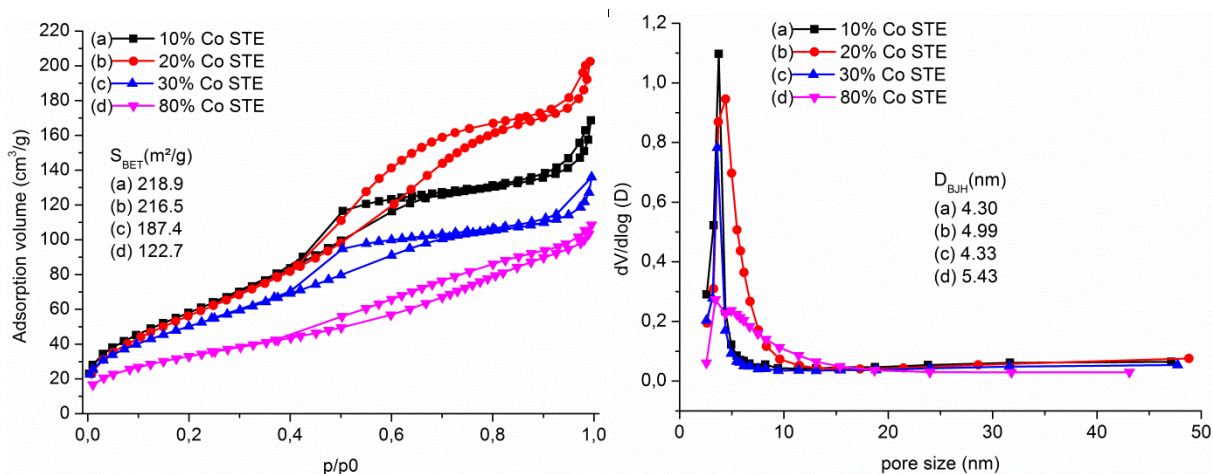


**Figure 3.21**  $\text{N}_2$  adsorption-desorption isotherms (left) and pore size distributions (right) for  $\text{CeO}_2$  samples modified by different proportions of  $\text{Co}_3\text{O}_4$  after STE treatment

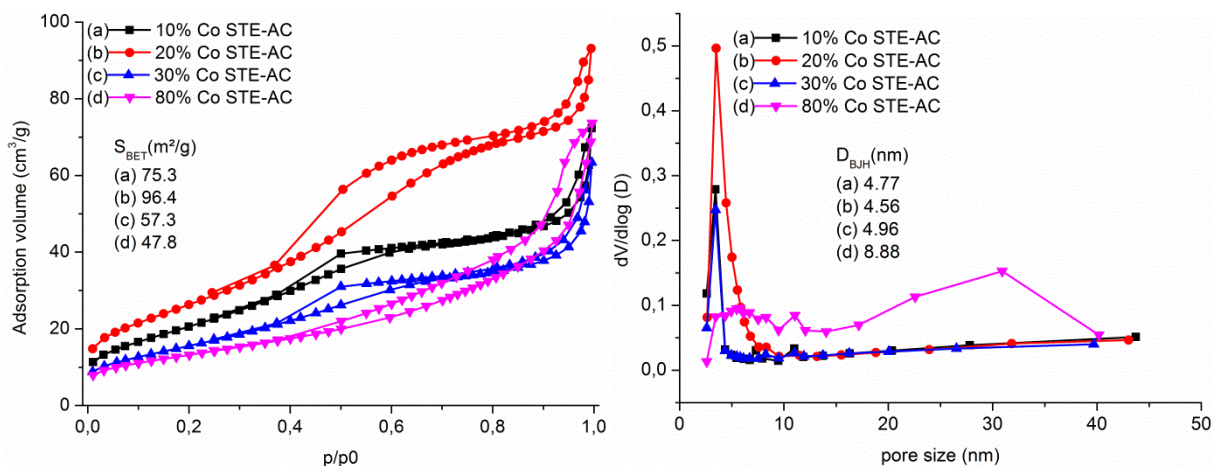


**Figure 3.22**  $\text{N}_2$  adsorption-desorption isotherms (left) and pore size distributions (right) for  $\text{CeO}_2$  samples modified by different proportions of  $\text{Co}_3\text{O}_4$  after STE-AC treatment

The different pore size types were also proven by the  $dV/d\log(D)$  value of the pore size distribution. Compared with the other samples with a small  $dV/d\log(D)$  value in the range of 10–50 nm, the sample prepared with 80% Co and treated by STE-AC had a large value in the corresponding range, which indicates a broad and inhomogeneous distribution of the pores. The  $S_{\text{BET}}$  value of STE samples decreased along with the increase of the Co amount. While  $S_{\text{BET}}$  is about 220  $\text{m}^2/\text{g}$  for STE sample with 10% Co, it is only about 120  $\text{m}^2/\text{g}$  when the Co amount was increased to 80%. After calcination in air, the surface area was reduced a lot for all samples, and the sample prepared with 20% Co has the highest surface area, about 96  $\text{m}^2/\text{g}$ .

### 3.3.2 Influence of the Co proportion on the catalytic properties

From Section 3.2.5, it is already known that the samples prepared by route **1** have almost the same catalytic activities before and after calcination in air, and the slightly ‘dirty’ surface even benefit the CO oxidation. Thus, for the samples synthesized by route **1** but with different Co proportion, only the samples treated by STE were used for CO oxidation, as shown in Figure 3.23. Basically, the higher the Co percentage is, the more  $\text{Co}_3\text{O}_4$  is on the surface of  $\text{CeO}_2$ , and the higher is the catalytic activity of  $\text{Co}_3\text{O}_4$  modified  $\text{CeO}_2$ .

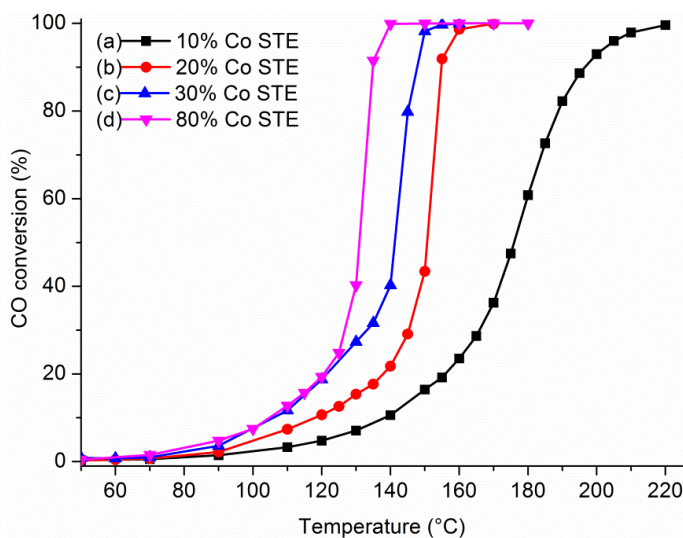


**Figure 3.23** CO conversion over  $\text{CeO}_2$  samples modified by different proportions of  $\text{Co}_3\text{O}_4$  after STE treatment

The temperature of 10% CO conversion/ignition temperature ( $T_{10\%}$ ), the temperature of 90% CO conversion ( $T_{90\%}$ ), reaction rate at 110 °C ( $r_{110^\circ\text{C}}$ ), specific reaction rates ( $R_{110^\circ\text{C}}$ ) and the reaction rates on the basis of the unit amount of Co ( $R_{\text{Co}110^\circ\text{C}}$ ) are summarized in Table 3.2 (CO conversion at 110 °C was below 20% for all samples). The  $T_{10\%}$  for STE samples are: 138 °C (Co 10%) > 117 °C (Co 20%) > 105 °C (Co 30%) = 105 °C (Co 80%), and the  $T_{90\%}$  are: 197 °C (Co 10%) > 155 °C (Co 20%) > 148 °C (Co 30%) > 134 °C (Co 80%). When the Co amount is smaller than 30%, the catalytic activity improved obviously with an increasing amount of Co. This is more clearly shown by the values of  $r_{110^\circ\text{C}}$  and  $R_{110^\circ\text{C}}$ . The values of  $r_{110^\circ\text{C}}$  and  $R_{110^\circ\text{C}}$  increased almost in direct proportion to the Co percentage. For example, the  $r_{110^\circ\text{C}}$  and  $R_{110^\circ\text{C}}$  values of 10% Co sample are  $5.30 \times 10^{-6}$  mol/s·g and  $2.42 \times 10^{-8}$  mol/s·m<sup>2</sup>, respectively. The

corresponding values of 20% Co sample are  $1.19 \times 10^{-5}$  mol/s·g and  $5.51 \times 10^{-8}$  mol/s·m<sup>2</sup>, almost twice the values for the sample with 10% Co. This is consistent with the  $R_{Co110^\circ C}$  value. When the Co ratio is below 30%, the  $R_{Co110^\circ C}$  of the samples have almost the same value of  $32 \pm 1$  mmol CO/mmol Co·h, thus the increased Co amount result in a higher CO catalytic activity. Further increase of the Co ratio to 80% does not much improve the material's CO oxidation ability. Especially in the low temperature range the activity of 80% Co sample is almost the same as that of the sample with 30% Co. The  $R_{Co110^\circ C}$  value of the sample with the 80% Co even decreased to 9.14 mmol CO/mmol Co·h. This may be because of the agglomerations of the Co<sub>3</sub>O<sub>4</sub> crystallites.

**Table 3.2** Summary of CO conversion for CeO<sub>2</sub> modified by different proportions of Co, sample were synthesized by route 1 and treated by STE

Co ratio	<sup>a</sup> D <sub>CeO2</sub>	<sup>b</sup> D <sub>Co3O4</sub>	<sup>c</sup> T <sub>10%</sub>	<sup>d</sup> T <sub>90%</sub>	<sup>e</sup> r <sub>110°C</sub>	<sup>f</sup> R <sub>110°C</sub>	<sup>g</sup> R <sub>Co110°C</sub>
(%)	(nm)	(nm)	(°C)	(°C)	(mol/s·g)	(mol/s·m <sup>2</sup> )	(mmol CO/mmol Co·h)
<b>10%</b>	3.0	/	138	197	$5.30 \times 10^{-6}$	$2.42 \times 10^{-8}$	31.07
<b>20%</b>	3.5	/	117	155	$1.19 \times 10^{-5}$	$5.51 \times 10^{-8}$	32.97
<b>30%</b>	2.5	27.5	105	148	$1.89 \times 10^{-5}$	$1.01 \times 10^{-7}$	32.70
<b>80%</b>	3.3	23.7	105	134	$2.06 \times 10^{-5}$	$1.68 \times 10^{-7}$	9.14

a CeO<sub>2</sub> crystal particle size calculated by Scherrer equation from XRD curves

b Co<sub>3</sub>O<sub>4</sub> crystal particle size calculated by Scherrer equation from XRD curves

c Reaction temperature for 10% CO conversion

d Reaction temperature for 90% CO conversion

e Reaction rate of CO oxidation at 110 °C per gram

f Normalized specific reaction rates of CO oxidation on a unit surface area at 110 °C

g Reaction rates on the basis of the unit amount of Co at 110 °C



### 3.4 Conclusion

Co<sub>3</sub>O<sub>4</sub> modified CeO<sub>2</sub> (Co:Ce = 1:4) was prepared by combination of sol-gel and solvothermal processing. The route by which Co was introduced clearly influenced the morphology of the composites on the nanoscale:

- (1) Using the single-source precursor Ce-POBC-Co resulted in a very homogeneous dispersion of Co oxide in the ceria matrix (samples **3-STE**);
- (2) When a pre-formed ceria gel was impregnated with Co(OAc)<sub>2</sub> under solvothermal conditions (samples **1-STE**), Co<sub>3</sub>O<sub>4</sub> particles were located on the surface of CeO<sub>2</sub> particles or agglomerates thereof. Only in this case were weak XRD reflections of Co<sub>3</sub>O<sub>4</sub> already observed after solvothermal treatment, in contrast to **2-STE** and **3-STE**;
- (3) In the third variation, i.e. sol-gel co-processing of CeB and Co(OAc)<sub>2</sub>, followed by solvothermal treatment, an intimate mixture of CeO<sub>2</sub> and Co<sub>3</sub>O<sub>4</sub> particles was obtained (Sample **2-STE**).

The results thus clearly show that these variations of the synthesis route resulted in three different morphologies on the nanoscale, despite the same Co:Ce ratio, the same metal precursors and the same processing steps (sol-gel processing + solvothermal treatment). The distribution of Co influenced the CeO<sub>2</sub> crystallite size, surface area and the catalytic activity. Catalyst **1-STE** with small Co<sub>3</sub>O<sub>4</sub> particles finely dispersed on the surface of CeO<sub>2</sub> exhibited the highest activity for CO oxidation, with an apparent activation energy of  $47.4 \pm 0.3$  kJ/mol, which is comparable to ceria-supported noble metals.

The Co proportion was changed from 10% to 80% for the route **1** procedure. Along with an increased Co proportion, the surface area of the materials decreased, while the ratio of Co<sub>3</sub>O<sub>4</sub> crystallite phase and the catalytic activity of the material increased. But when the catalytic reaction rates were normalized on the basis of the unit amount Co ( $R_{Co110^\circ C}$ ), the  $R_{Co110^\circ C}$  values were almost the same when the Co% was lower than 30%, about  $32 \pm 1$  mmol CO/mmol Co·h. But when the Co% increased to 80%, the  $R_{Co110^\circ C}$  value was only 9.14 mmol CO/mmol Co·h, which may be attributed to the agglomeration of Co<sub>3</sub>O<sub>4</sub> crystallite.

## 4. Graphene-CeO<sub>2</sub> and graphene-Co<sub>3</sub>O<sub>4</sub>-CeO<sub>2</sub> composites

### 4.1 Introduction

Previous research had shown that there were graphene-like organic residues on the surface of CeO<sub>2</sub> particles when EtOH was used as a solvent during the solvothermal treatment. The thus synthesized materials showed higher specific surface areas and better catalytic activity than the samples synthesized in H<sub>2</sub>O without graphene-like organic residues. There are also many reports that CeO<sub>2</sub>-graphene composites improved the catalytic behavior for the degradation of pollutants [61, 111-116], the activity for hydrogen production [117] or fuel cells [118], and the performance as sensors [119-121]. The property improvements of graphene-composited materials are mainly attributed to the good adsorption ability of graphene and the electron transfer between graphene and the oxide materials. For example, when 8 wt% chemically reduced graphene oxide (rGO) was loaded on CeO<sub>2</sub> nanowires (NWs), the photocatalytic activity for degradation of Rhodamine B was improved by a factor of 20, which can be attributed to the excellent absorption ability for the dye through  $\pi$ - $\pi$  conjugation as well as the effective inhibition of the recombination of photogenerated electrons because of the electronic interaction between CeO<sub>2</sub> NWs and rGO sheets [111].

Graphene can be prepared by many ways, like micro-mechanical exfoliation of highly ordered pyrolytic graphite, epitaxial growth, chemical vapor deposition, and the reduction of graphene oxide (GO) [122]. Although the graphene prepared from GO has more defects compared with the products from the first three methods, the reduction of GO still attracts much attentions because of two important advantages: (1) graphene can be produced using inexpensive graphite as raw material by cost-effective chemical methods with a high yield, and (2) the product is highly hydrophilic and can form stable aqueous colloids to facilitate the assembly of macroscopic structures by simple and cheap solution processes, which are important to the large-scale uses of graphene.

GO is made by oxidizing graphite in harsh environment with a strong acid and oxidant. First, graphite oxide is formed, which has a layered structure similar to graphite, but the plane of carbon atoms in graphite oxide is heavily decorated by oxygen-containing groups. These groups

not only expand the interlayer distance but also render the atomic-thick layers hydrophilic. As a result, these oxidized layers can be exfoliated in water under ultrasonication. If the exfoliated sheets contain only one or few layers of carbon atoms like graphene, these sheets are named graphene oxide (GO). The most attractive property of GO is that it can be (partly) reduced to graphene-like sheets by removing the oxygen-containing groups through thermal reduction (thermal annealing, or microwave and photo reduction) or chemical reduction (such as chemical reagent reduction, photocatalytic reduction, electrochemical reduction and solvothermal reduction) [122]. These reduction processes can cause partial (depending on the specific reduction way) de-oxygenation or restoration of long-range conjugated structures, thus parts of the GO defects are healed, and the products are named as reduced GO (rGO). The rGO are usually considered as one kind of chemically derived graphene. Some other names have also been given to rGO, such as functionalized graphene, chemically modified graphene, chemically converted graphene, or reduced graphene.

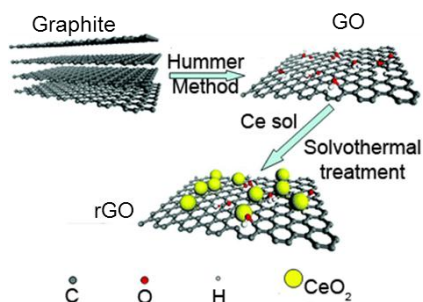


**Figure 4.1** Synthesis sketch of rGO -CeO<sub>2</sub> composites (GO: graphene oxide, rGO: reduced graphene oxide)

When graphene-oxide composites are prepared, chemical reduced graphene oxides (rGO) are normally used, because rGO can be easily prepared in a large scale [122-124] and the residual defects such as COOH etc. are beneficial for anchoring the oxide particles on the rGO. Thus in this part, GO was prepared by Hummers' method through oxidizing graphite, which was further used to prepare graphene-CeO<sub>2</sub> composites, as shown in Figure 4.1. The GO treated after solvothermal processing is named rGO according to a general definition [122], and the graphene mentioned in the following research also refers to rGO. The influence of the GO amount and the reductive agent (both EtOH and *L*-ascorbic acid (Vc)) were investigated on both rGO-CeO<sub>2</sub> and rGO-Co<sub>3</sub>O<sub>4</sub>-CeO<sub>2</sub> composite materials.

## 4.2 Synthesis of rGO-CeO<sub>2</sub> composites

### 4.2.1 Influence of the rGO amount

As the CeO<sub>2</sub> samples prepared from EtOH contained organic residues on the particle surface, which have graphene-like structures (section 2.3.3), pre-synthesized graphene oxide (GO) was introduced into the ceria gel, which will be reduced to graphene (rGO) after the solvothermal processing in EtOH, forming rGO-CeO<sub>2</sub> composites. The influence of the amount of rGO was investigated. CeO<sub>2</sub> was fixed to 5 mmol, and the GO amount changed from 0 g to 0.2 g.

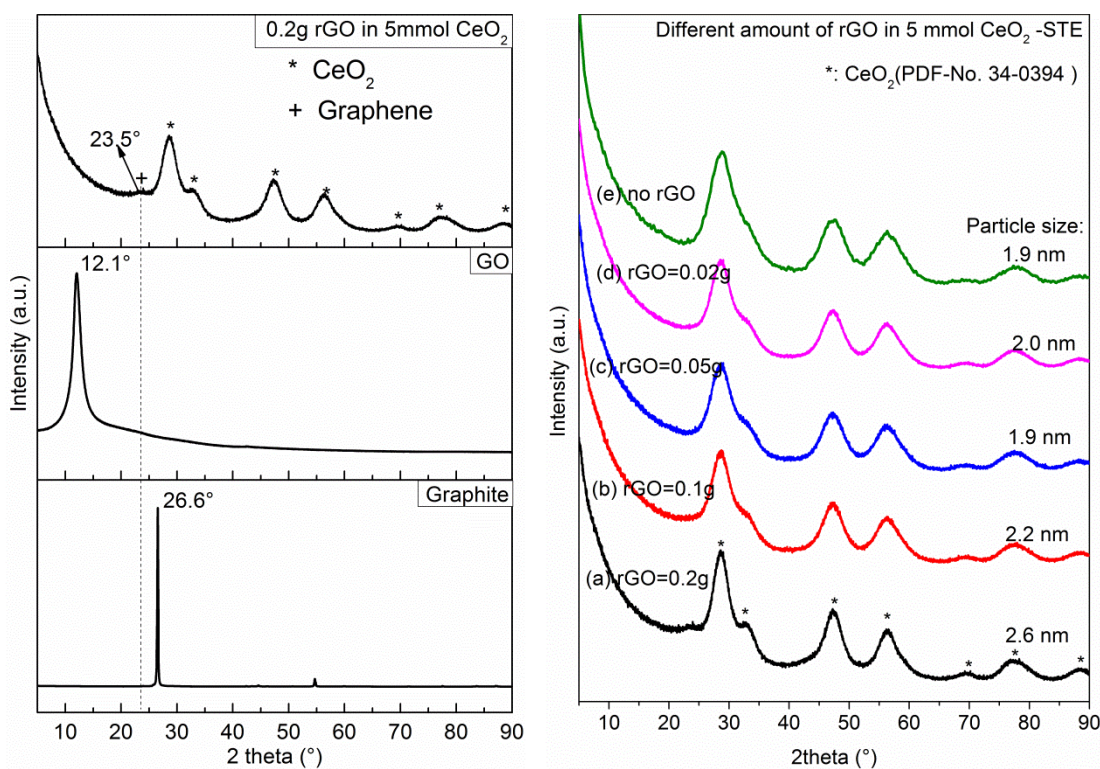


**Figure 4.2** XRD patterns of graphite, GO (left) and rGO-CeO<sub>2</sub> composites with different amounts of rGO (right) after STE treatment

GO was prepared by the modified Hummer method [125, 126]. The XRD patterns of GO and graphite are given in Figure 4.2 left. For graphite, the characteristic diffraction peak appears at 26.6°. For GO, the characteristic diffraction reflexion shifted to 12.1°, indicating that the graphite interlayer distance was enlarged by the oxidation procedure. When 0.2 g GO was dispersed in 5 mmol ceria-sol and after solvothermal treatment in EtOH without an extra



reductive agent, a weak reflexion at 23.5° was observed besides the CeO<sub>2</sub> peaks, which corresponds to the (002) reflexion of graphene [62, 93, 123, 124, 127-129]. This indicates that the reductive ability of EtOH is already enough to reduce GO.

When the rGO amount was less than 0.2 g, the graphene reflexion in the XRD patterns was not seen because of the weak signal (Figure 4.2 right), although the IR and Raman were similar. The changing of the rGO amount (from 0.2 g to 0 g) did not influence the CeO<sub>2</sub> phase a lot. All the samples have CeO<sub>2</sub> crystallite sizes of 1.9-2.6 nm (calculated from Scherrer's equation based on the strongest peak at 28.7°). The sample with 0.2 g rGO had a slightly larger CeO<sub>2</sub> crystallite size, which may be because the high amount of rGO was aggregated during solvothermal treatment, and the trapped CeO<sub>2</sub> particles merged into larger ones. The aggregation situation of rGO can be proven by Raman mapping in the following part.

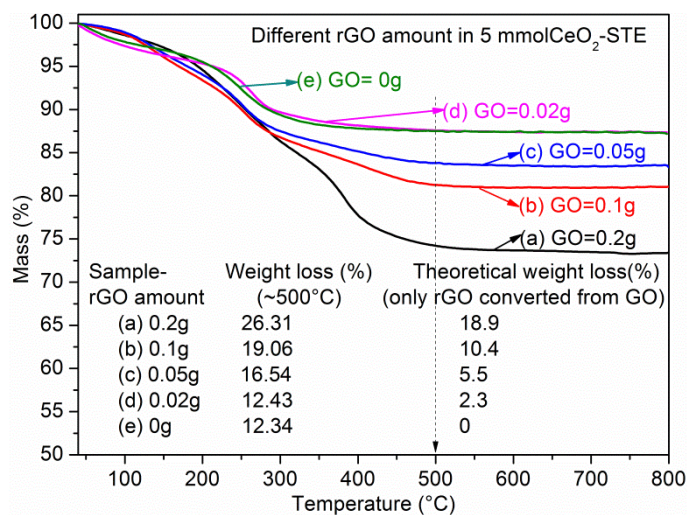


**Figure 4.3** TGA curves of rGO-CeO<sub>2</sub> composites with different amounts of rGO after STE treatment

The different rGO amounts can also be detected by TGA, as shown in Figure 4.3. As pure GO decomposed below 200 °C [124], the synthesized samples started weight loss over 250 °C, indicating that rGO was formed. Generally, the weight loss increased along with the amount of rGO. All the detected weight losses are larger than the theoretical ones, which are based on the added GO amount. This indicates that there are still other organic residues on the CeO<sub>2</sub> particles besides rGO converted from GO. But according to the Raman spectra shown in Figure 4.4, there is no extra organic band besides those of rGO. Combining with the results shown in section 2.3.3

(Figure 2.18), the organic residues from EtOH solvothermal treatment also showed graphene-like structures. The graphene formed on the CeO<sub>2</sub> particles therefore originate from two compositions: from GO and EtOH. Graphene formed from EtOH is about 11%, which is shown by the Figure 2.7(left) in section 2.3.1. Thus if all the GO was converted to rGO and attached on the CeO<sub>2</sub> particles, the real weight loss should be the theoretical weight loss plus 11%. This is valid for samples with a rGO amount  $\leq 0.1$  g, but not for sample with rGO amounts  $> 0.1$  g. This may be an indication that the sample with a rGO amount  $> 0.1$  g had some rGO which was not attached to the CeO<sub>2</sub> particles, and was removed along with the solvent.

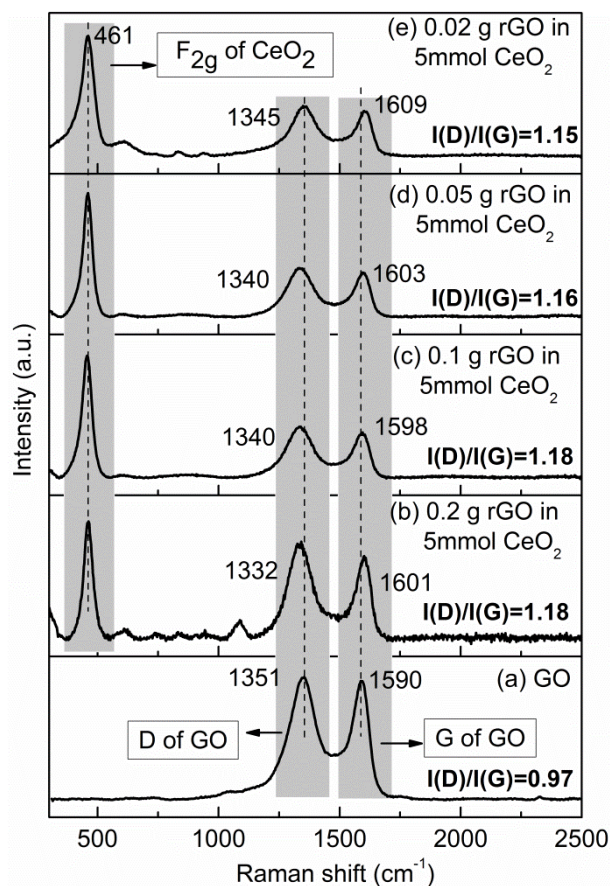


**Figure 4.4** Raman spectra of GO and rGO-CeO<sub>2</sub> composites with different amounts of rGO after STE treatment

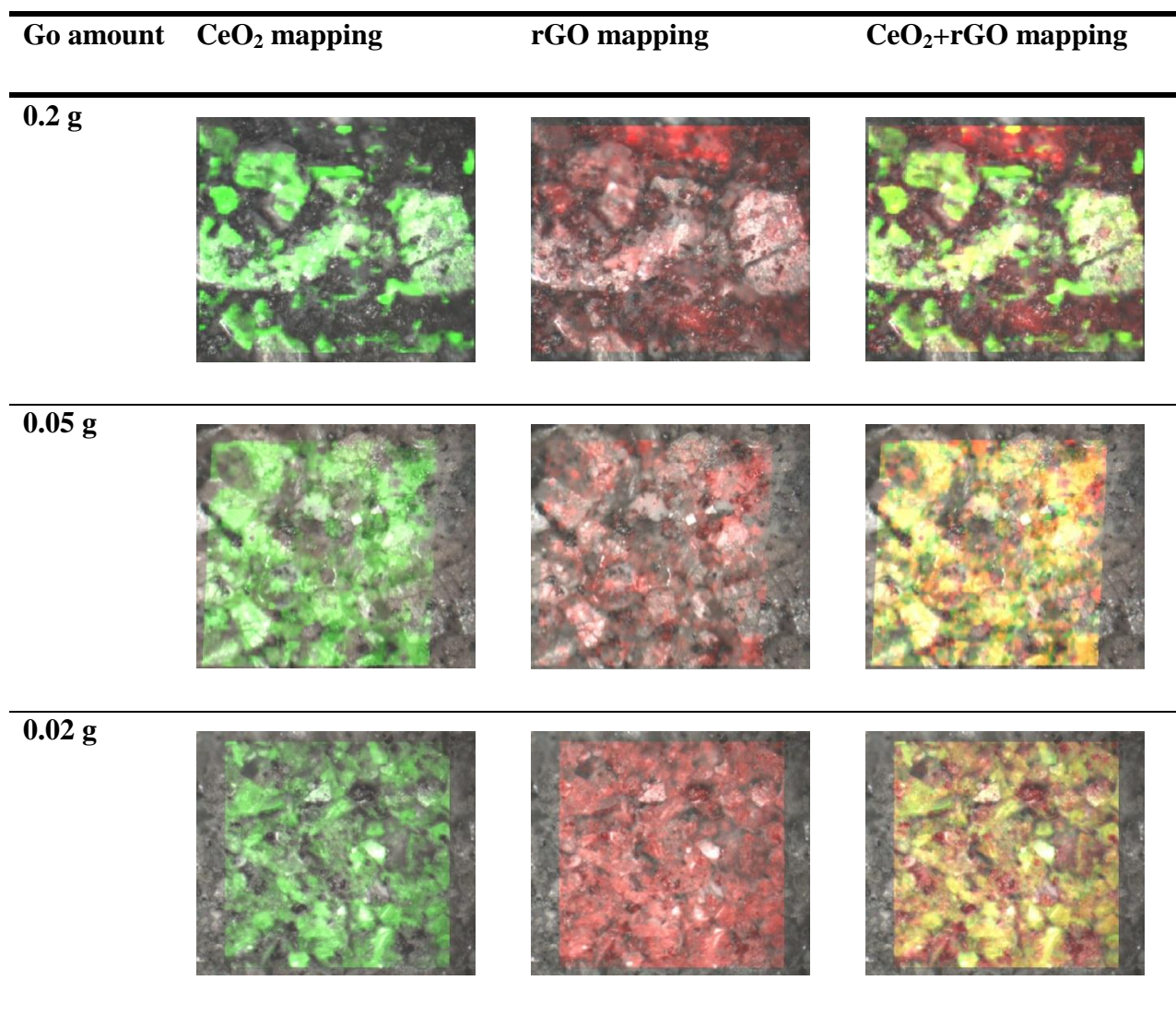
Raman spectroscopy was used to monitor the state of GO and rGO. GO showed the typical D-band and G-band at 1351 cm<sup>-1</sup> and 1590 cm<sup>-1</sup> respectively, with an intensity ratio I(D)/I(G) of 0.97. The D-band is related to a breathing mode of  $\kappa$ -point photons of A<sub>1g</sub> symmetry, and the G-

band can be attributed to the splitting of the E<sub>2g</sub> stretching mode of graphite which reflects the proportion of the sp<sup>2</sup> C atoms [93-95]. The intensity ratio I(D)/I(G) represents the degree of disorder in a graphite layer.

Generally the G- and D-bands have a slight shift to lower values when GO is reduced to graphene [130, 131]. For the synthesized rGO-CeO<sub>2</sub> composites, all the D-bands were shifted to lower values, indicating that the GO had been reduced to graphene. But all the G-bands were slightly shifted to a higher value when compared with that of GO. The red-shifting of the G-band may be attributed to the increased number of defects caused by stress from the oxygen states [93, 132-134]. The increased number of defects can be proven by the intensity ratio I(D)/I(G). I(D)/I(G) values for all rGO-CeO<sub>2</sub> composites are larger than that of GO, indicating that the defects of the graphite layer increased because of the removal of oxygen-containing groups during the reduction of GO, which has also been reported before [135, 136]. Furthermore, the F<sub>2g</sub> band of CeO<sub>2</sub> was also observed at 461 cm<sup>-1</sup>. Anchoring of CeO<sub>2</sub> on rGO will also cause an intensity decrease and up-shifting of the G-band because of the electron transfer [93, 128, 129].

Raman mapping was used to detect the distribution of rGO, as shown in Figure 4.5. As the Raman intensity was almost the same for GO amounts of 0.1 g and 0.05 g, only the Raman mappings for the samples with 0.2 g, 0.05 g and 0.02 g rGO are given here. When the rGO amount was 0.2 g, phase separation was observed by partial disappearance of the CeO<sub>2</sub> signal and the enhancement of rGO signal in the corresponding area, indicating agglomeration of rGO. This may be because of the high amount of GO, which could not disperse well after solvothermal treatment. But when the GO amount was reduced to 0.05 g, the Raman mapping showed no obvious phase separation, indicating that the rGO and CeO<sub>2</sub> were homogeneously dispersed. The dispersing situation of CeO<sub>2</sub> with 0.02 g rGO was almost the same as that with 0.05 g rGO, with homogeneous distribution of both phases.

**Figure 4.5** Raman mapping of rGO-CeO<sub>2</sub> composites with different amounts of rGO after STE treatment (mapping area: 500 μm×500 μm)



IR spectra showed also a clear change of graphite→GO→rGO (Figure 4.6). For graphite, there are no bands in the range of 3000-3500 cm<sup>-1</sup> and 1000-1750 cm<sup>-1</sup>, which correspond to OH and COO&CO groups, respectively. After Hummers' treatment, the graphite transformed into GO with strong signals in the region mentioned before, indicating that many COOH and COH groups were formed. After the solvothermal treatment, the intensity of OH (3000-3500 cm<sup>-1</sup>) and C-O (1042 cm<sup>-1</sup>) vibrations decreased while the intensity of COO (1250-1700 cm<sup>-1</sup>) increased, indicating part of the defects were healed and rGO was formed. Compared with the COO groups



of GO, the position of COO peaks were shifted from 1719 and 1613 cm<sup>-1</sup> to 1492 and 1391 cm<sup>-1</sup>, respectively. The shifts may be caused by anchoring of CeO<sub>2</sub> on graphene through the residual COO groups. The IR spectra of all rGO-CeO<sub>2</sub> composites are almost the same, and only the peak intensities are somewhat different.

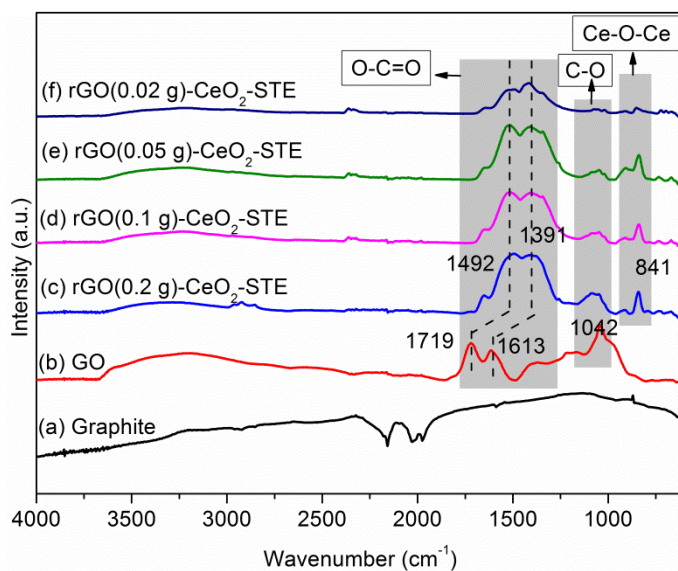


**Figure 4.6** IR spectra of graphite, GO and rGO-CeO<sub>2</sub> composites with different amounts of rGO after STE treatment

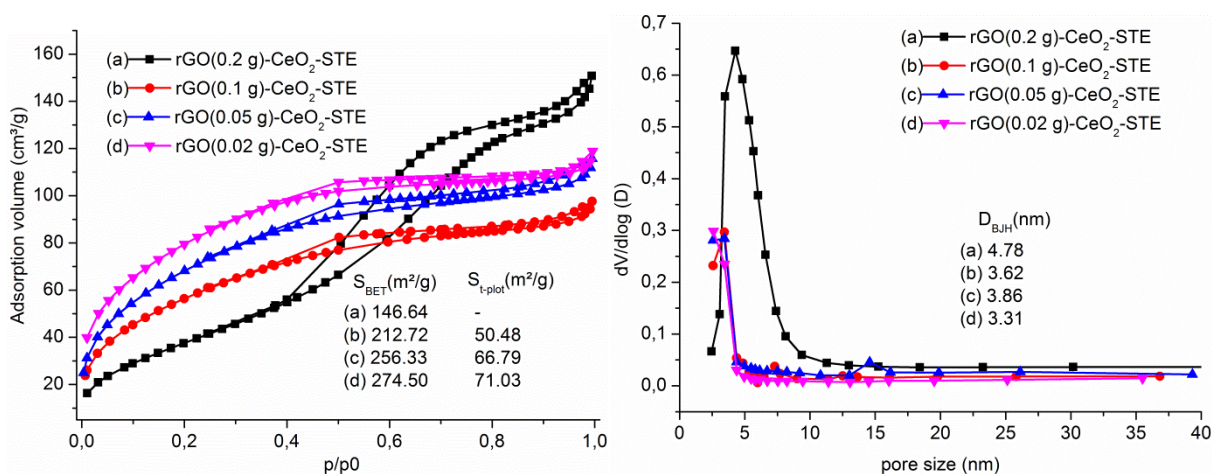


**Figure 4.7** N<sub>2</sub> adsorption-desorption isotherms (left) and pore size distributions (right) for the rGO-CeO<sub>2</sub> composites with different amounts of rGO after STE treatment

N<sub>2</sub> adsorption-desorption results for the rGO-CeO<sub>2</sub> composites with different amounts of rGO after STE treatment are shown in Figure 4.7 left. According to the IUPAC classification, only rGO-CeO<sub>2</sub> with 0.2 g rGO is a mesoporous material, while the others are materials with mainly micropores and a small portion of mesopores. This can also be seen from the pore size distribution (Figure 4.7 right). The sample with 0.2 g rGO has an average pore size of 4.8 nm, while the other samples have smaller pore sizes in the range of 3.3-3.8 nm. The surface area increased along with the decreasing of rGO amount, from 146.6 m<sup>2</sup>/g with 0.2 g rGO to 274.5 m<sup>2</sup>/g with 0.02 g rGO.

The rGO-CeO<sub>2</sub>-STE composite with 0.05 g rGO was tested for CO oxidation. For comparison, the CeO<sub>2</sub> sample after STE treatment is also shown, which was the same as in section 2.3.3 (Figure 2.14). The CO oxidation at different temperatures is shown in Figure 4.8, and the temperature of 10% CO conversion/ignition temperature (T<sub>10%</sub>), the temperature of 90% CO conversion T<sub>(90%)</sub>, the reaction rate at 250 °C (r<sub>250°C</sub>), specific reaction rates (R<sub>250°C</sub>) were summarized in Table 4.1.

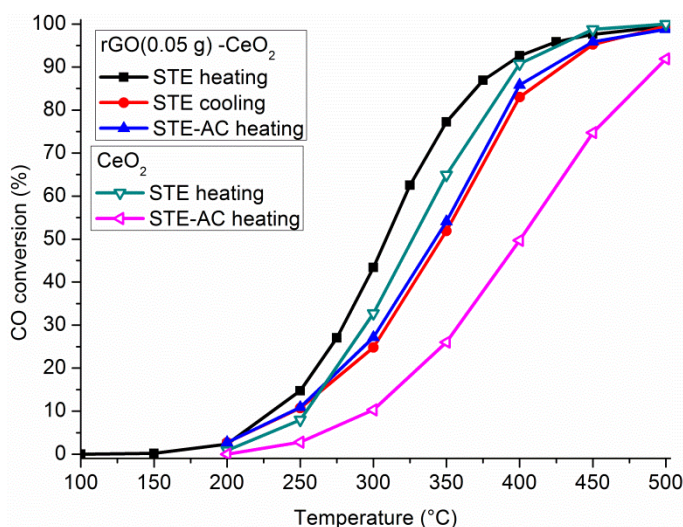


**Figure 4.8** CO oxidation at different temperatures for pure CeO<sub>2</sub> samples and 0.05 g rGO-CeO<sub>2</sub> composite (20 mg)

In order to study the catalytic stability of the rGO(0.05 g)-CeO<sub>2</sub>-STE composite along with the temperature, the sample was heated to 500 °C for a 100% conversion and then cooled down to 200°C for an about 2% conversion, followed by re-heated to 500 °C (named as rGO(0.05 g)-

CeO<sub>2</sub>-STE-AC). The activity of rGO(0.05 g)-CeO<sub>2</sub>-STE-AC is somewhat lower than that of rGO(0.05 g)-CeO<sub>2</sub>-STE at the same temperature. For example, the  $r_{250^{\circ}\text{C}}$  for rGO(0.05 g)-CeO<sub>2</sub>-STE composite during first heating is  $1.19 \times 10^{-5}$  mol/s·g, and the value changed to  $8.77 \times 10^{-6}$  mol/s·g for rGO(0.05 g)-CeO<sub>2</sub>-STE-AC. This decrease may be caused by the removal of graphene and reduction of the surface area. After the rGO(0.05 g)-CeO<sub>2</sub>-STE composite was calcined at 500 °C for 2 h, the surface area decreased from 256.3 m<sup>2</sup>/g to 55.5 m<sup>2</sup>/g.

Compared with the CeO<sub>2</sub> sample, the rGO(0.05 g)-CeO<sub>2</sub> composite showed better catalytic activity. For the rGO(0.05 g)-CeO<sub>2</sub> composite, the corresponding T<sub>10%</sub> and T<sub>90%</sub> for STE/STE-AC are 230/245 °C and 388/421 °C, which is lower than the values of CeO<sub>2</sub>-STE and CeO<sub>2</sub>-STE-AC samples (253/298 °C for T<sub>10%</sub> and 398/494 °C for T<sub>90%</sub>). When the  $r_{250^{\circ}\text{C}}$  and  $R_{250^{\circ}\text{C}}$  are calculated, the better quality of rGO(0.05 g)-CeO<sub>2</sub> composite is even more obvious, especially  $R_{250^{\circ}\text{C}}$  for rGO(0.05 g)-CeO<sub>2</sub>-STE-AC is  $1.56 \times 10^{-7}$  mol/s·m<sup>2</sup>, which is almost six times more than that of CeO<sub>2</sub> STE-AC ( $2.52 \times 10^{-8}$  mol/s·m<sup>2</sup>).

**Table 4.1** Summary of CO conversion for pure CeO<sub>2</sub> and rGO (0.05g) - CeO<sub>2</sub> composite

Sample	<sup>a</sup> S <sub>BET</sub> (m <sup>2</sup> /g)	<sup>b</sup> Weight loss (%)	<sup>c</sup> T <sub>10%</sub> (°C)	<sup>d</sup> T <sub>90%</sub> (°C)	<sup>e</sup> r <sub>250°C</sub> (mol/s·g)	<sup>f</sup> R <sub>250°C</sub> (mol/s·m <sup>2</sup> )
CeO <sub>2</sub> STE	277.0	12	253	398	$6.42 \times 10^{-6}$	$2.32 \times 10^{-8}$
CeO <sub>2</sub> STE-AC	88.9		298	494	$2.24 \times 10^{-6}$	$2.52 \times 10^{-8}$
rGO(0.05 g)-CeO <sub>2</sub> STE	256.3	16	230	388	$1.19 \times 10^{-5}$	$4.62 \times 10^{-8}$
rGO(0.05 g)-CeO <sub>2</sub> STE-AC	55.5		245	421	$8.77 \times 10^{-6}$	$1.56 \times 10^{-7}$

<sup>a</sup> BET surface area; error  $\pm$  5%

<sup>b</sup> weight loss from room temperature to 500 °C

<sup>c</sup> Reaction temperature for 10% CO conversion

<sup>d</sup> Reaction temperature for 90% CO conversion

<sup>e</sup> Reaction rate of CO oxidation at 250 °C per gram

<sup>f</sup> Normalized specific reaction rates of CO oxidation on a unit surface area at 250 °C

The advantage of the rGO(0.05 g)-CeO<sub>2</sub>-STE composite can also be seen from the CO temperature programmed reduction (CO-TPR) in Figure 4.9. For rGO(0.05 g)-CeO<sub>2</sub>-STE, both CO<sub>2</sub> and H<sub>2</sub> evolution showed signals earlier than those for CeO<sub>2</sub>-STE. Similar to the CeO<sub>2</sub>-STE samples, rGO(0.05 g)-CeO<sub>2</sub>-STE also showed three features: removal of surface lattice oxygen (<300 °C), water gas shift between CO and surface OH groups (300-500 °C), and extraction of bulk oxygen (>500 °C), respectively. Compared with the regions defined for CeO<sub>2</sub>-STE in section 2.3.3, all regions were shifted to lower temperatures by about 100 °C for rGO(0.05 g)-CeO<sub>2</sub>-STE. The abundant OH groups and faster electron transfer may contribute to the improvement of catalytic properties of rGO(0.05 g)-CeO<sub>2</sub>-STE.

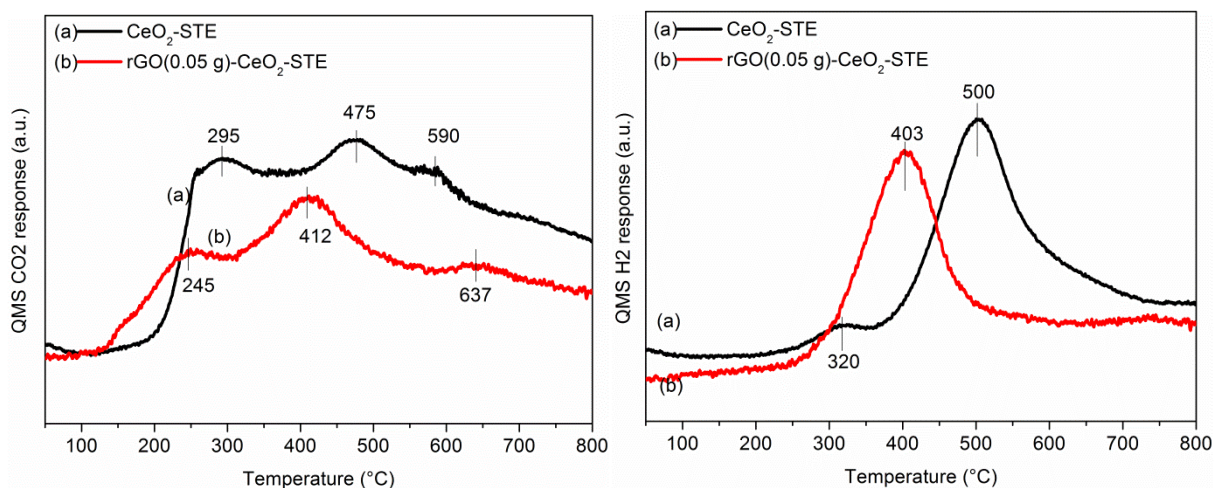


**Figure 4.9** CO<sub>2</sub> (left) and H<sub>2</sub> (right) evolution during CO-TPR over CeO<sub>2</sub>-STE and rGO(0.05 g)-CeO<sub>2</sub>-STE (20 mg sample)

#### 4.2.2 Influence of *L*-Ascorbic acid (Vc)

Although the rGO-CeO<sub>2</sub>-STE composite already showed better catalytic activity than CeO<sub>2</sub>-STE, the rGO started to decompose at about 250 °C (Figure 4.3), which is lower than the reported decomposition temperature for chemical reduced GO (about 300 °C). The quality of the synthesized graphene was not well enough, perhaps because no reductive agent was used during the solvothermal treatment, although some literature and the previous results showed that graphene can be formed in pure EtOH [137] or a EtOH/H<sub>2</sub>O mixture [138, 139] after solvothermal treatment.



*L*-Ascorbic acid (Vc) was chosen as a reductive agent to enhance the quality of graphene and increase its decomposition temperature. Vc has been reported to be an ideal substitute for hydrazine in the reduction of graphene oxide [122, 140-143], which is a mild reducing agent and antioxidant. It is oxidized with loss of one electron to form a radical cation and then with loss of a second electron to form dehydroascorbic acid [144], as shown in Figure 4.10.

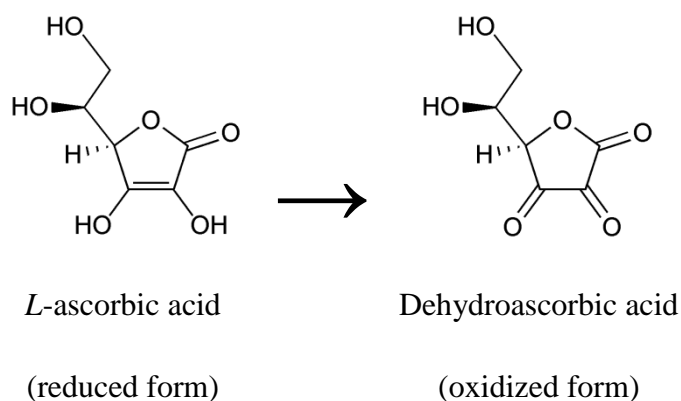


**Figure 4.10** Oxidation of *L*-ascorbic acid

After putting 0.02 g of GO into 5 mmol of ceria sol and ultrasonic dispersion for more than 2 h, the GO-Ce sol was transferred to a glass plate and dried to get the GO-Ce gel. Two different procedures were tried when Vc was used as reductive agent: (1) the GO-Ce gel was put into an autoclave with 30 mL EtOH and 1 g Vc, then sealed and solvothermally treated at 200 °C for 6 h. This sample is named Vc-rGO-CeO<sub>2</sub>-STE; (2) the GO-Ce gel was put into a flask with 30 mL EtOH and 1 g Vc, then it was refluxed at 150 °C for 6 h. This sample is named Vc-rGO-CeO<sub>2</sub>-reflux.

The TGA (Figure 4.11) and XRD (Figure 4.12) results show that the samples prepared with Vc by two different procedures are similar, but quite different to the samples prepared without Vc. The samples prepared with Vc have quite a large weight loss with almost the same value of 45% (Figure 4.11 (b) & (d)). When compared with the rGO-CeO<sub>2</sub> composite without Vc (Figure 4.11(a)), it appears that extra organic residues stayed on the surface of CeO<sub>2</sub>. The XRD patterns of the Vc reduced samples showed that the formation of crystalline CeO<sub>2</sub> was inhibited by Vc (Figure 4.12(a) & (c)), when compared with the sample prepared without Vc in Figure 4.2.

Thus further calcination at 350 °C was carried out to remove most organic residues. The TGA results showed that the weight loss of the AC350 °C samples changed by only about 5% until 500 °C. Crystalline CeO<sub>2</sub> also appeared in the calcined samples, but almost the same for the two procedures.

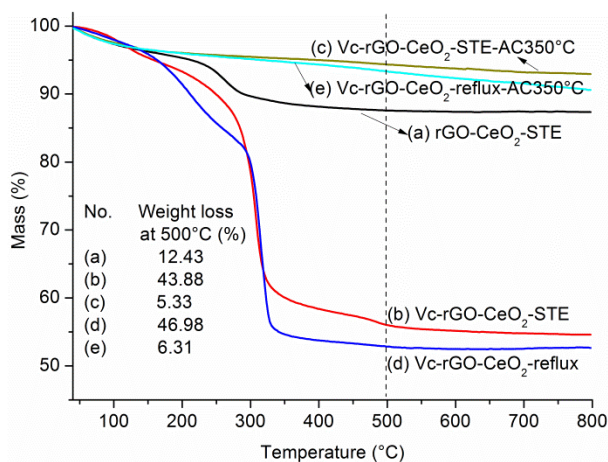


**Figure 4.11** TGA curves of rGO(0.02 g)-CeO<sub>2</sub> composites prepared with 1 g Vc

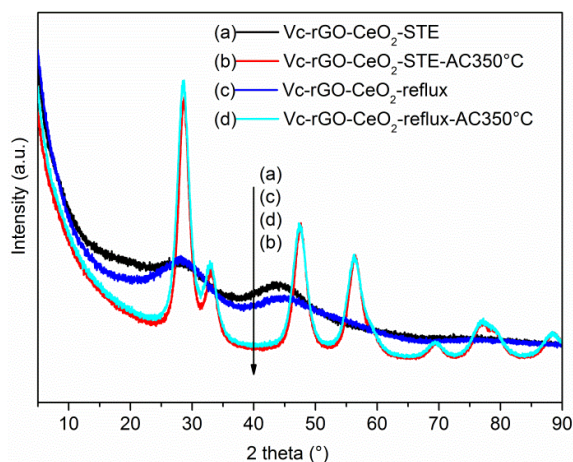


**Figure 4.12** XRD of rGO(0.02 g)-CeO<sub>2</sub> composites prepared with 1 g Vc

When comparing the IR spectra of samples prepared at different conditions, some interesting aspects can be found. The as-prepared sample of pure CeO<sub>2</sub>, rGO-CeO<sub>2</sub> composite, and Vc-rGO-CeO<sub>2</sub> composite (both STE and reflux) are shown in Figure 4.13, and the IR spectra of the corresponding calcined samples in Figure 4.14. The CeO<sub>2</sub>-STE (Figure 4.13(a)) and the rGO-CeO<sub>2</sub> composite (Figure 4.13 (b)) have quite similar IR spectra, except the Ce-O-Ce first overtone. The two Vc-rGO-CeO<sub>2</sub> (STE & reflux) are a little different in two aspects (Figure 4.13 (c) & (d)): (1) the peak intensity of the C-O band (~1050 cm<sup>-1</sup>) is stronger for the Vc-rGO-CeO<sub>2</sub> samples (especially the refluxed sample), which may be attributed to more COO and aromatic carbon groups (also from Raman in Figure 4.15) caused by Vc; (2) the band position of COO (1350-1580 cm<sup>-1</sup>): the Vc-rGO-CeO<sub>2</sub> samples have bands in the same region, but about 60 cm<sup>-1</sup> different from the sample without Vc.

When the two Vc-rGO-CeO<sub>2</sub> samples were further calcined at 500 °C (Figure 4.14 (e) & (f)), the C-O bands almost disappeared, while the COO band changed to the same position as for the other samples prepared without Vc and calcined at 500°C (Figure 4.14 (a) & (b)). The IR spectra

of two the Vc-rGO-CeO<sub>2</sub> samples calcined at 350 °C are almost the same as those at 500 °C, except the C-O peak at 1050 cm<sup>-1</sup>. The COO bands of all samples are almost at the same position, which may indicate that all samples contain the same carbon species after calcination. This is consistent with the work described in previous sections 2.3.3, as CeO<sub>2</sub>-STE samples already have graphene-like organic residues even without GO.

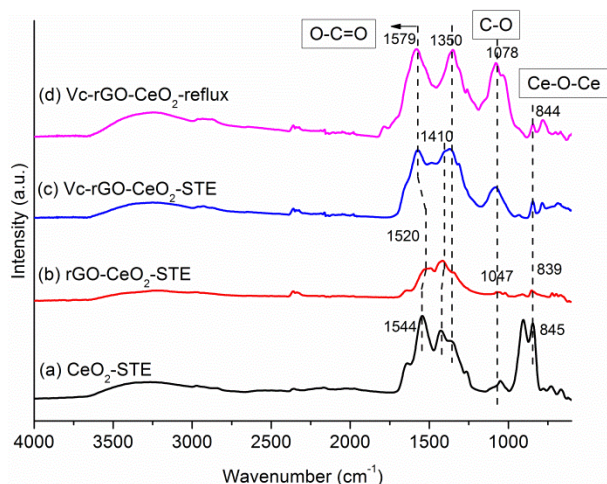


**Figure 4.13** IR spectra of as-prepared CeO<sub>2</sub> samples by various conditions

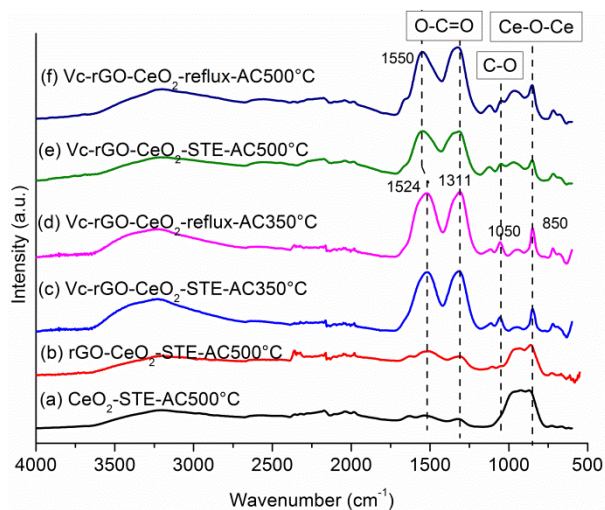


**Figure 4.14** IR spectra of calcined CeO<sub>2</sub> samples by various conditions

The Raman spectra showed that graphene reduced by Vc has a stronger G band than graphene reduced by EtOH. While the ratio of I(D)/I(G) is 1.15 for the rGO by EtOH-STE, the value is only 0.88 for rGO by Vc-STE, indicating that the number of defects in the graphite layer decreased by Vc reduction. But when the GO was reduced by Vc-reflux, the rGO characterization bands are not so clear, only a strong aromatic C-C band can be observed. This may be because the reaction temperature for reflux (150 °C) is lower than that for solvothermal treatment (200 °C), and the reduction degree is not high enough. This can also be proven by TGA (Figure 4.11) and IR (Figure 4.13). For TGA, part of the weight loss started at 200 °C for the Vc-reflux sample, while the weight loss for Vc-STE started at about 300 °C. The IR spectrum of the Vc-reflux sample also showed high intensity bands of O-C=O and C-O groups, which is also an indication that the degree of reduction is not high enough for the Vc-reflux sample. The following synthesis for rGO-Co<sub>3</sub>O<sub>4</sub>-CeO<sub>2</sub> therefore only used Vc-STE or EtOH-

STE procedures. After calcination at 350 °C for 2 h (Figure 4.15 right), the rGO structure has been destroyed for all samples, and only the CeO<sub>2</sub> F<sub>2g</sub> band was observed in Raman spectra.

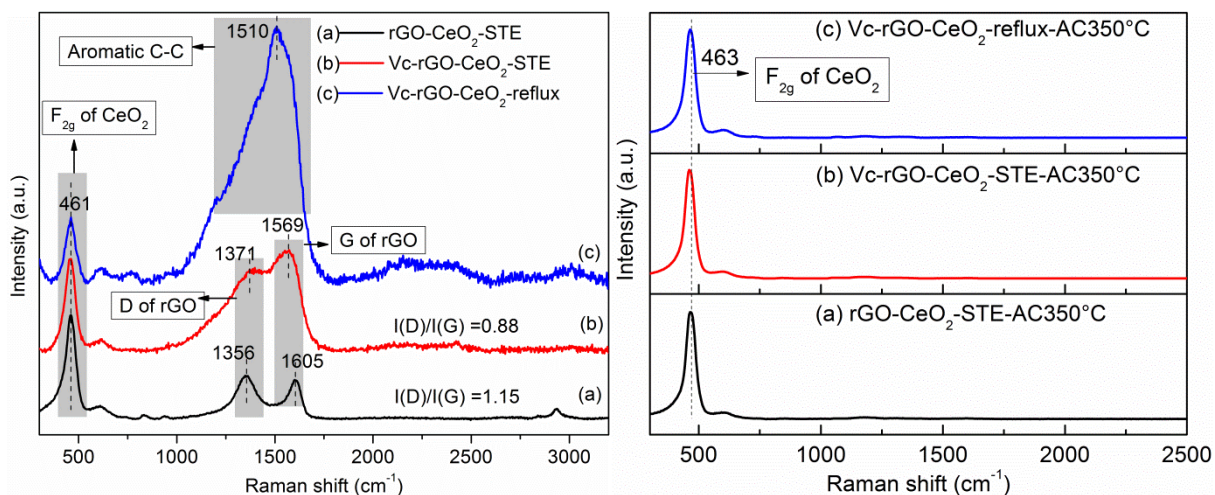


**Figure 4.15** Raman spectra of as-prepared Vc-rGO-CeO<sub>2</sub> (left) and after calcination at 350 °C for 2 h (right)

Although Raman spectroscopy showed that the defects of rGO were reduced when Vc was used as reductive agent, the surface areas of the Vc-rGO-CeO<sub>2</sub>-STE/reflux samples are quite low, smaller than 10 m<sup>2</sup>/g, i.e. they are non-porous materials (Figure 4.16 left). This can also be proven by the extremely low dV/dlog(D) value of the pore size distribution in Figure 4.16 right. In contrast, the sample synthesized at the same conditions but without Vc showed a high surface area of 274 m<sup>2</sup>/g, typical for micropores materials. The differences may be caused by the large proportion of organic residues from Vc, which blocked most of the pores.

After the samples were calcined at 350 °C for 2 h, the samples prepared with Vc changed to materials with large proportions of mesopores and small proportions of macropores, and with surface areas of 45-60 m<sup>2</sup>/g. The adsorption-desorption isotherm of the sample prepared without Vc is still microporous, with a lower surface area of 96.7 m<sup>2</sup>/g.



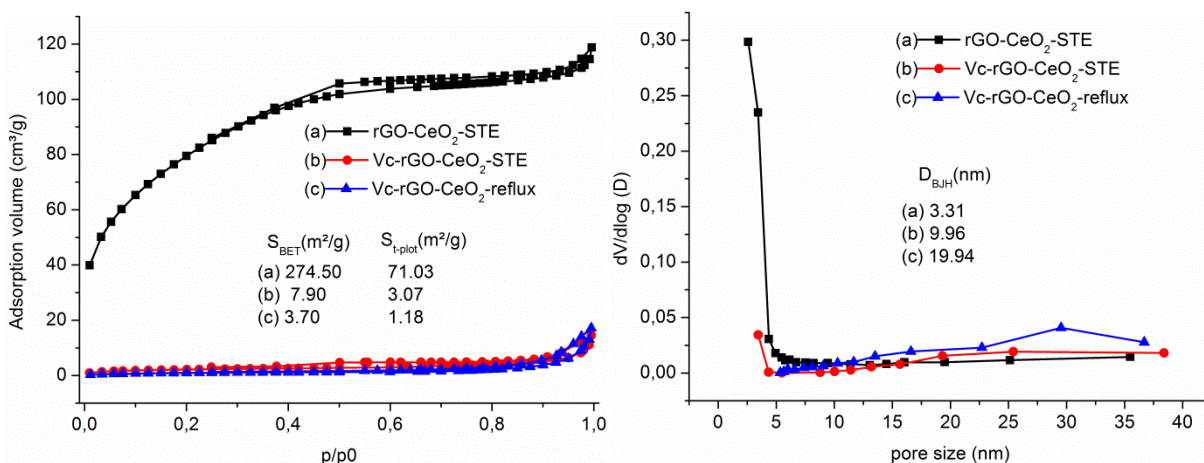


**Figure 4.16** N<sub>2</sub> adsorption-desorption isotherms (left) and pore size distributions (right) for as-prepared Vc-rGO-CeO<sub>2</sub>

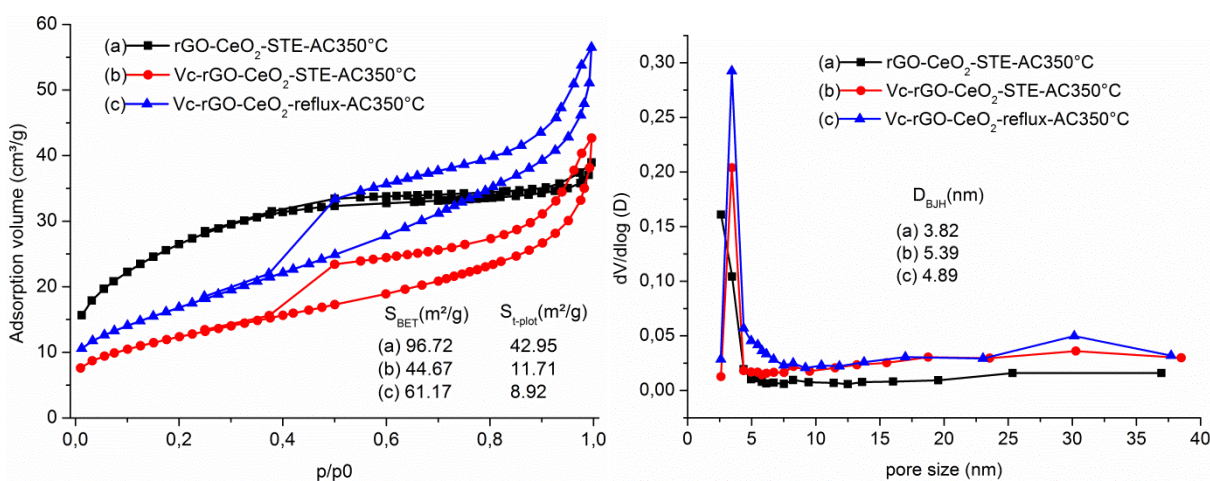


**Figure 4.17** N<sub>2</sub> adsorption-desorption isotherms (left) and pore size distributions (right) for as-prepared Vc-rGO-CeO<sub>2</sub> after calcination at 350 °C for 2 h

As the refluxing process did not give a better quality of rGO than STE, only rGO-CeO<sub>2</sub>-STE samples prepared without and with Vc were characterized by (HR)TEM, as shown in Figure 4.18. The dark grey areas belong to rGO. rGO-CeO<sub>2</sub>-STE (Figure 4.18 (a)) showed graphene with smaller size when compared with that of Vc- rGO-CeO<sub>2</sub>-STE (Figure 4.18 (b)). The distribution of CeO<sub>2</sub> on rGO is somewhat different for the two samples. In both samples the CeO<sub>2</sub> particles were not homogeneously dispersed on rGO, but the sample prepared without Vc was more inhomogeneous. It can be seen from Figure 4.18 (a') that some agglomerates or big particles

were formed and deposited on rGO, and a few free CeO<sub>2</sub> nanoparticles were even found outside the rGO. From Figure 4.18 (b') it can be seen the rGO consists of 3-4 layers.

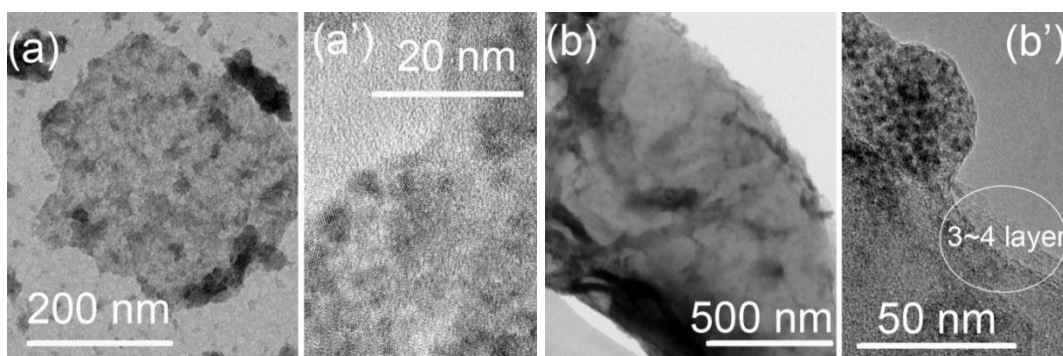


**Figure 4.18** (HR)TEM of rGO(0.02 g)-CeO<sub>2</sub>-STE samples (a, a') and Vc(1 g)-rGO(0.02 g)-CeO<sub>2</sub>-STE (b, b')

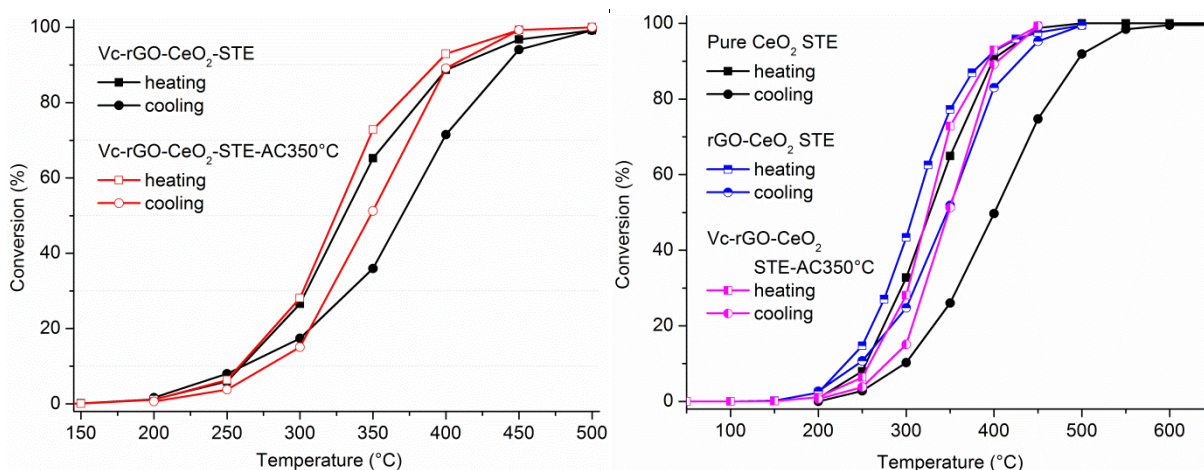


**Figure 4.19** CO conversion over Vc(1 g)-rGO(0.02 g)-CeO<sub>2</sub>-STE samples with different treatment (left) and comparison with CeO<sub>2</sub> samples synthesized under different conditions (right)

The sample Vc-rGO-CeO<sub>2</sub>, both after STE and STE-AC350 °C treatments, were tested for CO oxidation, as shown in Figure 4.19 left. It can be seen the STE-AC350 °C samples have slightly better catalytic activity, which may be due to a cleaner surface and higher surface area compared with the STE samples. As the catalytic activity is almost the same for both Vc-rGO-CeO<sub>2</sub>-STE and STE-AC350°C, Vc-rGO-CeO<sub>2</sub>-STE-AC350°C was used for comparisons with CeO<sub>2</sub>-STE and rGO-CeO<sub>2</sub>-STE samples, as shown in Figure 4.19 right. Vc-rGO-CeO<sub>2</sub>-STE-AC350°C and rGO-CeO<sub>2</sub>-STE have slightly better CO oxidation activity than pure CeO<sub>2</sub> STE. When the

reaction rate of CO oxidation at 250 °C per gram ( $r_{250^{\circ}\text{C}}$ ) was calculated and compared with the previous samples (Table 4.1 and Table 4.2),  $r_{250^{\circ}\text{C}}$  of Vc-rGO-CeO<sub>2</sub> samples is almost in the same range (in the order of  $10^{-6}$ ) as the values of rGO-CeO<sub>2</sub>-STE and CeO<sub>2</sub>-STE. But for the normalized specific reaction rates of CO oxidation on a unit surface area at 250 °C ( $R_{250^{\circ}\text{C}}$ ), the Vc-rGO-CeO<sub>2</sub>-STE samples (with  $10^{-7}$  order in Table 4.2) improved almost one order of magnitude compared to the other samples (with  $10^{-8}$  order in Table 4.1) due to the low surface area.

**Table 4.2** Summary of CO conversion for Vc-rGO-CeO<sub>2</sub> samples with different treatment

Sample	<sup>a</sup> S <sub>BET</sub> (m <sup>2</sup> /g)	<sup>b</sup> Weight loss (%)	<sup>c</sup> T <sub>10%</sub> (°C)	<sup>d</sup> T <sub>90%</sub> (°C)	<sup>e</sup> r <sub>250°C</sub> (mol/s·g)	<sup>f</sup> R <sub>250°C</sub> (mol/s·m <sup>2</sup> )
Vc-rGO-CeO <sub>2</sub> STE	7.9	43.88	260	408	4.78×10 <sup>-6</sup>	6.05×10 <sup>-7</sup>
Vc-rGO-CeO <sub>2</sub> STE-AC350°C	44.67*	5.33	258	392	5.08×10 <sup>-6</sup>	1.14×10 <sup>-7</sup>

<sup>a</sup> BET surface area; error ± 5%

<sup>b</sup> weight loss from room temperature to 500°C

<sup>c</sup> Reaction temperature for 10% CO conversion

<sup>d</sup> Reaction temperature for 90% CO conversion

<sup>e</sup> Reaction rate of CO oxidation at 250 °C per gram

<sup>f</sup> Normalized specific reaction rates of CO oxidation on a unit surface area at 250 °C

### 4.3 Synthesis of rGO-Co<sub>3</sub>O<sub>4</sub>-CeO<sub>2</sub> composites

Previous results of section 4.2 had shown that the small amount of GO and the use of Vc can improve the dispersion and the quality of rGO. In this section, the GO amount was fixed to 0.02 g to synthesize a rGO-Co<sub>3</sub>O<sub>4</sub>-CeO<sub>2</sub> composite. The molar ratio of Ce:Co was fixed to 4:1. Vc was used as a reductive agent and solvothermal treatment was applied. The influence of the Vc amount was investigated.



The weight loss of the rGO-CO<sub>3</sub>O<sub>4</sub>-CeO<sub>2</sub> composite after Vc-STE treatment started at about 250 °C (Figure 4.20 left). The weight loss increased along with the increasing Vc amount, from 12.1% (Vc=0 g) to 41.7% (Vc=1 g). Almost all of the rGO was removed at 350 °C. The sample calcined at 350 °C for 2 h therefore showed only little weight loss, which may be caused by carbonate adsorbed on the sample surface.

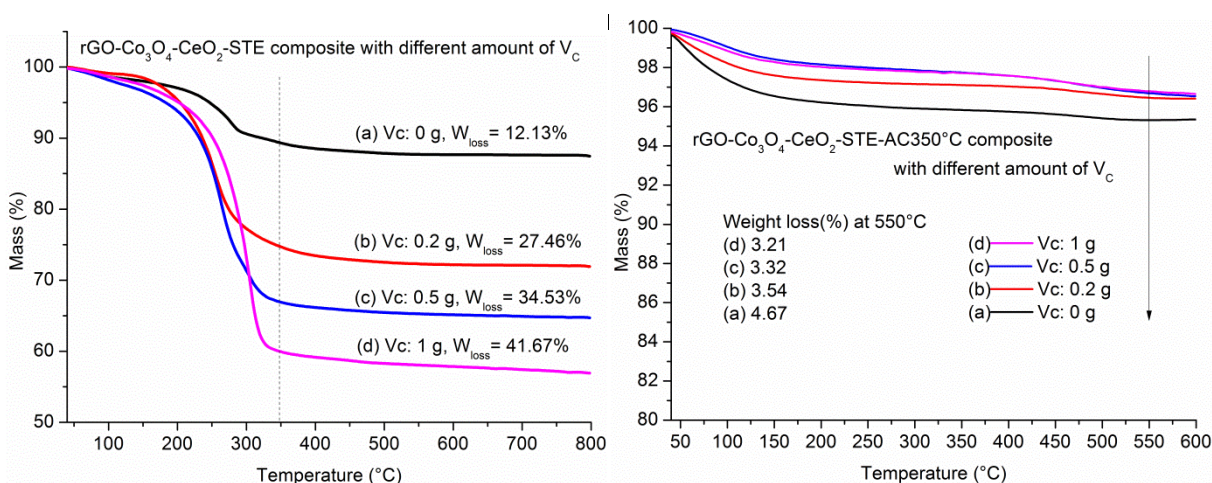


**Figure 4.20** TGA curves of rGO-CO<sub>3</sub>O<sub>4</sub>-CeO<sub>2</sub> composites prepared with different amounts of Vc after STE (left) and STE-AC350°C (right) treatment

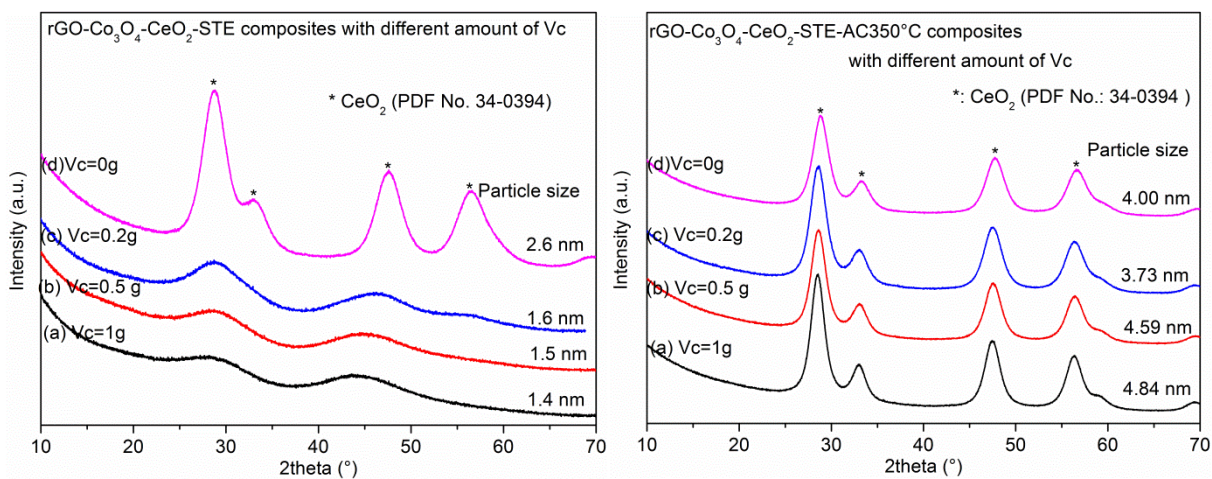


**Figure 4.21** XRD patterns of rGO-CO<sub>3</sub>O<sub>4</sub>-CeO<sub>2</sub> composites prepared with different amounts of Vc after STE (left) and STE-AC350°C (right) treatment

The XRD patterns (Figure 4.21 left) also showed that the use of Vc could inhibit the growth of the crystallite phases, similar to the Vc-rGO-CeO<sub>2</sub>-STE samples. The more Vc was used, the



smaller the CeO<sub>2</sub> crystallites were for rGO-Co<sub>3</sub>O<sub>4</sub>-CeO<sub>2</sub>-STE. The crystallite sizes of rGO-Co<sub>3</sub>O<sub>4</sub>-CeO<sub>2</sub>-STE composites were in the range of 1.4 nm (Vc=1 g) ~ 2.6 nm (Vc=0 g). Interestingly, although Co<sub>3</sub>O<sub>4</sub>-CeO<sub>2</sub> without rGO showed both Co<sub>3</sub>O<sub>4</sub> and CeO<sub>2</sub> crystalline phases after both STE and STE-AC treatment by route 1, the rGO-Co<sub>3</sub>O<sub>4</sub>-CeO<sub>2</sub> composites showed no indication of a crystalline Co<sub>3</sub>O<sub>4</sub> phase even after calcination at 350 °C for 2 h. After calcination at 350 °C for 2 h, the size of the CeO<sub>2</sub> crystallites increased to 3.7-4.8 nm, and the more Vc was used, the larger the crystallite size of the rGO-Co<sub>3</sub>O<sub>4</sub>-CeO<sub>2</sub>-STE-AC350°C was.

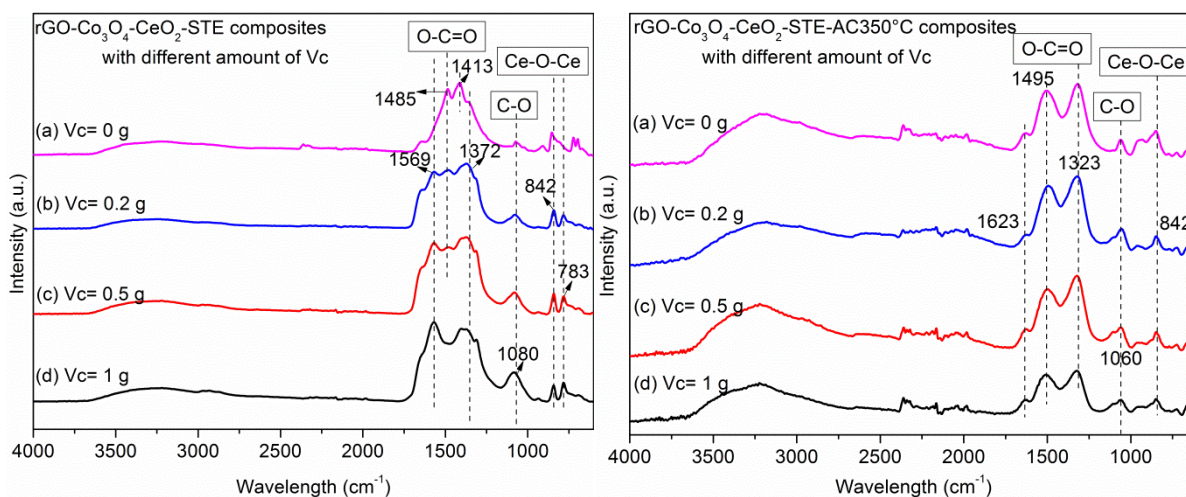


**Figure 4.22** IR spectra of rGO-Co<sub>3</sub>O<sub>4</sub>-CeO<sub>2</sub> composites prepared with different amounts of Vc after STE (left) and STE-AC350°C (right) treatment

The IR spectra of all Vc-STE treated rGO-Co<sub>3</sub>O<sub>4</sub>-CeO<sub>2</sub> composites are similar (Figure 4.22 left (b-d)), with strong bands at 1569 cm<sup>-1</sup> and 1372 cm<sup>-1</sup>, which belong to COO groups. The one synthesized without Vc showed a small difference (Figure 4.22 left (a)), with the strongest bands at 1485 cm<sup>-1</sup> and 1413 cm<sup>-1</sup>. These two bands also belong to COO groups; the difference is perhaps due to a different coordination situation. After calcination at 350 °C for 2 h (Figure 4.22 right), all samples have similar IR spectra, indicating the same carbonate species are on the surfaces.

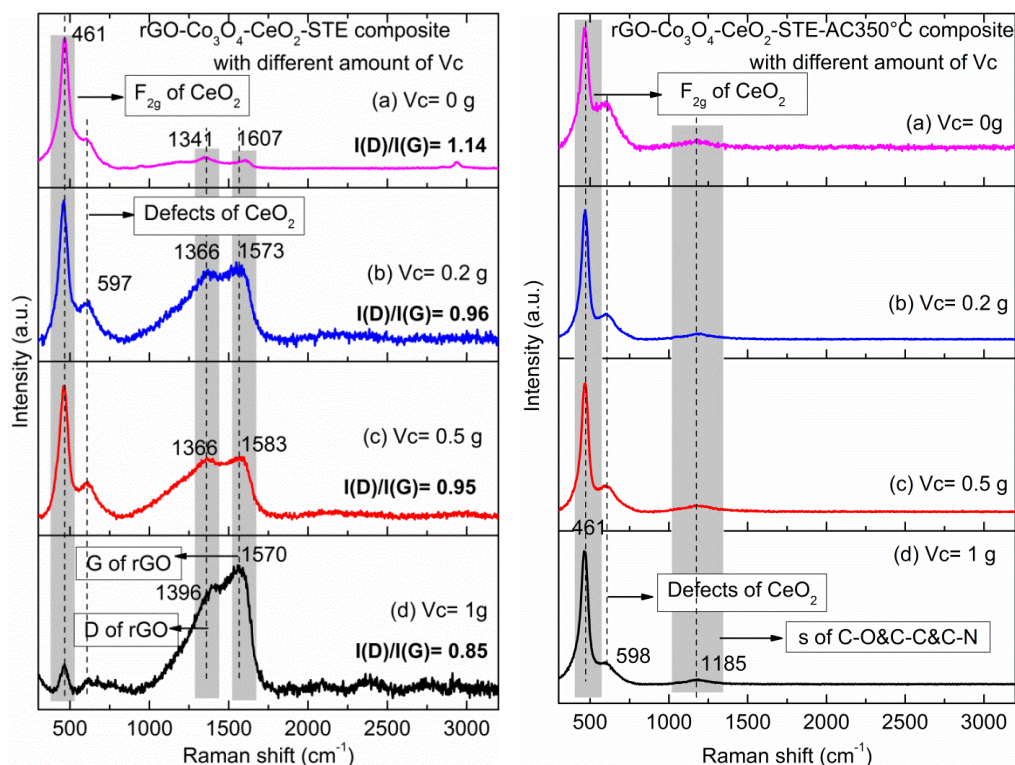


**Figure 4.23** Raman spectra of rGO-CO<sub>3</sub>O<sub>4</sub>-CeO<sub>2</sub> composites prepared with different amounts of Vc after STE (left) and STE-AC350°C (right) treatment

Similar spectra for the different samples were also observed with Raman spectroscopy (Figure 4.23). The Vc-STE samples (Figure 4.23 left (b-d)) showed stronger bands for rGO than the STE sample prepared without Vc (Figure 4.23 left (a)), indicating more rGO was formed when Vc was used, although the GO amount was the same. This is consistent with the weight loss in Figure 4.20. It can be seen that the D-bands for the Vc-STE samples are at around 1360 cm<sup>-1</sup> and the G-bands at around 1580 cm<sup>-1</sup>, as reported before [141]. For the sample prepared without Vc, the D-band and G-band are at 1341 cm<sup>-1</sup> and 1607 cm<sup>-1</sup> respectively, similar to the rGO-CeO<sub>2</sub>-STE samples in section 4.2.1. When compared with the bands of GO (D band: 1350 cm<sup>-1</sup>, G band: 1590 cm<sup>-1</sup>), the D-bands of Vc-STE samples are shifted to higher wavenumbers, while the G-bands are shifted to lower wavenumbers. The lower shifting of the G-bands indicates the formation of rGO, and the higher shifting of the D-bands is caused by the anchoring of CeO<sub>2</sub> particles (pure or modified by CO<sub>3</sub>O<sub>4</sub>) on rGO. This is reverse to the sample prepared without Vc, which shows a lower shift of the D-band and a higher shift of the G-band. The difference may be due to different amounts of rGO defects, as indicated by the intensity ratio I(D)/I(G). The value

of the I(D)/I(G) ratio increased with the decrease of the Vc amount. As I(D)/I(G) is a measure of disordered carbon, as expressed by the sp<sup>3</sup>/sp<sup>2</sup> carbon ratio, an increase of I(D)/I(G) means the degradation of the crystallinity of graphitic materials [96]. The increase of I(D)/I(G) is usually explained as a decrease in the average size but an increase of the numbers of defects of graphite (in the number of sp<sub>2</sub> domains) upon reduction [94]. Thus the defects of rGO were decreased with an increasing amount of Vc.

After calcination at 350°C for 2h, the rGO characteristic bands disappeared and only a weak band was seen at 1185 cm<sup>-1</sup>, which belongs to the C-O&C-C&C-N stretch. Besides the bands of carbon species, the characteristic band of CeO<sub>2</sub> was also observed at 461 cm<sup>-1</sup>. There was also a small shoulder at about 600 cm<sup>-1</sup>, which corresponds to the defects of CeO<sub>2</sub>, caused by oxygen vacancies [78, 145]. The defect band was more pronounced for the STE-AC350°C sample prepared without Vc, indicating that more oxygen vacancies were formed.

rGO-Co<sub>3</sub>O<sub>4</sub>-CeO<sub>2</sub> samples synthesized with different amounts of GO were also characterized by N<sub>2</sub> adsorptions before and after calcination at 350 °C for 2 h, as shown in Figure 4.24 and Figure 4.25. All the isotherms, except the one prepared without Vc, are typical for mesoporous materials. The isotherms of sample prepared without Vc is characteristic of a microporous material. The surface area increased with the decreasing amount of Vc for both STE and STE-AC350°C samples, from 47.4 to 161.8 m<sup>2</sup>/g for STE samples and from 60.3 to 99.8 m<sup>2</sup>/g for STE-AC350°C samples. Except the sample prepared with 1 g Vc, all the other STE-AC350°C have an about 60 m<sup>2</sup>/g smaller surface area than the corresponding STE samples. For the sample prepared with 1 g Vc, the STE-AC-350°C sample has even a slightly larger surface area (60.3 m<sup>2</sup>/g) than the STE sample (47.4 m<sup>2</sup>/g), which is consistent with the Vc-rGO-CeO<sub>2</sub> sample in section 4.2.2. Compared with Vc-rGO-CeO<sub>2</sub>, adding of the Co precursor changed the isotherms from nonporous materials to mesoporous materials, and also increased the surface area of the STE sample.



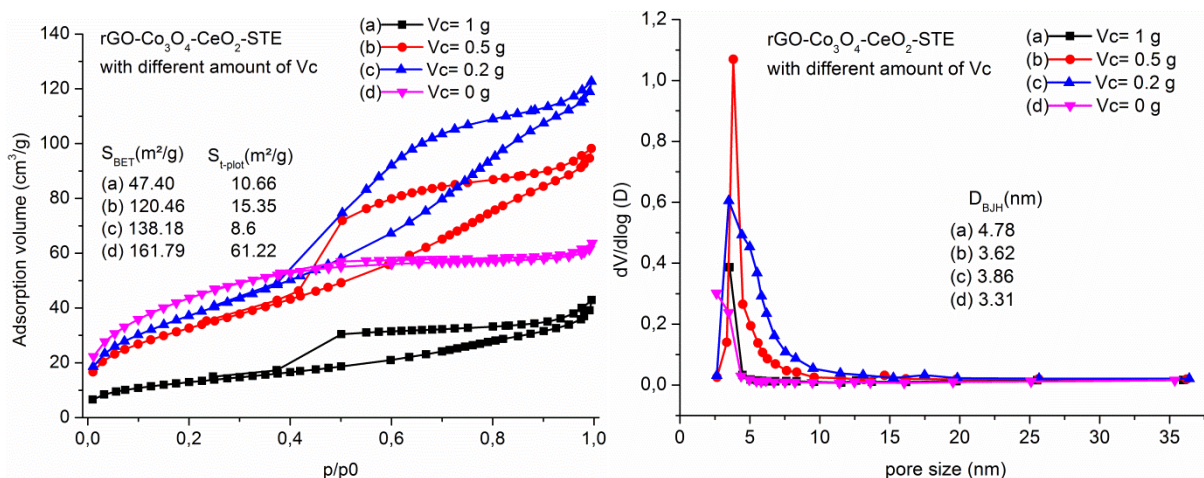


**Figure 4.24** N<sub>2</sub> adsorption-desorption isotherms (left) and pore size distributions (right) for rGO-Co<sub>3</sub>O<sub>4</sub>-CeO<sub>2</sub> composites prepared with different amounts of Vc after STE treatment

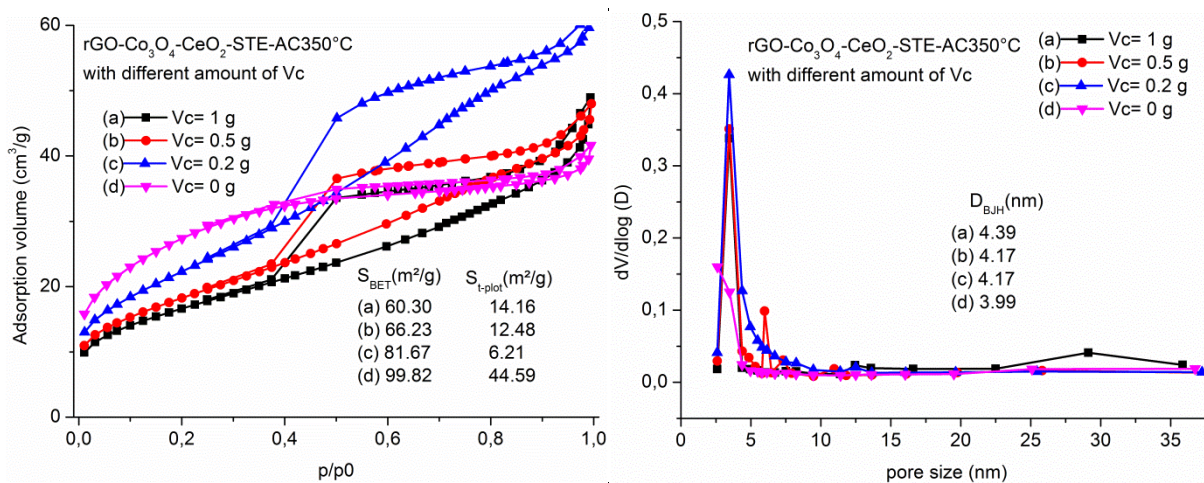


**Figure 4.25** N<sub>2</sub> adsorption-desorption isotherms (left) and pore size distributions (right) for rGO-Co<sub>3</sub>O<sub>4</sub>-CeO<sub>2</sub> composites prepared with different amounts of Vc after STE-AC350°C treatment

TEM measurements were carried out for the rGO-Co<sub>3</sub>O<sub>4</sub>-CeO<sub>2</sub>-STE samples synthesized with 0.2 g Vc and without Vc after STE treatment, as shown in Figure 4.26. It can be seen that the rGO-Co<sub>3</sub>O<sub>4</sub>-CeO<sub>2</sub>-STE samples synthesized with 0.2 g Vc (Figure 4.26 (a)) had a more homogeneous distribution of particles on rGO than the one without Vc (Figure 4.26 (b)), and the Co<sub>3</sub>O<sub>4</sub>-CeO<sub>2</sub> particles preferred to grow on rGO, although a few free particles can also be seen.

The rGO-Co<sub>3</sub>O<sub>4</sub>-CeO<sub>2</sub>-STE samples synthesized without Vc had agglomerates or big particles, similar to the rGO-CeO<sub>2</sub>-STE samples synthesized without Vc in section 4.2.2.

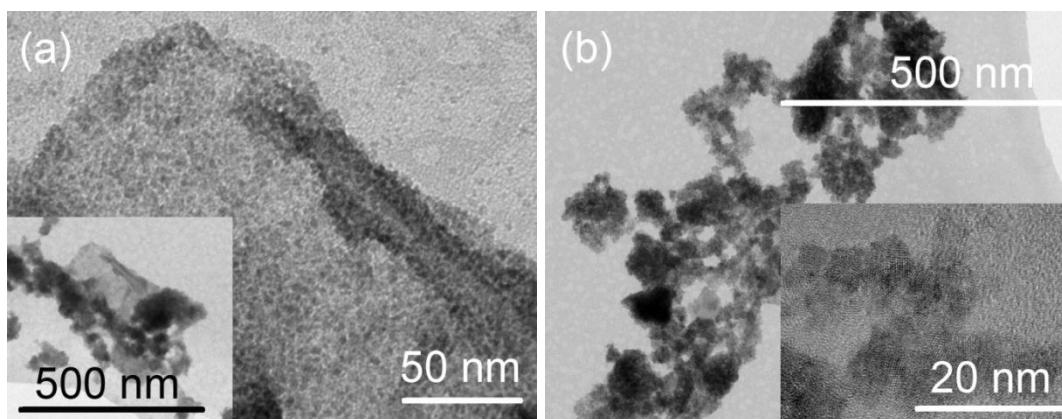


**Figure 4.26** TEM images of rGO-Co<sub>3</sub>O<sub>4</sub>-CeO<sub>2</sub> samples prepared with 0.2 g Vc (a) and without Vc (b) after STE treatment, the inserted images are of the same sample but with different magnification

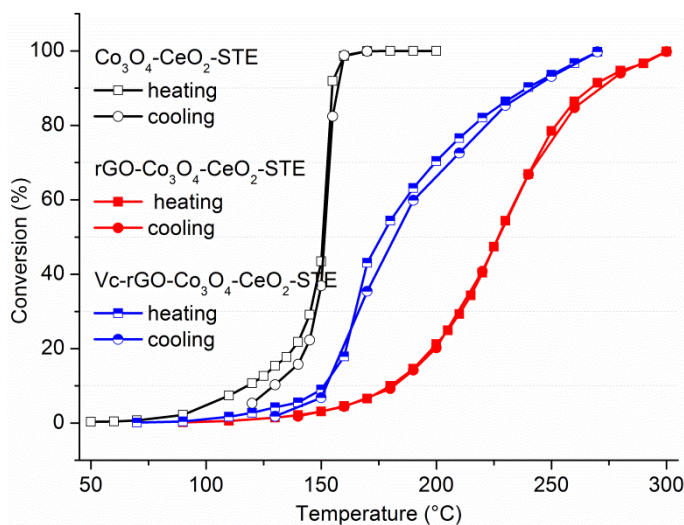


**Figure 4.27** CO conversion over rGO -Co<sub>3</sub>O<sub>4</sub>-CeO<sub>2</sub> samples prepared with 0.2 g Vc (sample Vc-rGO-Co<sub>3</sub>O<sub>4</sub>-CeO<sub>2</sub>) and without Vc (sample rGO-Co<sub>3</sub>O<sub>4</sub>-CeO<sub>2</sub>) after STE treatment. The CO oxidation of Co<sub>3</sub>O<sub>4</sub>-CeO<sub>2</sub> without rGO is also given for comparison

The rGO -Co<sub>3</sub>O<sub>4</sub>-CeO<sub>2</sub> samples prepared with 0.2 g Vc (sample Vc-rGO-Co<sub>3</sub>O<sub>4</sub>-CeO<sub>2</sub>) and without Vc (sample rGO-Co<sub>3</sub>O<sub>4</sub>-CeO<sub>2</sub>) were tested for CO oxidation, as shown in Figure 4.27. Vc-rGO-Co<sub>3</sub>O<sub>4</sub>-CeO<sub>2</sub> showed a better catalytic activity than rGO-Co<sub>3</sub>O<sub>4</sub>-CeO<sub>2</sub>, which proved

that Vc can improve the quality of rGO to benefit the CO oxidation. But both the rGO composited Co<sub>3</sub>O<sub>4</sub>-CeO<sub>2</sub> samples had worse performance than Co<sub>3</sub>O<sub>4</sub>-CeO<sub>2</sub> prepared without rGO, which is also reflected by T<sub>10%</sub>, T<sub>90%</sub> and the reaction rate r<sub>130°C</sub> listed in Table 4.4. This may be caused by two reasons: (1) the rGO composited Co<sub>3</sub>O<sub>4</sub>-CeO<sub>2</sub> samples had lower surface area than the sample prepared without rGO; (2) rGO trapped Co<sub>3</sub>O<sub>4</sub>, thus only small amount of Co<sub>3</sub>O<sub>4</sub> could interact with CeO<sub>2</sub>.

**Table 4.3** Summary of CO conversion for rGO -Co<sub>3</sub>O<sub>4</sub>-CeO<sub>2</sub> samples prepared with 0.2g Vc and without Vc after STE treatment

Sample	<sup>a</sup> S <sub>BET</sub> (m <sup>2</sup> /g)	<sup>b</sup> Weight loss (%)	<sup>c</sup> T <sub>10%</sub> (°C)	<sup>d</sup> T <sub>90%</sub> (°C)	<sup>e</sup> r <sub>130°C</sub> (mol/s·g)	<sup>f</sup> R <sub>130°C</sub> (mol/s·m <sup>2</sup> )
rGO-Co <sub>3</sub> O <sub>4</sub> -CeO <sub>2</sub> STE	161.79	12.13	179	266	2.28×10 <sup>-6</sup>	1.41×10 <sup>-8</sup>
Vc-rGO-Co <sub>3</sub> O <sub>4</sub> -CeO <sub>2</sub> STE	138.18	27.46	151	239	6.81×10 <sup>-6</sup>	4.93×10 <sup>-8</sup>
Co <sub>3</sub> O <sub>4</sub> -CeO <sub>2</sub> STE	216.50	11.80	117	155	2.48×10 <sup>-5</sup>	1.14×10 <sup>-7</sup>

<sup>a</sup> BET surface area; error ± 5%

<sup>b</sup> weight loss from room temperature to 500 °C

<sup>c</sup> Reaction temperature for 10% CO conversion

<sup>d</sup> Reaction temperature for 90% CO conversion

<sup>e</sup> Reaction rate of CO oxidation at 130 °C per gram

<sup>f</sup> Normalized specific reaction rates of CO oxidation on a unit surface area at 130 °C

#### 4.4 Conclusion

rGO was introduced into the CeO<sub>2</sub> and Co<sub>3</sub>O<sub>4</sub>-CeO<sub>2</sub> (Co:Ce=1:4) system, which were synthesized by the combination of sol-gel and solvothermal processing. The influence of the rGO amount and Vc as reductive agent on the structure of CeO<sub>2</sub> materials were investigated. The influence of the Vc amount on the structure of Co<sub>3</sub>O<sub>4</sub>- CeO<sub>2</sub> materials was also studied.

For rGO-CeO<sub>2</sub> composites, the rGO amount was adjusted from 0.2 g to 0.02 g per 5 mmol of CeO<sub>2</sub>. The crystallite size of CeO<sub>2</sub> decreased from 2.6 nm to 1.9 nm along with a decreasing rGO amount, while the surface area increased from 146.6 to 274.5 m<sup>2</sup>/g. The Raman spectra showed that rGO can be formed using EtOH as reductive agent, but with more defects on rGO. When the rGO amount was too high, rGO agglomerates formed. The TGA and Raman results indicated that all rGO components were removed when the samples were calcined at 350 °C for 2 h. The chosen rGO(0.05 g)-CeO<sub>2</sub>-STE sample showed better catalytic activity than a CeO<sub>2</sub>-STE sample.

In order to improve the quality of rGO, 1 g Vc was added additionally as reductive agent to synthesize rGO-CeO<sub>2</sub> composites, and both solvothermal treatment in EtOH and refluxing processing were tested. Raman results showed that solvothermal treatment can give rGO with better quality than refluxing, and rGO with fewer defects are formed with Vc. But the sample synthesized with Vc had a higher proportion of organic residues and a much lower surface area than those of samples synthesized without Vc.

Thus, the Vc amount was changed during the synthesis of rGO-Co<sub>3</sub>O<sub>4</sub>-CeO<sub>2</sub>. Along with the decrease of the Vc amount from 1 g to 0 g, the organic residues reduced from 41.7% to 12.1%, the CeO<sub>2</sub> crystallite size increased from 1.4 nm to 2.6 nm, the defects of rGO increased (because the I(D)/I(G) value of Raman spectra increased from 0.85 to 1.14), and the surface area increased from 47.4 to 161.8 m<sup>2</sup>/g. No crystalline Co<sub>3</sub>O<sub>4</sub> phases were observed for all rGO-Co<sub>3</sub>O<sub>4</sub>-CeO<sub>2</sub> samples, even after calcination at 350 °C for 2 h. This may be because the Co-containing species were dispersed on rGO, and 350 °C was not high enough to crystallize Co<sub>3</sub>O<sub>4</sub>, or the Co<sub>3</sub>O<sub>4</sub> crystallite phase is too small to be detected. Thus the CO oxidation activities of rGO-Co<sub>3</sub>O<sub>4</sub>-CeO<sub>2</sub> composites were lower than that of Co<sub>3</sub>O<sub>4</sub>-CeO<sub>2</sub> without rGO.



## 5. Summary

This thesis focused on the synthesis of CeO<sub>2</sub>-based materials (modified by Co<sub>3</sub>O<sub>4</sub> and/or graphene) by the sol-gel method starting from cerium tetra-butoxide. Different parameters were adjusted in order to get materials with high catalytic properties for CO oxidation.

First, pure CeO<sub>2</sub> was synthesized to elucidate the optimized parameters. It was found that the use of cerium alkoxides (CeB) as sol-gel precursor for ceria has clear advantages compared with (NH<sub>4</sub>)<sub>2</sub>[Ce(NO<sub>3</sub>)<sub>6</sub>] (CAN), resulting in CeO<sub>2</sub> with high yield and high surface area (Figure 5.1). Gels were prepared from acetaldoximate-substituted cerium *t*-butoxide in the presence of the surfactant F127. The latter served to create interparticle porosity after calcination. However, the post-synthesis treatment of the obtained gels had a larger influence on the resulting specific surface area than the composition of the starting mixture. Solvothermal treatment in either ethanol or water resulted in materials with distinctly higher specific surface areas and smaller crystallite sizes than by calcination alone. Specific surface areas of up to 277 m<sup>2</sup>/g were obtained which is unprecedented for ceria (commercial ceria ranges around 2 m<sup>2</sup>/g). Post-synthesis calcination of the gels allowed removing of the residual organic groups. Both the solvent used for solvothermal treatment and the calcination process can influence the Ce<sup>3+</sup>/Ce<sup>4+</sup> ratio. The highest Ce<sup>3+</sup> proportion was 18% for CeB/AO/F127-STE-AC.

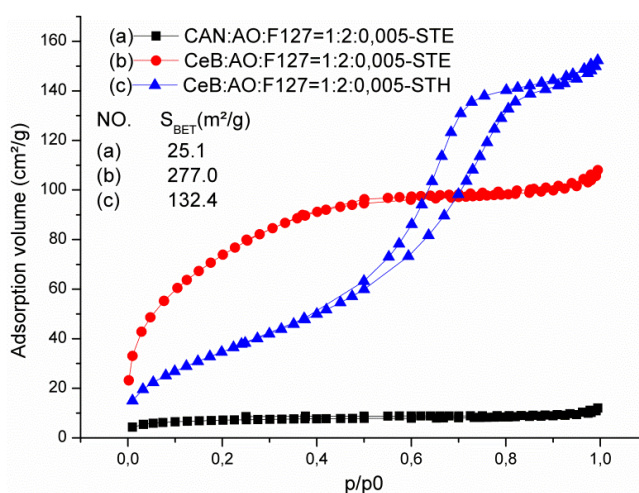


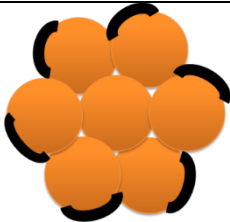
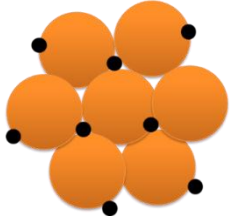
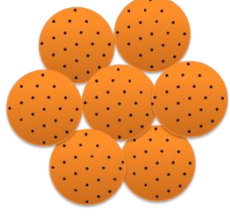
**Figure 5.1** N<sub>2</sub> adsorption-desorption isotherms of CeO<sub>2</sub> prepared from different precursors (CeB or CAN) and solvothermally treated in different solvents (STE: ethanol, STH: H<sub>2</sub>O)

Tests of CO oxidation on selected samples indicated that a high catalytic activity is related to a high surface area and the surface groups created by the post-synthesis treatment. With regard to the latter, solvothermal treatment of the samples in ethanol proved to be particularly efficient, because of abundant OH groups and graphene-like residues. The sample with the highest surface area ( $277 \text{ m}^2/\text{g}$ ) from solvothermal treatment with ethanol outperformed commercial ceria by a factor of 75.

Thus the samples were subsequently prepared by a combination of sol-gel and solvothermal processing. As the kind and amount of the organic residues was closely related to the solvothermal solvent rather than the gel composition, and the sample treated in ethanol showed better properties (higher surface area, higher  $\text{Ce}^{3+}$  proportion, more OH group and with graphene-like organic residues) than that treated in  $\text{H}_2\text{O}$ , the solvothermal solvent was fixed to ethanol and the solvothermal parameters (temperature and time) were adjusted to study their influence on the materials properties. Both the changes of solvothermal temperature and time had almost no influence on the size of crystalline  $\text{CeO}_2$  and the weight loss during calcination, but have a big effect on the surface area of the material. The higher the solvothermal temperature (up to  $200 \text{ }^\circ\text{C}$ ) and the shorter the reaction time was (ca. 6 h), the larger the surface area became (up to  $277 \text{ m}^2/\text{g}$ ).

The combination of sol-gel and solvothermal processing was adopted to synthesize  $\text{Co}_3\text{O}_4$  modified  $\text{CeO}_2$  (Co : Ce = 1:4), to lower the ignition temperature of  $\text{CeO}_2$  in CO oxidation processing. The route by which Co was introduced clearly influenced the morphology of the composites on the nanoscale. Using the single-source precursor Ce-POBC-Co resulted in a very homogeneous dispersion of Co oxide in the ceria matrix (samples **3**). When a pre-formed ceria gel was impregnated with  $\text{Co}(\text{OAc})_2$  under solvothermal conditions (samples **1**),  $\text{Co}_3\text{O}_4$  particles were located on the surface of the  $\text{CeO}_2$  particles or agglomerates thereof. Only in this case weak XRD reflections of  $\text{Co}_3\text{O}_4$  were already observed after solvothermal treatment, in contrast to **2**-STE and **3**-STE. In the third variation, i.e. sol-gel co-processing of CeB and  $\text{Co}(\text{OAc})_2$ , followed by solvothermal treatment, an intimate mixture of  $\text{CeO}_2$  and  $\text{Co}_3\text{O}_4$  particles was obtained (samples **2**). The different structures obtained by different preparation routes are sketched in Table 5. 1.

**Table 5. 1** Suggested structure of  $\text{Co}_3\text{O}_4$  modified  $\text{CeO}_2$  samples from different preparation routes (yellow:  $\text{CeO}_2$ , black:  $\text{Co}_3\text{O}_4$ )

Route	Procedure	Structure
1	$\text{Ce sol} \rightarrow \text{sol-gel} \rightarrow \text{Ce gel} \rightarrow \text{autoclave+gel} + \text{Co(OAc)}_2$	
2	$\text{Ce+Co sol} \rightarrow \text{sol-gel} \rightarrow \text{Ce+Co gel} \rightarrow \text{autoclave+gel}$	
3	$\text{Ce-POBC-Co sol} \rightarrow \text{sol-gel} \rightarrow \text{Ce+Co gel} \rightarrow \text{autoclave+gel}$	

The results clearly showed that these variations of the synthesis route resulted in three different morphologies on the nanoscale, despite the same Co : Ce ratio, the same metal precursors and the same processing steps (sol-gel processing + solvothermal treatment). The distribution of Co influenced the  $\text{CeO}_2$  crystallite size, surface area, organic residues and catalytic activity. **1-STE** with small  $\text{Co}_3\text{O}_4$  particles finely dispersed on the surface of  $\text{CeO}_2$  particles exhibited the highest activity for CO oxidation, with apparent activation energy of  $47.4 \pm 0.3$  kJ/mol. This is comparable to ceria-supported noble metals. The outcome of the work can be generalized in a way that fine-tuning of the synthesis parameters allows adjustment of a specific catalyst (composite) morphology on the nanoscale, which implications on the materials and catalytic properties.

The Co proportion was varied from 10% to 80% for the route **1** procedure. Along with an increased Co proportion, the surface area of the materials decreased, while the proportion of

crystalline  $\text{Co}_3\text{O}_4$  and the catalytic activity of the materials increased. When the catalytic reaction rates were normalized on the basis of the unit amount of Co ( $R_{\text{Co}110^\circ\text{C}}$ ), the  $R_{\text{Co}110^\circ\text{C}}$  values were almost the same when the Co% was lower than 30%, about  $32 \pm 1$  mmol CO/mmol Co·h. But when the Co% increased to 80%, the  $R_{\text{Co}110^\circ\text{C}}$  value was only 9.14 mmol CO/mmol Co·h, which may be attributed to the agglomeration of  $\text{Co}_3\text{O}_4$  crystallites.

As graphene-like organic residues were found after  $\text{CeO}_2$  and  $\text{Co}_3\text{O}_4\text{-CeO}_2$  solvothermal treatment in ethanol, graphene (rGO) was introduced into the  $\text{CeO}_2$  and  $\text{Co}_3\text{O}_4\text{-CeO}_2$  (Co:Ce=1:4) system. The influence of the rGO amount and L-ascorbic acid as reductive agent on the structure of  $\text{CeO}_2$  materials were investigated, while the influence of the amount of L-ascorbic acid on the structure of  $\text{Co}_3\text{O}_4\text{-CeO}_2$  materials was studied. For rGO- $\text{CeO}_2$  composites, the rGO amount was varied from 0.2 g to 0.02 g per 5 mmol of  $\text{CeO}_2$ . The crystallite size of the  $\text{CeO}_2$  decreased from 2.6 nm to 1.9 nm when the amount of rGO was reduced, while the surface area increased from 146.6 to 274.5  $\text{m}^2/\text{g}$ . Raman spectroscopy showed that the rGO can be formed only by using EtOH as reductive agent, but with more defects on rGO. When the rGO amount was too high, rGO agglomerated. TGA and Raman results indicated that all rGO components were removed when the samples were calcined at 350 °C for 2 h. The chosen rGO(0.05 g)- $\text{CeO}_2\text{-STE}$  sample showed better catalytic activity than  $\text{CeO}_2\text{-STE}$ .

In order to improve the quality of rGO, L-ascorbic acid was added additionally as reductive agent to synthesize rGO- $\text{CeO}_2$  and rGO- $\text{Co}_3\text{O}_4\text{-CeO}_2$  composites. This can improve the quality of rGO, but results in more organic residues and inhibits particle growth. The L-ascorbic acid amount was varied from 1 g to 0 g for rGO- $\text{Co}_3\text{O}_4\text{-CeO}_2$ . Along with decreasing amount of L-ascorbic acid, the organic residues were reduced from 41.7% to 12.1%, the  $\text{CeO}_2$  crystallite size increased from 1.4 nm to 2.6 nm, the defects of rGO increased ( $I(\text{D})/I(\text{G})$  of Raman spectra increased from 0.85 to 1.14), and the surface area increased from 47.4 to 161.8  $\text{m}^2/\text{g}$ . No crystalline  $\text{Co}_3\text{O}_4$  phases were observed for all rGO- $\text{Co}_3\text{O}_4\text{-CeO}_2$  samples, even after calcination at 350 °C for 2 h. CO oxidation showed that the rGO- $\text{Co}_3\text{O}_4\text{-CeO}_2$  composites were less catalytic active than that of  $\text{Co}_3\text{O}_4\text{-CeO}_2$ .

## 6. Experimental section

### 6.1 Characterization

#### 6.1.1 Materials structure characterization

**Thermogravimetric analysis (TGA)** was performed on a Netzsch Iris TG 209 C in a platinum crucible with a heating rate of 10 °C/min under synthetic air.

**Infrared spectra (IR)** were recorded on a Bruker Tensor 27 working in ATR Micro Focusing MVP-QL with a ZnSe crystal, using OPUS software version 4.0 for analysis.

**X-Ray powder diffraction (XRD)** measurements were performed on a Philips X'Pert diffractometer using Cu-K $\alpha$  radiation ( $\lambda=1.5406$  Å).

**Scanning electron micrographs (SEM)** were obtained on a Quanta 200 (FEI) equipped with a Genesis (EDAX) energy dispersive spectrometer, with a voltage of 7.5 kV.

**X-ray Photoelectron Spectra (XPS)** were measured on a Specs XPS system (XR 50 Mg/Al-Dual Anode, PHOIBOS 150 hemispherical analyser).

**Nitrogen sorption** measurements were performed on an ASAP 2020 (Micromeritics). The samples were degassed in vacuum at 80 °C for at least 5 h prior to measurement. The total surface area was calculated according to Brunauer, Emmett and Teller (BET), and the pore size distribution (from the desorption branch) according to Barrett, Joyner and Halenda (BJH).

**DR UV–Vis spectra** were recorded in the range 200–800 nm with K<sub>2</sub>Cr<sub>2</sub>O<sub>7</sub> as reference using PerkinElmer Lambda 750 UV/Vis spectrophotometer. Kubelka-Munk function was used to transform the diffuse reflectance spectra to absorption spectra. The band gap energies were calculated from the UV-Vis adsorption data using Tauc plot [83].

**High resolution transmission electron micrographs (HRTEM)** were recorded on a TECNAI F20 operated at 200 kV. Before the measurements, the samples were ultrasonically dispersed in EtOH for 30 min, and then deposited on copper grids covered with carbon films.

**Small-angle X-ray scattering (SAXS)** was performed with Cu-K $\alpha$  radiation from a rotating anode generator (Nanostar from BRUKER AXS) equipped with a pinhole camera and an area detector (VANTEC 2000).

**Raman spectra & mapping** were collected on a Horiba Jobin Yvon Micro-Raman spectrometer (LabRam 800 HR) equipped with an integral Olympus BX 41 microscope (20f objective) and a Peltier-cooled CCD detector, using the 632.8 nm line of a He–Ne laser (1.5 mW) for excitation. A 600 line grating was used for obtaining the Raman spectra. The Raman–Stokes spectra were recorded in the 3200–300 cm $^{-1}$  range of Raman shifts at 1.3 cm $^{-1}$  spectral resolution;  $\nu$  in cm $^{-1}$ ; relative intensities are given in % of the most intense peak. The spectrograph was calibrated using a Si wafer at 520 cm $^{-1}$  Raman-shift.

### 6.1.2 Catalytic properties test

**CO temperature-programmed reaction (CO-TPR)** over ceria-based samples (ca. 20 mg) was performed in a continuous-flow fixed-bed quartz reactor under atmospheric pressure. The catalyst samples were pre-treated with synthetic air at 200 °C for 30 min (heating step 10 °C/min) at a flow rate of 50 ml/min. After cooling to room temperature the samples were exposed to a mixture of 5 vol% CO and 95 vol% He (total flow 50 ml/min) at room temperature. Then the temperature was increased to 800 °C with a heating rate of 10 °C/min. The gas stream was analyzed by an online quadrupole mass spectrometer (QMS) (Prisma Plus QMG 220, Pfeiffer Vacuum) equipped with a Faraday detector.

**CO oxidation** was performed in a continuous-flow fixed-bed quartz reactor under atmospheric pressure. The tests were carried out at two different modes for different samples:

- (1) *Pure CeO<sub>2</sub> or graphene-CeO<sub>2</sub> composite (without Co<sub>3</sub>O<sub>4</sub> phase)*: An amount of 20 mg of each sample was loaded into the reactor and pretreated with synthetic air (30 mL/min) at 200 °C for 40 min (heating rate 10 °C/min). Then the sample was cooled to 30 °C in flowing synthetic air, and a mixture of 5 vol% CO, 10 vol% O<sub>2</sub> and 85 vol% He (total flow 50 mL/min) was introduced. The system was then heated to 650 °C with a ramping rate of 5 °C·min $^{-1}$ . The concentrations of CO and CO<sub>2</sub> in the outlet streams were monitored by gas chromatography with a HP-PLOT Q column and a flame ionization detector.

(2) *Co<sub>3</sub>O<sub>4</sub> modified CeO<sub>2</sub> or graphene -Co<sub>3</sub>O<sub>4</sub> -CeO<sub>2</sub> composite (with Co<sub>3</sub>O<sub>4</sub> phase)*: A 10 mg of the sample, mixed with quartz in order to avoid mass and heat transfer limitations, was loaded into the reactor and pretreated with synthetic air (50 mL min<sup>-1</sup>) at 200 °C for STE samples or 400 °C for STE-AC for 30 min (heating rate 10 °C min<sup>-1</sup>). Then the sample was cooled to 30 °C in the flow of synthetic air and 5 vol.% CO, 12.5 vol.% O<sub>2</sub> and 82.5 vol% He mixture (total flow 50 mL min<sup>-1</sup>) was introduced. Then the temperature was increased to 250 °C with a rate of 2.5 °C·min<sup>-1</sup>. The concentrations of CO and CO<sub>2</sub> in the outlet streams were monitored by gas chromatograph with HP - PLOT Q column and a flame ionization detector.

## 6.2 Synthesis of pure CeO<sub>2</sub> samples

All solvents were dried by standard methods, and all experiments involving metal alkoxides were carried out under moisture- and oxygen-free argon using standard Schlenk or glove box techniques. (NH<sub>4</sub>)<sub>2</sub>[Ce(NO<sub>3</sub>)<sub>6</sub>] was obtained from Alfa-Aesar and used as received. Commercial CeO<sub>2</sub> powder from Aldrich was used for comparison.

### 6.2.1 Synthesis of cerium *tert*-butoxide

Cerium *tert*-butoxide (CeB) was synthesized according to literature from (NH<sub>4</sub>)<sub>2</sub>[Ce(NO<sub>3</sub>)<sub>6</sub>] (CAN) and potassium *tert*-butoxide (KO<sup>t</sup>Bu) in 1,2-dimethoxyethane(DME) [146, 147]. Typically, 10 mmol CAN was put in one Schlenk tube, and dried under vacuum (<10<sup>-3</sup> mbar) for more than 5h. Then 50mL DME was put in as a solvent. The solution was stirred for more than 30 min until it became a red orange and clear solution. In another Schlenk tube, 60 mmol KO<sup>t</sup>Bu was dissolved in 20 mL DME. Then the CAN solution was added to the KO<sup>t</sup>Bu solution dropwise and stirred strongly, as heat and NH<sub>3</sub> would be produced during this process. After all CAN solution was added, the mixture was a yellow turbid liquid. Then the mixture was further stirred overnight to get a complete reaction. The mixture was filtered to remove the white precipitate (KNO<sub>3</sub>), and the yellow to green liquid was heated to 80 °C to get rid of the DME solvent. The oily residue obtained after removal of the solvent was used directly for sol-gel processing without further purification. XPS spectra proved that the sample contained no residual potassium (from the preparation).



### 6.2.2 CeO<sub>2</sub> synthesized with different post-synthesis treatment

A sol was prepared from CeB : acetaldoxime(AO):F127: 1,2-dimethoxyethane (DME) in the ratio 1:2:0.005:40. In some reactions F127 was left out. In a typical experiment, 5 mmol of **CeB** was dissolved in 10 mL of DME, then 10 mmol of AO was added and the mixture was stirred for 30 min. Then 0.025 mmol of F127 was added and the mixture was additionally stirring for 1h. No water was added in this stage. The sol was then deposited onto glass sheets (20×30 cm<sup>2</sup>), which had been cleaned with 10% KOH, *i*PrOH and acetone and dried at 100 °C. The as-deposited films were exposed to ambient humidity at room temperature for 24 h. The obtained solids were then scraped off with a razor blade to get a gel powder. The gel powders were then treated by different methods:

- Calcination at 500 °C in air for 2 h in an Al<sub>2</sub>O<sub>3</sub> crucible; heating rate 2 °C/min (AC);
- Calcination at 500 °C in N<sub>2</sub> for 3 h in an Al<sub>2</sub>O<sub>3</sub> crucible, followed by calcination in air for 2 h; heating rate 2 °C/min (NAC).
- Solvothermal treatment at 200 °C for 6 h (ST) in a 60 mL autoclave with 30 mL solvent (gel prepared from 5 mmol **CeB**). Two different solvents were used, *viz.* EtOH (STE) and H<sub>2</sub>O (STH).
- Solvothermal treatment, followed by calcination as described for AC (ST-AC).

For comparison, (NH<sub>4</sub>)<sub>2</sub>[Ce(NO<sub>3</sub>)<sub>6</sub>] (**CAN**) was used instead of **CeB**. The synthesis protocol (see also Figure 2.1) was the same as described above. The labelling of the samples is as follows: precursor composition–calcination method. For example, CeB/AO/F127-AC is a sample prepared from CeB, AO and F127, followed by calcination in air (AC).

#### 6.2.2.1 Synthesis of CeB/AO/F127-AC

The gel powder, obtained as described at the beginning of section 6.2.2, was put into an Al<sub>2</sub>O<sub>3</sub> crucible, and heated to 500 °C with 2 °C/min in the air. After holding at 500 °C for 2 h, the sample was cooled naturally to room temperature.

$$D_{\text{XRD}}: 9.2 \text{ nm}; \quad S_{\text{BET}}: 12.8 \text{ m}^2/\text{g}; \quad D_{\text{BJH}}: 12.1 \text{ nm}$$

#### 6.2.2.2 Synthesis of CeB/AO/F127-NAC

The gel powder, obtained as described at the beginning of section 6.2.2, was put into a ceramic boat and transferred in a horizontal quartz tube. It was first calcined at 500 °C for 3 h in

N<sub>2</sub> with a ramping rate of 2 °C/min, and followed by calcination in air at 500 °C for 2 h. The sample was cooled naturally to room temperature.

$$\mathbf{D_{XRD}}: 8.6 \text{ nm}; \quad \mathbf{S_{BET}}: 20.1 \text{ m}^2/\text{g}; \quad \mathbf{D_{BJH}}: 11.1 \text{ nm}$$

#### **6.2.2.3 Synthesis of CeB/AO/F127-STE**

The gel from 5 mmol CeB was obtained as described at the beginning of section 6.2.2, and then put into a 60 mL autoclave with 30 mL EtOH. The autoclave was sealed and put into an oven at 200 °C. After heating for 6 h, the autoclave was cooled to room temperature by cold water. Then the sample was centrifuged and washed at least 3 times by EtOH and H<sub>2</sub>O. Then the powder was dried at 105 °C overnight to get the final sample.

$$\mathbf{D_{XRD}}: <3 \text{ nm}; \quad \mathbf{S_{BET}}: 277.0 \text{ m}^2/\text{g}; \quad \mathbf{D_{BJH}}: 3.4 \text{ nm}$$

#### **6.2.2.4 Synthesis of CeB/AO/F127-STE-AC**

Part of the sample prepared in section 6.2.2.3 was put in an Al<sub>2</sub>O<sub>3</sub> crucible and calcined at 500 °C in air for 2 h with 2 °C/min ramping rate.

$$\mathbf{D_{XRD}}: 4.0 \text{ nm}; \quad \mathbf{S_{BET}}: 88.9 \text{ m}^2/\text{g}; \quad \mathbf{D_{BJH}}: 3.9 \text{ nm}$$

#### **6.2.2.5 Synthesis of CeB/AO/F127-STH**

The gel from 5 mmol CeB was obtained as described at the beginning of section 6.2.2, and then put into a 60 mL autoclave with 30 mL H<sub>2</sub>O. The following procedure was the same as that of section 6.2.2.3.

$$\mathbf{D_{XRD}}: 5.1 \text{ nm}; \quad \mathbf{S_{BET}}: 133.6 \text{ m}^2/\text{g}; \quad \mathbf{D_{BJH}}: 5.5 \text{ nm}$$

#### **6.2.2.6 Synthesis of CeB/AO/F127-STH-AC**

Part of the sample prepared in section 6.2.2.5 was put in an Al<sub>2</sub>O<sub>3</sub> crucible and calcined at 500 °C for 2 h with 2 °C/min ramping rate in the air.

$$\mathbf{D_{XRD}}: 5.3 \text{ nm}; \quad \mathbf{S_{BET}}: 132.4 \text{ m}^2/\text{g}; \quad \mathbf{D_{BJH}}: 5.4 \text{ nm}$$

#### **6.2.2.7 Synthesis of CAN/AO/F127-AC**

CAN was used as cerium precursor instead of CeB. The synthesis procedure was the same as that of section 6.2.2.1.

$$\mathbf{D_{XRD}}: 19.6 \text{ nm}; \quad \mathbf{S_{BET}}: 20.0 \text{ m}^2/\text{g}; \quad \mathbf{D_{BJH}}: 4.8 \text{ nm}$$

#### 6.2.2.8 Synthesis of CAN/AO/F127-NAC

CAN was used as cerium precursor instead of CeB. The synthesis procedure was the same as that of section 6.2.2.2.

$$D_{\text{XRD}}: 17.4 \text{ nm}; \quad S_{\text{BET}}: 0.5 \text{ m}^2/\text{g}; \quad D_{\text{BJH}}: - \text{ nm}$$

#### 6.2.2.9 Synthesis of CAN/AO/F127-STE

CAN was used as cerium precursor instead of CeB. The synthesis procedure was the same as that of section 6.2.2.3.

$$D_{\text{XRD}}: 10.0 \text{ nm}; \quad S_{\text{BET}}: 25.1 \text{ m}^2/\text{g}; \quad D_{\text{BJH}}: 10.2 \text{ nm}$$

#### 6.2.2.10 Synthesis of CAN/AO/F127-STE-AC

Part of the sample prepared in section 6.2.2.9 was put in an  $\text{Al}_2\text{O}_3$  crucible and calcined at 500 °C in air for 2 h with 2 °C/min ramping rate.

$$D_{\text{XRD}}: 10.2 \text{ nm}; \quad S_{\text{BET}}: 38.5 \text{ m}^2/\text{g}; \quad D_{\text{BJH}}: 3.5 \text{ nm}$$

#### 6.2.2.11 Synthesis of CAN/AO/F127-STH

CAN was used as cerium precursor instead of CeB. The synthesis procedure was the same as that of section 6.2.2.5. But there was no powder after the hydrothermal treatment, and only a clear solution as the starting one was got.

### 6.2.3 CeO<sub>2</sub> synthesized with different sol composition

#### 6.2.3.1 Synthesis of CeB-STE

5 mmol of CeB was dissolved in 10 mL of DME and then deposited onto glass sheets (20×30 cm<sup>2</sup>), which had been cleaned with 10% KOH, *i*PrOH and acetone and dried at 100 °C. The as-deposited films were exposed to ambient humidity at room temperature for 24 h. The obtained solids were then scraped off with a razor blade to get a gel powder. The gel was put into a 60 mL autoclave with 30 mL EtOH. The autoclave was sealed and put into an oven with 200 °C. After heating for 6 h, the autoclave was cooled to room temperature by cold water. Then the sample were centrifuged and washed at least 3 times by EtOH and H<sub>2</sub>O. Then the powder was at 105 °C overnight to get the final sample.

$$S_{\text{BET}}: 193.3 \text{ m}^2/\text{g}; \quad D_{\text{BJH}}: 4.5 \text{ nm}$$

### 6.2.3.2 Synthesis of CeB-STE-AC

Part of the sample prepared in section 6.2.3.1 was put in an Al<sub>2</sub>O<sub>3</sub> crucible and calcined at 500 °C in air for 2 h with 2 °C/min ramping rate.

$$\mathbf{D}_{\text{XRD}}: 4.9 \text{ nm}; \quad \mathbf{S}_{\text{BET}}: 22.4 \text{ m}^2/\text{g}; \quad \mathbf{D}_{\text{BJH}}: 5.0 \text{ nm}$$

### 6.2.3.3 Synthesis of CeB/AO-STE

5 mmol of CeB was dissolved in 10 mL of DME, then 10 mmol of AO was added and the mixture was stirred for 30 min. The sol was deposited onto glass sheets, followed by the procedure the same as that in section 6.2.3.1.

$$\mathbf{S}_{\text{BET}}: 210.5 \text{ m}^2/\text{g}; \quad \mathbf{D}_{\text{BJH}}: 3.2 \text{ nm}$$

### 6.2.3.4 Synthesis of CeB/AO-STE-AC

Part of the sample prepared in section 6.2.3.3 was put in an Al<sub>2</sub>O<sub>3</sub> crucible and calcined at 500 °C in air for 2 h with 2 °C/min ramping rate.

$$\mathbf{D}_{\text{XRD}}: 4.3 \text{ nm}; \quad \mathbf{S}_{\text{BET}}: 92.4 \text{ m}^2/\text{g}; \quad \mathbf{D}_{\text{BJH}}: 3.1 \text{ nm}$$

### 6.2.3.5 Synthesis of CeB/F127-STE

5 mmol of CeB was dissolved in 10 mL of DME, then 0.025 mmol of F127 was added and the mixture was stirred for 1 h. The sol was deposited onto glass sheets, followed by the procedure the same as that in section 6.2.3.1.

$$\mathbf{S}_{\text{BET}}: 246.9 \text{ m}^2/\text{g}; \quad \mathbf{D}_{\text{BJH}}: 6.2 \text{ nm}$$

### 6.2.3.6 Synthesis of CeB/F127-STE-AC

Part of the sample prepared in section 6.2.3.5 was put in an Al<sub>2</sub>O<sub>3</sub> crucible and calcined at 500 °C in air for 2 h with 2 °C/min ramping rate.

$$\mathbf{D}_{\text{XRD}}: 3.9 \text{ nm}; \quad \mathbf{S}_{\text{BET}}: 153.3 \text{ m}^2/\text{g}; \quad \mathbf{D}_{\text{BJH}}: 5.3 \text{ nm}$$

### 6.2.3.7 Synthesis of CeB-STH

The gel powder was prepared as described in section 6.2.3.1. When the gel was treated by solvothermal processing, H<sub>2</sub>O was used as solvent rather than EtOH. The autoclave was also kept at 200 °C for 6 h, and then treated as described in section 6.2.3.1.

$$\mathbf{S}_{\text{BET}}: 146.6 \text{ m}^2/\text{g}; \quad \mathbf{D}_{\text{BJH}}: 3.8 \text{ nm}$$

#### **6.2.3.8 Synthesis of CeB-STH-AC**

Part of the sample prepared in section 6.2.3.7 was put in an Al<sub>2</sub>O<sub>3</sub> crucible and calcined at 500 °C in air for 2 h with 2 °C/min ramping rate.

$$\mathbf{D_{XRD}: 3.6 \text{ nm}; \quad S_{BET}: 143.3 \text{ m}^2/\text{g}; \quad D_{BJH}: 3.7 \text{ nm}}$$

#### **6.2.3.9 Synthesis of CeB/AO-STH**

The gel powder was prepared as described in section 6.2.3.3, and treated as described in section 6.2.3.7.

$$\mathbf{S_{BET}: 167.1 \text{ m}^2/\text{g}; \quad D_{BJH}: 5.7 \text{ nm}}$$

#### **6.2.3.10 Synthesis of CeB/AO-STH-AC**

Part of the sample prepared in section 6.2.3.9 was put in an Al<sub>2</sub>O<sub>3</sub> crucible and calcined at 500 °C in air for 2 h with 2 °C/min ramping rate.

$$\mathbf{D_{XRD}: 4.4 \text{ nm}; \quad S_{BET}: 165.8 \text{ m}^2/\text{g}; \quad D_{BJH}: 5.6 \text{ nm}}$$

#### **6.2.3.11 Synthesis of CeB/F127-STH**

The gel powder was prepared by the same procedure as in section 6.2.3.5, and treated as described in section 6.2.3.7.

$$\mathbf{S_{BET}: 181.3 \text{ m}^2/\text{g}; \quad D_{BJH}: 4.6 \text{ nm}}$$

#### **6.2.3.12 Synthesis of CeB/F127-STH-AC**

Part of the sample prepared in section 6.2.3.11 was put in an Al<sub>2</sub>O<sub>3</sub> crucible and calcined at 500 °C in air for 2 h with 2 °C/min ramping rate.

$$\mathbf{D_{XRD}: 4.4 \text{ nm}; \quad S_{BET}: 178.5 \text{ m}^2/\text{g}; \quad D_{BJH}: 4.7 \text{ nm}}$$

### **6.2.4 CeO<sub>2</sub> synthesized under different solvothermal conditions**

#### **6.2.4.1 Synthesis of CeB/AO/F127-STE at different temperature**

The synthesis procedure was the same as described in section 6.2.2.3, the sol composition (CeB/AO/F127), the solvothermal solvent (EtOH) and the solvothermal time (6 h) were the same, only the solvothermal temperature was varied from 140 °C to 200 °C.

Temperature (°C)	D <sub>XRD</sub> (nm)	S <sub>BET</sub> (m <sup>2</sup> /g)	D <sub>BJH</sub> (nm)
140	1.89	195.9	3.65
170	2.07	196.4	3.44
200	2.12	277.0	3.43

#### 6.2.4.2 Synthesis of CeB/AO/F127-STE at different reaction times

The synthesis procedure was the same as described in section 6.2.2.3, the sol composition (CeB/AO/F127), the solvothermal solvent (EtOH) and the solvothermal temperature (200 °C) were the same, only the solvothermal time was varied from 3 h to 24 h.

Time (h)	D <sub>XRD</sub> (nm)	S <sub>BET</sub> (m <sup>2</sup> /g)	D <sub>BJH</sub> (nm)
3	2.46	199.3	3.44
6	2.12	277.0	3.43
12	3.33	185.0	3.86
18	3.17	136.4	4.98
24	3.46	95.8	7.51

#### 6.2.4.3 Synthesis of CeB/AO/F127-sol-STE

5 mmol of CeB was dissolved in 10 mL of DME, then 10 mmol of AO was added and the mixture was stirred for 30 min. Then 0.025 mmol of F127 was added and the mixture was additionally stirred for 1 h. 20 mL EtOH was added into the sol to get a 30 mL solution. Then the 30 mL solution was transferred to a 60 mL autoclave directly. The autoclave was sealed and kept at 200 °C for 6 h or 18 h. After that the autoclave was cooled to room temperature by cold water. Then the sample was centrifuged and washed at least 3 times by EtOH and H<sub>2</sub>O. Then the powder was dried at 105 °C overnight to get the final sample.

Time (h)	D <sub>XRD</sub> (nm)	S <sub>BET</sub> (m <sup>2</sup> /g)	D <sub>BJH</sub> (nm)
6	2.12	244.1	4.75
18	2.17	250.1	5.29

### 6.3 Synthesis of Co<sub>3</sub>O<sub>4</sub> modified CeO<sub>2</sub> samples

Cerium *tert*-butoxide (CeB) was synthesized as described in section 6.2.1. Cobalt acetate tetrahydrate, Co(OAc)<sub>2</sub>·4H<sub>2</sub>O was taken as a Co source. All solid chemicals were dried at <10<sup>-3</sup> mbar for more than 5 h to get rid of H<sub>2</sub>O. After drying under vacuum for 5 h, almost all H<sub>2</sub>O of the Co(OAc)<sub>2</sub>·4H<sub>2</sub>O were removed. The dried Co(OAc)<sub>2</sub>·4H<sub>2</sub>O was named as Co(OAc)<sub>2</sub> to distinguish with the original one.

#### 6.3.1 Synthesis of the Ce-L-B-L'-Co single source precursor

##### 6.3.1.1 Synthesis of the POBC-H ligand

*p*-Carboxybenzaldehyde oxime (POBC-H) was synthesized as previously described [15, 16]. *p*-Carboxybenzaldehyde (4.5 g, 30 mmol) and NH<sub>2</sub>OH·HCl (3.13 g, 45 mmol) was dissolved in 90 mL of ethanol and then mixed with NaOAc (3.7 g, 45 mmol) in water (90 mL). The solution was refluxed for 5 h. The solution was then extracted three times by ethyl acetate (EtOH/ethyl acetate ratio 1:4), once with brine and dried over Na<sub>2</sub>SO<sub>4</sub>. Evaporating the solvent under reduced pressure resulted in 4.31 g of the *E*-isomer of POBC-H (yield 87 %).

<sup>1</sup>H NMR (*d*<sub>6</sub>-DMSO): δ = 7.71 (d, 2H, Ph), 7.94 (d, 2H, Ph), 8.21 (s, 1H, CH=N), 11.52 (s, br, 1H, NOH), 12.99 ppm (s,br, 1H, OH); <sup>13</sup>C NMR (*d*<sub>6</sub>-DMSO): δ = 126.40 (Ph) , 129.66 (Ph), 131.11 (C-C=NOH), 137.16 (C-COOH), 147.51 (C=N), 166.90 ppm (COOH).

##### 6.3.1.2 Synthesis of single source precursor

2 mmol of POBC-H and 1 mmol of Co(OAc)<sub>2</sub>·4H<sub>2</sub>O were put into Schlenk tube and dried at <10<sup>-3</sup> mbar for 5 h to get rid of water. Then 5 mL of DME was added and the mixture stirred until a clear purple solution was formed. Then a solution of 1 mmol of CeB in 5 mmol of DME was added and further stirred for 30 min, during which the color of the solution changed to brown, indicating the formation of Ce-POBC-Co SSP.

#### 6.3.2 Synthesis of Co<sub>3</sub>O<sub>4</sub> modified CeO<sub>2</sub> by different routes

The chemical ratio of all precursor components was the same, viz. CeB : Co(OAc)<sub>2</sub> : oximate groups : F127 = 0.8 : 0.2 : 1.6 : 0.005. While the oximate groups for *route 1* and *route 2* were only AO, they were both the oximate group of POBC and AO with a 1:3 ratio for *route 3* (see below).



### 6.3.2.1 Synthesis of $\text{Co}_3\text{O}_4$ modified $\text{CeO}_2$ by 'route 1'

4 mmol of CeB was dissolved in 20 ml of DME, 8 mmol of AO was added and then the mixture was stirred for 30 min. After addition of 0.025 mmol of F127, the mixture was additionally stirred for 1 h. No water was added in this stage. The sol was then deposited onto glass sheets ( $20 \times 30 \text{ cm}^2$ ), which had been cleaned with 10% KOH, *i*PrOH and acetone and dried at  $100 \text{ }^\circ\text{C}$ . The as-deposited films were exposed to ambient humidity at room temperature for 24 h. The obtained solid was then scraped off with a razor blade. The thus obtained gel powder was put into the Teflon liner of the autoclave (60 mL), and 30 mL of EtOH was added, followed by addition of 1 mmol of  $\text{Co}(\text{OAc})_2$  and stirring for 10 min. Then the autoclave was sealed and heated at  $200 \text{ }^\circ\text{C}$  for 6 h. The product was washed at least 3 times with EtOH and  $\text{H}_2\text{O}$  and finally dried at  $105 \text{ }^\circ\text{C}$  overnight. The sample was named '1-STE'. Part of the sample was further heat-treated in air at  $500 \text{ }^\circ\text{C}$  for 2 h (ramping rate:  $2 \text{ }^\circ\text{C}/\text{min}$ ) and is named '1-STE-AC'.

Sample	$D_{\text{XRD}}$ (nm) of $\text{CeO}_2$	$S_{\text{BET}}$ ( $\text{m}^2/\text{g}$ )	$D_{\text{BJH}}$ (nm)
1-STE	3.5	216.5	4.99
1-STE-AC	5.8	96.4	4.56

### 6.3.2.2 Synthesis of $\text{Co}_3\text{O}_4$ modified $\text{CeO}_2$ by 'route 2'

4 mmol of CeB was dissolved in 20 ml of DME, then 8 mmol of AO was added and the mixture was stirred for 30 min, followed by addition of 0.025 mmol of F127 and stirring for an additional 1 h. Then 1 mmol of  $\text{Co}(\text{OAc})_2$  was added and the mixture stirred for additional 30 min. A gel powder was obtained as described for *route 1*. Then the gel powder was put into autoclave with 30 mL pure EtOH and solvocritically treated at  $200 \text{ }^\circ\text{C}$  for 6 h. The product was washed at least 3 times by EtOH and  $\text{H}_2\text{O}$  and finally dried at  $105 \text{ }^\circ\text{C}$  overnight. The sample was named '2-STE'. Part of the sample was further heat-treated in air at  $500 \text{ }^\circ\text{C}$  for 2 h (ramping rate:  $2 \text{ }^\circ\text{C}/\text{min}$ ) and is named '2-STE-AC'.

Sample	$D_{\text{XRD}}$ (nm) of $\text{CeO}_2$	$S_{\text{BET}}$ ( $\text{m}^2/\text{g}$ )	$D_{\text{BJH}}$ (nm)
2-STE	2.7	236.6	7.30
2-STE-AC	6.7	67.6	9.69

### 6.3.2.3 Synthesis of $\text{Co}_3\text{O}_4$ modified $\text{CeO}_2$ by ‘route 3’

As the ratio of Ce:Co in the Ce-CO single source precursor (SSP) is 1:1, extra Ce source needed to be added to get the Ce:Co ratio of 4:1. First 1mmol Ce-POBC-Co SSP was prepared as described in section 6.3.1.2. In another Schlenk tube, 6 mmol of AO was added into a solution of 3 mmol of CeB in 15 mL DME and the mixture was stirred for 30 min. Then the extra Ce solution was mixed with the SSP, and 0.025 mmol of F127 was added and stirred for another 30 min. The sol was treated as that of *route 2*. The as-synthesized sample was named ‘3-STE’ and the sample heat-treated in air was named as ‘3-STE-AC’.

Sample	$D_{\text{XRD}}$ (nm) of $\text{CeO}_2$	$S_{\text{BET}}$ ( $\text{m}^2/\text{g}$ )	$D_{\text{BJH}}$ (nm)
3-STE	2.5	273.2	5.32
3-STE-AC	7.5	25.9	9.04

### 6.3.3 Synthesis of $\text{CeO}_2$ modified by different proportion of $\text{Co}_3\text{O}_4$ via ‘route 1’

The molar percentage of  $\text{Co}(\text{OAc})_2/(\text{CeB} + \text{Co}(\text{OAc})_2)$  (Co% as short) was varied from 10% to 80% and *route 1* was used. The sample with Co% of 20% was the same as the sample synthesized in section 6.3.2.1.

#### 6.3.3.1 Synthesis of $\text{Co}_3\text{O}_4$ modified $\text{CeO}_2$ with 10% Co

The synthesis procedure was the same as described in section 6.3.2.1, but the amount of CeB was changed to 4.5 mmol, AO to 9 mmol and  $\text{Co}(\text{OAc})_2$  to 0.5 mmol. The obtained sample was named ‘1-STE 10%Co’.

Sample	$D_{\text{XRD}}$ (nm) of $\text{CeO}_2$	$S_{\text{BET}}$ ( $\text{m}^2/\text{g}$ )	$D_{\text{BJH}}$ (nm)
1-STE 10%Co	3.0	218.9	4.30

#### 6.3.3.2 Synthesis of $\text{Co}_3\text{O}_4$ modified $\text{CeO}_2$ with 30% Co

The synthesis procedure was the same as described in section 6.3.2.1, but the amount of CeB was changed to 3.5 mmol, AO to 7 mmol and  $\text{Co}(\text{OAc})_2$  to 1.5 mmol. The obtained sample was named ‘1-STE 30%Co’.

Sample	D <sub>XRD</sub> of CeO <sub>2</sub> (nm)	D <sub>XRD</sub> of Co <sub>3</sub> O <sub>4</sub> (nm)	S <sub>BET</sub> (m <sup>2</sup> /g)	D <sub>BJH</sub> (nm)
<i>1-STE 30%Co</i>	2.5	27.5	187.4	4.33

### 6.3.3.3 Synthesis of Co<sub>3</sub>O<sub>4</sub> modified CeO<sub>2</sub> with 80% Co

The synthesis procedure was the same as described in section 6.3.2.1, but the amount of CeB was changed to 1 mmol, AO to 2 mmol and Co(OAc)<sub>2</sub> to 4 mmol. The obtained sample was named '1-STE 80%Co'.

Sample	D <sub>XRD</sub> of CeO <sub>2</sub> (nm)	D <sub>XRD</sub> of Co <sub>3</sub> O <sub>4</sub> (nm)	S <sub>BET</sub> (m <sup>2</sup> /g)	D <sub>BJH</sub> (nm)
<i>1-STE 80%Co</i>	3.3	23.7	122.7	5.43

## 6.4 Synthesis of graphene-CeO<sub>2</sub> and graphene-Co<sub>3</sub>O<sub>4</sub>-CeO<sub>2</sub> composites

### 6.4.1 Synthesis of graphite oxide

Graphite oxide (GO) was synthesized from graphite flakes by the modified Hummer's method [125, 126]. Natural graphite flake powder was obtained from Aldrich. Before the GO preparation, an additional graphite oxidation procedure was carried out in order to oxidize the graphite completely. The graphite flake powder (10 g) was put into an 80 °C solution of concentrated H<sub>2</sub>SO<sub>4</sub> (50 mL), K<sub>2</sub>S<sub>2</sub>O<sub>8</sub> (10 g), and P<sub>2</sub>O<sub>5</sub> (10 g). The resultant dark blue mixture was thermally isolated and allowed to cool to room temperature over a period of 6 h. The mixture was then carefully diluted with distilled water, filtered, and washed on the filter until the rinse water pH became near neutral. The product was dried in air at ambient temperature overnight to form pre-oxidized graphite.

Then the pre-oxidized graphite was used further for oxidation by Hummers' method. 2 g pre-oxidized graphite was put into 100 mL cold concentrated H<sub>2</sub>SO<sub>4</sub>. Then 8 g KMnO<sub>4</sub> was added slowly with stirring and cooling. During this stage, the temperature of the mixture was not allowed to rise over 20 °C. The mixture was then stirred at 35 °C for 2 h. After that 100 mL H<sub>2</sub>O was added and further stirred for 15 min. The reaction was quenched by adding extra 300mL H<sub>2</sub>O and 20 mL of 30% H<sub>2</sub>O<sub>2</sub> solution, after which the color of the mixture changed to bright yellow. The mixture was filtered and washed with 1:10 HCl solution (1 L) in order to remove metal ions. Then the GO product was suspended in 200 mL distilled water to give a viscous,

brown, dispersion, which was then transferred into a big Petri dish. After drying under vacuum, a thin GO layer was obtained, which was cut into small pieces.

#### 6.4.2 Synthesis of rGO-CeO<sub>2</sub> composites

##### 6.4.2.1 With different amounts of rGO

5 mmol of CeB was dissolved in 10 mL of DME, then 10 mmol of AO was added and the mixture was stirred for 30 min. Then 0.025 mmol of F127 was added and the mixture was additionally stirring for 1h. No water was added in this stage. Then different amount of GO (0.02-0.2 g) was added into the sol, which was additionally stirred for 30 min, and then ultrasonically dispersed for at least 2 h. The sol was then deposited onto glass sheets (20×30 cm<sup>2</sup>), which had been cleaned with 10% KOH, *i*PrOH and acetone and dried at 100 °C. The as-deposited films were exposed to ambient humidity at room temperature for 24 h. The obtained solids were then scraped off with a razor blade to get a gel powder. The gel from 5 mmol CeB was put into a 60 mL autoclave with 30 mL EtOH. The autoclave was sealed and put into an oven with 200 °C. After heating for 6 h, the autoclave was cooled to room temperature by cold water. Then the sample was centrifuged and washed at least 3 times by EtOH and H<sub>2</sub>O. Then the powder was dried at 105°C overnight to get the final sample. The samples were named as rGO(x g)-CeO<sub>2</sub>-STE, where x is the weight of GO.

GO amount	D <sub>XRD</sub> of CeO <sub>2</sub> (nm)	S <sub>BET</sub> (m <sup>2</sup> /g)	D <sub>BJH</sub> (nm)
0.2 g	2.6	146.64	4.78
0.1 g	2.2	212.72	3.62
0.05 g	1.9	256.33	3.86
0.02 g	2.0	274.50	3.31

##### 6.4.2.2 Influence of L-ascorbic acid

The GO amount was fixed to 0.02 g, and the gel preparation was the same as described in section 6.4.2.1. Then the gel was treated by two different procedures with L-ascorbic acid (Vc) as reductive agent:

(1) **STE**: The gel from 5 mmol CeB was put into a 60 mL autoclave with 30 mL EtOH and 1 g Vc. The autoclave was sealed and put into an oven at 200 °C. After heating for 6 h, the

autoclave was cooled to room temperature by cold water. Then the sample was centrifuged and washed at least 3 times by EtOH and H<sub>2</sub>O. Then the powder was dried in the oven at 105 °C overnight to get the final sample. The sample was named as Vc-rGO-CeO<sub>2</sub>-STE.

(2) **Reflux:** The gel from 5 mmol CeB was put into a 100 mL flask with 50 mL EtOH and 1 g Vc. Then it was refluxed for 6 h at 150 °C. After that the flask was cooled naturally. Then the sample was centrifuged and washed at least 3 times by EtOH and H<sub>2</sub>O. Then the powder was dried at 105 °C overnight to get the final sample. The sample was named as Vc-rGO-CeO<sub>2</sub>-reflux.

Processing with Vc	Weight loss at 500°C	S <sub>BET</sub> (m <sup>2</sup> /g)	D <sub>BJH</sub> (nm)
<i>STE</i>	43.88	7.90	9.96
<i>STE-AC350°C</i>	5.33	44.67	5.39
<i>Reflux</i>	46.98	3.70	19.94
<i>Reflux-AC350°C</i>	6.31	61.17	4.89

#### 6.4.3 Synthesis of rGO-Co<sub>3</sub>O<sub>4</sub>-CeO<sub>2</sub> composites

The rGO-Co<sub>3</sub>O<sub>4</sub>-CeO<sub>2</sub> composite were prepared by modifying the method in section 6.3.2.1, in which the cobalt precursor was added after the formation of Ce gel. Here the rGO amount was fixed to 0.02 g and different amounts of Vc (0-1 g) were used.

Generally, 4 mmol of CeB was dissolved in 10 mL of DME, then 8 mmol of AO was added and the mixture was stirred for 30 min. Then 0.025 mmol of F127 was added and the mixture was additionally stirring for 1 h. No water was added in this stage. Then 0.02 g GO was added into the sol, which was further stirred for 30 min and then ultrasonically dispersed for at least 2h. The sol was then deposited onto glass sheets (20×30 cm<sup>2</sup>), which had been cleaned with 10% KOH, *i*PrOH and acetone and dried at 100 °C. The as-deposited films were exposed to ambient humidity at room temperature for 24 h. The obtained solids were then scraped off with a razor blade to get a gel powder. The gel from 4 mmol CeB was put into a 60 mL autoclave with 30 mL EtOH, followed by addition of 1 mmol of Co(OAc)<sub>2</sub> and different amount of Vc (0-1 g). After further stirring for 10 min, the autoclave was sealed and put into an oven at 200 °C. After heating for 6 h, the autoclave was cooled to room temperature by cold water. Then the sample was centrifuged and washed at least 3 times with EtOH and H<sub>2</sub>O. Then the powder was dried in the oven at 105 °C overnight to get the final sample.

<b>STE sample</b>	<b>D<sub>XRD</sub> of CeO<sub>2</sub> (nm)</b>	<b>S<sub>BET</sub> (m<sup>2</sup>/g)</b>	<b>D<sub>BJH</sub> (nm)</b>
<b>With different Vc amount</b>			
<i>1 g</i>	1.4	47.40	4.78
<i>0.5 g</i>	1.5	120.46	3.60
<i>0.2 g</i>	1.6	138.18	3.86
<i>0 g</i>	2.6	161.79	3.31

Parts of the above samples were calcined at 350 °C in air for 2 h to remove the rGO.

<b>STE-AC350°C sample</b>	<b>D<sub>XRD</sub> of CeO<sub>2</sub> phase (nm)</b>	<b>S<sub>BET</sub> (m<sup>2</sup>/g)</b>	<b>D<sub>BJH</sub> (nm)</b>
<b>With different Vc amount</b>			
<i>1 g</i>	4.84	60.30	4.39
<i>0.5 g</i>	4.59	66.23	4.17
<i>0.2 g</i>	3.73	81.67	4.17
<i>0 g</i>	4.00	99.82	3.99

## 7. References

- [1] J. Satcher, in, <https://www.llnl.gov/str/May05/Satcher.html>, 2005.
- [2] U. Schubert, N. Hüsing, *Synthesis of inorganic materials*, John Wiley & Sons, **2012**.
- [3] U. Schubert, *Accounts Chem Res*, **40** (2007) 730-737.
- [4] S.O. Baumann, A. Du, C. Artner, C. Maurer, U. Schubert, *Monatsh. Chem.*, **143** (2012) 1637-1642.
- [5] M. Czakler, C. Artner, U. Schubert, *Eur J Inorg Chem*, (2012) 3485-3489.
- [6] M. Lomoschitz, H. Peterlik, K. Zorn, S.O. Baumann, U. Schubert, *J. Mater. Chem.*, **20** (2010) 5527-5532.
- [7] C. Maurer, B. Baumgartner, S. Pabisch, J. Akbarzadeh, H. Peterlik, U. Schubert, *Dalton Trans.*, **43** (2014) 950-957.
- [8] C. Maurer, E. Pittenauer, M. Puchberger, G. Allmaier, U. Schubert, *ChemPlusChem*, **78** (2013) 343-351.
- [9] S.H. Tolbert, *Nat. Mater.*, **11** (2012) 749-751.
- [10] K.-M. Huang, C.-L. Ho, H.-J. Chang, M.-C. Wu, *Nanoscale Res Lett*, **8** (2013) 306.
- [11] S. Badilescu, P.V. Ashrit, *Solid State Ionics*, **158** (2003) 187-197.
- [12] N. Dhiman, B.P. Singh, A.K. Gathania, *J. Nanophotonics*, **6** (2012) 063511, 063511 pp.
- [13] H. Peterlik, H. Rennhofer, V. Torma, U. Bauer, M. Puchberger, N. Hüsing, S. Bernstorff, U. Schubert, *J Non-Cryst Solids*, **353** (2007) 1635-1644.
- [14] R. Deshmukh, U. Schubert, *J. Mater. Chem.*, **21** (2011) 18534-18536.
- [15] J. Yang, J. Akbarzadeh, C. Maurer, H. Peterlik, U. Schubert, *J. Mater. Chem.*, **22** (2012) 24034-24041.
- [16] J. Yang, M. Puchberger, R. Qian, C. Maurer, U. Schubert, *Eur. J. Inorg. Chem.*, **2012** (2012) 4294-4300.
- [17] G. Hua, L. Zhang, G. Fei, M. Fang, *J. Mater. Chem.*, **22** (2012) 6851-6855.
- [18] V. Stetsovych, F. Pagliuca, F. Dvorak, T. Duchon, M. Vorokhta, M. Aulicka, J. Lachnits, S. Schernich, I. Matolinova, K. Veltruska, T. Skala, D. Mazur, J. Myslivecek, J. Libuda, V. Matolin, *J. Phys. Chem. Lett.*, **4** (2013) 866-871.
- [19] R. Prasad, P. Singh, *Catal. Rev.: Sci. Eng.*, **54** (2012) 224-279.
- [20] M. Kipnis, *Appl. Catal., B*, **152-153** (2014) 38-45.



- [21] R. Tiefenthaller, Master thesis, in Institute of material chemistry, Vienna University of Technology, Vienna, October 2012.
- [22] R.J. Gorte, *AIChE J.*, 56 (2010) 1126-1135.
- [23] H.-J. Freund, G. Meijer, M. Scheffler, R. Schloegl, M. Wolf, *Angew. Chem., Int. Ed.*, 50 (2011) 10064-10094.
- [24] G.S. Zafiris, R.J. Gorte, *J. Catal.*, 140 (1993) 418-423.
- [25] T. Bunluesin, R.J. Gorte, G.W. Graham, *Appl. Catal., B*, 15 (1998) 107-114.
- [26] Q. Fu, A. Weber, M. Flytzani-Stephanopoulos, *Catal. Lett.*, 77 (2001) 87-95.
- [27] Y. Huang, A. Wang, X. Wang, T. Zhang, *Int. J. Hydrogen Energy*, 32 (2007) 3880-3886.
- [28] Y. Gao, W. Wang, S. Chang, W. Huang, *ChemCatChem*, 5 (2013) 3610-3620.
- [29] M. Cargnello, V.V.T. Doan-Nguyen, T.R. Gordon, R.E. Diaz, E.A. Stach, R.J. Gorte, P. Fornasiero, C.B. Murray, *Science*, 341 (2013) 771-773.
- [30] C.-W. Tang, C.-B. Wang, S.-H. Chien, *Catal. Lett.*, 131 (2009) 76-83.
- [31] M.P. Woods, P. Gawade, B. Tan, U.S. Ozkan, *Appl. Catal., B*, 97 (2010) 28-35.
- [32] L.F. Liotta, C.G. Di, G. Pantaleo, G. Deganello, *Appl. Catal., B*, 70 (2007) 314-322.
- [33] M. Dhakad, T. Mitshuhashi, S. Rayalu, P. Doggali, S. Bakardjiva, J. Subrt, D. Fino, H. Haneda, N. Labhsetwar, *Catal. Today*, 132 (2008) 188-193.
- [34] A. Trovarelli, *Catal. Rev. - Sci. Eng.*, 38 (1996) 439-520.
- [35] J. Guzman, S. Carrettin, A. Corma, *J. Am. Chem. Soc.*, 127 (2005) 3286-3287.
- [36] M.-N. Guo, C.-X. Guo, L.-Y. Jin, Y.-J. Wang, J.-Q. Lu, M.-F. Luo, *Mater. Lett.*, 64 (2010) 1638-1640.
- [37] J. Xu, L.-C. Wang, Y.-M. Liu, Y. Cao, H.-Y. He, K.-N. Fan, *Catal. Lett.*, 133 (2009) 307-313.
- [38] H.Z. Yang, H. Yu, Y. Ji, X.M. Yu, H. Zhu, Z.M. Li, *Mater. Res. Innovations*, 15 (2011) 391-393.
- [39] M. Zaharescu, A. Wittmar, V. Teodorescu, C. Andronescu, M. Wittmar, M. Veith, *Z. Anorg. Allg. Chem.*, 635 (2009) 1915-1924.
- [40] D.-E. Zhang, A.-M. Chen, M.-Y. Wang, J.-Y. Gong, X.-B. Zhang, S.-Z. Li, G.-Q. Han, A.-L. Ying, Z.-W. Tong, *Funct. Mater. Lett.*, 4 (2011) 97-100.
- [41] Y. Song, J. Wei, Y. Yang, Z. Yang, H. Yang, *J. Mater. Sci.*, 45 (2010) 4158-4162.
- [42] V.D. Araujo, W. Avansi, H.B. de Carvalho, M.L. Moreira, E. Longo, C. Ribeiro, M.I.B. Bernardi, *CrystEngComm*, 14 (2012) 1150-1154.

- [43] Z. Dohcevic-Mitrovic, A. Golubovic, M. Radovic, V. Fruth, A. Kremenovic, A. Meden, B. Babic, M. Scepanovic, Z.V. Popovic, *Phys. Status Solidi A*, 208 (2011) 1399-1402.
- [44] W. Shan, H. Guo, C. Liu, X. Wang, *J. Rare Earths*, 30 (2012) 665-669.
- [45] C.S. Riccardi, R.C. Lima, M.L. dos Santos, P.R. Bueno, J.A. Varela, E. Longo, *Solid State Ionics*, 180 (2009) 288-291.
- [46] J. Wang, M. Shen, J. Wang, J. Gao, J. Ma, S. Liu, *Catal. Today*, 175 (2011) 65-71.
- [47] B. Wang, X. Wu, R. Ran, Z. Si, D. Weng, *J. Mol. Catal. A: Chem.*, 356 (2012) 100-105.
- [48] F. He, X. Meng, X. Shen, J. Xiang, P. Wang, *J. Sol-Gel Sci. Technol.*, 61 (2012) 551-557.
- [49] K. Zhou, X. Wang, X. Sun, Q. Peng, Y. Li, *J. Catal.*, 229 (2005) 206-212.
- [50] H. Li, G. Lu, D. Qiao, Y. Wang, Y. Guo, Y. Guo, *Catal. Lett.*, 141 (2011) 452-458.
- [51] S.A. Hassanzadeh-Tabrizi, E. Taheri-Nassaj, *J. Am. Ceram. Soc.*, 94 (2011) 3488-3493.
- [52] H.R. Pouretedal, Z. Tofangsazi, M.H. Keshavarz, *J. Alloys Compd.*, 513 (2012) 359-364.
- [53] L. Qi, Q. Yu, Y. Dai, C. Tang, L. Liu, H. Zhang, F. Gao, L. Dong, Y. Chen, *Appl. Catal., B*, 119-120 (2012) 308-320.
- [54] L.F. Liotta, M. Ousmane, C.G. Di, G. Pantaleo, G. Deganello, G. Marci, L. Retailleau, A. Giroir-Fendler, *Appl. Catal., A*, 347 (2008) 81-88.
- [55] X.-D. Hou, Y.-Z. Wang, Y.-X. Zhao, *Catal. Lett.*, 123 (2008) 321-326.
- [56] L.F. Liotta, C.G. Di, G. Pantaleo, A.M. Venezia, G. Deganello, *Appl. Catal., B*, 66 (2006) 217-227.
- [57] C.-W. Tang, M.-C. Kuo, C.-J. Lin, C.-B. Wang, S.-H. Chien, *Catal. Today*, 131 (2008) 520-525.
- [58] Y.L. Min, G.Q. He, Q.J. Xu, Y.C. Chen, *Dalton Trans.*, 42 (2013) 12284-12292.
- [59] T. Lu, Y. Zhang, H. Li, L. Pan, Y. Li, Z. Sun, *Electrochim. Acta*, 55 (2010) 4170-4173.
- [60] Y. Zhang, H. Li, L. Pan, T. Lu, Z. Sun, *J. Electroanal. Chem.*, 634 (2009) 68-71.
- [61] M. Srivastava, A.K. Das, P. Khanra, N.H. Kim, J.H. Lee, *Adv. Mater. Res.*, 747 (2013) 242-245.
- [62] S. Yu, Q. Liu, W. Yang, K. Han, Z. Wang, H. Zhu, *Electrochim. Acta*, 94 (2013) 245-251.
- [63] C.O. Avellaneda, M.A.C. Berton, L.O.S. Bulhoes, *Sol. Energy Mater. Sol. Cells*, 92 (2008) 240-244.
- [64] M.C. Ferrara, E. Piscopiello, A.M. Laera, L. Pilloni, S. Mazzarelli, L. Tapfer, *J. Sol-Gel Sci. Technol.*, 60 (2011) 333-339.
- [65] D. Keomany, C. Poinsignon, D. Deroo, *Sol. Energy Mater. Sol. Cells*, 33 (1994) 429-441.
- [66] K. Nakagawa, Y. Murata, M. Kishida, M. Adachi, *Chem. Lett.*, 34 (2005) 296-297.

- [67] K. Nakagawa, Y. Murata, M. Kishida, M. Adachi, M. Hiro, K. Susa, *Mater. Chem. Phys.*, 104 (2007) 30-39.
- [68] D. Chen, L. Cao, F. Huang, P. Imperia, Y.-B. Cheng, R.A. Caruso, *J. Am. Chem. Soc.*, 132 (2010) 4438-4444.
- [69] R. Chen, V. Trieu, H. Natter, K. Stowe, W.F. Maier, R. Hempelmann, A. Bulan, J. Kintrup, R. Weber, *Chem. Mater.*, 22 (2010) 6215-6217.
- [70] J. Yang, H. Peterlik, M. Lomoschitz, U. Schubert, *J. Non-Cryst. Solids*, 356 (2010) 1217-1227.
- [71] S.O. Baumann, M. Puchberger, U. Schubert, *Dalton Trans.*, 40 (2011) 1401-1406.
- [72] J. Yang, L. Lukashuk, H. Li, K. Foettinger, G. Rupprechter, U. Schubert, *Catal. Lett.*, 144 (2014) 403-412.
- [73] K.S.W. Sing, D.H. Everett, R.A.W. Haul, L. Moscou, R.A. Pierotti, J. Rouquerol, T. Siemieniewska, *Pure Appl. Chem.*, 57 (1985) 603-619.
- [74] C. Slostowski, S. Marre, O. Babot, T. Toupance, C. Aymonier, *Langmuir*, 28 (2012) 16656-16663.
- [75] C. Ho, J.C. Yu, T. Kwong, A.C. Mak, S. Lai, *Chem. Mater.*, 17 (2005) 4514-4522.
- [76] X.D. Zhou, W. Huebner, *Appl. Phys. Lett.*, 79 (2001) 3512-3514.
- [77] L. Wu, H.J. Wiesmann, A.R. Moodenbaugh, R.F. Klie, Y. Zhu, D.O. Welch, M. Suenaga, *Phys. Rev. B: Condens. Matter Mater. Phys.*, 69 (2004) 125415/125411-125415/125419.
- [78] Y. Lee, G. He, A.J. Akey, R. Si, M. Flytzani-Stephanopoulos, I.P. Herman, *J. Am. Chem. Soc.*, 133 (2011) 12952-12955.
- [79] W.Y. Pong, H.Y. Chang, H.I. Chen, J.R. Chang, *Surf. Rev. Lett.*, 15 (2008) 123-131.
- [80] E. Beche, P. Charvin, D. Perarnau, S. Abanades, G. Flamant, *Surf. Interface Anal.*, 40 (2008) 264-267.
- [81] P. Patsalas, S. Logothetidis, L. Sygellou, S. Kennou, *Phys. Rev. B: Condens. Matter Mater. Phys.*, 68 (2003) 035104/1-13.
- [82] J. Li, G. Lu, H. Li, Y. Wang, Y. Guo, Y. Guo, *J. Colloid Interface Sci.*, 360 (2011) 93-99.
- [83] S.P. Tandon, J.P. Gupta, *Phys. Status Solidi*, 38 (1970) 363-367.
- [84] G.-R. Li, D.-L. Qu, L. Arurault, Y.-X. Tong, *J. Phys. Chem. C*, 113 (2009) 1235-1241.
- [85] Z. Wu, M. Li, S.H. Overbury, *J. Catal.*, 285 (2012) 61-73.
- [86] M. Li, S. Zhou, Y. Zhang, G. Chen, Z. Hong, *Appl. Surf. Sci.*, 254 (2008) 3762-3766.
- [87] X. Wu, S. Yin, Q. Dong, C. Guo, T. Kimura, J.-i. Matsushita, T. Sato, *J. Phys. Chem. C*, 117 (2013) 8345-8352.

- [88] A.A. Davydov, *Infrared spectroscopy of adsorbed species on the surface of transition metal oxides*, John Wiley & Sons Ltd, **1990**.
- [89] C. Ho, J.C. Yu, T. Kwong, A.C. Mak, S. Lai, *Chem. Mater.*, 17 (**2005**) 4514-4522.
- [90] P. Kondratyuk, *Spectrochim. Acta, Part A*, 61A (**2005**) 589-593.
- [91] K. Nakamoto, *Infrared and Raman spectra of inorganic and coordination compounds. Part A, Theory and applications in inorganic chemistry*, Wiley New York, **1997**.
- [92] C. Artner, M. Czakler, U. Schubert, *Chem. - Eur. J.*, 20 (**2014**) 493-498.
- [93] Q. Ling, M. Yang, R. Rao, H. Yang, Q. Zhang, H. Liu, A. Zhang, *Appl. Surf. Sci.*, 274 (**2013**) 131-137.
- [94] F. Tuinstra, J.L. Koenig, *J. Chem. Phys.*, 53 (**1970**) 1126-1130.
- [95] K.N. Kudin, B. Ozbas, H.C. Schniepp, R.K. Prud'homme, I.A. Aksay, R. Car, *Nano Lett.*, 8 (**2008**) 36-41.
- [96] A.C. Ferrari, J. Robertson, *Phys. Rev. B: Condens. Matter Mater. Phys.*, 61 (**2000**) 14095-14107.
- [97] V. Torma, H. Peterlik, U. Bauer, W. Rupp, N. Husing, S. Bernstorff, M. Steinhart, G. Goerigk, U. Schubert, *Chem Mater*, 17 (**2005**) 3146-3153.
- [98] L.-X. Yang, Y.-J. Zhu, L. Li, L. Zhang, H. Tong, W.-W. Wang, G.-F. Cheng, J.-F. Zhu, *Eur. J. Inorg. Chem.*, (**2006**) 4787-4792.
- [99] A. Jha, C.V. Rode, *New J. Chem.*, 37 (**2013**) 2669-2674.
- [100] P. Gawade, B. Bayram, A.-M.C. Alexander, U.S. Ozkan, *Appl. Catal., B*, 128 (**2012**) 21-30.
- [101] B. Meng, Z. Zhao, X. Wang, J. Liang, J. Qiu, *Appl. Catal., B*, 129 (**2013**) 491-500.
- [102] J.-Y. Luo, M. Meng, X. Li, X.-G. Li, Y.-Q. Zha, T.-D. Hu, Y.-N. Xie, J. Zhang, *J. Catal.*, 254 (**2008**) 310-324.
- [103] J.-Y. Luo, M. Meng, Y.-Q. Zha, L.-H. Guo, *J. Phys. Chem. C*, 112 (**2008**) 8694-8701.
- [104] I. Luisetto, S. Tuti, B.E. Di, *Int. J. Hydrogen Energy*, 37 (**2012**) 15992-15999.
- [105] M. Kang, M.W. Song, C.H. Lee, *Appl. Catal., A*, 251 (**2003**) 143-156.
- [106] A. Yee, S.J. Morrison, H. Idriss, *J. Catal.*, 186 (**1999**) 279-295.
- [107] P. Bera, A. Gayen, M.S. Hegde, N.P. Lalla, L. Spadaro, F. Frusteri, F. Arena, *J. Phys. Chem. B*, 107 (**2003**) 6122-6130.
- [108] S. Shimada, T. Takei, T. Akita, S. Takeda, M. Haruta, *Stud. Surf. Sci. Catal.*, 175 (**2010**) 843-847.
- [109] S. Zeng, X. Fu, T. Zhou, X. Wang, H. Su, *Fuel Process. Technol.*, 114 (**2013**) 69-74.

- [110] K. Tao, Y. Zhang, S. Terao, Y. Yoneyama, T. Kawabata, K. Matsuda, S. Ikeno, N. Tsubaki, *Chem. Eng. J.*, 170 (2011) 258-263.
- [111] K. Huang, M. Lei, Y.J. Wang, C. Liang, C.X. Ye, X.S. Zhao, Y.F. Li, R. Zhang, D.Y. Fan, Y.G. Wang, *Powder Diffr.*, 29 (2014) 8-13.
- [112] X. Wang, D. Liu, S. Song, H. Zhang, *J. Am. Chem. Soc.*, 135 (2013) 15864-15872.
- [113] Y.M. Kim, B.H. Cho, W.B. Ko, *Asian J. Chem.*, 25 (2013) 8178-8180.
- [114] K. Huang, Y.H. Li, S. Lin, C. Liang, X. Xu, Y.F. Zhou, D.Y. Fan, H.J. Yang, P.L. Lang, R. Zhang, Y.G. Wang, M. Lei, *Mater. Lett.*, 124 (2014) 223-226.
- [115] Z. Ji, X. Shen, J. Yang, G. Zhu, K. Chen, *Appl. Catal., B*, 144 (2014) 454-461.
- [116] M. Srivastava, A.K. Das, P. Khanra, M.E. Uddin, N.H. Kim, J.H. Lee, *J. Mater. Chem. A*, 1 (2013) 9792-9801.
- [117] Z.-L. Wang, J.-M. Yan, Y.-F. Zhang, Y. Ping, H.-L. Wang, Q. Jiang, *Nanoscale*, 6 (2014) 3073-3077.
- [118] H. Chen, J. Duan, X. Zhang, Y. Zhang, C. Guo, L. Nie, X. Liu, *Mater. Lett.*, 126 (2014) 9-12.
- [119] S.K. Jha, C.N. Kumar, R.P. Raj, N.S. Jha, S. Mohan, *Electrochim. Acta*, 120 (2014) 308-313.
- [120] X. Zhao, Y. Du, W. Ye, D. Lu, X. Xia, C. Wang, *New J. Chem.*, 37 (2013) 4045-4051.
- [121] Y. Yang, C. Tian, L. Sun, R. Lue, W. Zhou, K. Shi, K. Kan, J. Wang, H. Fu, *J. Mater. Chem. A*, 1 (2013) 12742-12749.
- [122] S. Pei, H.-M. Cheng, *Carbon*, 50 (2012) 3210-3228.
- [123] C. Nethravathi, M. Rajamathi, *Carbon*, 46 (2008) 1994-1998.
- [124] T. Kuila, A.K. Mishra, P. Khanra, N.H. Kim, J.H. Lee, *Nanoscale*, 5 (2013) 52-71.
- [125] N.I. Kovtyukhova, P.J. Ollivier, B.R. Martin, T.E. Mallouk, S.A. Chizhik, E.V. Buzaneva, A.D. Gorchinskiy, *Chem. Mater.*, 11 (1999) 771-778.
- [126] W.S. Hummers, Jr., R.E. Offeman, *J. Am. Chem. Soc.*, 80 (1958) 1339.
- [127] Y. Wang, C.X. Guo, J. Liu, T. Chen, H. Yang, C.M. Li, *Dalton Trans.*, 40 (2011) 6388-6391.
- [128] X. Wang, X. Li, D. Liu, S. Song, H. Zhang, *Chem. Commun. (Cambridge, U. K.)*, 48 (2012) 2885-2887.
- [129] Z. Ji, X. Shen, M. Li, H. Zhou, G. Zhu, K. Chen, *Nanotechnology*, 24 (2013) 115603.
- [130] S. Stankovich, D.A. Dikin, R.D. Piner, K.A. Kohlhaas, A. Kleinhammes, Y. Jia, Y. Wu, S.T. Nguyen, R.S. Ruoff, *Carbon*, 45 (2007) 1558-1565.

- [131] T.N. Lambert, C.A. Chavez, B. Hernandez-Sanchez, P. Lu, N.S. Bell, A. Ambrosini, T. Friedman, T.J. Boyle, D.R. Wheeler, D.L. Huber, *J. Phys. Chem. C*, 113 (2009) 19812-19823.
- [132] D. Joung, V. Singh, S. Park, A. Schulte, S. Seal, S.I. Khondaker, *J. Phys. Chem. C*, 115 (2011) 24494-24500.
- [133] J. Lu, J.-x. Yang, J. Wang, A. Lim, S. Wang, K.P. Loh, *ACS Nano*, 3 (2009) 2367-2375.
- [134] J. Lee, K.S. Novoselov, H.S. Shin, *ACS Nano*, 5 (2011) 608-612.
- [135] Z.-J. Fan, W. Kai, J. Yan, T. Wei, L.-J. Zhi, J. Feng, Y.-M. Ren, L.-P. Song, F. Wei, *ACS Nano*, 5 (2011) 191-198.
- [136] Y. Fu, X. Wang, *Ind. Eng. Chem. Res.*, 50 (2011) 7210-7218.
- [137] N.R. Khalid, Z. Hong, E. Ahmed, Y. Zhang, H. Chan, M. Ahmad, *Appl. Surf. Sci.*, 258 (2012) 5827-5834.
- [138] X. Wang, D. Liu, S. Song, H. Zhang, *Chem. - Eur. J.*, 19 (2013) 5169-5173.
- [139] S. Ghasemi, S.R. Setayesh, A. Habibi-Yangjeh, M.R. Hormozi-Nezhad, M.R. Gholami, *J. Hazard. Mater.*, 199-200 (2012) 170-178.
- [140] J. Zhang, H. Yang, G. Shen, P. Cheng, J. Zhang, S. Guo, *Chem. Commun.*, 46 (2010) 1112-1114.
- [141] J. Gao, F. Liu, Y. Liu, N. Ma, Z. Wang, X. Zhang, *Chem. Mater.*, 22 (2010) 2213-2218.
- [142] M.J. Fernandez-Merino, L. Guardia, J.I. Paredes, S. Villar-Rodil, P. Solis-Fernandez, A. Martinez-Alonso, J.M.D. Tascon, *J. Phys. Chem. C*, 114 (2010) 6426-6432.
- [143] V. Dua, S.P. Surwade, S. Ammu, S.R. Agnihotra, S. Jain, K.E. Roberts, S. Park, R.S. Ruoff, S.K. Manohar, *Angew. Chem., Int. Ed.*, 49 (2010) 2154-2157, S2154/2151-S2154/2120.
- [144] H. Borsook, H.W. Davenport, C.E.P. Jeffreys, R.C. Warner, *J. Biol. Chem.*, 117 (1937) 237-279.
- [145] Q.-Y. Wen, H.-W. Zhang, Q.-H. Yang, Y.-Q. Song, J.Q. Xiao, *J. Magn. Magn. Mater.*, 321 (2009) 3110-3113.
- [146] W.J. Evans, T.J. Deming, J.M. Olofson, J.W. Ziller, *Inorg Chem*, 28 (1989) 4027-4034.
- [147] P.S. Gradeff, F.G. Schreiber, K.C. Brooks, R.E. Sievers, *Inorg. Chem.*, 24 (1985) 1110-1111.

## 8. Curriculum vitae

### Personal Data

---

Name	Dr. Jingxia Yang
Address	Portnergasse 15/27, 1220, Wien
Citizenship	Chinese
Date of Birth	September 17 <sup>th</sup> , 1983
Email	<a href="mailto:yjx09tj@gmail.com">yjx09tj@gmail.com</a>

### Education

---

Since 07/2012	Experimental work for Dr. rer. nat. thesis (Supervisor: Prof. Ulrich Schubert) Institute of Material Chemistry, Vienna University of Technology, Austria
09/2005-03/2010	Master-doctor combined studies for Material Science (Doctor of Engineering, Supervisor: Prof. Zhengguo Jin) School of Materials Science and Engineering, Tianjin University, China
10/2008-06/2009	Experimental work for part of Dr. Eng. thesis (Supervisor: Prof. Ulrich Schubert) Institute of Material Chemistry, Vienna University of Technology, Austria
09/2001-06/2005	Bachelor studies of inorganic and nonmetallic material science and engineering School of Materials Science and Engineering, Tianjin University, China

### Work Experience

---

Since 07/2012	Project assistant (working group of Prof. Ulrich Schubert & Prof. Günther Rupprechter) 'Synthesis of CeO <sub>2</sub> -based materials by a combination sol-gel and solvotherand processing and their application as CO catalyst' Institute of Material Chemistry, Vienna University of Technology, Austria
---------------	---



- 
- 04/2011-03/2012     Project assistant (working group of Prof. Ulrich Schubert)  
‘Design & synthesis of heterometallic single source precursor (Ti-Zn) for Sol-gel Processing’  
Institute of Material Chemistry, Vienna University of Technology, Austria
- 04/2010-06/2012     Research and teaching assistant (working group of Prof. Zhanglian Hong)  
‘Preparation of TiO<sub>2</sub> materials with periodic structures for photocatalytic application’  
Department of Materials Science and Engineering, Zhejiang University, China
- 10/2008-06/2009     Project assistant (working group of Prof. Ulrich Schubert)  
‘Modification of titanium alkoxide and preparations of hybrid mesoporous TiO<sub>2</sub> materials by sol-gel method’  
Institute of Material Chemistry, Vienna University of Technology, Austria
- 03/2005-03/2010     Project assistant (working group of Prof. Zhheguo Jin)  
‘Synthesis of sulfides and selenides thin films by liquid method (CBD, SILAR, electrodeposition) for solar cell application’  
School of Materials Science and Engineering, Tianjin University, China

## Publications

---

- Y. Zhang, J. Feng, Q. Sai, M. Ma, J. Yang, Y. Liu, Sol-gel Synthesis and Photoluminescence Characterization of Ba<sub>2</sub>SiO<sub>4</sub>:Eu<sup>2+</sup> Green Phosphors for White-LED Application, *Integr. Ferroelectr.*, 154 (2014) 128-134.
- J. Yang, L. Lukashuk, H. Li, K. Foettinger, G. Rupprechter, U. Schubert, High Surface Area Ceria for CO Oxidation Prepared from Cerium t-Butoxide by Combined Sol-Gel and Solvothermal Processing. *Catal. Lett.* 144 (2014) 403-412.
- J. Yang, H. Peterlik, C. Maurer, U. Schubert, Sol-gel synthesis of ZnTiO<sub>3</sub> using a single-source precursor based on p-carboxybenzaldehyde oxime as linker, *J. Mater. Chem.*, 22 (2012) 24034-24041.
- J. Yang, M. Puchberger, R. Qian, C. Maurer, U. Schubert, Zinc(II) Complexes with Dangling Functional Organic Groups, *Eur. J. Inorg. Chem.*, 2012 (2012) 4294-4300.
- Z. Hong, Y. Zhang, X. Jiao, C. He, N.R. Khalid, J. Yang, Solvothermal Preparation of Carbon-Enhanced TiO<sub>2</sub>/Graphene Composite and Its Visible Light Photocatalytic Properties, *Integr. Ferroelectr.*, 138 (2012) 152-158.
- Y. Zhang, J. Yang, J. Xu, Q. Gao, Z. Hong, Controllable synthesis of hexagonal and orthorhombic YFeO<sub>3</sub> and their visible-light photocatalytic activities, *Mater. Lett.*, 81 (2012) 1-4.

- 
- J. Yang, Y. Zhang, Z. Hong, R. Ma, D. Zhang, X. Wang, C. Sun, Z. Hu, Preparations of TiO<sub>2</sub> nanocrystal coating layers with various morphologies on Mullite fibers for infrared opacifier application, *Thin Solid Films*, 520 (2012) 2651-2655.
  - J. Chu, Z. Jin, W. Wang, H. Liu, D. Wang, J. Yang, Z. Hong, Influence of anionic concentration and deposition temperature on formation of wurtzite CdS thin films by in situ chemical reaction method, *J. Alloys Compd.*, 517 (2012) 54-60.
  - J. Chu, Z. Jin, S. Cai, J. Yang, Z. Hong, An in-situ chemical reaction deposition of nanosized wurtzite CdS thin films, *Thin Solid Films*, 520 (2012) 1826-1831.
  - L. Ren, Z. Jin, S. Cai, J. Yang, Z. Hong, Green synthesis by diethylene glycol based solution process and characterization of SnS nanoparticles, *Crystal Research and Technology*, 47 (2012) 461-466.
  - H. Tao, Z. Jin, W. Wang, J. Yang, Z. Hong, Preparation and characteristics of CdS thin films by dip-coating method using its nanocrystal ink, *Mater. Lett.*, 65 (2011) 1340-1343.
  - L. Ren, Z. Jin, W. Wang, H. Liu, J. Lai, J. Yang, Z. Hong, Preparation and characterization of SnS nanocrystals by a triethanolamine-assisted diethylene glycol solution synthesis, *Appl. Surf. Sci.*, 258 (2011) 1353-1358.
  - J. Yang, H. Peterlik, M. Lomoschitz, U. Schubert, Preparation of mesoporous titania by surfactant-assisted sol-gel processing of acetaldoxime-modified titanium alkoxides, *J. Non-Cryst. Solids*, 356 (2010) 1217-1227.
  - J. Yang, Z. Jin, C. Li, W. Wang, Y. Chai, Electrodeposition of CuInSe<sub>2</sub> films by an alternating double-potentiostatic method using nearly neutral electrolytes, *Electrochem. Commun.*, 11 (2009) 711-714.
  - J. Yang, Z. Jin, Y. Chai, H. Du, T. Liu, T. Wang, Growth and characterization of CuInSe<sub>2</sub> thin films prepared by successive ionic layer adsorption and reaction method with different deposition temperatures, *Thin Solid Films*, 517 (2009) 6617-6622.
  - T. Wang, Z. Jin, Y. Shi, W. Li, J. Yang, Kinetic Growth of One-Dimensional Zinc-Blende CdTe Nanocrystals by Aqueous Synthesis at Low Temperature, *Cryst. Growth Des.*, 9 (2009) 5077-5082.
  - J. Yang, Z. Jin, T. Liu, C. Li, Y. Shi, An investigation into effect of cationic precursor solutions on formation of CuInSe<sub>2</sub> thin films by SILAR method, *Sol. Energy Mater. Sol. Cells*, 92 (2008) 621-627.
  - J. Yang, Z. Jin, C. Li, T. Wang, T. Liu, Formation of rod-crystals on CuInSe<sub>2</sub> thin films by SILAR method using CH<sub>3</sub>-(CH<sub>2</sub>)<sub>11</sub>-C<sub>6</sub>H<sub>4</sub>-SO<sub>3</sub>Na surfactant, *Mater. Lett.*, 62 (2008) 4177-4180.
  - T. Liu, Z. Jin, J. Yang, L. Feng, Preparation and process chemistry of SnO<sub>2</sub> films derived from SnC<sub>2</sub>O<sub>4</sub> by the aqueous sol-gel method, *J. Am. Ceram. Soc.*, 91 (2008) 1939-1944.